Jordan Journal of
PHYSICS
An International Peer-Reviewed Research Journal

Volume 15, No. 5, Dec. 2022, Jumada2 1444 H

Jordan Journal of Physics (*JJP*): An International Peer-Reviewed Research Journal funded by the Scientific Research and Innovation Support Fund, Jordan, and published quarterly by the Deanship of Research and Graduate Studies, Yarmouk University, Irbid, Jordan.

Manuscripts should be submitted to:

Prof. Mahdi Salem Lataifeh
Editor-in-Chief, Jordan Journal of Physics
Deanship of Research and Graduate Studies
Yarmouk University-Irbid-Jordan
Tel. 00 962 2 7211111 Ext. 2075
E-mail: *jjp@yu.edu.jo*
Website: *http://Journals.yu.edu.jo/jjp*

Jordan Journal of
PHYSICS
An International Peer-Reviewed Research Journal

Volume 15, No. 5, Dec. 2022, Jumada2 1444 H

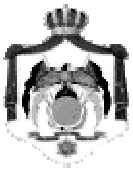

The Hashemite Kingdom of Jordan

Yarmouk University

Jordan Journal of PHYSICS

An International Peer-Reviewed Research Journal

Funded by the Scientific Research and Innovation Support Fund

Volume 15, No. 5, Dec. 2022, Jumada2 1444 H

Instructions to Authors

Instructions to authors concerning manuscript organization and format apply to hardcopy submission by mail, and also to electronic online submission via the Journal homepage website (http://jjp.yu.edu.jo).

Manuscript Submission

1- **E-mail to** : jjp@yu.edu.jo

2- **Online**: Follow the instructions at the journal homepage website.

Original *Research Articles*, *Communications* and *Technical Notes* are subject to critical review by minimum of two competent referees. Authors are encouraged to suggest names of competent reviewers. *Feature Articles* in active Physics research fields, in which the author's own contribution and its relationship to other work in the field constitute the main body of the article, appear as a result of an invitation from the Editorial Board, and will be so designated. The author of a *Feature Article* will be asked to provide a clear, concise and critical status report of the field as an introduction to the article. *Review Articles* on active and rapidly changing Physics research fields will also be published. Authors of *Review Articles* are encouraged to submit two-page proposals to the Editor-in-Chief for approval. Manuscripts submitted in *Arabic* should be accompanied by an Abstract and Keywords in English.

Organization of the Manuscript

Manuscripts should be typed double spaced on one side of A4 sheets (21.6 x 27.9 cm) with 3.71 cm margins, using Microsoft Word 2000 or a later version thereof. The author should adhere to the following order of presentation: Article Title, Author(s), Full Address and E-mail, Abstract, PACS and Keywords, Main Text, Acknowledgment. Only the first letters of words in the Title, Headings and Subheadings are capitalized. Headings should be in **bold** while subheadings in *italic* fonts.

Title Page: Includes the title of the article, authors' first names, middle initials and surnames and affiliations. The affiliation should comprise the department, institution (university or company), city, zip code and state and should be typed as a footnote to the author's name. The name and complete mailing address, telephone and fax numbers, and e-mail address of the author responsible for correspondence (designated with an asterisk) should also be included for official use. The title should be carefully, concisely and clearly constructed to highlight the emphasis and content of the manuscript, which is very important for information retrieval.

Abstract: A one paragraph abstract not exceeding 200 words is required, which should be arranged to highlight the purpose, methods used, results and major findings**.**

Keywords: A list of 4-6 keywords, which expresses the precise content of the manuscript for indexing purposes, should follow the abstract.

PACS: Authors should supply one or more relevant PACS-2006 classification codes, (available at http://www.aip.org/pacs/pacs06/pacs06-toc.html)

Introduction: Should present the purpose of the submitted work and its relationship to earlier work in the field, but it should not be an extensive review of the literature (e.g., should not exceed 1 ½ typed pages).

Experimental Methods: Should be sufficiently informative to allow competent reproduction of the experimental procedures presented; yet concise enough not to be repetitive of earlier published procedures.

Results: should present the results clearly and concisely.

Discussion: Should be concise and focus on the interpretation of the results.

Conclusion: Should be a brief account of the major findings of the study not exceeding one typed page.

Acknowledgments: Including those for grant and financial support if any, should be typed in one paragraph directly preceding the References.

References: References should be typed double spaced and numbered sequentially in the order in which they are cited in the text. References should be cited in the text by the appropriate Arabic numerals, enclosed in square brackets. Titles of journals are abbreviated according to list of scientific periodicals. The style and punctuation should conform to the following examples:

1. Journal Article:

a) Heisenberg, W., Z. Phys. 49 (1928) 619.
b) Bednorz, J. G. and Müller, K. A., Z. Phys. B64 (1986) 189
c) Bardeen, J., Cooper, L.N. and Schrieffer, J. R., Phys. Rev. 106 (1957) 162.
d) Asad, J. H., Hijjawi, R. S., Sakaji, A. and Khalifeh, J. M., Int. J. Theor. Phys. 44(4) (2005), 3977.

2. Books with Authors, but no Editors:

a) Kittel, C., "Introduction to Solid State Physics", 8th Ed. (John Wiley and Sons, New York, 2005), chapter 16.
b) Chikazumi, S., C. D. Graham, JR, "Physics of Ferromagnetism", 2nd Ed. (Oxford University Press, Oxford, 1997).

3. Books with Authors and Editors:

a) Allen, P. B. "Dynamical Properties of Solids", Ed. (1), G. K. Horton and A. A. Maradudin (North-Holland, Amsterdam, 1980), p137.
b) Chantrell, R. W. and O'Grady, K., "Magnetic Properities of Fine Particles" Eds. J. L. Dormann and D. Fiorani (North-Holland, Amsterdam, 1992), p103.

4. Technical Report:

Purcell, J. "The Superconducting Magnet System for the 12-Foot Bubble Chamber", report ANL/HEP6813, Argonne Natt. Lab., Argonne, III, (1968).

5. Patent:

Bigham, C. B., Schneider, H. R., US patent 3 925 676 (1975).

6. Thesis:

Mahmood, S. H., Ph.D. Thesis, Michigan State University, (1986), USA (Unpublished).

7. Conference or Symposium Proceedings:

Blandin, A. and Lederer, P. Proc. Intern. Conf. on Magnetism, Nottingham (1964), P.71.

8. Internet Source:

Should include authors' names (if any), title, internet website, URL, and date of access.

9. Prepublication online articles (already accepted for publication):

Should include authors' names (if any), title of digital database, database website, URL, and date of access.

For other types of referenced works, provide sufficient information to enable readers to access them.

Tables: Tables should be numbered with Arabic numerals and referred to by number in the Text (e.g., Table 1). Each table should be typed on a separate page with the legend above the table, while explanatory footnotes, which are indicated by superscript lowercase letters, should be typed below the table.

Illustrations: Figures, drawings, diagrams, charts and photographs are to be numbered in a consecutive series of Arabic numerals in the order in which they are cited in the text. Computer-generated illustrations and good-quality digital photographic prints are accepted. They should be black and white originals (not photocopies) provided on separate pages and identified with their corresponding numbers. Actual size graphics should be provided, which need no further manipulation, with lettering (Arial or Helvetica) not smaller than 8 points, lines no thinner than 0.5 point, and each of uniform density. All colors should be removed from graphics except for those graphics to be considered for publication in color. If graphics are to be submitted digitally, they should conform to the following minimum resolution requirements: 1200 dpi for black and white line art, 600 dpi for grayscale art, and 300 dpi for color art. All graphic files must be saved as TIFF images, and all illustrations must be submitted in the actual size at which they should appear in the journal. Note that good quality hardcopy original illustrations are required for both online and mail submissions of manuscripts.

Text Footnotes: The use of text footnotes is to be avoided. When their use is absolutely necessary, they should be typed at the bottom of the page to which they refer, and should be cited in the text by a superscript asterisk or multiples thereof. Place a line above the footnote, so that it is set off from the text.

Supplementary Material: Authors are encouraged to provide all supplementary materials that may facilitate the review process, including any detailed mathematical derivations that may not appear in whole in the manuscript.

Revised Manuscript and Computer Disks

Following the acceptance of a manuscript for publication and the incorporation of all required revisions, authors should submit an original and one more copy of the final disk containing the complete manuscript typed double spaced in Microsoft Word for Windows 2000 or a later version thereof. All graphic files must be saved as PDF, JPG, or TIFF images.

Allen, P.B., "…….", in: Horton, G.K., and Muradudin, A. A., (eds.), "Dynamical…….", (North……..), pp….

Reprints

Twenty (20) reprints free of charge are provided to the corresponding author. For orders of more reprints, a reprint order form and prices will be sent with the article proofs, which should be returned directly to the Editor for processing.

Copyright

Disclaimer

Indexing

JJP is currently indexing in:

Scopus	ULRICHSWEB GLOBAL SERIALS DIRECTORY

Jordan Journal of
PHYSICS
An International Peer-Reviewed Research Journal

Volume 15, No. 5, Dec. 2022, Jumada2 1444 H

Table of Contents:

Volume 15, Number 5, 2022. pp. 429-444

Jordan Journal of Physics

REVIEW ARTICLE

The Status of Green Synthesis of Silver Nanoparticles Using Plant Extracts during Last Fifteen Years

Banaz S. Haji[a] and **Azeez A. Barzinjy**[b,c]

[a] *Department of Physics, College of Education, Salahaddin University-Erbil, Kurdistan Region, Iraq.*
[b] *Scientific Research Center, Soran University, Kurdistan Region, Iraq*
[c] *Department of Physics Education, Faculty of Education, Tishk International University-Erbil, Kurdistan Region, Iraq.*

Doi: **https://doi.org/10.47011/15.5.1**

Received on: 01/07/2022; *Accepted on: 17/08/2022*

Abstract: Nanoparticles (NPs) are tiny particles with their dimensions ranging between1and100 nm. These are gaining cumulative attention owing to their vast use in different fields of applications. There are three main methods for synthesizing NPs; namely, physical, chemical and biological methods. Physical methods consume a lot of energy and time, require expensive vacuum systems and high temperatures and on top of all, they are not environmentally friendly. Chemical methods, in general, are expensive, increase the particle toxicity and perhaps harm human health and the environment. In addition, hazardous chemicals gather on the top of NPs and confine their applications. Therefore, green method is an alternative replacement to the traditional chemical and physical methods for synthesizing NPs. The existing phytochemicals, for instance in plant extracts, own a remarkably high ability for reducing metal ions within a short time comparing with other microorganisms, which require a longer incubation period. This study is concentrating on green synthesis of silver (Ag) NPs, owing to the significance of Ag NPs whose optical properties depend on their size and shape. In addition, Ag NPs possess numerous applications, especially in solar cells, water treatment and medicine. This review aims to highlight the remarkable growth of green synthesis of Ag NPs, in terms of publications, citations, active and productive researchers, targeting journals and the eminent countries in this regard. This review, also, is highlights the most utilized plants for producing Ag NPs in fourteen years; i.e., 2007-2021.This review, also, evaluating the most acceptable proposed mechanism for biosynthesizing Ag NPs using plant extracts. We believe that this review article will facilitate and brighten the road in front of researchers who want to initiate their study with the biosynthesis of Ag NPs from plant extracts.

Keywords: Silver nanoparticles, Green synthesis, Plant extracts, Stabilizing agents, Reducing agents.

Corresponding Author: Azeez Abdullah Barzinjy **Email**: azeez.azeez@su.edu.krd

1. Introduction

Nanotechnology is a rapidly expanding subject that has likely been utilized in a wide range of commercial products. Through generating nanoparticles (NPs) and nanoproducts, new and size-dependent physical and chemical characteristics that differ considerably from bulk materials can be produced [1]. In recent years, the scientific community has made a significant progress in the field of nanoscience and nanotechnology [2]. Nanoparticles have improved properties due to certain features, such as high surface area per unit volume and quantum confinement. Quantum confinement causes a relatively larger value of energy band gap which can offer improved optoelectronic devices, thermal applications, batteries and sensors as a semiconductor material. Nanomaterials have been utilized in countless applications owing to their exclusive features. Innovative, effective requests of nanomaterials and nanostructures can be perceived in drug delivery [3, 4], nano-medicine [4, 5], food packing [5, 6], disinfected processes [7], correlative microscopy [8], imaging [9, 10], optics [11], micro-electronics [12], three-dimensional (3D) lithography [13, 14], renewable energy [15, 16], wastewater treatment [17] and catalysis [18, 19].

NPs can be categorized into two wide-ranging groups; *i.e.,* organic and inorganic NPs. Inorganic NPs are semiconductor NPs (ZnO, ZnS, CdS), metallic NPs (Au, Ag, Cu, Al) and magnetic NPs (Co, Fe, Ni) [20]. Organic NPs are carbon-based NPs for instance quantum dots, fullerenes and carbon nanotubes. The demands for gold (Au) and silver (Ag) NPs are increasing speedily owing to their greater features and flexible characteristics [21]. Metallic NPs, generally, have numerous compensations [22]. Firstly, their optical characteristics can be controlled effortlessly; in other words, they are outstanding optical absorbers [23]. Secondly, they can be employed in numerous requests to achieve some precise resolutions; for example, speedy thermal reaction [24], erosion resistance [25], recyclability [26] and many others.

In this review, the authors are focusing on Ag NPs owing to their sole and progressive applications in different fields, comprising medical, food, health-care, customer and industrialized resolves, owing to their exclusive physical and chemical characteristics. These, also, comprise optical, electrical, thermal and biological features. In addition, the superiority of Ag NPs is as a result of their nature, dimension, crystallinity, configuration and construction compared to the bulk analogues [27, 28]. These innovations have been employed in a large scope of possible applications; for example, biomedical tools, medicine, renewable energies, makeups, ecological remediation, food, user and industrialized resolves [29].

Ag NPs synthesis, and in general that of other NPs, can be conducted through two main methods; *i.e.*, top-down and bottom-up methods [30]. In the top-down method, the NPs are created from the bulk material. In the bottom-up method, the NPs can be produced through the nucleation and growth processes of the atoms. The first method, also known as a physical method, consists of a set of separate techniques; ball or mechanical milling [31, 32], laser ablation [33-35], evaporation condensation [36], electromagnetic levitation gas condensation (ELGC) [37], ultra-sonication [38-40], lithography [41, 42], spray pyrolysis [43-45], radiolysis [46], arc discharge [47-49] and photo-irradiation [50] which are among the examples of the physical methods. These methods can be used for extensive construction, but they are expensive, not safe and time-consuming methods [51]. In the bottom-up, or chemical, methods, the chemical substances can be utilized to reduce metallic cations to procedure zero-charged metallic atoms, then these metallic atoms undergo nucleation and the growth state to form metallic NPs [52]. The chemical methods are mostly accompanied by the addition of stabilizers to deliver stability, avoid aggregation, control morphology and provide compatible properties [53]. Sol-gel method [54-56], traditional chemical reduction [57-59], inverse micelle [60, 61], co-precipitation [62], chemical vapor deposition [63], solvo-thermal [64, 65] and electrochemical reduction [66, 67] are the most utilized chemical methods for producing metallic NPs, such as Ag NPs [68]. The chemical methods provide a harmful impact on the manufacturers and operators due to employing hazardous chemical materials as reducing, capping and stabilizing agents. Consequently, the chemical methods cause numerous troubles for the human and the environment simultaneously. Hence, currently, investigators started focusing on the green

method for synthesizing NPs [69]. This interest sees its impact significantly in the number of publications, especially in recent years (Fig. 1).

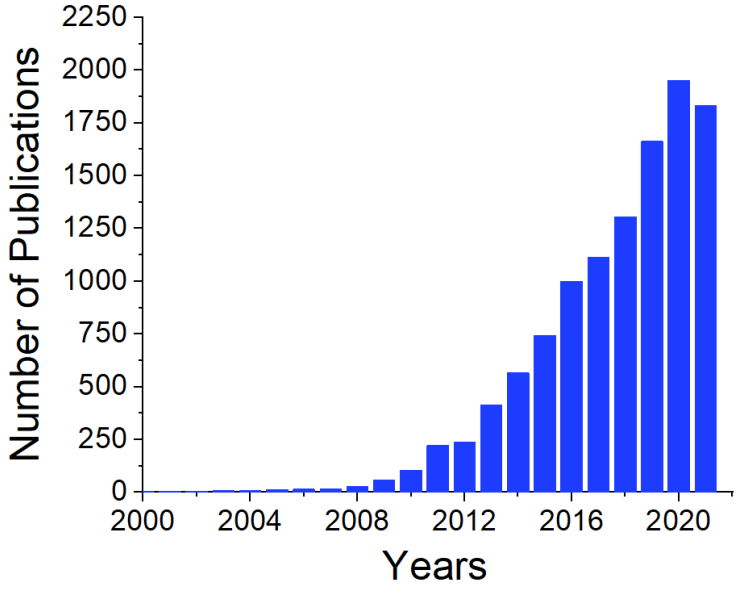

FIG. 1, Number of publications of green synthesis of NPs (using web of science).

In addition, the fabrication of nanomaterials using biological method is gaining more attention in many countries due to its ease, eco-friendliness, low cost and avoiding toxic chemicals (Fig. 2). Green synthesis of NPs includes using natural materials, such as plants and microorganisms, such as bacteria, fungi, algae and yeasts [70]. Nevertheless, compared to bacteria, fungi, algae and yeasts, the available phytochemicals in plant extracts own an extremely higher aptitude for reducing metal ions in a short period of time [71, 72].

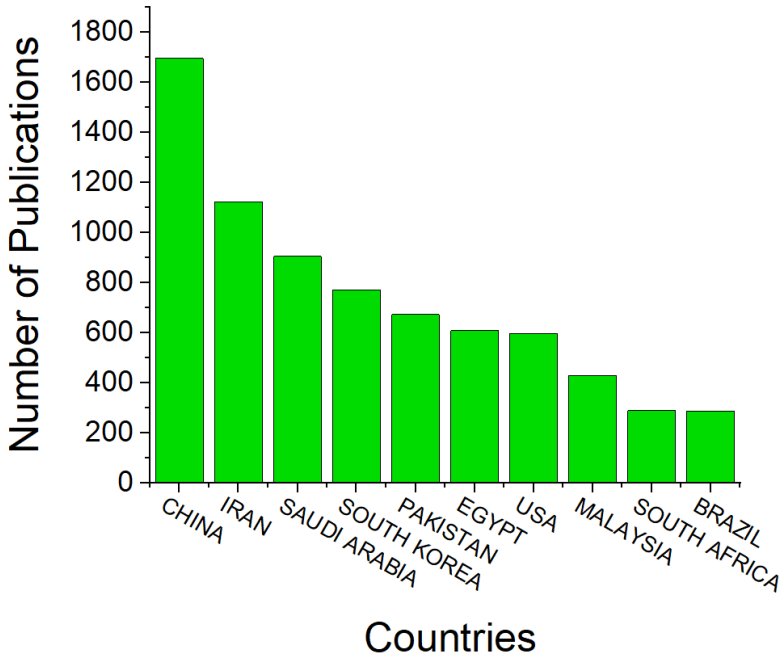

FIG. 2. Top-ten countries using green-synthesis methods for NPs preparation (web of science).

Thus, plant extracts are observed as an outstanding source for synthesizing metallic NPs. Besides, plant-based synthesis process, for synthesizing NPs, is a foremost procedure over the microorganism procedure owing to its straightforwardness, quickness and avoiding of culture maintenance [73]. Likewise, plant supplies, such as flowers, leaves, seeds, stems, fruits and peels, have been utilized as reducing and capping agents in NPs fabrication procedure [74].

This review article is a continuation of our recent works [20, 75-85] regarding green synthesis of nanomaterials. This review is highlighting green synthesis of Ag NPs using plant extracts. The novelty of this review is that the relevant readers can get necessary information regarding green synthesis of Ag NPs in terms of publications, citations, productive researchers, targeting journals and countries in this respect. This review, similarly, highlights the most employed plant extracts for fabricating Ag NPs from 2007 to 2021. The most acceptable proposed mechanism for biosynthesizing Ag NPs using plant extracts is also presented in this investigation. According to our best knowledge, this review article will simplify and brighten the road for the relevant researchers who need to start their journey with the biosynthesis of Ag NPs from plant extracts.

2. Materials and Methods

The data of this investigation was collected *via* an online database. "Web of Science" version 5.35 as a data source was used. Since it contains a large number of authoritative data and is often used as a scientific, academic and fact-finding resource for scholarly publications, the Web of Science has been used to cover and access data. The current study, based mainly on the Web of Science, selected all the data related to the synthesis of green Ag NPs from 2007 until December 2021 and the research necessitated the exact selection of titles, keywords and abstracts extensively.

3. Results and Discussion

Ag, possessing the atomic number 47, is a lustrous, ductile and malleable metal that is slightly harder than gold. It is one of the most fundamental components of our planet. It can be found in nature as a natural component, in amalgamation with other metals; for instance, gold, as well as raw materials; namely, chlorargyrite and argentite. Chemically, silver holds four dissimilar oxidation states; *i.e.,* Ag^{0}, Ag^{1+}, Ag^{2+} and Ag^{3+} [86]. Nevertheless, it is a chemically inactive component; however, it can respond to nitric acid or hot intense sulfuric acid, making solvable silver salts. Even though it has outstanding heat and electrical conductivities, its uses in the electrical sector have been severely constrained owing to its higher cost [87]. The metallic form of silver is water-insoluble; nevertheless, its metallic salts; for instance silver nitrate ($AgNO_3$) and silver chloride (AgCl), are dissolving in water easily. This study is focusing on the green synthesis of Ag NPs using plant extracts, during 14 years, from 2007 to 2021. According to the Web of Science, there are 292 published articles, some of which are very essential and suitable, especially for new researchers in green synthesis of Ag NPs. It can be seen, in Fig. 3, that the pace of publishing increases exponentially over time. This trend is, perhaps, due to the importance of this topic.

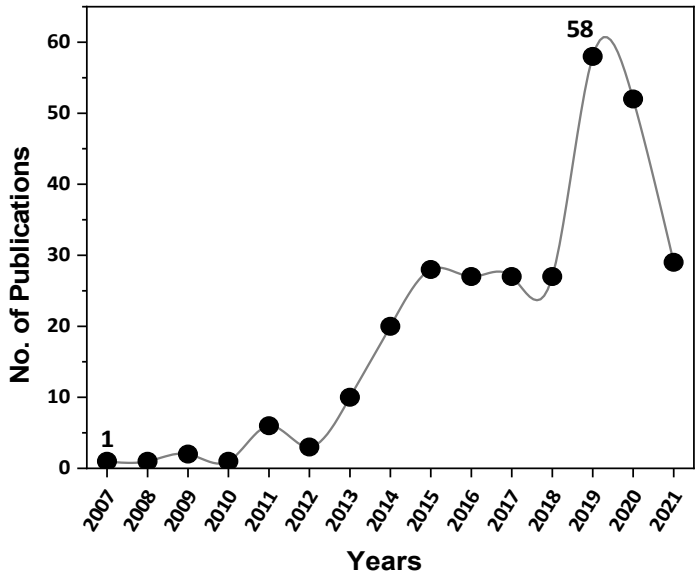

FIG. 3. Development of published articles regarding Ag NPs from 2007 to 2021.

It can be noticed from Fig. 3 that in 2007, there was only one published article about Ag NPs. After that, the number of scientific articles in this field increased dramatically. Consequently, one can predict that the applications of Ag NPs have increased intensely in several fields. These applications cover medical, food, sensors, solar cells, health-care, consumer and many industrial purposes. This is not astonishing, since Ag NPs possess unique physical and chemical properties when it goes to the nanoscale. Also, optical, electrical and thermal properties of Ag NPs improve compared with the silver bulk analogues. In the last three years, one can observe that the number of publications is increasing noticeably. With all of the challenges that faced the world in 2020 owing to COVID-19 and social distancing, the greatest rate of publishing was in 2019 and the number of publications started to decrease in 2020. Although the number of published articles in 2020 has decreased slightly compared to 2019, the highest number of citations has been made for the articles that have been published in that year (Fig. 4).

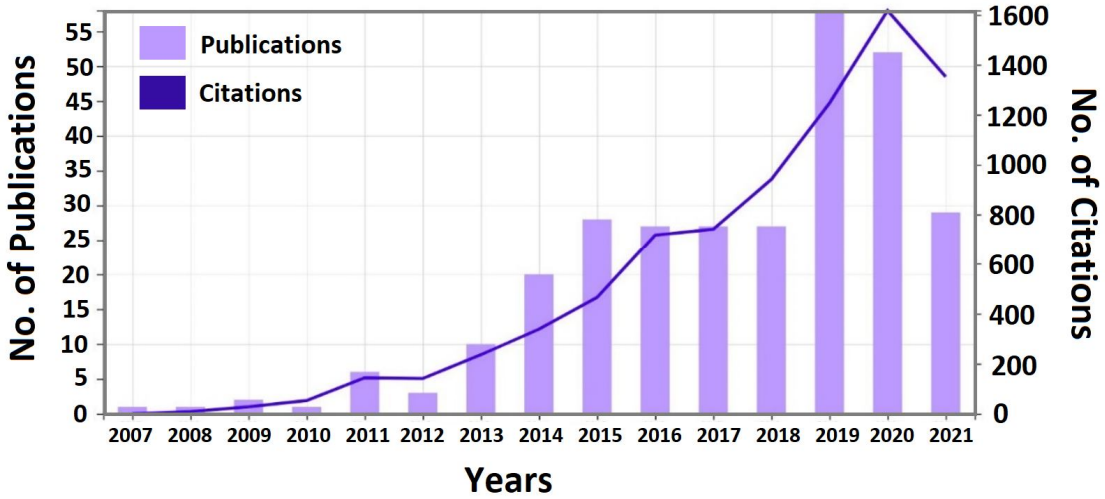

FIG. 4. Number of citations and publications per year.

3.1 Studying the Top Ten Journals

There are many scientific journals in which it is possible to publish extensive scientific studies in various fields of science. However, choosing the most appropriate and best one is an important matter that requires great knowledge and effort. In this part of our study, we highlighted the top ten journals in terms of the quantity of publications in the green synthesis of Ag NPs using plant extracts. It can be seen, from Table 1, that ten reputable journals have been selected according to their relatively high impact factors. It can be stated that during this selected time; *i.e.,* from 2007-2021, 62 publications, regarding green synthesis of Ag NPs using different plant extracts, were published in these journals. About 24% of these articles were published in "RSC advances" Journal, about 14% of these articles were published in the international journal of biological macromolecules, while the other remaining journals took about 8% each of the publications, respectively. In terms of the impact factors of these selected journals, one can notice, from Table 1, that the highest impact factor goes to carbohydrate polymers journal, which published only 4 articles, while the lowest impact factor goes to materials research express journal, which published 5 articles during this period of time. In addition, in terms of the country of origin for these selected journals, each of the United Kingdom and Netherlands took 30% of these journals, while the United States took 20% and each of Germany and New Zealand took only 10% of theses journals. Moreover, more than 38% of these articles were published in the United Kingdom, more than 30% in Netherlands and more than 16% in the United States. The reaming 16% went to Germany and New Zealand. Table 1 also shows that the highest accepting rate among these selected journals goes to the RSC advances, while the lowest accepting rate goes to both of carbohydrate polymers and international journal of nanomedicine, respectively.

TABLE 1. The top ten journals regarding green synthesis of Ag NPs during 2007-2021.

No.	Journal name	Number of publications	Country	Impact factor (2020)
1	RSC advances	15	United Kingdom	3.361
2	International journal of biological macromolecules	9	Netherlands	6.953
3	Materials science & engineering c-materials for biological applications	5	Netherlands	7.328
4	Applied surface science	5	Netherlands	6.707
5	Journal of applied polymer science	5	United States	3.125
6	Journal of cluster science	5	United States	3.061
7	Green processing and synthesis	5	Germany	2.83
8	Materials research express	5	United Kingdom	1.62
9	Carbohydrate polymers	4	United Kingdom	9.381
10	International journal of nanomedicine	4	New Zealand	6.4

3.2 The Countries/ Regions

The researchers in this review believe that investigating interest in the synthesis of green Ag NPs from plant extracts at the country level is important to researchers, but explaining the reason for this interest is even more important. Accordingly, another attempt of this investigation was highlighting the top ten countries that have an active role in this field. Table 2 shows the most productive countries, in terms of number of publications, in the field of green synthesis of Ag NPs.

TABLE 2. Top ten countries for Ag NPs research during the study period.

No.	Country	Region	Number of publications
1	India	South Asia	118
2	China	East Asia	46
3	South Korea		33
4	United States	North America	27
5	Saudi Arabia	Middle East Asia	18
6	Iran	Central Asia	16
7	Turkey	Europe	10
8	Malaysia	Southeast Asia	9
	South Africa	South Africa	9
9	Brazil	South America	8
10	Egypt	Northeast Africa	7
	Taiwan	East Asia	7

It can be seen, from Table 2, that India is at the forefront in this group. Within this period of time, between 2007 and 2021, 118 reliable articles have been published in India regarding the green synthesis of Ag NPs using plant extracts between 2007 and 2021. The second country is China which published 46 articles in this area. Nanotechnology is a rapidly expanding field of science and it brings benefits to many areas of science and industry. East Asia region, including (China, Taiwan, South Korea, India and Iran), published (80.19%) of the publications in the top ten countries in fourteen years. It was followed by America (11.36%), Africa (5.19%) and Europe (3.25%) regions, as shown in Fig. 5.The authors believe that the secret of this great interest is in the abundance of plants and the vast green space in these countries [88, 89]. These consequences show that Ag NPs represent one of the most popular types of NPs, owing to their application in many fields [90]. As stated before, there are many different ways to obtain Ag NPs; however, green-synthesis method using plant extracts is undoubtedly a leading method [91]. This is attributed to the many benefits associated with this method [92].

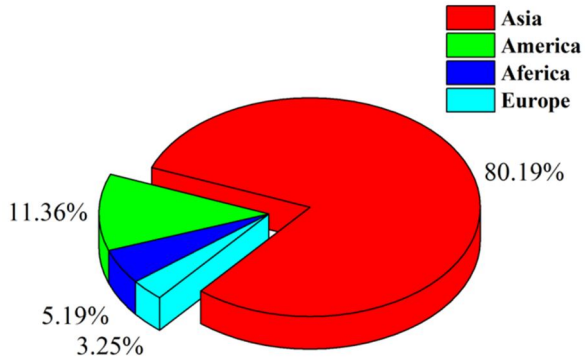

FIG. 5. Effective continental participation for the green synthesis of Ag NPs.

3.3 Covering Ten Most Cited Researches

A large number of published research indicates that the synthesis of NPs through biosynthesis methods is environmentally friendly and inexpensive [93]. Although the number of citations does not reflect the degree of importance of the published work, it indicates the interest of the scientific community in this work [94]. Table 3 lists the top ten most cited works in the field of green synthesis of Ag NPs. It can be noticed, from Table 3, that there are 2256 citations in all of the published research regarding green synthesis of Ag NPs. Kumar *et al.* conducted a research entitled; "*Silver-nanoparticle-embedded antimicrobial paints based on vegetable oil"* in 2008, which possesses the highest citations (732). This work has been published in "*Nature Materials*" journal [95]. This study is about the addition of Ag NPs to paint that shows excellent antimicrobial properties through killing both Gram-positive human pathogens (*Staphylococcus aureus*) and Gram-negative bacteria (*Escherichia coli*). The process developed here is quite general and can be applied in the synthesis of a variety of metal NPs in oil medium. This approach is an eco-friendly method to synthesize metal NPs for embedded paint, in a single step, that can be utilized from household paint [95]. The second most cited publication belongs to Tolaymat *et al.* with 518 citations, entitled "*An evidence-based environmental perspective of manufactured silver nanoparticles in syntheses and applications: A systematic review and critical appraisal of peer-reviewed scientific papers*". This study was published in the journal of "*Science of the Total Environment*" [96]. The third article is cited only 321 times and was published by Shao *et al.* in 2015 under the title of "*Preparation, Characterization and Antibacterial Activity of Silver Nanoparticle-decorated Graphene Oxide Nanocomposite*" [97]. The fourth investigation under the title "*An environmentally benign antimicrobial nanoparticle based on a silver-infused lignin core*", published in the journal "*Nature Nanotechnology*" in 2015 by Richter *et al.,* possesses 290 citations [98]. The fifth article was "*Humic Acid-induced Silver Nanoparticle Formation under Environmentally Relevant Conditions*" with 222 citations and was published in 2011 in the journal "*Environmental Science & Technology*" [99]. These articles are five out of the ten most cited research articles, helping related readers and researchers understand and summarize the status of the green synthesis of Ag NPs.

TABLE 3. Top ten cited studies regarding Ag NPs during the study time.

No.	Articles	Authors	Publishing journals	Year of publication	Citations
1	Silver-nanoparticle-embedded antimicrobial paints based on vegetable oil	-Kumar, A -Vemula, PK -Ajayan, PM -John, G1	Nature Materials	2008	732
2	An evidence-based environmental perspective of manufactured silver nanoparticles in syntheses and applications: A systematic review and critical appraisal of peer-reviewed scientific papers	-Tolaymat, TM -El Badawy,M -Genaidy,A -Scheckel,KG -Luxton,TP -Suidan,M	Science of the Total Environment	2010	518

No.	Articles	Authors	Publishing journals	Year of publication	Citations
3	Preparation, Characterization and Antibacterial Activity of Silver Nanoparticle-decorated Graphene Oxide Nanocomposite	-Shao, W -Liu, XF -Min, HH -Dong, GH -Feng, QY -Zuo, SL	Acs Applied Materials & Interfaces	2015	321
4	An environmentally benign antimicrobial nanoparticle based on a silver-infused lignin core	-Richter, AP -Brown, JS -Bharti, B -Wang, A -Gangwal, S -Houck, K -Hubal, EAC -Paunov, VN -Stoyanov, SD -Velev, OD	Nature Nanotechnology	2015	290
5	Humic Acid-induced Silver Nanoparticle Formation under Environmentally Relevant Conditions	-Akaighe, N -MacCuspie, RI -Navarro, DA -Aga, DS -Banerjee, S -Sohn, M -Sharma, VK	Environmental Science & Technology	2011	222
6	Green synthesis of silver nanoparticles: Biomolecule-nanoparticle organizations targeting antimicrobial activity	-Roy, A -Bulut, O -Some, S -Mandal, AK -Yilmaz, MD	Rsc Advances	2019	206
7	Green synthesis of biopolymer-silver nanoparticle nanocomposite: An optical sensor for ammonia detection	-Pandey, S -Goswami, GK -Nanda, KK	International Journal of Biological Macromolecules	2012	186
8	Phytosynthesis of Silver Nanoparticles Using *Gliricidia sepium* (Jacq.)	-Rajesh, R -Jaya, L -Niranjan, K -Vijay, M -Sahebrao, K	Current Nanoscience	2009	178
9	Physicochemical properties of gelatin/silver nanoparticle antimicrobial composite films	-Kanmani, P -Rhim, JW	Food Chemistry	2014	174
10	Graphene oxide and shape-controlled silver nanoparticle hybrids for ultrasensitive single-particle surface-enhanced Raman scattering (SERS) sensing	-Fan,W -Lee,YH -Pedireddy, S -Zhang, Q -Liu, TX -Ling, XY	Nanoscale	2014	161

It can be seen, from Table 3, that the citation number is decreasing dramatically from article 5 to 10. According to the best of our knowledge, analyzing the top 10 articles in terms of the number of citations as well as the target journal helps related researchers reach the corrected journal easily, in addition to showing the importance of the selected articles in terms of science, application and presentation.

3.4 Authors' Profiling

There are several international standards that highlight the reputation of researchers and highlight the reliability of their research. Among these standards are the number of publications, H-index, total citations and field of the research, which measure the academic output of a researcher [100]. Table 4 highlights the top ten most productive researchers in the field of green

synthesis of Ag NPs, as measured by the number of publications, H-index, total citation and citation per study. Vijay Kumar acknowledged 5 papers in the topic of green synthesis of Ag NPs, with a total of 118 citations. Each of Sneha Mohan Bhagyaraj, Baskaralingam Vaseeharan, Sekar Vijayakumar and Shishir V. Kumar has published four articles in the field of green synthesis of Ag NPs. Individually, Sangiliyandi Gurunathan, Chen, Xi, Resat Apak, Ravi Kumar Gundampati and Hasan, Syed Hadi has published three articles in the field of green synthesis of Ag NPs. On the other hand, Resat Apak comes on the top researchers in the list through having 435 articles and 16414 citations. Sangiliyandi Gurunathan, in turn, has the highest H-index: 61, followed by Resat Apak who has H-index: 58.

TABLE 4. Top ten authors in the field of Ag NPs along the study period.

No.	Authors	Publication in the field of study	All publications	H-index	Total citations	Citations in this field
1	Vijay Kumar	5	57	12	453	118
2	Sneha Mohan Bhagyaraj	4	35	11	478	85
3	Baskaralingam Vaseeharan	4	236	44	7047	81
4	Sekar Vijayakumar	4	66	23	1796	81
5	Shishir V Kumar	4	11	7	215	50
6	Sangiliyandi Gurunathan	3	192	61	15350	186
7	Chen, Xi	3	6	6	155	131
8	Resat Apak	3	435	58	16414	114
9	Ravi Kumar Gundampati	3	62	14	680	113
10	Hasan, Syed Hadi	3	92	34	3349	113

3.5 Mechanism of the Biosynthesis of Ag NPs from Plant Extracts

Biosynthesis, photosynthesis or green synthesis of NPs has the advantages of reducing energy consumption [101]. This synthesizing method is far away from using hazardous/toxic chemical elements, sophisticated and costly laboratories for NPs preparation [102]. In plant extracts-mediated green synthesis of Ag NPs (Fig. 6), it is possible to produce NPs through the reaction of the secondary metabolites present in the plant extracts, such as flavonoids, terpenes, alkaloids, phenols, saccharides and many others [103]. The available phytochemicals in the plant extracts are acting as reducing, capping and stabilizing agents [104]. These hydroxyl groups are able to reduce Ag^{+} ions into metallic zerovalent Ag^{0} [105]. After the reduction process, the zerovalent metal will go to the nucleation stage (Fig. 6) within a short burst. After that, the capping process will initiate around the surface of the Ag NPs. These capping agents work as stabilizers or binding molecules that stop over agglomeration and stabilize the interaction of NPs within the surrounding medium [106]. The race among capping and growth rate regulates the size of the NPs [107]. The key function of a capping agent throughout the synthesizing of the NPs is to control the nucleation procedure and agglomeration when the essential amount is utilized to successfully stabilize the NPs. The outcomes of the UV-Vis spectroscopy analysis indicated that all the synthesized Ag NPs possess blue-shifted absorption spectrum, while the surface Plasmon resonance of the bulk Ag is around 1000 nm [108]. Incalculable chemical capping agents are employed to control the synthesis of NPs. Nevertheless, in the green synthesis method using plant extracts, for instance, the plant extract can provide the capping agents and there is no need to add external capping agents [109]. Normally, the flavonoids initiate the capping on the NPs, while phenolic combinations make multi-chelating bonds and stabilize the NPs after nucleation, resulting in the formation of different-sized NPs [110].Additionally, proteins are an outstanding basis of characteristic functional groups that can be employed in moderating the surface of the NPs; *i.e.,* as a capping agent [111]. In the absence of the capping agent, metal, after reduction, will agglomerate and precipitate out. Both reducing and stabilizing agents play important roles in controlling the particle sizes, shapes, monodispersity and polydispersity phases. In general, the available phytochemical in the plant extract plays a very important role in the synthesizing process, especially in protecting the process from unexpected agglomeration and controlling the size and shape of the NPs [112].

FIG. 6. The biosynthesis of Ag NPs from plant extracts has been proposed as a process.

3.6 Covering the Plant

The biosynthesis method using plant extracts provides a large-scale production of Ag NPs, which is a logical remedy for the increasing demand for Ag NPs. Plant extract, in general, possesses diverse active biomolecules, such as phenolic acids, sugars, terpenoids, alkaloids, polyphenol and proteins that play a vital role in this biological reduction and stabilization of silver ions [113]. The leaves of the plant are more preferential than the whole plant in the synthesizing process due to the availability of the important phytochemicals that participate in reducing, capping and stabilizing the NPs [114]. The structure of some active biomolecules is capable of reducing and stabilizing Ag ions. Structures of some secondary metabolites, such as *Rutin, Genistein*, *Quercetin*, *Gallic acid*, *Daldzein* and *Papaverine*, are important for reducing and stabilizing stages in synthesizing Ag NPs. The size and shape of Ag NPs depend on the following parameters: concentration of the utilized plant extract, concentration of the Ag salts, reaction temperature, reaction time and reaction pH value [115]. Kumar *et al.* [116] studied the use of marine seaweed, *Gracilaria corticated*, in an attempt to produce Ag NPs. The extract was gradually heated to 60 °C for 20 min in a heating mantle for the reduction of metal ions to occur. The study revealed that the Ag NPs possess a spherical shape and the NPs sizes were in the range 18-46nm. The synthesized Ag NPs were characterized by UV–Vis spectroscopy, FTIR spectroscopy, transmission electron microscopy (TEM), dynamic light scattering (DLS) measurements and zeta potential. The result showed that the biosynthesized Ag NPs from *Gracilaria corticate* have an effective antifungal activity against *Candida albicans* and *C. glabrata* [116]. In another attempt by Prakash *et al.* [117], Ag NPs were synthesized using *Mimusops elengi,* L.leaf extract. The extract of *Mimusops elengi* L. was mixed with $AgNO_3$ solution. This reaction continued uninterrupted until the solution appeared to change its color from light green to dark brown. The synthesized Ag NPs were reported to exhibit a spherical shape and the range of the NPs size was between 55 and 83 nm. The biosynthesized Ag NPs were characterized using different characterization techniques. In addition, the green synthesized Ag NPs showed higher antimicrobial efficacy against multi-drug resistant clinical isolates [117]. Muniyappan *et al.* [118] synthesized Ag NPs using *Dalbergia spinosa* leaves extract. The results showed that the reducing sugars and flavonoids were primarily responsible for the bio-reduction process of Ag ions. TEM analysis showed that the Ag NPs were nearly spherical in shape with an average size of 18 ± 4 nm. Ag NPs were characterized by UV-Vis spectroscopy, TEM and FTIR analysis [118]. In another attempt, Singh *et al.* [119] biosynthesized Ag NPs using *Anabaena doliolum* and their antimicrobial and antitumor activities have been investigated. Singh *et al.* results indicated that the original color of the mixture was changed from reddish blue to dark brown after the addition of silver nitrate solution within one hour, suggesting the formation of Ag NPs. The formation of the Ag NPs was also monitored by the UV-Vis spectroscopy analysis when the SPR peak was recorded at 420 nm. TEM images revealed well-dispersed, spherical Ag NPs with particle sizes ranging from 10 to 50 nm. The X-ray diffraction analysis suggested a highly crystalline nature of the Ag NPs. FTIR analysis indicated that the hydroxyl (-OH) group is

available around the biosynthesized Ag NPs due to the sincerity of these NPs for moisture [120]. On the other hand, *Enteromrpha flexuosa* was utilized by Yousefzadi *et al.* [121] as a reducing and stabilizing agent for synthesizing Ag NPs. They stated that the colorless reaction mixture was turned into a dark brown color solution after 60 minutes, indicating the biotransformation of ionic Ag to reduced Ag atoms, as a result of the surface Plasmon resonance phenomenon. The color change was occurring because the active molecules present in the extract reduce the Ag metal ions into Ag NPs. The intensity of the color change was increased in direct proportion to the incubation period of nanoparticle synthesis. The formation of Ag NPs was monitored by UV-Vis absorption spectra at 200 to 600 nm, where an intense band was clearly detected at 430 nm, confirming the formation of Ag NPs [121]. Salari *et al.* [122] biosynthesized Ag NPs using *Spirogyra varians* extract. The average crystalline size was estimated to be around 17.6 nm and the SEM analysis confirmed the formation of relatively uniform NPs. These NPs showed an absorption peak at 430 nm in the UV-Vis spectrum [122]. Table 5 summarizes utilizing 27 different types of plants used for synthesizing Ag NPs.

TABLE 5. The utilized plant extracts for synthesizing Ag NPs.

No.	Name of plant	Size and morphology	UV-Vis SPR peak	Date of publication	Reference
1	*Gracilaria corticata*	18-46nm; Spherical	420nm	25-Jul-2012	[116]
2	*Mimusope elengi*	55-83nm; Spherical	434nm	18-Mar-2013	[117]
3	*Piper nigrum*	4-50nm; hexagonal and Spherical	460nm	15-Jan-2014	[123]
4	*Aloe vera*	70nm; Spherical	400nm	20-Nov-2014	[124]
5	*Dalbergia spinosa*	18nm; spherical	439nm	8-Mar-2014	[118]
6	*Anabaena dolioluma*	10-50nm; Spherical		30-Jun-2014	[120]
7	*Enteromorpha flexuosa*	2-32nm; Spherical	430nm	20-Aug-2014	[121]
8	*Spirogyra varians*	17.6nm; quasi-spheres	430nm	12-Oct-2014	[122]
9	*Pedalium murex*	10-150nm; Spherical	424-430nm	16-May- 2015	[125]
10	*Calliandra haematocephala*	70nm; Spherical	414nm	16-Jun-2015	[126]
11	*Eucalyptus globulus*	1.9-4.3nm and 5-25nm, with and without microwave treatment; Spherical	428nm	1-Jul-2015	[127]
12	*Ocimum sanctum*	14.6nm; Spherical	429nm	30-Jul-2015	[128]
13	*Synechococcus sp.*	140nm; Spherical	420+3.2	17-Des-2015	[129]
14	*Phlomis*	19-30nm; Spherical	440nm	16-Jan-2016	[130]
15	*Gracilaria birdiae*	20.2-94.9nm; Spherical	400-420nm	22-Apr-2016	[131]
16	*Saccharina japonica*	14.77nm; Spherical	432nm	21-Sep-2016	[132]
17	*Convolvulus arvensis*	28nm; Spherical	430nm	19-Des-2016	[133]
18	*Elephantopus scaber*	37nm; Spherical	420nm	6- Jul-2017	[134]
19	*Enteromorpha compressa*	4-24nm; Spherical	421nm	14-Mar-2017	[135]
20	*Erythrina suberosa*	15-34nm; Spherical	$\sim 428nm$	17-Mar-2017	[136]
21	*Cichorium intybus*	Various sizes depending on [metal]-to-[extract] ratio; Spherical	~ 420	25-Mar-2017	[137]
22	*Caulerpa serrulata*	10nm;Spherical-ellipsoidal	412nm	23-Jun-2017	[138]
23	*Salvia leriifolia*	27nm; Spherical	460nm	23-jul-2017	[139]
24	*Caulerpa racemose*	10nm; Spherical	413nm	13-Aug-2017	[140]
25	*Alpinia katsumadai*	12.6nm; quasi-spherical	416-420nm	15-Aug-2017	[141]
26	*Phyllanthus amarus*	30-42nm; flower-like	421nm	17-Oct-2017	[142]
27	*Nelumbo nucifera*	12.9nm; quasi-spherical	415nm	18-Jan-2018	[143]

It can be stated that Table 5 is extremely important, since it shows the suitable plant extracts for producing the desirable size, morphology and shape of Ag NPs.

4. Conclusion

Recently, Ag NPs have received massive consideration by researchers owing to their potential applications in many fields of science. The traditional methods for synthesizing Ag NPs have an operative harvest; however, they are accompanied by restrictions, like utilizing toxic materials and high operating cost and energy requests. The use of plant extracts to synthesize Ag NPs is the subject of this review, since this method is the most widely used, sustainable, inexpensive and easy one of all methods being used. This method attracted the consideration of researchers owing to the fact that plant extracts are safe to use and a source of numerous phytochemicals. The available phytochemicals inside plant extracts have been utilized as potential reducing, capping and stabilizing agents for synthesizing Ag NPs. There are sufficient published articles regarding green synthesis of Ag NPs; however, the current review, unalike previous reviews, summarizes the green synthesis method of Ag NPs in terms of the top ten journals, top ten countries, ten most cited researches and top ten authors in this field. The most suitable mechanism of the biosynthesis of Ag NPs from plant extracts is discussed extensively. The utilized plant extracts for synthesizing Ag NPs from the top articles analyzed alongside with the impact of numerous parameters on the size, shape, morphology of Ag NPs have been studied comprehensively.

This study precisely focused on the status of green synthesis of Ag NPs using plant extracts in the last 15 years, starting from 2007 to 2021. This extensive review helps in understanding and identifying new developments regarding the green synthesis of Ag NPs, as well as directing researchers, especially new ones, to the most important findings of the case studies and studying the gaps in order to find opportunities for conducting relevant research. Moreover, this study covers a large number of the most significant plants that were used to prepare Ag NPs with different sizes and shapes, which will help researchers in determining the best plant type and working on it. This study showed that the number of publications is increasing dramatically. The trend is continued, with the exception of a modest dip in 2020, owing to the COVID-19 pandemic and global social isolation.

References

[1] Ju-Nam, Y. and Lead, J.R., Science of the Total Environment, 400 (1-3) (2008) 396.

[2] Kareem, M. et al., IOP Conference Series: Materials Science and Engineering, (IOP Publishing, 2020).

[3] Austin, L.A. et al., Archives of Toxicology, 88 (7) (2014) 1391.

[4] Ramos, M.A.D.S. et al., International Journal of Nanomedicine, 13 (2018) 1179.

[5] Chen, F. et al., Journal of Colloid and Interface Science, 521 (2018) 261.

[6] Al-Shabib, N.A. et al., Scientific Reports, 6 (1) (2016) 1.

[7] Wu, K. et al., International Journal of Nanomedicine, 10 (2015) 7241.

[8] Van Hest, J. et al., Journal of Microscopy, 274 (1) (2019) 13.

[9] Zhang, K. et al., Journal of Colloid and Interface Science, 537 (2019) 316.

[10] Jafari, S. et al., Biomedicine & Pharmacotherapy, 109 (2019) 1100.

[11] Liu, J. et al., Optical Materials, 89 (2019) 100.

[12] Sharma, A. et al., Metals, 8 (5) (2018) 347.

[13] Mihyun, L., Zenobi-Wong, M. and Chang, J., "Google Patents", (2019).

[14] Fantino, E. et al., Advanced Materials, 28 (19) (2016) 3712.

[15] Wongrat, E. et al., Materials Research Innovations, 23 (2) (2019) 66.

[16] Xie, H. et al., Materials Letters, 234 (2019) 311.

[17] Morsi, R.E. et al., International Journal of Biological Macromolecules, 97 (2017) 264.

[18] Veisi, H., Azizi, S. and Mohammadi, P., Journal of Cleaner Production, 170 (2018) 1536.

[19] Choudhary, M.K., Kataria, J. and Sharma, S., Journal of Cleaner Production, 198 (2018) 882.

[20] Barzinjy, A. et al., Jordan J. Phys., 13 (2) (2020) 123.

[21] Herizchi, R. et al., Artificial Cells, Nanomedicine and Biotechnology, 44 (2) (2016) 596.

[22] Barzinjy, A. et al., Jordan J. Phys., 12 (1) (2019) 45.

[23] Wang, L., Hasanzadeh Kafshgari, M. and Meunier, M., Advanced Functional Materials, 30 (51) (2020) 2005400.

[24] Coronado, E.A., Encina, E.R. and Stefani, F.D., Nanoscale, 3 (10) (2011) 4042.

[25] Yan, Y. et al., Wear, 267 (5-8) (2009) 683.

[26] Astruc, D., Lu, F. and Aranzaes, J.R., Angewandte Chemie - International Edition, 44 (48) (2005) 7852.

[27] Syafiuddin, A. et al., Journal of the Chinese Chemical Society, 64 (7) (2017) 732.

[28] Atwater, H.A. and Polman, A., Materials for sustainable energy: A collection of peer-reviewed research and review articles from Nature Publishing Group, (2011) 1.

[29] De, M., Ghosh, P.S. and Rotello, V.M., Advanced Materials, 20 (22) (2008) 4225.

[30] Rafique, M. et al., Artificial Cells, Nanomedicine and Biotechnology, 45 (7) (2017) 1272.

[31] Khayati, G.R. and Janghorban, K., Advanced Powder Technology, 23 (6) (2012) 808.

[32] Khayati, G. and Janghorban, K., Advanced Powder Technology, 23 (3) (2012) 393.

[33] Verma, S. et al., Colloids and Surfaces A: Physicochemical and Engineering Aspects, 527 (2017) 23.

[34] Boutinguiza, M. et al., Materials Letters, 231 (2018) 126.

[35] Arboleda, D.M. et al., Materials Characterization, 140 (2018) 320.

[36] Simchi, A. et al., Materials & Design, 28 (3) (2007) 850.

[37] Malekzadeh, M. and Halali, M., Chemical Engineering Journal, 168 (1) (2011) 441.

[38] Hui, K. et al., Acta Materialia, 64 (2014) 326.

[39] Raghavendra, G.M. et al., Carbohydrate Polymers, 152 (2016) 558.

[40] Jung, J. et al., International Journal of Biological Macromolecules, 107 (2018) 2285.

[41] Javey, A. and Dai, H., Journal of the American Chemical Society, 127 (34) (2005) 11942.

[42] Wu, J. et al., Nanoscale, 6 (2) (2014) 749.

[43] Shih, S.-J. and Chien, I.-C., Powder Technology, 237 (2013) 436.

[44] Jang, H.D. et al., Aerosol Science and Technology, 49 (7) (2015) 538.

[45] Keskar, M. et al., Nanoscale Advances, 1(2) (2019) 627.

[46] Juby, K. et al., Carbohydrate Polymers, 89 (3) (2012) 906.

[47] Ashkarran, A.A., Current Applied Physics, 10 (6) (2010) 1442.

[48] Kumar, P. et al., Advanced Science Letters, 22 (1) (2016) 3.

[49] Zhang, H. et al., Journal of Materials Science, 52 (6) (2017) 3375.

[50] Manikprabhu, D. and K. Lingappa, Journal of Pharmacy Research, 6 (2) (2013) 255.

[51] Vijayan, R., Joseph, S. and Mathew, B., Bionanoscience, 8 (1) (2018) 105.

[52] De Yoreo, J.J. and Vekilov, P.G., Reviews in Mineralogy and Geochemistry, 54 (1) (2003) 57.

[53] Khan, M. et al., Dalton Transactions, 47 (35) (2018) 11988.

[54] Jadalannagari, S. et al., Applied Nanoscience, 4 (2) (2014) 133.

[55] Ueno, S. et al., Nanomaterials, 5 (2) (2015) 386.

[56] Kumar, K.A. et al., Applied Surface Science, 472 (2019) 40.

[57] Lee, S.J. et al., Applied Surface Science, 432 (2018) 317.

[58] Wang, Y. et al., Journal of the American Chemical Society, 135 (5) (2013) 1941.

[59] Dugandžić, V. et al., Analytica Chimica Acta, 946 (2016) 73.

[60] Singha, D., Barman, N. and Sahu, K., Journal of Colloid and Interface Science, 413 (2014) 37.

[61] Matsuhisa, N. et al., Nature Materials, 16 (8) (2017) 834.

[62] Ciobanu, C.S. et al., BioMed Research International, 2013 (2013) 1.

[63] Kuzminova, A. et al., Surface and Coatings Technology, 294 (2016) 225.

[64] Wani, I.A. et al., Materials Research Bulletin, 45 (8) (2010) 1033.

[65] Chen, D. et al., Journal of Materials Science: Materials in Electronics, 22 (1) (2011) 6.

[66] Guzmán, M.G., Dille, J. and Godet, S., Int J. Chem. Biomol. Eng., 2 (3) (2009) 104.

[67] Khaydarov, R.A. et al., Journal of Nanoparticle Research, 11 (5) (2009) 1193.

[68] Chitsazi, M.R. et al., Artificial Cells, Nanomedicine and Biotechnology, 44 (1) (2016) 328.

[69] Amin, S. et al., Current Analytical Chemistry, 17 (4) (2021) 438.

[70] Saratale, R.G. et al., Colloids and Surfaces B: Biointerfaces, 170 (2018) 20.

[71] Saravanan, A. et al., Chemosphere, 1 (2020) 128580.

[72] Ovais, M. et al., Applied Microbiology and Biotechnology, 102 (16) (2018) 6799.

[73] Vijayaraghavan, K. and Ashokkumar, T., Journal of Environmental Chemical Engineering, 5 (5) (2017) 4866.

[74] Shamaila, S. et al., Applied Materials Today, 5 (2016) 150.

[75] Barzinjy, A.A. et al., Eurasian Journal of Science & Engineering, 4 (3) (2019) 74.

[76] Azeez, H.H. and Barzinjy, A.A., Desalination Water Treat., 190 (2020) 179.

[77] Barzinjy, A.A. et al., Inorganic and Nano-metal Chemistry, 50 (8) (2020) 620.

[78] Barzinjy, A.A. and Azeez, H.H., SN Applied Sciences, 2 (5) (2020) 1.

[79] Barzinjy, A.A. et al., Current Organic Synthesis, 17 (7) (2020) 558.

[80] Barzinjy, A.A. et al., Journal of Materials Science: Materials in Electronics, 31 (2020) 11303.

[81] Barzinjy, A.A. et al., Micro- & Nano-Letters, 15 (6) (2020) 415.

[82] Nasrollahzadeh, M. et al., Materials Research Bulletin, 102 (2018) 24.

[83] Sajadi, S.M. et al., ChemistrySelect, 3 (43) (2018) 12274.

[84] Shnawa, B.H. et al., Emergent Materials, 1 (2021) 1.

[85] Talabani, R.F. et al., Nanomaterials, 11 (9) (2021) 2421.

[86] Riedel, S. and Kaupp, M., Coordination Chemistry Reviews, 253 (5-6) (2009) 606.

[87] Wang, M.Y. et al., Materials Letters, 107 (2013) 311.

[88] Wu, C. et al., Frontiers in Environmental Science, 9 (2021) 181.

[89] Al-Ibrashy, M. and Gaber, T., Built and Natural Environment Research Papers, 1 (2011) 63.

[90] Natsuki, J., Natsuki, T. and Hashimoto, Y., Int. J. Mater. Sci. Appl., 4 (5) (2015) 325.

[91] Geoprincy, G. et al., Asian Journal of Pharmaceutical and Clinical Research, 6 (1) (2013) 8.

[92] Gour, A. and Jain, N.K., Artificial Cells, Nanomedicine and Biotechnology, 47 (1) (2019) 844.

[93] El Shafey, A.M., Green Processing and Synthesis, 9 (1) (2020) 304.

[94] Frey, B.S. and Rost, K., Journal of Applied Economics, 13 (1) (2010) 1.

[95] Kumar, A. et al., Nature Materials, 7 (3) (2008) 236.

[96] Tolaymat, T.M. et al., Science of the Total Environment, 408 (5) (2010) 999.

[97] Shao, W. et al., ACS Applied Materials & Interfaces, 7 (12) (2015) 6966.

[98] Richter, A.P. et al., Nature Nanotechnology, 10 (9) (2015) 817.

[99] Akaighe, N. et al., Environmental Science & Technology, 45 (9) (2011) 3895.

[100] Meho, L.I. and Rogers, Y., Journal of the American Society for Information Science and Technology, 59 (11) (2008) 1711.

[101] Jadoun, S. et al., Environmental Chemistry Letters, 19 (1) (2021) 355.

[102] Martínez-Cabanas, M. et al., Nanomaterials, 11 (7) (2021) 1679.

[103] Marslin, G. et al., Materials, 11 (6) (2018) 940.

[104] Javed, R. et al., Journal of Nanobiotechnology, 18 (1) (2020) 1.

[105] Behravan, M. et al., International Journal of Biological Macromolecules, 124 (2019) 148.

[106] Sharma, P. et al., Materials Chemistry and Physics, 258 (2021) 123899.

[107] Perala, S.R.K. and Kumar, S., Langmuir, 29 (31) (2013) 9863.

[108] Nate, Z. et al., MRS Advances, 3 (42-43) (2018) 2505.

[109] Chugh, D., Viswamalya, V. and Das, B., Journal of Genetic Engineering and Biotechnology, 19 (1) (2021) 1.

[110] Abomuti, M.A. et al., Biology, 10 (11) (2021) 1075.

[111] Marișca, O.T. and Leopold, N., Materials, 12 (7) (2019) 1131.

[112] Basnet, P. et al., Journal of Photochemistry and Photobiology B: Biology, 183 (2018) 201.

[113] Castro, L. et al., Process Biochemistry, 46 (5) (2011) 1076.

[114] Shankar, S.S. et al., Nature Materials, 3 (7) (2004) 482.

[115] Bhaumik, J. et al., ACS Biomaterials Science & Engineering, 1 (6) (2015) 382.

[116] Kumar, P., Selvi, S.S. and Govindaraju, M., Applied Nanoscience, 3 (6) (2013) 495.

[117] Prakash, P. et al., Colloids and Surfaces B: Biointerfaces, 108 (2013) 255.

[118] Muniyappan, N. and Nagarajan, N., Process Biochemistry, 49 (6) (2014) 1054.

[119] Singh, A. et al., Biotechnology Reports, 25 (2020) 00427.

[120] Singh, G. et al., Journal of Microbiology and Biotechnology, 24 (10) (2014) 1354.

[121] Yousefzadi, M., Rahimi, Z. and Ghafori, V., Materials Letters, 137 (2014) 1.

[122] Salari, Z. et al., Journal of Saudi Chemical Society, 20 (4) (2016) 459.

[123] Paulkumar, K. et al., The Scientific World Journal, 1 (2014) 2014.

[124] Medda, S. et al., Applied Nanoscience, 5 (7) (2015) 875.

[125] Anandalakshmi, K., Venugobal, J. and Ramasamy, V., Applied Nanoscience, 6 (3) (2016) 399.

[126] Raja, S., Ramesh, V. and Thivaharan, V., Arabian Journal of Chemistry, 10 (2) (2017) 253.

[127] Ali, K. et al., Plos One, 10 (7) (2015) 0131178.

[128] Jain, N. et al., Plos One, 10 (7) (2015) 0134337.

[129] Keskin, S. et al. Journal of Nano Research, 40 (2016) 120.

[130] Allafchian, A. et al., Journal of Nanostructure in Chemistry, 6 (2) (2016) 129.

[131] de Aragao, A.P. et al., Arabian Journal of Chemistry, 12 (8) (2019) 4182.

[132] Sivagnanam, S.P. et al., Green Processing and Synthesis, 6 (2) (2017) 147.

[133] Hamedi, S., Shojaosadati, S.A. and Mohammadi, A., Journal of Photochemistry and Photobiology B: Biology, 167 (2017) 36.

[134] Francis, S. et al., Artificial Cells, Nanomedicine and Biotechnology, 46 (4) (2018) 795.

[135] Ramkumar, V.S. et al., Biotechnology Reports, 14 (2017) 1.

[136] Mohanta, Y.K. et al., Frontiers in Molecular Biosciences, 4 (2017) 14.

[137] Gallucci, M.N. et al., Materials Letters, 197 (2017) 98.

[138] Aboelfetoh, E.F., El-Shenody, R.A. and Ghobara, M.M., Environmental Monitoring and Assessment, 189 (7) (2017) 1.

[139] Baghayeri, M. et al., Applied Organometallic Chemistry, 32 (2) (2018) 4057.

[140] Kathiraven, T. et al., Applied Nanoscience, 5 (4) (2015) 499.

[141] He, Y. et al., RSC Advances, 7 (63) (2017) 39842.

[142] Ajitha, B. et al., Advanced Powder Technology, 29 (1) (2018) 86.

[143] He, Y. et al., New Journal of Chemistry, 42 (4) (2018) 28828.

Volume 15, Number 5, 2022. pp. 445-456

Jordan Journal of Physics

ARTICLE

Noise-dissipation Correlated Dynamics of a Double-well Bose-Einstein Condensate-reservoir System

Kalai K. Rajagopal, Gafurjan Ibragimov, Risman M. Hasim and **Idham A. Alias**

INSPEM & Department of Mathematics, University Putra Malaysia, 43400 Serdang, Selangor, Malaysia.

Doi: **https://doi.org/10.47011/15.5.2**

Received on: 31/12/2020; *Accepted on: 08/06/2021*

Abstract: In this work, we study the dissipative dynamics of a double-well Bose-Einstein condensate (BEC) out-coupled to reservoir at each side of its trap. The sub-system comprises of a simple Bose-Hubbard model, where the interplay of atom-tunneling current and inter-particle interaction are the main quantum features. The contact with two separate heat baths causes dissipation and drives the system into a non-equilibrium state. The system is well described by the Generalized Quantum Heisenberg-Langevin equation. We considered two Markovian dissipative BEC systems based on (i) the mean-field model (MF), where the internal noise has been averaged out and (ii) the noise-correlated model (FDT). Physical quantities, such as population imbalance, coherence and entanglement of the system, are computed for the models. The two-mode BEC phases, such as the quantum tunneling state and the macroscopic quantum-trapping state, evolved into complicated dynamics by controlling the non-linear interaction and dissipation strengths. We found that many important quantum features produced by the noise-correlated FDT model are not captured by the mean-field model.

Keywords: Double-well BEC, Dissipation, Noise, Markovian, Non-Markovian, Fixed points.

PACS: 03.75 Lm, 03.65 Yz, 03.75 Gg, 05.

1. Introduction

Bose-Einstein Condensate (BEC) in a double-well system exhibits quantum features mimicking the physics of Boson Josephson Junction (BJJ) dynamics in superconductors. Tunneling transport of atoms between the wells causes BEC population to oscillate even if there is no disparity between the number of atoms in each well, resulting in a modulated quantum collapse and revival; for instance, see [1, 2]. Macroscopic quantum coherence is then established within the system. However, stronger on-site boson-boson repulsive interaction suppresses the oscillations of population imbalance and goes upon a critical value, resulting in a novel macroscopic quantum self-trapping state, where atoms start localizing within their respective wells. This phenomenon is known as the Macroscopic Quantum Self-Trapping (MQST); for instance, see [2-4].

Experimental measurements, such as Josephson tunneling and thermal-induced phase fluctuations on the double-well BEC system, were reported in the monograph [5-7]. Measurements on the Josephson's AC and DC effects on the BJJ were made by Levy et al. [8] and interference-fringe experiments were performed by Hofferberth et al. [9]. Enormous

Corresponding Author: Kalai Kumar Rajagopal **Email**: kkrajagop@gmail.com

progress has been made following this experimental work.

System-environmental interaction under experimental conditions complicates the study of the transition from the quantum regime to the classical regime. Dissipation caused by irreversible coupling of quantum state with the environment creates a major obstacle in the long-time coherent control of quantum state. For a double-well BEC interacting with the environment setting, dissipation is found to be the major factor causing the destruction of MQST phases, as reported extensively in the theoretical literature [10-19]. On the contrary, researchers led by Sandro Wimberger [13, 15] have shown that dissipation in concurrence with inter-particle interaction enhances coherence under a specific condition. The double-well BEC is routinely realized with almost perfect control on atom-atom and external potential; for example in the experimental groups of Albiez et al. [5] and Gati et al. [6]. Resonance behaviour of coherence is anticipated to be realized in near future experiments. In the other direction, an experimental group led by Herwig Ott [20, 21, 47, 48] carried out a number of successful experiments applying localized dissipation to control the dynamic evolution of BEC, making this line of research very exciting.

Generally, inter-particle repulsive interaction [2-4, 14] cannot be neglected in any realistic BEC system. The physics of interacting BEC can be complicated in the presence of excitations. However, in this work, we neglect the existence of excitation, assuming weak-coupling approximation as in [22, 23]. In their works, two independent condensates having atoms in their lowest eigen-modes are merged and coherently out-coupled to their respective reservoirs. The interaction of condensate boson atoms in the traps with the reservoir induces dissipation in the system. The spectral function that couples the trap atoms with the reservoir modes determines the Markovian or non-Markovian operational dynamics of the system; see for instance [24-27].

Most studies on the dissipative double-well BEC-reservoir system encapsulate Markovian dynamics, leaving vast space for research on the non-Markovian operational basis. The emergence of new problems, such as quantum thermometry and quantum refrigerant [49, 50], led to many loopholes and excitement in this line of research. We follow the same motivation to explore our dissipative model of interest employing the generalized quantum Langevin equation (GQLE) which is discussed in great detail in the textbooks [22, 28, 30]. The advantage of using the latter mathematical approach is its feasibility to transform complicated stochastic differential equations into ordinary differential equations.

The paper is organized as follows. We describe the Hamiltonian of the double-well BEC-reservoir system by showing how it caters for Markovian or non-Markovian operational dynamics in Section 2. The Hamiltonian of the model and the dynamical equations can be found in our earlier works [29, 33]. Section 3 and its sub-section 3.1 discuss the mean-field model of our system. The system subjected to noise correlation and dissipation is described in Section 4. Results of the model physical quantities produced by the model are illustrated and discussed in the following sub-sections. A brief conclusion is given in Section 5.

2. Double-well BEC Out-coupled to Reservoirs

The Hamiltonian of the double-well BEC out-coupled to a dual multi-mode field (reservoirs) is succinctly denoted by the relation $H_{tot}=H_s+H_c+H_m+H_{s-c}+H_{s-m}$. The double-well (or two-mode) BEC sub-system is then represented by the sub-Hamiltonian:

$$H_s = \omega\ (\hat{a}^\dagger\ \hat{a} + \hat{b}^\dagger\ \hat{b}) + \Omega\ (\hat{a}^\dagger\ \hat{b} + \hat{b}^\dagger\ \hat{a}) + \mathrm{U}/2\ [\ \hat{a}^\dagger\ \hat{a}\ \hat{a}\ \hat{a} + b^\dagger\ \hat{b}\ \hat{b}\ \hat{b}\ ]. \quad (1)$$

Here, $(\hat{a}^\dagger,\ \hat{a})$ and $(\hat{b}^\dagger,\ \hat{b})$ are the set of creation and annihilation operators of the boson at traps A and B, respectively. Ω is the coupling strength between the two modes, ω is the trap frequency, U is the on-site interaction strength. We set $\hbar$=1; hence, all energies are measured in frequency units.

The two multi-mode reservoir fields are represented by $H_c = \sum_k \omega_k\ \hat{c}_k^\dagger\ \hat{c}_k$ and $H_m = \sum_k \omega_k\ \hat{m}_k^\dagger\ \hat{m}_k$, whereas they are connected at each side of the traps (A, B). The reservoirs are composed of closely spaced oscillators with frequencies ω_k with corresponding creation and annihilation operators $(\hat{c}_k^\dagger,\ \hat{c}_k)$ and $(\hat{m}_k^\dagger,\ \hat{m}_k)$. They are assumed to be in thermal equilibrium, satisfying:

$$\langle\ \hat{c}_k^\dagger\ (0)\ \rangle = \langle\ \hat{c}_k\ (0)\ \rangle = \langle \hat{m}_k^\dagger\ (0)\ \rangle = \langle\ \hat{m}_k\ (0)\ \rangle = 0$$

$\langle\, \hat{c}_k^\dagger\,(0)\, \hat{c}_{k'}(0)\,\rangle = \delta_{kk'}\, N_1(\omega_{k'})$

$\langle\, \hat{m}_k^\dagger\,(0)\, \hat{m}_{k'}(0)\,\rangle = \delta_{kk'}\, N_2\,(\omega_{k'})$

$\langle\, \hat{c}_k(0)\, \hat{c}_{k'}(0)\rangle = \langle\, \hat{m}_k(0)\, \hat{m}_{k'}(0)\rangle = 0$

$\langle \hat{c}_k^\dagger\,(0)\, \hat{c}_{k'}^\dagger(0)\rangle = \langle\, \hat{m}_k^\dagger\,(0)\, \hat{m}_{k'}^\dagger(0)\rangle = 0$

Here, $N_1(\omega)$ =1/[exp(ω/k_BT_1) – 1] and $N_2(\omega)$ =1/[exp(ω/k_BT_2) – 1] represent the thermal average boson numbers for reservoirs A and B, with Boltzmann constant k_B for temperatures (T_1, T_2), respectively. The interaction between the system and the reservoirs are denoted by the following sub-Hamiltonians

$H_{s-c} = \sum_k g_k\,(\hat{a}_k\,\hat{c}_k^\dagger + \hat{c}_k\,\hat{a}_k^\dagger)$ and $H_{s-m} = \sum_k f_k\,(\hat{b}_k\hat{m}_k^\dagger + \hat{b}_k^\dagger\hat{m}_k)$ (2)

where g_k or f_k is the bi-linear out-coupling function of traps A or B, respectively. The dynamical property of this system can be studied by solving the Heisenberg equation of motion $\frac{d\,\hat{O}}{dt} = -\frac{i}{\hbar}\,[\,\hat{O},\,\hat{H}\,]$, as shown in the textbooks [23,30]:

$\frac{d\hat{a}}{dt}$ = - $i\,\omega\,\hat{a} - i\,\Omega\,\hat{b}$- $i\,U\,\hat{a}^\dagger\hat{a}\,\hat{a} + \hat{F}_1$ (t) - $\int_0^t dt'$ $K(t\text{-}t')\,\hat{a}(t')$ (3)

$\frac{d\hat{b}}{dt}$ = - $i\,\omega\,\hat{b} - i\,\Omega\,\hat{a}$- $i\,U\,\hat{b}^\dagger\hat{b}\,\hat{b} + \hat{F}_2$ (t) - $\int_0^t dt'$ $M(t\text{-}t')\,\hat{b}(t')$ (4)

where $\hat{F}_1$ = - $i\sum_k g_k\,\hat{c_k}$ (0) $e^{-i\omega_k t}$ and $\hat{F}_2$ (t) = - $i\sum_k f_k\,\hat{c_k}$ (0) $e^{-i\omega_k t}$ correspond to the noise operators with reservoir variables. The last terms are the dissipation part with memory kernels $K(t) = \sum_k {g_k}^2\, e^{-i\omega_k t}$ and $M(t) = \sum_k {f_k}^2\, e^{-i\omega_k t}$. Applying OU memory kernels in the form $K(t) = Q_1\gamma\, e^{-\gamma t}$ and $M(t) = Q_2\gamma\, e^{-\gamma t}$ (OU referred to the authors of [31] who first used this function as memory kernel) attributes to the non-Markovian operational dynamics, whereas using memory-less kernels in the form K_δ(t)= $Q_1\,\delta(t)$ and M_δ(t)= $Q_2\,\delta(t)$ generates Markovian dynamics; see for example the works studied in [22, 26, 29, 32, 33].

3. The Dynamics of Mean-field Model (MF)

In general, there is no exact remedies for such non-linear operator equations, but an approximate solution can always be obtained by averaging them and decorrelating higher-order correlation operator functions into products of lower ones. In the present work, we decorrelate the third-order moment appearing on the right-hand side of Eqs. (3) and (4) by the relation:

$\langle a^\dagger aa\rangle \sim \langle a^\dagger\rangle\langle a\rangle\langle a\rangle$ and $\langle b^\dagger bb\rangle \sim \langle b^\dagger\rangle\langle b\rangle\langle b\rangle$. (5)

This means that third-order correlated operators are approximated by the product of their single-operator expectation values. This truncation is valid in the macroscopic limit, since the covariance vanishes as O($\frac{1}{N}$) (where N is the total number atom of the system) if the many-particle quantum state is close to pure BEC [2-4,14, 36, 37]. In other words, the mean-field approach is valid and well described for the macroscopic system (system with large number of atoms, $N \to \infty$).

The breakdown of mean-field model is by large, due to the neglect of higher order moments of the quantum state and not a consequence of a failure of the standard semi-classical Gross-Pitaevskii dynamics; see for example the discussion in the textbook of Pethick and Smith [34]. To overcome this problem, one has to truncate higher-order expectation values at a later stage than in Eq. (5)

$\langle a_j^\dagger a_k a_l\rangle \approx \langle a_j^\dagger\rangle\langle a_k a_l\rangle + \langle a_j^\dagger a_k\rangle\langle a_l\rangle + \langle a_j^\dagger a_l\rangle\langle a_k\rangle - 2\langle a_j^\dagger a_k a_l\rangle$ (6)

and derive the equation of motion for the correlation functions $\langle a_j^\dagger a_k\rangle$ and $\langle a_j a_k\rangle$, as suggested in [35]. However, this approach also finds its limitations and is later improved by the Bogoliubov back-reaction (BBR) method developed by Amichay Vardi's group [36].

Defining $\alpha = \langle\hat{a}\rangle$, $\alpha^* = \langle\hat{a}^\dagger\rangle$, $\beta = \langle\hat{b}\rangle$ and $\beta^* = \langle\hat{b}^\dagger\rangle$ with n(t)=$\alpha^2 + \beta^2 = n_A(t) + n_B$(t) denote the total particle number at a certain time t in the double-well. For large reservoir systems, averages $\langle\hat{F}_1\rangle$ and $\langle\hat{F}_2\rangle$ vanish. The Markovian operational dynamics of our model is obtained by choosing memory-less dissipation kernels K_δ(t) = $Q_1\,\delta(t)$ and M_δ(t) = $Q_2\,\delta(t)$ for Eqs. (3) and (4). We obtain the following set of coupled differential equations:

$\frac{d\alpha}{dt}$ = -$i\,(\omega - Q_1)\alpha$- $i\,\Omega\beta$-i U $|\alpha|^2\alpha$, (7)

$\frac{d\beta}{dt}$ = -$i\,(\omega - Q_2)\beta$-$i\,\Omega\alpha$- i U $|\beta|^2\beta$, (8)

Re-writing the variables (α, β) as $\alpha = |\alpha|exp\,(i\,\theta_a)$ and $\beta = |\beta|exp\,(i\,\theta_b)$, the population-imbalance parameter is defined by s = ($|\alpha|^2$-

$|\beta|^2$)/n(t) with a relative phase $\theta = \theta_a - \theta_b$. By calculating $\frac{ds}{dt} = \sum_j \frac{\partial s}{\partial \alpha_j}\frac{\partial \alpha_j}{\partial t}$, where $\alpha_j = \{\alpha, \beta\}$, and comparing the imaginary parts of $\frac{d(\alpha\beta^*)}{dt} = \frac{d(|\alpha||\beta|\exp(-i\theta))}{dt}$, one obtains the following set of equation:

$$\frac{ds}{dt} = -2\sqrt{1 - s^2}\sin\theta - \zeta(1 - s^2), \quad (9)$$

$$\frac{d\theta}{dt} = \frac{2s\cos\theta}{\sqrt{1-s^2}} - \chi s, \quad (10)$$

where $\zeta = (Q_2 - Q_1)/\Omega$ is the dissipation bias and $\chi = nU/\Omega$ is the ratio of inter-particle interaction with tunneling coupling strength. The model equations are then governed by the latter control parameters. Time has been rescaled in unit Ω. The fixed points are obtained by setting $(\dot{s} = 0, \dot{\theta} = 0)$; we obtain:

$$\sin\theta = \frac{\zeta}{2}\sqrt{1 - s^2} \text{ and } \cos\theta = \frac{\chi}{2}\sqrt{1 - s^2}\ . \quad (11)$$

Using trigonometry identity $\sin^2\theta + \cos^2\theta = 1$, we find $s = \pm\sqrt{1 - \frac{4}{\chi^2+\zeta^2}}$. Hence, we can identify the location of fixed points $(s, \theta) = (0, \arcsin\frac{\zeta}{2})$, $(0, \pi - \arcsin\frac{\zeta}{2})$, $(\sqrt{1 - \frac{4}{\chi^2+\zeta^2}}, \arccos\pi - \frac{\chi}{\chi^2+\zeta^2})$ and $(-\sqrt{1 - \frac{4}{\chi^2+\zeta^2}}, \arccos\pi - \frac{\chi}{\chi^2+\zeta^2})$.

Jacobian matrix for the non-dissipative two-mode BEC based on Eqs. (9) and (10) is as follows:

$$J = \begin{pmatrix} \frac{\partial \dot{s}}{\partial s} & \frac{\partial \dot{s}}{\partial \theta} \\ \frac{\partial \dot{\theta}}{\partial s} & \frac{\partial \dot{\theta}}{\partial \theta} \end{pmatrix} = \begin{pmatrix} 2s\sin\theta/\sqrt{1-s^2} - 2\zeta s & -2\sqrt{1-s^2}\cos\theta \\ -\chi + 2\cos\theta/\sqrt[3]{1-s^2} & -2s\sin\theta/\sqrt{1-s^2} \end{pmatrix} \quad (12)$$

3.1 Inter-particle Interaction and Dissipation Effect on the Mean-field System

We numerically solve Eqs. (9) and (10) [phase-space equations of the MF model] for appropriate initial conditions using Matlab ODE-45 solver [39, 40], which is an efficient tool for solving simple non-stiff differential equations. A relatively small number of atoms is used to maintain the validity of two-mode BEC model. For example, 100 atoms are distributed in appropriate proportions among the traps initially.

The population-imbalance invariant with control parameters (χ, ζ) is illustrated in Fig. 1. The left-most panels are evolutions for the dissipation free case. As the inter-particle interaction increases, one observes phase changes from Quantum Tunneling state (QTS) to Macroscopic Self-trapping state (MQST). In the transition from MQST to Josephson oscillations (as the atom numbers are dropping), one sees something like "periodic doubling" (blue curve in the figure). One could expect some sort of resonance to occur as the system's phases change from QTS to MQST as one sweep through from weak to stronger non-linearity.

The middle and right-most panels of Fig. 1 are the dynamics in the presence of dissipation. Competition between atom tunneling and atom losses to the reservoir is seen to be affecting the dynamics. Comparing the evolution of figures between these two sets of panels, one can deduce that stronger dissipation coupled with inter-particle interaction causes dramatic changes in the dynamics of the system (irregular reduction in the population-imbalance oscillation amplitude). In other words, dissipation has perturbed the period-doubling effect and starts delocalizing atoms (damped oscillation) as the atom number drops. However, for the strongly inter-particle interacting case, in the last bottom left panels, dissipation is seen to drive back MQST to QTS, as the non-linearity of the system gets weaker in proportion to reducing atom number.

Stability characteristics of the fixed points can be determined by finding the eigenvalues of the Jacobian matrix, as shown in the differential equations textbooks [41, 42]. It was also shown by the researchers in [3, 14, 43] that the eigenvalues of the Jacobian matrix depict the type of fixed points and the stability of them. For instance, two imaginary eigenvalues denote an elliptic fixed point, two real eigenvalues denote a hyperbolic fixed point. A saddle fixed point occurs when two real eigenvalues lie on the different sides of zeros. Complex eigenvalue with a negative real part depicts an attractor, while a complex eigenvalue with positive real part depicts a repeller.

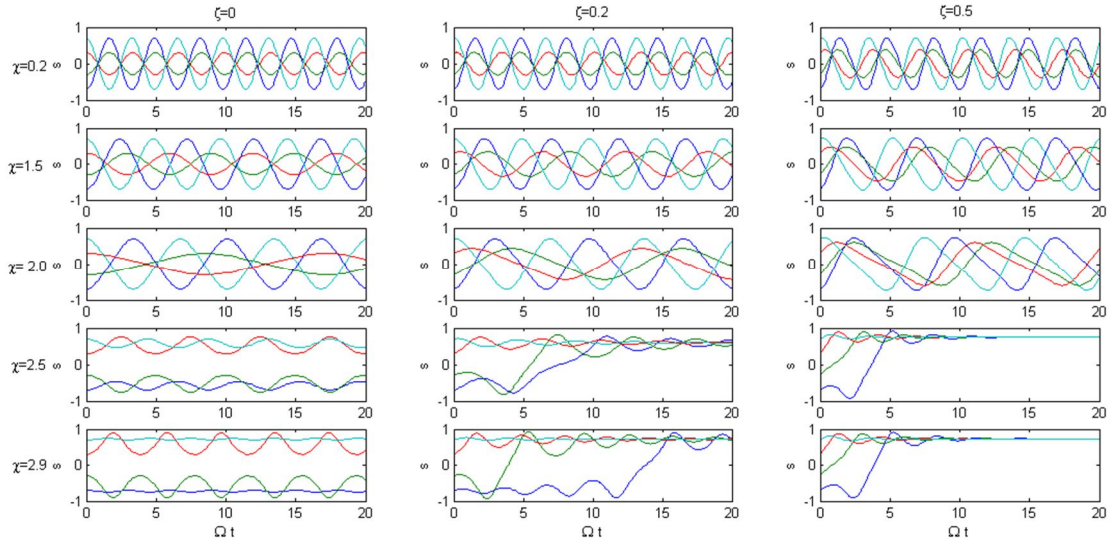

FIG. 1. Evolution of population imbalance s as a function of Ωt in variation with dissipation strengths ζ for various inter-particle interaction strengths χ. Phases are evolving from Quantum Tunneling state (QTS) (Josephson's oscillations) at χ = 0.2 to Macroscopic Quantum Self-trapping (partially localized oscillations) at χ=2.5 onward. Coloured lines correspond to initial conditions (s(0), $\theta(0)$): (-0.7,0) blue-line, (-0.3,0) green line, (0.3,0) red-line and (0.7,0) light-blue line.

Fig. 2 shows a comparison of dissipative and dissipation-free phase space trajectory (s, θ) evolutions in variation with inter-particle interaction strengths (increasing from top to bottom order). Phases are evolving from Quantum Tunneling state (QTS) (all elliptic fixed points) at χ = 0.2 to Macroscopic Quantum Self-trapping (MQST) state (a combination of hyperbolic and elliptic fixed points) at χ = 2.0 onwards. The middle and right-most panels show perturbation to phases shown in the left panel in the presence of dissipation. Top left-most panel of Fig. 2 depicts the phase diagram for the weak on-site interaction χ = 0.2. Three elliptic fixed points at locations (s, θ) = (0, $\pm\pi$), (0,0) are easily noticeable for the dissipation-free case. The effect of dissipation is noticeable at theχ middle (ζ= 0.2) and right-most panels (ζ=0.5) of Fig. 2. The presence of dissipation causes the pair of elliptic fixed points to be attracted to each other. Also, there is a slight shift in the locations of the fixed points.

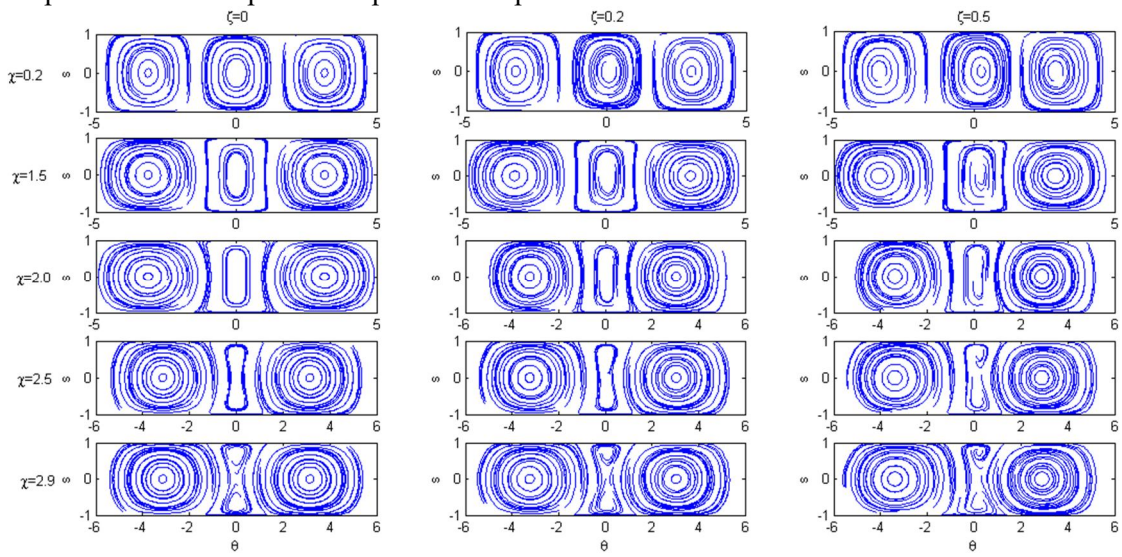

FIG. 2. Evolution of phase diagrams (s, θ) in variation with inter-particle interaction strengths (increasing χ from top to bottom order) subjected to three dissipation strengths ζ=0,0.2,0.5. Initial conditions are in the ranges $-1 \leq s(0) \leq 1$ and $-\pi \leq \theta(0) \leq \pi$ while the trajectories run for Ωt=3. Phases are evolving from Quantum Tunelling state (QTS) (all elliptic fixed points) at χ=0.2 to Macroscopic Quantum Self-trapping state (a combination of hyperbolic and elliptic fixed points) at χ=2.5 onward corresponding to Figure 2. Phase difference, θ, is plotted in unit radian.

Looking at the horizontal row of panels with χ = 2.5, the phase diagram clearly exhibits two elliptic fixed points at (s, θ) = (0, -π), (0, π) and a single hyperbolic fixed point at (0,0) for the dissipation-free case (left-most panel). In the strongly interacting case without dissipation, one observes the splitting of one of the elliptic fixed points into two novel elliptic points and one hyperbolic fixed point; this is the famous self-trapping effect reported by Milburn et al. [2], Raghavan et al. [4] and observed experimentally by Albiez et al. [5]. Dissipation introduced in the system (right-most panel of Fig. 2) generates a pair of attractor and repeller at (0.6, 0) and (-0.6, 0), respectively. There is no change of location for the other two fixed points, but the dynamics can be seen to be corrugated by the presence of dissipation.

Bottom-most Fig. 2 is the phase portrait for stronger on-site interaction χ = 2.9. A corrugated hyperbolic fixed point at (0, 0) and two elliptic fixed points at (0, $\pm\pi$) were found for the non-dissipative case (the last row left-most panel). The system generates four fixed points for the dissipation case (last row of middle and right-most panels). The fixed points are located at ($\pm$ 0.72, 0) and (0, $\pm\,\pi$). Fixed points at (0.72, 0) are attractors, while the ones at (-0.72,0) are repellers. The other two fixed points at (0, $\pm\pi$) are elliptic. The above stability characteristics of fixed points are deduced from the eigenvalue result of its Jacobian matrix.

4. The Fluctuation-dissipation Noise Correlated (FDT) Model

There are shortcomings for the use of mean-field approximation. For instance, quantum fluctuations are completely neglected and they also fail badly at dynamical instabilities [35]. Also, the system noise is suppressed since the thermal noise expectation value $\langle F_j{}^{\dagger}(t)\rangle = \langle F_j(t)\rangle = 0$ assuming a large thermal reservoir. Hence, noise correlation effects are completely neglected in the system. In this work, we implement the double-well BEC system subjected to noise correlation and Markovian dissipation. We call this description the FDT model.

Physical quantities, such as population of traps ($n_A = \langle \hat{a}^{\dagger}\,\hat{a}\rangle$, $n_B = \langle \hat{b}^{\dagger}\hat{b}\,\rangle$), coherence and other noise-correlated terms, are computed by their second-order moments using Eqs. (3) and (4) and applying the product rule: $\frac{d\langle \hat{O}^{\dagger}\,\hat{O}\rangle}{dt} = \langle \frac{d\hat{O}}{dt}\,\hat{O}\rangle + \langle \hat{O}\,\frac{d\hat{O}}{dt}\rangle$. Performing some algebra, we obtain the following set of second-order moment evolution equations:

$$\frac{d\langle \hat{a}^{\dagger}\hat{a}\rangle}{dt} = -2\,Q_1\,\langle \hat{a}^{\dagger}\,\hat{a}\rangle + i\,\Omega\,\langle \hat{b}^{\dagger}\hat{a}\rangle - i\,\Omega\,\langle \hat{a}^{\dagger}\hat{b}\rangle + \langle \hat{F}_1^{\dagger}\,\hat{a}\,\rangle + \langle \hat{a}^{\dagger}\,\hat{F}_1\rangle \quad (13)$$

$$\frac{d\langle \hat{b}^{\dagger}\hat{b}\rangle}{dt} = -2\,Q_2\,\langle \hat{b}^{\dagger}\,\hat{b}\rangle + i\,\Omega\,\langle \hat{a}^{\dagger}b\rangle - i\,\Omega\,\langle \hat{b}^{\dagger}\hat{a}\rangle + \langle \hat{F}_2^{\dagger}\,\hat{b}\,\rangle + \langle \hat{b}^{\dagger}\,\hat{F}_2\rangle \quad (14)$$

$$\frac{d\langle \hat{a}^{\dagger}\hat{b}\rangle}{dt} = -\,(Q_1{+}Q_2\,)\;\;\langle \hat{a}^{\dagger}\,\hat{b}\rangle + i\,\Omega\,\langle \hat{b}^{\dagger}\hat{b}\rangle - i\,\Omega\,\langle \hat{a}^{\dagger}\hat{a}\rangle + iU\,\langle a^{\dagger}\,\hat{b}\,\rangle\,(n_A - n_B). \quad (15)$$

The noise terms in the above equations denoted by ($\hat{F}_1$, $\hat{F}_2$) obey the two-point correlations relation; see for example [23, 28]:

$$\langle \hat{F}_1(t')\,\hat{F}_2(t'')\rangle = Q_1\,N_1(\omega)\,\delta(\,t' - t") \quad (16)$$

$$\langle \hat{F}_1(t')\,\hat{F}_2(t'')\rangle = Q_2\,N_2(\omega)\,\delta(\,t' - t") \quad (17)$$

It needs to be mentioned that Eqs. (16) and (17) indicate Fluctuation-Dissipation theorem (FDT) for the Markovian system [for non-Markovian system, we have different relations than those above], which reads that fluctuation-due reservoir contributes to the dissipation in the system. In the above set of equations, the terms $\langle \hat{F}_1^{\dagger}\,\hat{a}\,\rangle = \langle \hat{a}^{\dagger}\,\hat{F}_1\rangle = (Q_1/2)\;N_1(\omega)$ and $\langle \hat{F}_2^{\dagger}\,\hat{b}\,\rangle = \langle \hat{b}^{\dagger}\,\hat{F}_2\rangle = (Q_2/2)\;N_2(\omega)$ were obtained using Eqs. (16) and (17) and employing the technique shown in the textbook [28].

The fourth-order moments generated in deriving Eqs. (13) - (15) have been de-correlated by a basic relation $\langle \hat{A}\,\hat{B}\hat{C}\hat{D}\,\rangle \approx \langle \hat{A}\hat{B}\rangle\langle \hat{C}\hat{D}\rangle$. The set of dynamical equations above are governed by the trap frequency ω, tunneling coupling constant Ω, inter-particle interaction strength U, dissipation strengths (Q_1, Q_2) and the reservoir temperatures (T_1, T_2).

4.1 Comparison between the MF and FDT Models and Their Illustrations

We compare the FDT model Eqs. (13) - (15) with MF model Eqs. (7) and (8) in terms of their physical quantities, such as population imbalance, coherence and entanglement. Again, we distribute 100 atoms in appropriate proportions among the traps as their initial condition. The trap frequency is set at ω/Ω = 5. Dissipation strengths (Q_1, Q_2) and the ratio

between inter-particle interaction with tunneling strength U/Ω are treated as control parameters for the system dynamics. Reservoir temperatures are fixed at $k_B T_1/\Omega = k_B T_2/\Omega = 2$, while the trap frequency is set at $\omega/\Omega = 5$.

4.1.1 Population Imbalance

The non-dissipative two-mode BEC exhibits quantum tunneling state (QTS) at weaker inter-particle interaction as can be noticed in Fig. 3(a), while a macroscopic self-trapping state (MQST) is realized in Fig. 3(b) for a stronger interaction regime [2, 4]. The population imbalance at QTS displays Rabi Josephson oscillation, whereas MQST shows partially localized oscillation.

Fig. 3(b) shows decaying oscillation and continuous reduction of population amplitude. The QTS phase is destroyed by dissipation in both models. Fig. 3(d) indicates a drive back from MQST to QTS. The MF model drives the system quicker to its equilibrium state compared to the FDT model. As the atom numbers are dropping, one sees something like a "period doubling" for the FDT model. The slower decay into the equilibrium for the FDT model is due to noise and dissipation in the system, sustaining the dynamics.

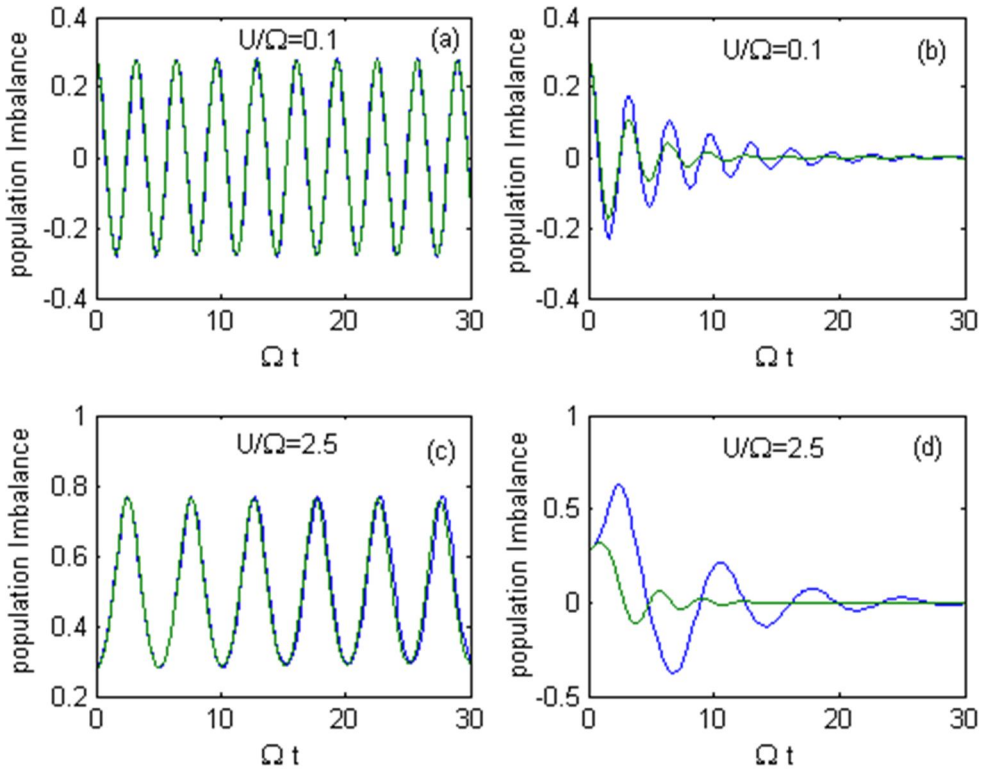

FIG. 3. Population imbalance as a function of Ωt. Top panels are for weak inter-particle interaction strength U/Ω = 0.1, while lower panels are for its stronger counterpart U/Ω = 2.5. Figs. (a) and (c) correspond to non-dissipative dynamics representing QTS and MQST, respectively. Figs. (b) and (d) are their corresponding system with dissipation strength Q_1/Ω=0.1 and Q_2/Ω=0.2. Other fixed parameters are trap frequencies ω/Ω=5 and reservoir temperatures $k_B\ T_1/\Omega$=2 and $k_B\ T_2/\Omega$=2 . Initial atom distribution for traps (A, B) is (64, 36). The blue line corresponds to the noise-correlated (FDT) model, while the green line is for the MF model.

4.1.2 Coherence in the System

The coherence of the many-body quantum state can be determined using the first-order correlation function between wells $g_{ab}^{(1)} = \left[\langle \hat{a}^\dagger \hat{b}\rangle + \langle \hat{b}^\dagger \hat{a}\rangle\right]/n(t)$ [13]. We compare the coherence produced by the two models (FDT *vs.* MF) in Fig. 4 for various inter-particle interaction strengths.

The MF model shows a sharp exponential decay of coherence in the traps for this weak inter-particle interaction limit $U \leq 2\Omega$. The FDT model, however, sustains stable coherence for this range of interaction strength, maintaining pure condensate state. This interesting feature, we believe, is due to the balance between noise and dissipation factor that is peculiar to the system, supporting fluctuation dissipation theorem.

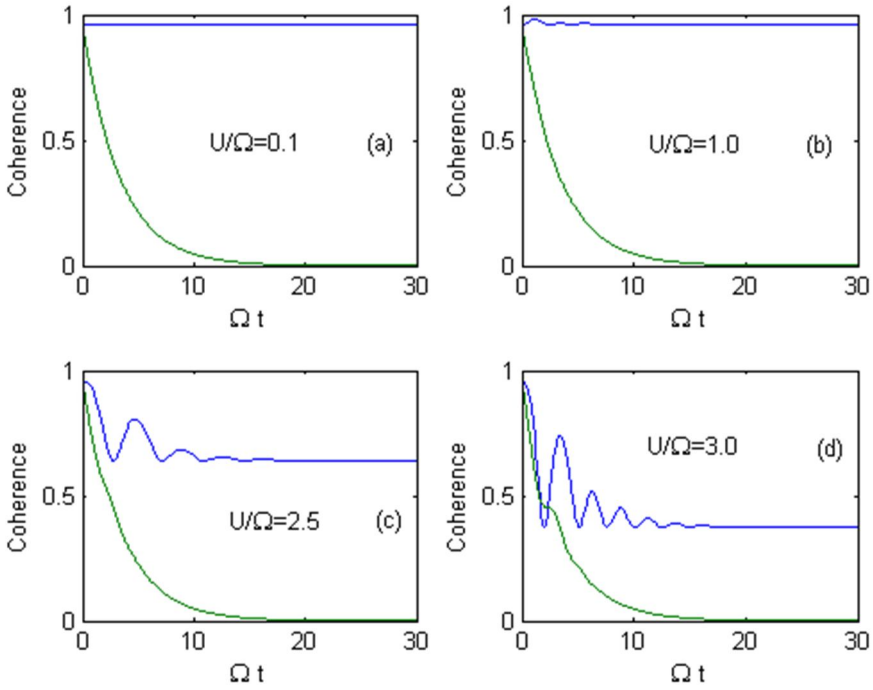

FIG. 4. Coherence dynamics as a function of Ωt computed in variation with the inter-particle interaction strength U/Ω. Trap frequencies, reservoir temperatures, dissipation strengths and initial atom distribution at traps (A,B) are the same as in Figure 3. Blue and green lines correspond to the noise-correlated Markovian model and the mean-field model (MF), respectively.

We found that dissipation drives the initial state of the system to a different quantum state for the stronger inter-particle interaction regimes $U \geq 2.5\ \Omega$. In this limit, both models show a decrease in the first-order coherence, indicating the destruction of the condensate. The initial state of the systems is unstable; they fragmented into a meta-stable equilibrium state, similarly reported by Kordas et al. [44]. The sudden jump to a local maximum coherence after a short transient period is understood to be a stochastic resonant (SR) effect reported by Witthaut et al. (2008) [13]. Such phenomena occur for dissipative systems at a stronger non-linear interaction only.

The MF model also exhibits similar transient BEC fragmentation and formation of resonant state, but cannot sustain it, as the coherence decays sharply. However, the FDT model based on noise and dissipation balancing supports the meta-stable equilibrium for longer sustainable periods. The oscillatory dynamics in Fig. 4 (c) and (d) for the FDT model is due its competition between dissipation and atom losses, which eventually creates the meta-stable state.

4.1.3 Entanglement

To investigate the inter-modal entanglement between BEC atoms, we use the Hillery-Zubairy criteria [45, 46] defined by the following relations, $HZ1 = \langle \hat{n}_A\, \hat{n}_B \rangle - \left|\langle \hat{a}^\dagger \hat{b} \rangle\right|^2$ or $HZ2 = \langle \hat{n}_A \rangle \langle \hat{n}_B \rangle - \left|\langle \hat{a}\hat{b} \rangle\right|^2$ for which $HZ1 < 0$ or $HZ2 < 0$, indicating entanglement. HZ1 criterion is the suitable candidate for our models; therefore, it is plotted in Fig. 5.

Interestingly, the domain of non-classicality (entanglement) detected through HZ1 criterion depends on the ratio of non-linear interaction and coherence. The MF model does not show entanglement, because equation HZ1 is zero based on its decorrelation approximation and mean-field definition. In this situation, the system remains close to pure BEC throughout its evolution. FDT model is highly entangled even at weak interaction. For weak interaction, higher atom-tunneling rate enhances coherence in the system. However, the atom-density fluctuations at each trap weakened by atom losses to the reservoir (referring to equation HZ1). We have mentioned earlier that coherence is sustained by the FDT model, which supports our argument. The BEC was fragmented into meta-stable equilibrium state for stronger inter-particle interaction ($U \geq 2.5\ \Omega$). Such phenomena are also captured by the entanglement evolution shown in Fig. 4 (c) and Fig. 4 (d).

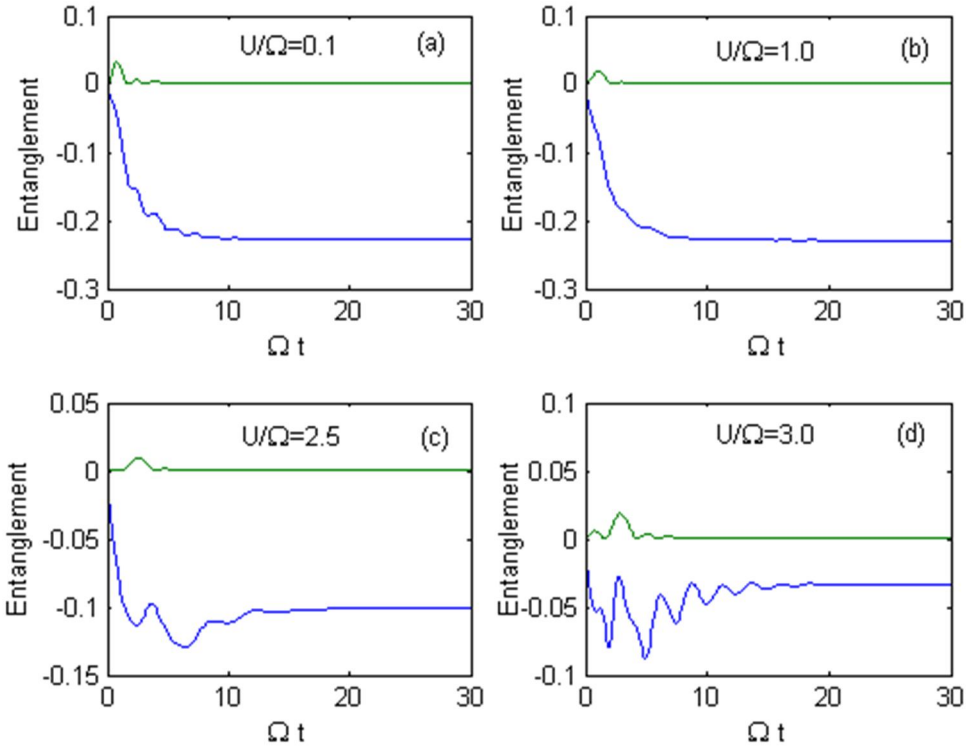

FIG. 5. HZ-1 criterion in the time domain Ωt for various inter-particle interaction strengths. Caption is still the same as in Figure 3.

5. Conclusion

We have studied the dynamical properties of a double-well BEC out-coupled to a dual-reservoir system. Dissipation in the system arises from the interaction of condensate atoms with the out-coupled multi-mode reservoirs. The macroscopic dynamics of BEC modes are described within the mean-field and noise-correlated models.

We started by analyzing the dynamics induced by the mean-field model (MF) subjected to Markovian dissipation. We have shown how the system evolved from its initial equilibrium phases (QTS and MQST) and perturbed in variation with the applied control parameters (non-linear interaction and dissipation strengths). Later, we considered the noise-correlated model (FDT) and computed the physical quantities, such as population imbalance, coherence and entanglement. The FDT model obeys the fluctuation dissipation theorem, which recognizes fluctuation in the reservoir as the main source of dissipation in the system. However, the noise correlation is suppressed in the MF model.

We have shown that noise correlation and dissipation have crucial effects on computing physical quantities, such as population imbalance, coherence or entanglement of the system. Dissipation destroys the two-mode BEC phases; namely, QTS and MQST, which occur at the opposite interacting regimes (weak *versus* strong). Coherence of the system is enhanced for weaker non-linear interaction strength (due to increasing tunneling rate), hence promoting non-classical (quantum) behavior. Dissipation drives back MQST to QTS phase reaching a meta-stable state before being destroyed, as the non-linearity of the system gets weaker in proportion to reducing atom number. The mentioned process is much weaker and slower in the FDT model compared to the MF model.

The present work opens up a new research direction to analyze possible formation of non-linear structures, like the breather state (especially at stronger non-linear interaction and dissipation regime) similar to the system studied by Kordas et al. [44]. We have shown that the mean-field model (where noise correlation is suppressed) is not able to detect quantum properties, like coherence and entanglement, especially at the stronger non-linear interaction and dissipation regime, where new quantum features emerge. We hope that the formation of breather state is also realized in experiment using a simple system like our double-well BEC-reservoir models.

Acknowledgement

The present research was initially supported by the National Fundamental Research Grant Scheme FRGS of Malaysia, 01-01-17-1921FR. Part of the work was presented at "ICRAAM 2020" Conference held at Kuala Lumpur on 4th - 6th February 2020. We highly appreciate the deep and insightful comments of our reviewers in improving the content of this manuscript.

Appendix: The Mean-field Non-Markovian Dynamics

The non-Markovian operational dynamic model is obtained by choosing memory dissipation kernels K_1 (t) = Q_1 exp (-γ t) and M_1(t) = Q_2 exp(-γ t) for Eqs. (3) and (4). Following the prescribed steps in Section 3, we obtain the mean-field set of coupled differential equations:

$$\frac{d\alpha}{dt} = -i\omega\alpha - i\Omega\beta - iU|\alpha|^2\alpha - Q_1\int_0^t dt' \exp(-\gamma[t-t'])\,\alpha(t'), \quad \text{(A1)}$$

$$\frac{d\beta}{dt} = -i(\omega)\beta - i\Omega\alpha - iU|\beta|^2\beta - Q_2\int_0^t dt' \exp(-\gamma[t-t'])\beta(t'). \quad \text{(A2)}$$

The following are the set of phase-space dynamical equations for our non-Markovian system:

$$\frac{ds}{dt} = -2\sqrt{1-s^2}\sin\theta - \zeta(1-s^2) - \left[\frac{1+s}{n}\right][\beta^* Y + \beta Y^*] - \left[\frac{1-s}{n}\right][\alpha^* X + \alpha X^*] \quad \text{(A3)}$$

$$\frac{d\theta}{dt} = \frac{2s\cos\theta}{\sqrt{1-s^2}} - \chi s - \Im\left\{\frac{Y^*}{\beta^*} + \frac{X}{\alpha}\right\}, \quad \text{(A4)}$$

where $\Im$ stands for the imaginary part. In the above equations, the non-local memory kernel terms are represented by new variables:

$$X(t) = -Q_1\int_0^t dt' \exp(-\gamma[t-t'])\,\alpha(t') \quad \text{(A5)}$$

$$Y(t) = -Q_2\int_0^t dt' \exp(-\gamma[t-t'])\beta(t') \quad \text{(A6)}$$

Satisfying

$$\dot{X} = \gamma X(t) - \gamma Q_1 \alpha(t) \quad \text{(A7)}$$

$$\dot{Y} = \gamma Y(t) - \gamma Q_1 \beta(t). \quad \text{(A8)}$$

The phase-space variables (s, θ) are not in closed form; they require extra variables (α, β,X, Y). Hence, we need to solve a higher-dimensional non-linear problem now. The six-dimensional equilibrium point is determined by setting $(\dot{\alpha}=0, \dot{\beta}=0, \dot{s}=0, \dot{\theta}=0, \dot{X}=0, \dot{Y}=0)$. We start by solving the simplest equation first. Eqs. (A7) and (A8) lead to the solution $X_j = -Q_1\alpha_j$ and $Y_j = -Q_2\beta_j$. Substitution into Eq. (A3) and Eq. (A4) leads to obtain the following relations:

$$\sin\theta_j = \frac{\zeta}{2}\sqrt{1-s_j^2} \quad \text{(A9)}$$

$$\cos\theta_j = \frac{\chi}{2}\sqrt{1-s_j^2} \quad \text{(A10)}$$

$$s_\pm = \pm\sqrt{1-\frac{4}{\chi^2+\zeta^2}} \quad \text{(A11)}$$

where the control parameters are $\zeta = (Q_2 - Q_1)/\Omega$ and $\chi = nU/\Omega$. The four fixed points (in six-dimensional space) are $P_{j=1,2,3,4} = (\alpha_j, \beta_j, X_j, Y_j, s_j, \theta_j)$:

$$P_1 = (\alpha_1, \beta_1, -Q_1\alpha_1, -Q_2\beta_2, 0, \sin^{-1}\tfrac{\zeta}{2}),$$

$$P_2 = (\alpha_2, \beta_2, -Q_1\alpha_2, -Q_2\beta_2, 0, \pi - \sin^{-1}\tfrac{\zeta}{2}),$$

$$P_3 = (\alpha_3, \beta_3, -Q_1\alpha_3, -Q_2\beta_3, \sqrt{1-\tfrac{4}{\chi^2+\zeta^2}}, \pi - \cos^{-1}\tfrac{\chi}{\chi^2+\zeta^2})$$

and

$$P_4 = (\alpha_4, \beta_4, -Q_1\alpha_4, -Q_2\beta_4, -\sqrt{1-\tfrac{4}{\chi^2+\zeta^2}}, \pi - \cos^{-1}\tfrac{\chi}{\chi^2+\zeta^2})$$

where (α_j, β_j) are obtained by solving the following non-linear coupled equations:

$$(-i\omega - Q_1 - iU|\alpha_j|^2)\alpha_j - i\Omega\beta_j = 0 \quad \text{(A12)}$$

$$-i\Omega\alpha_j + (-i\omega - Q_2 - iU|\beta_j|^2)\beta_j = 0. \quad \text{(A13)}$$

The above set of equations was derived from $\dot{\alpha} = 0$ and $\dot{\beta} = 0$ of Eqs. (A1) and (A2). The stability characteristic of the system has to be solved by 6 × 6 Jacobian matrix applying fixed points P_j. The Jacobian matrix is:

$$Z = \begin{pmatrix} z_{11} & -i & 1 & 0 & 0 & 0 \\ -i & z_{22} & 0 & 0 & 0 & 0 \\ -Q_1\alpha & 0 & -\gamma & 0 & 0 & 0 \\ 0 & -Q_2\beta & 0 & -\gamma & 0 & 0 \\ z_{51} & z_{52} & z_{53} & z_{54} & z_{55} & z_{56} \\ z_{61} & 0 & z_{63} & 0 & z_{65} & z_{66} \end{pmatrix} \quad \text{(A14)}$$

where $z_{11} = -i\omega - 2iU|\alpha|^2$, $z_{22} = -i\omega - 2iU|\beta|^2$, $z_{51} = \frac{1-s}{n}X^*$, $z_{52} = -\frac{1+s}{n}Y^*$,

$z_{53} = \frac{1-s}{n}\alpha^*$, $z_{54} = -\frac{1+s}{n}\beta^*$, $z_{55} = \frac{2s}{\sqrt{1-s^2}}\sin\theta - \frac{\alpha^*X+\alpha X^*}{n} - \frac{\beta^*Y+\beta Y^*}{n}$, $z_{56} = \frac{-2s\,\cos\theta}{\sqrt{1-s^2}}$, $z_{61} = -\Im\left(-\frac{X}{\alpha^*}\right)$, $z_{63} = \Im\left(\frac{1}{\alpha}\right)$, $z_{65} = \frac{2\cos\theta}{\sqrt[3]{1-s^2}} - \chi$ and $z_{66} = \frac{-2\,s\,\sin\theta}{\sqrt{1-s^2}}$.

For example, we can test the above result for interaction-free (χ= 0), dissipative (ζ = 0.1) systems, with other given parameters ω = 2.0, γ = 10, $Q_2 = 0.2$ and Q_1 =0.1, which takes a fixed point P_1 = (0, 0, 0, 0, 0, 0.05); thus, we have:

$$Z_{P1} = \begin{pmatrix} -2i & -i & 1 & 0 & 0 & 0 \\ -i & -2i & 0 & 0 & 0 & 0 \\ -1 & 0 & -10 & 0 & 0 & 0 \\ 0 & -2 & 0 & -10 & 0 & 0 \\ 0 & 0 & 0 & 0 & 0 & 0 \\ 0 & 0 & 0 & 0 & 2 & 0 \end{pmatrix} \quad \text{(A15)}$$

which gives a set of eigenvalues (-0.19 - 3.06i, -0.20 - 1.02i, -9.80 + 0.02i, -9.81+ 0.06i, 0, 0) that verifies a damped oscillatory motion of the system.

References

[1] Javanainen, J., Physical Review Letters, 57 (25) (1986) 3164.

[2] Milburn, G.J., Corney, J.F., Wright, E.M. and Walls, D.F., Physical Review A, 55 (6) (1997) 4318.

[3] Smerzi, A., Fantoni, S., Giovanazzi, S. and Shenoy, S.R., Physical Review Letters, 79 (25) (1997) 4950.

[4] Raghavan, S., Smerzi, A., Fantoni, S. and Shenoy, S.R., Physical Review A, 59 (1) (1999) 620.

[5] Albiez, M., Gati, R., Froelling, J., Hunsmann, S., Cristiani, M. and Oberthaler, M.K., Physical Review Letters, 95 (1) (2005) 010402.

[6] Gati, R., Hemmerling, B., Froelling, J., Albiez, M. and Oberthaler, M.K., Physical Review Letters, 96 (13) (2006) 130404.

[7] Zibold, T., Nicklas, E., Gross, C. and Oberthaler, M.K., Physical Review Letters, 105 (20) (2010) 204101.

[8] Levy, S., Lahoud, E., Shomroni, I. and Steinhauer, J., Nature, 449 (7162) (2007) 579.

[9] Hofferberth, S., Lesanovsky, I., Schumm, T., Imambekov, A., Gritsev, V., Demler, E. and Schmiedmayer, J., Nature-Physics, 4 (6) (2008) 489.

[10] Ruostekoski, J. and Walls, D.F., Physical Review A, 58 (1) (1998) R50.

[11] Khodorkovsky, Y., Kurizki, G. and Vardi, A., Physical Review Letters, 100 (22) (2008) 220403.

[12] Boukobza, E., Chuchem, M., Cohen, D. and Vardi, A., Physical Review Letters, 102 (18) (2009) 180403.

[13] Witthaut, D., Trimborn, F. and Wimberger, S., Physical Review Letters, 101 (20) (2008) 200402.

[14] Trimborn, F., Witthaut, D. and Wimberger, S., Journal of Physics B: Atomic, Molecular and Optical Physics, 41 (17) (2008) 171001.

[15] Witthaut, D., Trimborn, F., and Wimberger, S., Physical Review A, 79 (3) (2009) 033621.

[16] Wang, W., Fu, L.B. and Yi, X.X., Physical Review A, 75 (4) (2007) 045601.

[17] Huang, Y., Tan, Q.S., Fu, L.B. and Wang, X., Physical Review A, 88 (6) (2013) 063642.

[18] Ghasemian, E. and Tavassoly, M.K., Physics Letters A, 380 (40) (2016) 3262.

[19] Ghasemian, E. and Tavassoly, M.K., Laser Physics, 27 (9) (2017) 095202.

[20] Guarrera, V., Wuertz, P., Ewerbeck, A., Vogler, A., Barontini, G. and Ott, H., Physical Review Letters, 107 (16) (2011) 160403.

[21] Barontini, G., Labouvie, R., Stubenrauch, F., Vogler, A., Guarrera, V. and Ott, H., Physical Review Letters, 110 (3) (2013) 035302.

[22] Lindenberg, K. and West, B.J., "The Non-equilibrium Statistical Mechanics of Open and Closed Systems", (VCH New York, 1990).

[23] Scully, M.O. and Zubairy, M.S., "Quantum Optics", (Cambridge University Press, 1997).

[24] Lazarou, C., Nikolopoulos, G.M. and Lambropoulos, P., Journal of Physics B: Atomic, Molecular and Optical Physics, 40 (12) (2007) 2511.

[25] Nikolopoulos, G.M., Lazarou, C. and Lambropoulos, P., Journal of Physics B: Atomic, Molecular and Optical Physics, 41 (2) (2008) 025301.

[26] Rajagopal, K.K., Physica A: Statistical Mechanics and Its Applications, 429 (5) (2015) 231.

[27] Rajagopal, K.K. and Muniandy, S.V., Physica A: Statistical Mechanics and Its Applications, 434 (2015) 164.

[28] Yamamoto, Y. and Imamoglu, A., "Mesoscopic Quantum Optics", (John Wiley & Sons, Inc., New York, 1999).

[29] Rajagopal, K.K. and Ibragimov, G., Brazilian Journal of Physics, 50 (2) (2020) 178.

[30] Weiss, U., "Quantum Dissipative Systems", 3rd Edition, (World Scientific, Singapore, 2008).

[31] Uhlenbeck, G.E. and Ornstein, L.S., Physical Review, 36 (1930) 823.

[32] Sargsyan, V.V., Adamian, G.G., Antonenko, N.V. and Lacroix, D., Physical Review A, 90 (2) (2014) 022123.

[33] Rajagopal, K.K. and Ibragimov, G., Brazilian Journal of Physics, 51 (2021) 944.

[34] Pethick, C.J. and Smith, H., "Bose-Einstein Condensation in Dilute Gases", (Cambridge University Press, 2008).

[35] Trimborn, F., Witthaut, D. and Korsch, H.J., Physical Review A, 79 (1) (2009) 013608.

[36] Anglin, J.R. and Vardi, A., Physical Review A, 64 (1) (2001) 013605.

[37] Vardi, A, Yurovsky, V.A. and Anglin, J.R., Physical Review A, 64 (6) (2001) 063611.

[38] Tikhonenkov, I., Anglin, J.R. and Vardi, A., Physical Review A, 75 (1) (2007) 013613.

[39] Constantinides, A. and Mostoufi, N., "Numerical Methods for Chemical Engineers with Matlab Applications with Cdrom", (Prentice Hall PTR, 1999).

[40] Shampine, L.F., Gladwell, I., Shampine, L. and Thompson, S., "Solving ODEs with Matlab", (Cambridge University Press, 2003).

[41] Perko, L., "Differential Equations and Dynamical Systems", Volume 7, (Springer Science & Business Media, 2013).

[42] Barreira, L. and Valls, C., "Dynamical Systems: An Introduction", (Springer Science & Business Media, 2012).

[43] Bo, C., Lin, W.S. and Xi, Y.X., Chinese Physics Letters, 27 (7) (2010) 070303.

[44] Kordas, G., Wimberger, S. and Witthaut, D., Physical Review A, 87 (4) (2013) 043618.

[45] Hillery, M. and Zubairy, M.S., Physical Review Letters, 96 (5) (2006) 050503.

[46] Hillery, M. and Zubairy, M.S., Physical Review A, 74 (3) (2006) 032333.

[47] Labouvie, R., Santra, B., Heun, S., Wimberger, S. and Ott, H., Physical Review Letters, 115 (2015) 050601.

[48] Labouvie, R., Santra, B., Heun, S., Wimberger, S. and Ott, H., Physical Review Letters, 116 (2016) 235302.

[49] Kosloff, R., Quantum Thermodynamics: Entropy, 15 (2013) 2100.

[50] Hofer, P.P., Perarnau-Llobet, M., Miranda, L.D.M., Haack, G., Silva, R., Brask, J.B. and Brunner, N., New Journal of Physics, 19 (12) (2017) 123037.

Volume 15, Number 5, 2022. pp. 457-467

Jordan Journal of Physics

ARTICLE

The Existence of a Universal Frame of Reference, in Which it Propagates Light, is Still an Unresolved Problem of Physics

Karol Szostek[a] and **Roman Szostek**[b]

[a]*Department of Aerospace and Space Engineering, Rzeszow University of Technology, Rzeszow, Poland.*
[b]*Department of Quantitative Methods, Rzeszow University of Technology, Rzeszow, Poland.*

Doi: **https://doi.org/10.47011/15.5.3**
Received on: 01/02/2021; *Accepted on: 29/04/2021*

Abstract: This article shows that the existence of a universal frame of reference, in which light propagates, is still an unresolved problem of physics. The analyzed articles show that the rejection of the idea of ether due to Michelson-Morley's and Kennedy-Thorndike's experiments was too hasty. The zero results of these experiments can be explained by the theory with a universal frame of reference, in which light propagates. The fact that one-way speed of light has never been accurately measured and that there is a well-documented effect showing the anisotropy of space from the perspective of our frame of reference, which is the dipolar anisotropy of cosmic microwave background radiation, further substantiates theories with a universal frame of reference. The article shows that the null result of the Michelson-Morley and Kennedy-Thorndike experiments does not determine the Lorentz symmetry.

Keywords: Lorentz transformation, Coordinate and time transformation, Universal frame of reference, Anisotropy of cosmic microwave background radiation, One-way speed of light.

1. Introduction

In 1887, an experiment was conducted by Michelson-Morley [11], while in 1932, an improved version of it was carried out; i.e., Kennedy-Thorndike's experiment [7]. In these experiments, the light flow times along the two interferometer arms were compared with great accuracy. The aim of these experiments was to detect the motion of Earth in relation to hypothetical universal frame of reference (UFR, ether), in which light propagates. Relying on classical kinematics based on Galileo's transformation, which was then the only available theory describing the properties of time and space, the results of these experiments were predicted. From a simple geometric analysis, it follows that the time of light flow along the interferometer arm (back and forth) must depend on the angle between the arm and the direction of Earth's velocity in relation to ether [29], [30].

The results of these experiments did not show such a relation and therefore, they were read as an evidence that a universal frame of reference in which light is propagated does not exist and that one-way speed of light in vacuum (in a homogeneous gravitational field) is constant in all inertial frames of reference. Such views on the interpretation of these experiments have become established in physics. They are provided in textbooks and lectures on physics [29], [30].

Corresponding Author: Roman Szostek **Email**: rszostek@prz.edu.pl

The zero results of the Michelson-Morley's and Kennedy-Thorndike's experiments have shown that an average speed of light on the path to mirror and back is the same in every direction and in every inertial frame of reference. This is contrary to predictions of the classical kinematics with distinguished frame of reference, in which light is propagated. However, this is not an evidence that a universal frame of reference does not exist and that one-way speed of light in vacuum is constant in all inertial systems. These experiments have shown that ether does not exist in such a meaning, in which classical kinematics described it. After all, predictions of these experiments were calculated on the basis of classical kinematics. The experiment results showed that these forecasts were incorrect. The mistake in the interpretation of these experiments consisted in the fact that these conclusions were generalized in such a way that since ether cannot exist in a meaning in which classical mechanics described it, ether cannot exist in any other meaning.

This article provides an overview of publications in which is returned to UFR idea. These publications have shown that Michelson-Morley's and Kennedy-Thorndike's experiments have been misinterpreted for over 100 years, because in fact these experiments have not shown that ether does not exist. These experiments also did not show that the one-way speed of light in vacuum is constant. Michelson-Morley's and Kennedy-Thorndike's experiments can be explained by the theory with a universal frame of reference [19], [20], [21]. What is more, there are an infinite number of such theories [22]. Each of these theories models a reality with different physical properties.

These studies show that the Lorentz violation transformations are acceptable according to the zero result of the Michelson-Morley and Kennedy-Thorndike experiments.

2. One-way Speed of Light

In [32], an analysis of numerous experiments was carried out, in which the speed of light was measured. This analysis shows that the exact one-way speed of light has never been measured. The problem of measuring this speed results from that it is unknown how distant clocks can be synchronized without the use of an electromagnetic signal, where the speed must be measured with these clocks. In one-way speed of light measurement, it is also impossible to rely on clocks that were next to each other at the time of synchronization and then were separated from each other as out-of-synchronization clocks in relative motion. For these reasons, in all precise laboratory measurements of the speed of light, only an average speed of light covering the path along closed trajectory was measured. In such experiments, light always returns to the starting point. The same applies to Michelson-Morley's and Kennedy-Thorndike's experiments.

The speed of light measurement shows that an average speed of light in vacuum on the path back and forth is always constant. Due to the local nature of such measurements, caused by the small dimensions of measuring devices, it is considered to be the speed of light in a homogeneous gravitational field.

Despite the fact that there is no precise measurement of one-way speed of light, it is widely believed that the constancy of one-way speed of light in vacuum (in a constant gravitational field) is an experimental fact.

3. Modifications of the Lorentz Transformation

In 1905, Albert Einstein announced the Special Theory of Relativity [5]. It was widely recognized as a theory explaining the results of experiments with light. The Special Theory of Relativity was derived from three assumptions:

A. Coordinate and time transformation «inertial frame of reference – inertial frame of reference» is linear.

B. All inertial systems are equivalent.

This assumption means that there is no such a physical phenomenon which distinguishes the inertial system. It means that there is no such phenomenon for which the absolute rest is needed to explain. It also means that there is no physical phenomenon that allows a direction in space to be distinguished; that is, for each observer, space is isotropic. Mathematically, it results from this assumption that each coordinate and time transformation has coefficients with exactly the same numerical values as inverse transformation (with the accuracy to the sign resulting from the velocity direction between the systems).

C. Speed of light c in vacuum is the same in every direction and in all inertial systems.

The most important property of the Special Theory of Relativity is that the space is isotropic for an observer from any inertial system. According to this theory, there is no experiment that distinguishes a certain direction in space. Therefore, any experiment that distinguishes a certain direction in space will prove the incorrectness of this theory.

Since then, attempts have been made to return to the idea of ether by modifying Lorentz's transformation, on which the Special Theory of Relativity is based. This approach is described in articles [10], [15], [16], [17], [28].

In [28], the author described transformation from any inertial frame of reference U' to system U related with UFR in the form of:

$$t = \frac{1}{\sqrt{1-(v/c)^2}}t' \tag{1}$$

$$x = \frac{1}{\sqrt{1-(v/c)^2}}vt' + \sqrt{1-(v/c)^2}\cdot x' . \tag{2}$$

The speed v is a speed of the inertial system U' relative to UFR. Reverse transformation from system U related with UFR to any inertial system U' has the form of:

$$t' = \sqrt{1-(v/c)^2}\cdot t \tag{3}$$

$$x' = \frac{1}{\sqrt{1-(v/c)^2}}(-vt + x) . \tag{4}$$

In [10], the authors presented a derivation of transformation (3)-(4). They received this transformation from the Lorentz's transformation after changing the way of synchronizing clocks in inertial frames of reference.

These studies were developed by Selleri in [16] and [17]. In his work, he gave a formula for one-way speed of light in vacuum, resulting from transformation (3)-(4), which can be written in the form of:

$$c'_{\alpha'} = \frac{c^2}{c + v\cos\alpha'} . \tag{5}$$

Angle α' is the angle, measured by the observer, between the vector of its speed v in relation to the UFR and the vector of the speed c of light.

In [10], [16] and [17], as well as in [15], other transformations and discussions on this subject are presented.

Actually, in all works on Lorentz's transformation modification, new transformations were treated only as a different mathematical record of the Special Theory of Relativity. Most of the authors did not comment on this, but in [10], it was written directly: "*In this case, any reference frame ... can be chosen to be the ether system*" and "*thus, the much debated question concerning the empirical equivalence of special relativity and an ether theory taking into account time dilatation and length contraction but maintaining absolute simultaneity can be answered affirmatively*".

4. Special Theory of Ether

4.1 Assumptions of the Special Theory of Ether

A different approach to derivation of kinematics with a universal frame of reference is presented in [19]-[23]. In this case, the reasoning is based on an analysis of Michelson-Morley's and Kennedy-Thorndike's experiments with different assumptions than those underlying the Special Theory of Relativity. In this way, the Special Theory of Ether was derived. Michelson-Morley's and Kennedy-Thorndike's experiments have been analyzed in these works with the following assumptions:

I. Coordinate and time transformation «inertial frame of reference – inertial frame of reference» is linear.

II. For each motionless observer in relation to the universal frame of reference, the space is isotropic; i.e., it has the same properties in each direction.

III. There is at least one inertial frame of reference in which the speed of light in a vacuum is the same in each direction. This system is called a universal frame of reference. This one-way speed of light constant is indicated by the symbol $c = constant$.

IV. The average speed of light in the vacuum flowing way back and forth is constant for each observer from the inertial frame of reference. This average speed does not depend on the observer's velocity in relation to the universal frame of reference, nor on the direction of light propagation. This average

speed is also indicated by the symbol $c = constant$ (this results from the Michelson-Morley and Kennedy-Thorndike experiments).

According to these assumptions, there are infinitely many Special Theories of Ether with different physical properties. These theories differ, for example, in how bodies moving in relation to the universal frame of reference undergo transverse contraction or transverse elongation (i.e., in the direction perpendicular to the velocity v at which the body moves in relation to the universal frame of reference). If in the inertial system the body has the width D_y', then for the observer who is stationary in relation to the universal frame of reference, it is $\psi(v)$ times wider; i.e., it has the width:

$$D_y = \psi(v) D_y' . \tag{6}$$

4.2 Transformations of the Special Theory of Ether

In [19], [20], [21], a transformation of the Special Theory of Ether was derived, in which there is no transverse elongation (i.e., when $\psi(v) = 1$). This transformation is as identical as the Tangherlini's transformation (1)-(4) presented in [28].

Due to assumption that $\psi(v) = 1$, there are also:

$$y' = y \quad \text{and} \quad z' = z . \tag{7}$$

In this new approach, the Lorentz's transformation was not modified by changing the method of clock synchronization, but the transformation was derived from the basics through analysis of experiments. Thanks to explicit assumptions of the new theory, it was possible to generalize the transformation (1)-(4) and show that there are infinitely many theories with a universal frame of reference, which are according to Michelson-Morley's and Kennedy-Thorndike's experiments [22].

In [22], a general form of transformation was derived for any function $\psi(v)$. Coordinate and time transformations from any inertial system U' to U system related with UFR have a form of:

$$\begin{cases} t = \dfrac{\psi(v)}{\sqrt{1-(v/c)^2}} t' \\ x = \dfrac{\psi(v)}{\sqrt{1-(v/c)^2}} v t' + \psi(v)\sqrt{1-(v/c)^2} \cdot x' \\ y = \psi(v) y' \\ z = \psi(v) z' \end{cases} \tag{8}$$

Reverse transformations from U system related with UFR to any inertial system U' have the form of:

$$\begin{cases} t' = \dfrac{\sqrt{1-(v/c)^2}}{\psi(v)} t \\ x' = \dfrac{1}{\psi(v)\sqrt{1-(v/c)^2}} (-vt + x) \\ y' = \dfrac{y}{\psi(v)} \\ z' = \dfrac{z}{\psi(v)} \end{cases} \tag{9}$$

In order for a function $\psi(v)$ to have a natural physical interpretation, it should be continuous and meet the following conditions:

$$\psi(0) = 1 \tag{10}$$

$$\psi(v) \geq 0 . \tag{11}$$

If the space is supposed to be isotropic (for an observer immobile relative to the ether), it must additionally occur that:

$$\psi(v) = \psi(-v) . \tag{12}$$

Each of transverse elongation functions $\psi(v)$ defines a different theory of kinematics. It suffices to note that on the basis of (8) or (9), time dilatation between the inertial system U' and U system related with UFR depends on the transverse elongation function $\psi(v)$, as expressed by the formula:

$$dt' = \frac{\sqrt{1-(v/c)^2}}{\psi(v)} dt . \tag{13}$$

Time dilatation depends to the function $\psi(v)$; i.e., if kinematics differs in the function $\psi(v)$, there is a different time dilatation. Time dilatation is an effect that can be measured experimentally and therefore, if models differ in time dilatation, they describe other kinematics. In addition, it results that time dilatation can be

a basis for falsification of various theories described in transformations (8)-(9).

Ref. [22] presents three special cases of transformation (8). One of the special cases of these transformations is Tangherlini's transformation (1)-(4), which is obtained when:

$$\psi(v) = 1. \tag{14}$$

Then, transformation (8) assumes the form (1)-(2). For such a transformation, the kinematic and dynamics of bodies analyzed in [19] are obtained. In this case of the Special Theory of Ether, transverse contraction or elongation does not occur. The Special Theory of Ether without transverse contraction is closely linked to the Special Theory of Relativity by Einstein, because in both of these theories, there is neither a transverse contraction nor an elongation.

If it is assumed that:

$$\psi(v) = \frac{1}{\sqrt{1-(v/c)^2}} \geq 1, \tag{15}$$

then transformation (8) takes the form of:

$$\begin{cases} t = \dfrac{1}{1-(v/c)^2}\, t' \\ x = \dfrac{1}{1-(v/c)^2}\, vt' + x' = vt + x' \\ y = \dfrac{1}{\sqrt{1-(v/c)^2}}\, y' \\ z = \dfrac{1}{\sqrt{1-(v/c)^2}}\, z' \end{cases} \tag{16}$$

For such transformation, we obtain kinematics in which there is no longitudinal contraction; i.e., in the direction parallel to v velocity and x axis (FitzGerald-Lorentz contraction). At the same time, there is a lateral elongation (in a direction perpendicular to v velocity).

If it is assumed that:

$$\psi(v) = \sqrt{1-(v/c)^2} \leq 1, \tag{17}$$

then transformation (8) takes the form of:

$$\begin{cases} t = t' \\ x = vt' + (1-(v/c)^2)\, x' \\ y = \sqrt{1-(v/c)^2} \cdot y' \\ z = \sqrt{1-(v/c)^2} \cdot z' \end{cases} \tag{18}$$

For such a transformation, we obtain kinematics in which time is absolute. It is very interesting that there is a possible theory with an absolute time that meets the conditions of Michelson-Morley's and Kennedy-Thorndike's experiments.

If two inertial systems U_1 and U_2 move relative to UFR along one straight with v_1 and v_2 velocities respectively, then the transformation between these systems is a complex of transformations (8) and (9). This transformation takes the form of:

$$\begin{cases} t_1 = \dfrac{\psi(v_2)}{\psi(v_1)} \dfrac{\sqrt{1-(v_1/c)^2}}{\sqrt{1-(v_2/c)^2}}\, t_2 \\ x_1 = \dfrac{\psi(v_2)}{\psi(v_1)} \dfrac{v_2 - v_1}{\sqrt{1-(v_1/c)^2}\sqrt{1-(v_2/c)^2}}\, t_2 \\ \qquad + \dfrac{\psi(v_2)}{\psi(v_1)} \dfrac{\sqrt{1-(v_2/c)^2}}{\sqrt{1-(v_1/c)^2}}\, x_2 \\ y_1 = \dfrac{\psi(v_2)}{\psi(v_1)}\, y_2 \\ z_1 = \dfrac{\psi(v_2)}{\psi(v_1)}\, z_2 \end{cases} \tag{19}$$

4.3 Properties of the Special Theories of Ether

The Special Theory of Relativity and Special Theories of Ether are alternative models of kinematics.

If in STE without transverse contraction ($\psi(v) = 1$) the observer is motionless with regard to ether, then predictions of this theory are as identical as predictions for any observer in STR (Fig. 1).

Differences between theories occur when in STE without transverse contraction the observer moves with regard to ether. In STR, all inertial systems are equivalent; i.e., there is no universal frame of reference. For this reason, according to STR, it is not possible to measure the absolute speed using local measurement. This means that for each observer, the space is completely isotropic (has the same properties in each direction). However, according to STE without

transverse contraction, the observer can use a local measurement to determine the direction of its movement in relation to UFR. This means that for observers moving in relation to UFR, the space is not isotropic (has different properties in different directions). This is the most important difference between the Special Theory of Relativity and the Special Theory of Ether without transverse contraction.

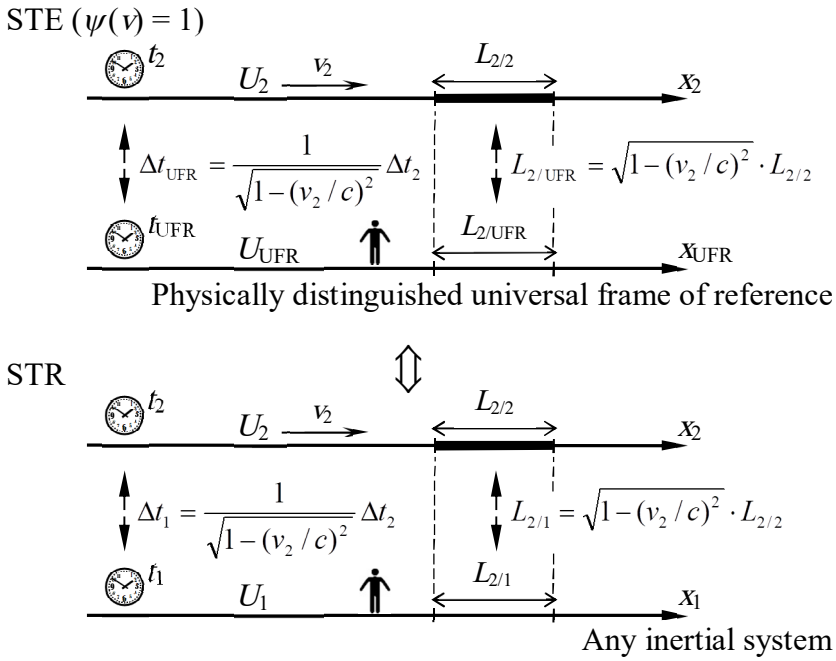

FIG. 1. Similarities between STR and STE ($\psi(v) = 1$) [source [21]].

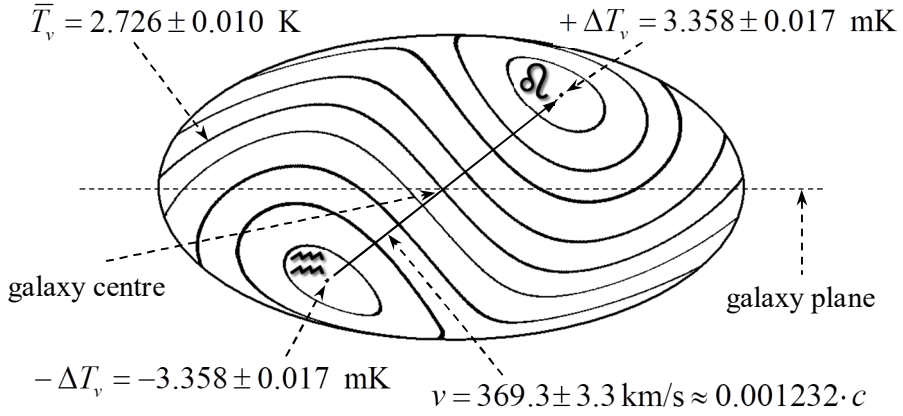

FIG. 2. Dipolar anisotropy of cosmic microwave background shown in Hammer-Aitoff projection [source [23]].

With reference to the above, if predictions of the Special Theory of Ether without transverse contraction were to be real, then in astronomical observations, some anisotropy should be visible. It turns out that such a phenomenon exists and it is very well studied. This is the dipolar anisotropy of cosmic microwave background [18].

From the perspective of our frame of reference, which is associated with the Solar System, the cosmic microwave background is heterogeneous. The strongest heterogeneity of cosmic microwave background has a dipole form, as shown in Fig. 2. From the direction of Leo constellation reaches us microwave of a slightly higher frequency (higher temperature), while from the direction of Aquarius

constellation reaches us microwave of a slightly lower frequency (lower temperature).

In the Special Theory of Ether, the cosmic microwave background can be an electromagnetic thermal radiation of ether (black-body radiation). In fact, satellite measurements have shown that cosmic microwave background has a black-body radiation distribution of temperature 2.726±0.010K [18]. If the cosmic microwave background is the thermal radiation of ether, it is produced at all times, throughout the space, including in our immediate vicinity. Therefore, in this radiation, the distribution of galaxies is very poorly visible. So, cosmic microwave background did not arise in the early universe as is commonly believed today.

If the universe is homogeneous and filled with homogeneous ether, the cosmic microwave background should be homogeneous in the ether system. The dipolar anisotropy of this radiation as measured in our reference frame is caused by the Doppler effect that results from the movement of the Solar System relative to ether.

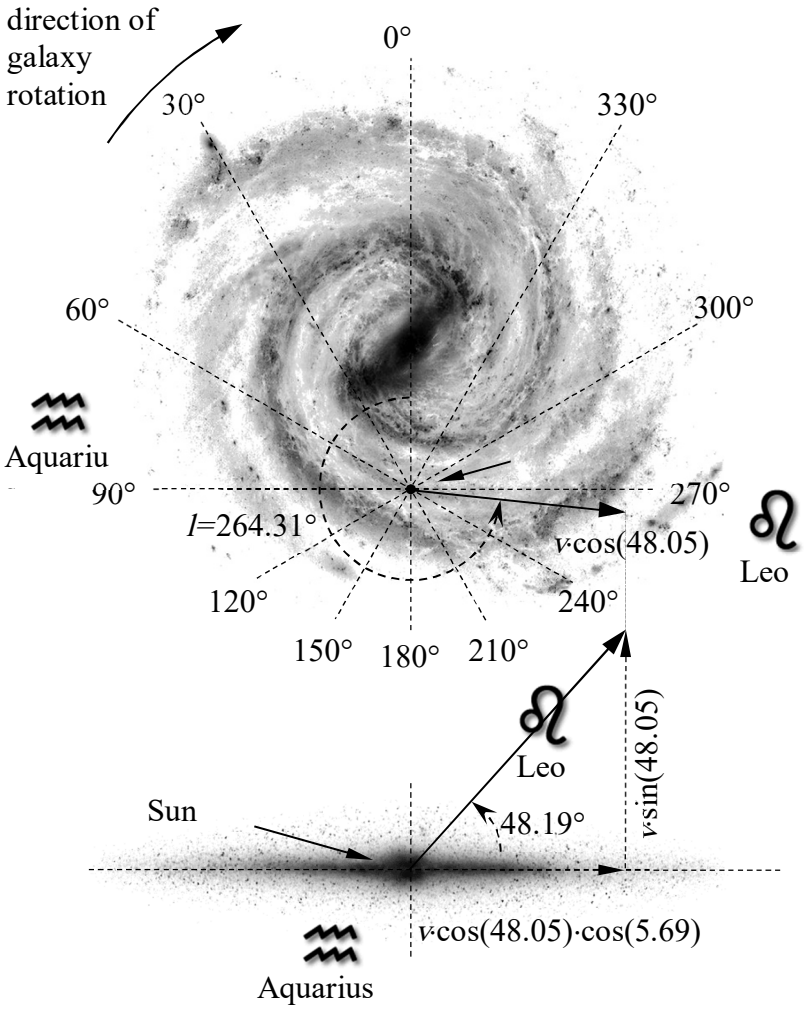

FIG. 3. The velocity of the Solar System in relation to the ether. The projection is on the plane of the galaxy and on the plane perpendicular to the plane of the galaxy (90°-270°). The top view of the Milky Way galaxy (with marked galactic coordinates) and side view [source [22]].

In such an interpretation, the dipolar anisotropy of cosmic microwave background can be used to determine the velocity at which the solar system moves in relation to UFR. This velocity is specified in [22]. Its value is 369.3 km/s = 0.0012 c and it is directed towards the Leo constellation (Fig. 3). This corresponds to galactic coordinates (source [18]):

$$l = 264.31° \pm 0.16°$$
$$b = 48.05° \pm 0.10° \quad (20)$$

Experimental falsification of STE is not easy due to the low speed of the Solar System relative

to ether. For a speed of 369.3 km/s, the anisotropy effects of space predicted by STE are very slight. Therefore, falsification of this theory requires especially designed experiments and their completion with a sufficiently high accuracy [21].

In [22], on the basis of transformation (8) and (9), a formula for one-way speed of light in vacuum $c'_{\alpha'}$ running in any direction in a form identical to that of formula (5) has been derived. It shows that one-way speed of light (5) does not depend on the transverse-elongation function $\psi(v)$. Functional diagrams (5) are shown in Fig. 4.

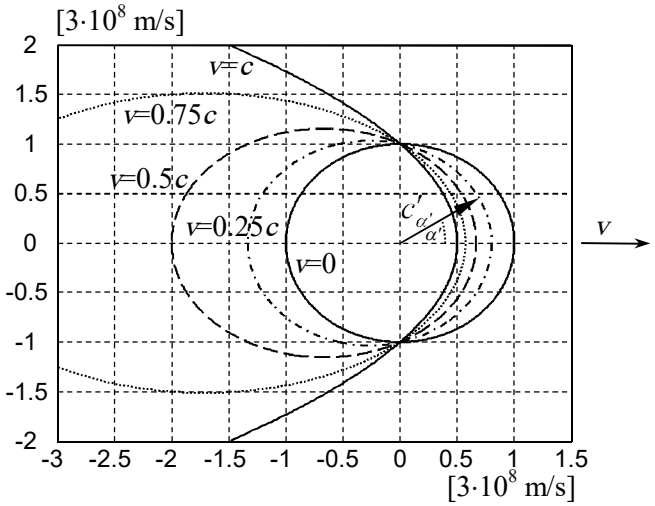

FIG. 4. One-way speed of light $c'_{\alpha'}$ predicted by STE in the inertial system for $v = 0, 0.25c, 0.5c, 0.75c, c$ [source [22]].

In the monograph shown in [19], on the basis of transformations (8) and (9), a more general formula for one-way speed of light was derived, for the light that flows through a medium. If the observer is motionless in relation to this medium, then the one-way speed of light for the observer is expressed by the formula:

$$c'_{s\alpha'} = \frac{c^2 c_s}{c^2 + c_s v\cos\alpha'}. \tag{21}$$

The symbols α', v and c have the same meaning as in formula (5). The speed c_s is the light speed in a medium in relation to UFR as seen by the motionless observer relative to UFR.

The formula (20) comes down to formula (5) if only place $c_s = c$. According to this relation, an average speed of light on the path of L-length to the mirror and back is as follows:

$$\begin{cases} c'_{sr} = \dfrac{2L}{t'_{s\alpha'} + t'_{s(\pi+\alpha')}} = \\ = \dfrac{2L}{\dfrac{L}{\dfrac{c^2 c_s}{c^2 + c_s v\cos\alpha'}} + \dfrac{L}{\dfrac{c^2 c_s}{c^2 + c_s v\cos(\pi+\alpha')}}} \end{cases} \tag{22}$$

$$\begin{cases} c'_{sr} = \dfrac{2}{\dfrac{c^2 + c_s v\cos\alpha'}{c^2 c_s} + \dfrac{c^2 - c_s v\cos\alpha'}{c^2 c_s}} \\ = \dfrac{2}{\dfrac{2c^2}{c^2 c_s}} = c_s \end{cases} \tag{23}$$

From relation (23), it results that c_s is also an average speed of light on the path to mirror and back in the motionless medium relative to a movable observer.

Although the one-way speed of light expressed by formula (21) depends on angle α' and speed v, the average speed of light on the path to mirror and back is always constant and it is c_s. If the speed of light has the properties described by formula (21), then Michelson-Morley's and Kennedy-Thorndike's experiments are unable to detect a universal frame of reference in which light is propagated.

From the above results, the widely accepted view of Michelson-Morley's and Kennedy-Thorndike's experiments proving that there is no universal frame of reference in which light is propagated and that the one-way speed of light in vacuum is the same for every observer, is

false [20]. What is more, there are infinitely many theories with a universal frame of reference, which are according to the results of Michelson-Morley's and Kennedy-Thorndike's experiments (theories included in transformations (8)-(9)) [22].

From the above results, it also follows that Michelson-Morley's and Kennedy-Thorndike's experiments are not sufficient to justify the Special Theory of Relativity and Lorentz symmetry [21].

In the monograph in [19], it is shown that if one-way speed of light is expressed in formula (5) or formula (21), then the average speed of light flowing along closed trajectory is always constant, even if various sections of this trajectory lead through various media. Therefore, Michelson-Morley's and Kennedy-Thorndike's experiments cannot detect UFR, even for very complex configurations of these experiments.

Proposals of measurement systems, which may allow to measure one-way speed of light and falsification of various kinematics theories, are presented in patents [27] and [33]. In these systems, remote clocks are synchronized with a rotating rod, which is a diameter of the rotating wheel. These systems probably will not allow for a very precise measurement of the one-way speed of light. Their aim is precise enough measurement to reveal the anisotropy of this speed. In the monograph in [19], the minimal requirements were designated for the device from patent [27], at which the anisotropy of one-way speed of light resulting from the Special Theory of Ether should be visible; formula (5).

Adopting that one-way speed of light can depend on a direction of its emission does not distinguish any direction in space. It is about the speed of light measured by a movable observer. The speed at which the observer moves in relation to ether distinguishes the characteristic direction in space, but only for this observer. For the motionless observer in relation to ether, the speed of light is always constant and does not depend on a direction of its emission. If the observer moves in relation to ether, then the space is not symmetrical. In this case, it will be like for an observer sailing on water and measuring the speed of waves on water. Although the waves propagate at a constant speed in each direction, the wave speed of the sailing observer will vary in different directions. For this reason, the presented theory based on assumptions I-IV, in a simple way explains the dipolar anisotropy of cosmic microwave background. Within the presented theory, this anisotropy is caused by the Doppler effect, which results from the Solar System motion relative to a universal frame of reference in which light is distributed (i.e., also cosmic microwave background) [22].

5. Final Conclusions

The Special Theory of Relativity has numerous experimental grounds. Michelson-Morley's and Kennedy-Thorndike's experiments are also consistent with it, but are not sufficient in order to demonstrate its correctness [22], [23]. These experiments can be explained with the use of various theories, in which a physically distinguished universal frame of reference occurs.

Lorentz's transformation, on which kinematics of the Special Theory of Relativity are based, can be recorded in various ways, after changing the method of clock synchronization in inertial systems. If, as a result of the changed synchronization of clocks, an inertial frame of reference is distinguished, it can be any inertial system. New transformations obtained in this way are treated as a different model of the same Special Theory of Relativity. The interpretation of such models is such that the distinguished inertial system does not have any unique physical features, but is distinguished artificially.

Transformations of the Special Theory of Ether were not created by modifying the transformations previously known, but were derived from the basics (assumptions I-IV). Thanks to this, it was possible to derive completely new transformations (8)-(9) according to Michelson-Morley's and Kennedy-Thorndike's experiments. In the Special Theory of Ether, the universal frame of reference is a real system, not a freely chosen inertial frame of reference. According to the Special Theory of Ether, a universal frame of reference is distinguished from all inertial frames of reference by its physical properties. It is an only frame of reference in which the space is isotropic. From the perspective of any other inertial system, the space is not isotropic. However, related effects are very minor in inertial systems moving with low velocities relative to ether (non-relativistic speeds) [21]. In

this case, it is similar to any other relativistic effect.

There is a very well documented astronomical observation, which shows that from the perspective of our frame of reference, the space is not isotropic [18]. This is the dipolar anisotropy of cosmic microwave background (Figure 2). There is a frame of reference in which the cosmic microwave background is isotropic. According to the Special Theory of Relativity, space should be isotropic for each observer; therefore, the dipolar anisotropy of the cosmic microwave background requires a special explanation within this theory. The existence of such a universal frame of reference is an argument in favour of the Special Theory of Ether and shows Lorentz symmetry breaking [21].

In theories with any space-filling medium, there may be an anisotropy for an observer moving in relation to this medium (even if such medium is isotropic). This property of the theory with the distinguished medium is consistent with the measurement of dipolar anisotropy of cosmic microwave background (CMB) discussed in Noble Lecture by G. Smoot [18]. If the cosmic microwave background is the thermal radiation of the distinguished isotropic medium (radiation of the black body), then the cosmic microwave background is isotropic in the reference frame associated with this medium, but shows dipolar anisotropy in the reference frames of reference moving in relation to the medium. In the Special Theory of Relativity, such an effect does not occur, because this theory is based on the assumption that physically, the space is isotropic and homogeneous for each observer from an inertial frame of reference.

For each kinematics it is possible to derive many dynamics. Examples for Special Theory of Ether were derived in monograph [19]. The examples for Special Theory of Relativity were derived in [25].

In [23], it was shown that the Lorentz transformations should be given a different interpretation than the one adopted in the Special Theory of Relativity. It has been shown that the commonly adopted interpretation of STR mathematics is incorrect, as it is a theory with desynchronized clocks that cause the unreal time to elapse measurements in inertial systems moving in relation to the observer. Incorrectly calibrated clocks are the cause of numerous paradoxes of STR.

The problem that mathematical formulas can be assigned different physical interpretations is not just about the Lorentz transformation. For example, in [26], it was shown that gravitational waves should be interpreted as an ordinary modulation of gravitational field intensities. The modulation resulting from the General Theory of Relativity is a property of a system of rotating bodies, not a property of the gravitational interaction, as is commonly believed today.

Ref. [24] explains what time is in physical theories and presents a proof that the mathematics of kinematics of the Special Theory of Relativity does not indicate that the speed of light in a vacuum is the maximum speed in nature. The notion that the speed of light in a vacuum is an impassable speed results from the overinterpretation of the mathematics on which the kinematics of STR is based. Ref. [24] shows that because in the Special Theory of Relativity and Special Theory of Ether kinematics a light signal is used to synchronize the clocks, a light clock is automatically introduced in these theories as a time standard. In other words, STR and STE are theories in which time is measured by the light clock. These are theories that describe the practical aspects of using such clocks. Therefore, in these theories, there is a time dilation phenomenon which is a natural property of the light clock.

Ref. [8] presents the original definition of acceleration in the Special Theory of Relativity, while Ref. [9] develops the formalism for three-vector and four-vector relative velocity. Refs. [12] and [13] relate to important insights into time dilation in relativity, while Ref. [14] presents alternative ideas for relativity. Numerous works discussed the zero result of the Michelson-Morley experiment, from which time dilation and the Lorentz-FitzGerald contraction results [1, 31]. Ref. [3] presents an analysis of various problems related to the Special Theory of Relativity, while Ref. [2] analyzes the generalized Sagnac effect in inertial frames as well as rotating frames. There are also published papers showing the paradoxes of the Special Theory of Relativity concerning rotating frames of reference [6]. Ref. [4] is investigating the subject of relativistic velocity addition. There are many papers on relativistic mechanics with significant theoretical results.

References

[1] Akram, L., Maghrebian Journal of Pure and Applied Science, 6 (2) (2020) 60.

[2] Choi, Y.-H., Canadian Journal of Physics, 95 (8) (2017) 761.

[3] Choi, Y.-H., Journal of the Korean Physical Society, 72 (10) (2018) 1110.

[4] Choi, Y.-H., Open Physics, 20 (1) (2022) 155.

[5] Einstein, A., Annalen der Physik, 17 (1905) 891. / Einstein, A., "O elektrodynamice ciał w ruchu" (in Polish), In: "5 prac, które zmieniły oblicze fizyki". (Wydawnictwa Uniwersytetu Warszawskiego, Biblioteka Klasyków Nauki, Warszawa, 2008).

[6] Javanshiry, M., International Journal of Mathematics and Mathematical Sciences, 2021 (ID 2706705) (2021) 1.

[7] Kennedy, R.J. and Thorndike, E.M., Physical Review, 42 (3) (1932) 400.

[8] Koczan, G.M., Results in Physics, 24 (2021) 104121.

[9] Koczan, G.M., Acta Physica Polonica A, 4 (139) (2021) 401.

[10] Mansouri, R. and Sexl, R.U., General Relativity and Gravitation, 8 (7) (1977) 497.

[11] Michelson, A.A. and Morley, E.W., Am. J. Sci., 34 (1887) 333.

[12] Nawrot, W., Physics Essays, 17 (4) (2004) 518.

[13] Nawrot, W., Physics Essays, 27 (4) (2014) 598.

[14] Nawrot, W., International Journal of Theoretical and Mathematical Physics, 7 (5) (2017) 95.

[15] Rizzi, G., Ruggiero, M.L. and Serafini, A., Foundations of Physics, 34 (12) (2004) 1835.

[16] Selleri, F., Foundations of Physics, 26 (5) (1996) 641.

[17] Selleri, F., Foundations of Physics Letters, 10 (1) (1997) 73.

[18] Smoot, G.F., Reviews of Modern Physics, 79 (2007) 1349.

[19] Szostek, K. and Szostek, R., "Special Theory of Ether", (Publishing House Amelia, Rzeszów, Poland, 2015), ISBN 978-83-63359-81-2.

[20] Szostek, K. and Szostek, R., Journal of Modern Physics, 8 (11) (2017) 1868.

[21] Szostek, K. and Szostek, R., Moscow University Physics Bulletin, 73 (4) (2018) 413.

[22] Szostek, K. and Szostek, R., Results in Physics, 8 (2018) 429.

[23] Szostek, R., Moscow University Physics Bulletin, 75 (6) (2020) 684.

[24] Szostek, R., Applied Sciences, 12 (12) (ID 6272) (2022) 1.

[25] Szostek, R., Open Physics, 17 (2019) 153.

[26] Szostek, R., Bulletin of the Karaganda University, Physics Series, 4 (96) (2019) 39.

[27] Szostek, K. and Szostek, R., Polish Patent Office, patent number 227641, application number P.414434 of 20.10.2015.

[28] Tangherlini, F.R., A Dissertation, Stanford University, (1958), (reprint in: The Abraham Zelmanov Journal, 2 (2009)).

[29] Taylor, E. F. and Wheeler, J.A., "Space time Physics", (W. H. Freeman and Company, New York 1992).

[30] Ugarow, W.A., "Special Theory of Relativity", (Mir Publishers, 1979).

[31] Yuan, T., Open Access Library Journal, 8 (11) (e8011) (2021) 1.

[32] Yuan, Z.Z., "Special Relativity and Its Experimental Foundation", Singapore, (World Scientific Publishing, 1997).

[33] Zhu, X., Chinese Patent Office, patent number CN101000265 A, application number CN 200610172796 of 31.21.2006.

Volume 15, Number 5, 2022. pp. 469-476

Jordan Journal of Physics

ARTICLE

Numerical Calculations of Energies for an Infinite Potential Well with Sinusoidal Bottom

Ahmad Jaber, Ayham Shaer, Sami Mukhiemer and **Sami Al-Jaber**

Physics Department, Faculty of Science, An-Najah National University, Nablus, West Bank, Palestine.

Doi: **https://doi.org/10.47011/15.5.4**

Received on: 26/02/2021; *Accepted on: 30/06/2021*

Abstract: We present an investigation for a particle confined in an infinite well with sinusoidal bottom, using the perturbation theory and numerical solution for the Schrödinger equation to obtain the eigen energies and wavefunctions. Potential strength and potential oscillation dependence of the state are examined and analyzed. It is shown that the particle in a box with sinusoidal bottom does not show up the Klauder phenomenon when the perturbations are gradually reduced to zero. The research results show that the potential oscillation significantly affects certain quantum states and, therefore, the ability to manipulate the energy difference between the states. In addition, our results for the present system converge to their corresponding values for the unperturbed one in the high-potential oscillation limit.

Keywords: Infinite well, Perturbation theory, Sinusoidal potential, Numerical calculations, Klauder phenomenon.

Introduction

Since the proposal of the infinite potential well as a hypothetical model set up to demonstrate the differences between both classical and quantum points of view regarding the movement of a free particle in some confinement, the research in this area never stopped. The infinite potential well was extensively studied under different constraints and modifications [1-5]. Even though the infinite potential well is a hypothetical model, it remains a good candidate for a lot of quantum applications [6-7], and its analytical solution is still widely used for variational and numerical techniques in quantum mechanics [8-9].

The traditional version of the infinite potential well (flat bottom) exhibits the well-known energy eigenvalues and normalized eigenfunctions given by:

$$E_n = \frac{\hbar^2 \pi^2 n^2}{2ML^2}, \Phi_n = \sqrt{\frac{2}{L}} \sin\left(\frac{n\pi x}{L}\right) \quad (1)$$

where M, L, and n denote the confined particle's mass, the well's width and the quantum number (n = 1, 2, 3, …), respectively. Changing the shape of the bottom of the well is expected to result in some modifications of the system's eigenvalues and the corresponding wave functions.

The sinusoidal potential is considered the general case for any periodic potential, since one can use Fourier series to write any periodic potential in terms of sine and cosine. Very recently, a prototypical model of a one-dimensional metallic monatomic solid containing non-interacting electrons was studied, where the potential energy has been considered to be sinusoidal [10]. Also, Sakly et al. [11] have investigated the electronic states using the

Corresponding Author: Ayham Shaer **Email**: ayham.shaer@najah.edu

sinusoidal potential for $Cd_{1-x}Zn_xS$ quantum dot superlattices with a finite barrier at the boundary.

In 2008, Alhaidari and Bahlouli [12] studied the infinite potential well with sinusoidal bottom and proposed an ability to get the exact energy eigenvalues from the solution of a three-term recursion relation. In their work, they also showed a possibility of the Klauder phenomenon (where the system for a certain perturbation will not give the same states as unperturbed Hamiltonian when the perturbation is turned off; mathematically:

$\lim_{\lambda\to 0}\langle H_0 + \lambda H'\rangle \neq \langle H_0\rangle$.

Three years later, Dhatt and Bhattachrayya [13] restudied the same system for the potential well by perturbative and variational methods and concluded the non-existence of Klauder phenomenon as perturbation goes to zero. Their work was carried out for the ground-state energy in the lowest perturbation orders by applying the standard Rayleigh-Schrödinger perturbation theory.

In the present work, the Schrödinger equation has been solved for the particle in an infinite well with sinusoidal bottom by using perturbative and numerical methods and the effect of the bottom potential parameters (potential oscillation and strength) on the energy and states of the particle has also been studied.

In the rest of this article, we present the theoretical framework and Hamiltonian in next section. Then, numerical calculations and illustrations are presented, and the last section is devoted for remarks and conclusions.

Theoretical Framework

The one-dimensional time-independent Schrödinger equation for a particle confined in an infinite square well with a cosine sinusoidal bottom is given by:

$$\left(-\frac{\hbar^2}{2\,m}\frac{d^2}{dx^2}+V(x)\right)\psi(x)=E\,\psi(x), \tag{2}$$

where

$$V(x)=\begin{cases} C\cos\left(\frac{k\pi x}{L}\right) & 0<x<L \\ \infty & elsewhere \end{cases} \tag{3}$$

For the sake of simplicity, units are set such that $\hbar$ = 2m = 1.

Since the analytical solution of the above equation is not attainable and to obtain an approximate solution for this system, one can follow the perturbation-method steps. Dhatt et al provided a solution for the ground state with integer values of *k* [13] as:

$$E_1(k=1,C)=\left(\frac{\pi}{L}\right)^2-C^2\frac{L^2}{12\pi^2}+O(C^4) \tag{4}$$

$$E_1(k=2,C)=\left(\frac{\pi}{L}\right)^2-\frac{C}{2}-C^2\frac{L^2}{32\pi^2}+C^3\frac{L^4}{512\pi^4}+O(C^4) \tag{5}$$

$$E_1(k\geq 3,C)=\left(\frac{\pi}{L}\right)^2-C^2\frac{L^2}{2\pi^2(k^2-4)}+O(C^4) \tag{6}$$

with the approximate ground-state wave function given by:

$$\Psi_1(k=1,C)=\Phi_1-C\frac{L^2}{6\pi^2}\Phi_2+C^2\frac{L^4}{96\pi^4}\Phi_3+O(C^3) \tag{7}$$

$$\Psi_1(k=2,C)=\Phi_1-C\frac{L^2}{16\pi^2}\Phi_3+C^2\frac{L^4}{256\pi^4}\left[\Phi_3+\frac{1}{3}\Phi_5\right]+O(C^3) \tag{8}$$

where Φ_i refers to the normalized parent box states given by:

$$\Phi_i=\sqrt{\frac{2}{L}}\sin\left(\frac{i\,\pi\,x}{L}\right). \tag{9}$$

To make a general view, we proceeded via a perturbative route:

$$E_n(C)=E_n^{(0)}+\langle\Phi_n^{(0)}|V|\Phi_n^{(0)}\rangle+\sum_{m\neq n}\frac{\left|\langle\Phi_m^{(0)}|V|\Phi_n^{(0)}\rangle\right|^2}{E_n^{(0)}-E_m^{(0)}}+O(C^3) \tag{10}$$

and obtained a closed-form correction (up to second order) for any quantum state energy with integer values of *k* with the help of the following integral relation:

$$\int_0^L\frac{2}{L}\sin\left(\frac{n\pi x}{L}\right)\cos\left(\frac{k\pi x}{L}\right)\sin\left(\frac{m\pi x}{L}\right)\,dx=\begin{cases}-\frac{1}{2}\ if\ k=m+n\\ \frac{1}{2}\ if\ k=|m-n|\\ 0\ otherwise\end{cases} \tag{11}$$

where n, k, and m are positive integers.

The energy for any state (n) for a given integer (k) and strength (c) is given by:

$$E_n(c,k) = \frac{\pi^2 n^2}{L^2} - \frac{1}{2}\, c\, \delta_{k-2n} - \frac{c^2 L^2}{4\pi^2(k^2+2kn)} + \frac{c^2 L^2\,(1-\delta_{k-2n})\Theta\,(|k-n|-\epsilon)}{4\pi^2(2kn-k^2)} \quad (12)$$

where ϵ is a small positive number to avoid the undefined value for the step function, $\Theta(0)$. For the ground state (n=1), Eq. (12) has been tested with previously mentioned Eqs. (4 - 6).

To be able to investigate the effect of larger values of C – where the perturbative approximated solution is not accurate – and the non-integer values of k, the Numerov numerical method was performed, and the eigen energies were calculated.

The Numerov method is a specialized integration formula for numerically integrating differential equations of the form:

$$\psi''(x) = f(x)\psi(x). \quad (13)$$

For the time-independent 1-D Schrödinger equation,

$$f(x) = -\frac{2m(E-V(x))}{\hbar^2}. \quad (14)$$

Choosing a grid spacing $\Delta x = x_i - x_{i-1}$, the integration formula is given by:

$$\psi_{i+1} = \frac{\psi_{i-1}(12-\Delta x^2 f_{i-1}) - 2\psi_i(5\Delta x^2 f_i + 12)}{\Delta x^2 f_{i+1} - 12} + O(\Delta x^6) \quad (15)$$

And by shooting a trial energy and iteration over the grid domain, one can find the numerical energy and wavefunction. Interested readers can refer to [14].

Results and Discussion

In this section, we present our results for an infinite well with sinusoidal bottom and prefer to use L=1 in the numerical calculations.

To give a good picture about the sinusoidal bottom, we plot in Fig. 1 the infinite box for different values of k; so it is shown that the number of full waves (oscillations) equals $\frac{k}{2}$, and the even (odd) number of k exhibits a symmetric (antisymmetric) behavior around the middle point of the well ($\frac{L}{2}$),

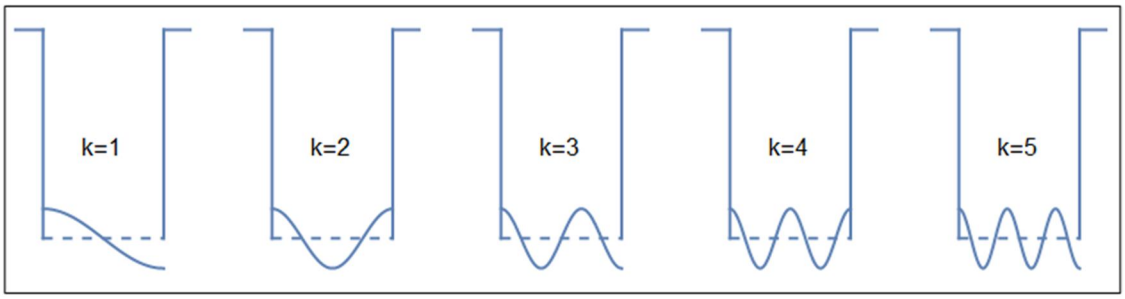

FIG. 1. Schematic plot of the infinite box for different integer values of k.

In Table 1, we provide the numerical value of energies for the ground state and few excited states for the particle in both cases, flat (unperturbed) and sinusoidal bottom well, for different values of potential amplitude (C) and potential oscillation (k), to show the agreement between the correlated energy (up to second-order correction) and quasi-exact numerical energy.

TABLE 1. Numerical values of energies (a.u) for the inner four states of the system, with L=1.

Quantum number	Energy		$E^{perturbative}$ $E^0+E^1+E^2$			$E^{numerical}$		
	Unperturbed energy		C= 2	C= 10	C=20	C= 2	C= 10	C=20
1	9.8696	K = 1	9.83583	9.02526	6.49223	9.83585	9.03972	6.70011
		K = 2	8.85694	4.55298	-1.39691	8.8571	4.57252	-1.24561
2	39.4784	K = 1	39.4919	39.8162	40.8294	39.4919	39.8015	40.6187
		K = 2	39.4699	39.2673	38.6341	39.4701	39.2676	38.6378
3	88.8264	K = 1	88.8322	88.9712	89.4054	88.8322	88.9714	89.4076
		K = 2	88.8328	88.9848	89.4597	88.8326	88.9652	89.3083
4	157.914	K = 1	157.917	157.994	158.235	157.917	157.994	158.236
		K = 2	157.917	157.998	158.251	157.917	157.998	158.248

Results show good agreement between the two methods, especially for low values of C, so the higher perturbative corrections can be neglected. Meanwhile, for larger values of C (when the perturbation becomes comparable to the ground-state energy), the effect of higher-order corrections becomes significant for ground state (n = 1) and less significant for higher states (n > 1), which agrees with the limitation of perturbation method. For a given value of C, the higher states are less sensitive to perturbation than the lower states. From this point of view, one can conclude that the perturbation method is suitable to investigate this problem for small values of C and so numerical calculations lead to a more reliable result for this reason, the Numerov numerical method has been used to produce all the following illustrations, while the perturbation analytical expressions for energy have been considered for some explanations.

The ground-state energy has been plotted in Fig. 2 as a function of the bottom potential amplitude for different integer values of k (the k = 2 case has been plotted separately in Fig. 2b). Fig. 2a clearly shows that as k increases, the effect of the perturbation becomes less significant and the ground-state energy becomes closer to the unperturbed one; notice k = 60 case. Eq. (12) shows that the first-order correction equals zero for any integer value of k, except for (k = 2); so, it is expected that all major corrections come from the second-order correction term. As it is known, the second-order correction of the ground state always reduces the energy of the ground state. In contrast to the above remarks, the ground-state energy for (k = 3) is less than (k = 1) energy.

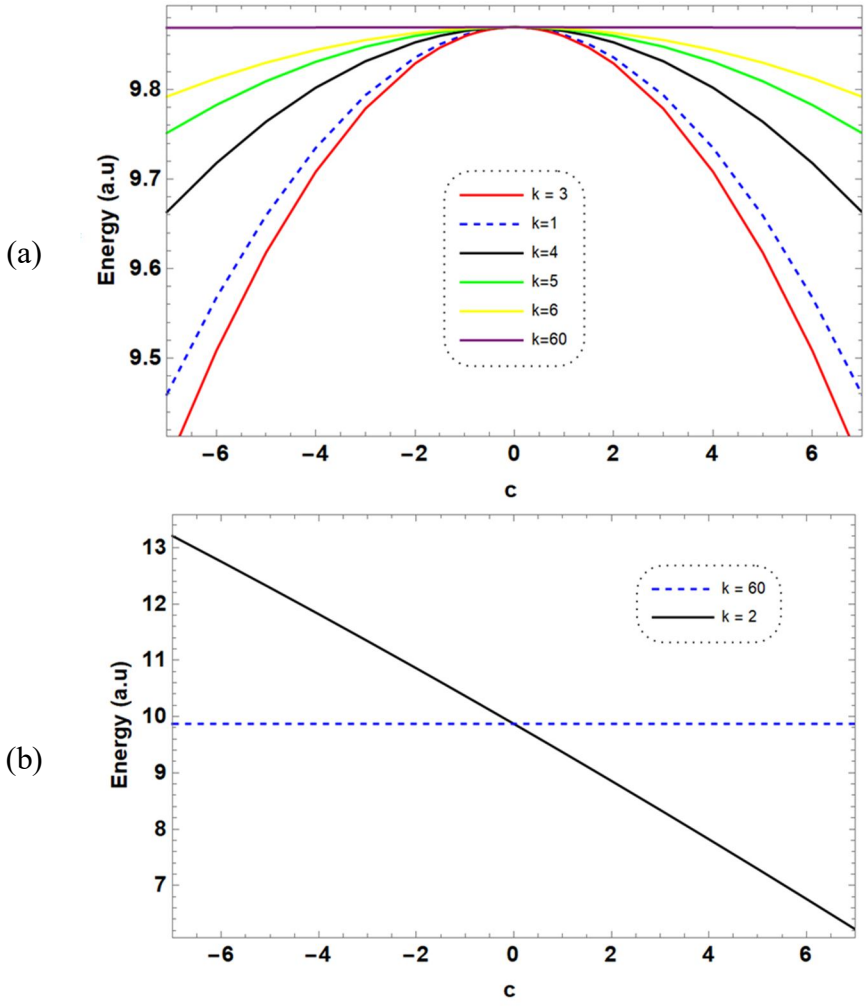

FIG. 2. Ground-state energy *versus* the perturbation strength c, for different values of k.

For Fig. 2b, the k = 2 case, the major contribution comes from the first-order correction; so, the curve shows a linear dependence between the ground-state energy and C with a slope almost $-\frac{1}{2}$.

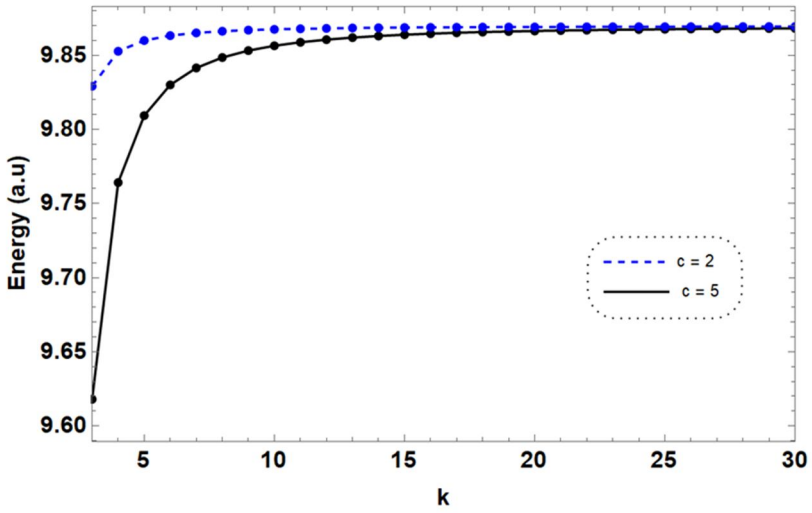

FIG. 3. Ground-state energy as a function of k for different values of C.

To ensure the above discussion for large values of k, the ground-state energy as a function of k for two values of C has been plotted, as shown in Fig. 4. The plot shows the independence of energy on the value of C as k increases. This is due to the very large number of oscillations (or wavelengths) in the well, which means that there is no enough time for the electron to catch up with the perturbation, leading to the flat bottom potential solution.

Now, for the higher state, for example, n = 2 (see Fig. 4).

(a)

(b)

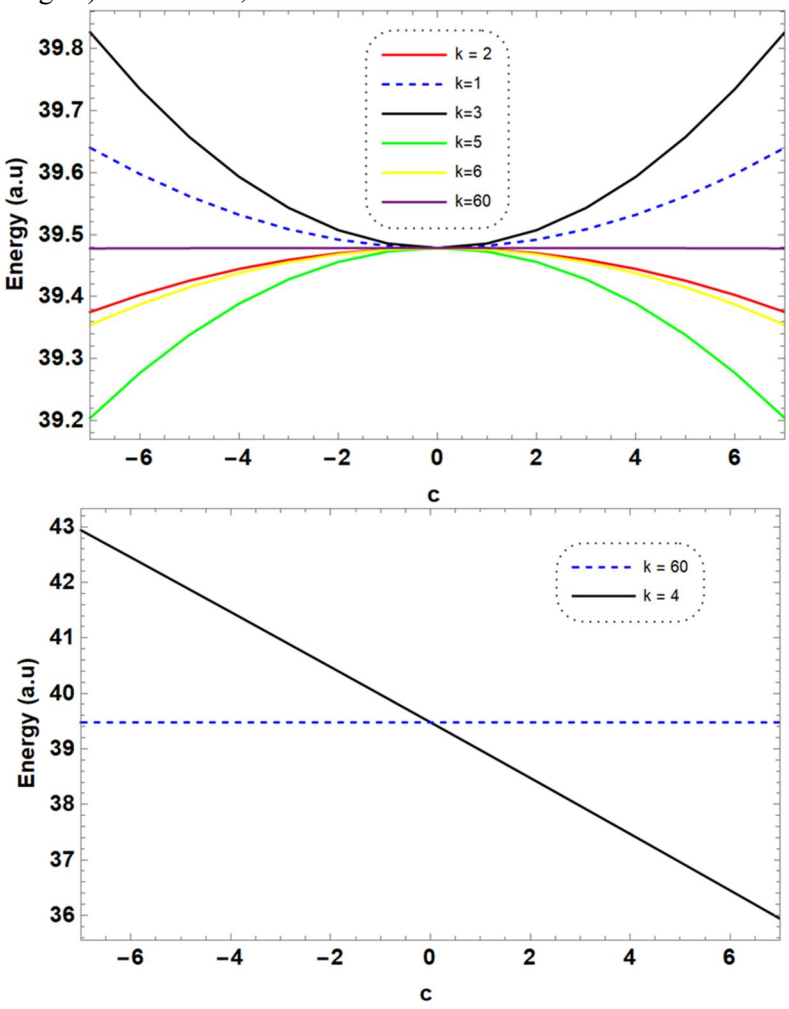

FIG. 4. Energy as a function of C for different values of k for the first excited state.

For the sake of comparison with previously published work [12], we plot the total state in the same unit as ref. [12], where the plot exactly matches the previous one for k=1, which shows no Klauder phenomenon. From Fig. 4, in that reference, there are extra nodes in n = 1 and n = 2. To ensure this here, we plotted the wave function for the two cases $k = 1$ and $k = 2$; no any further node has appeared.

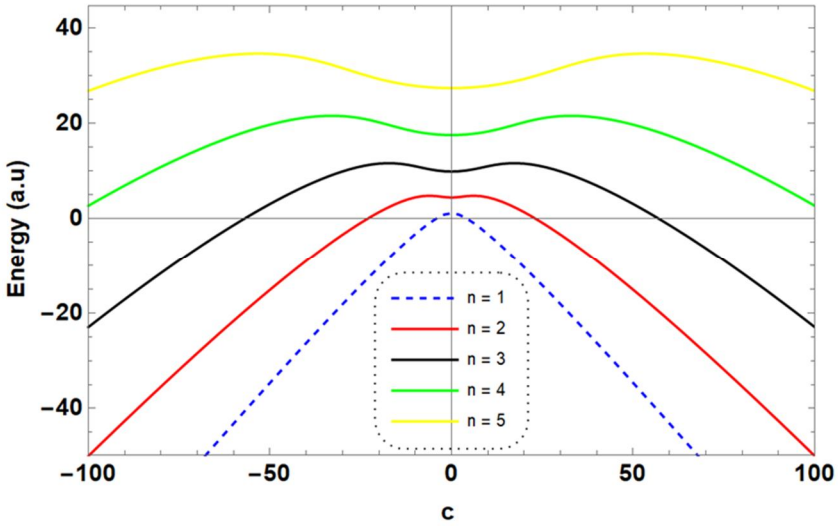

FIG. 5. Energy spectra as a function of C, for $k = 1$.

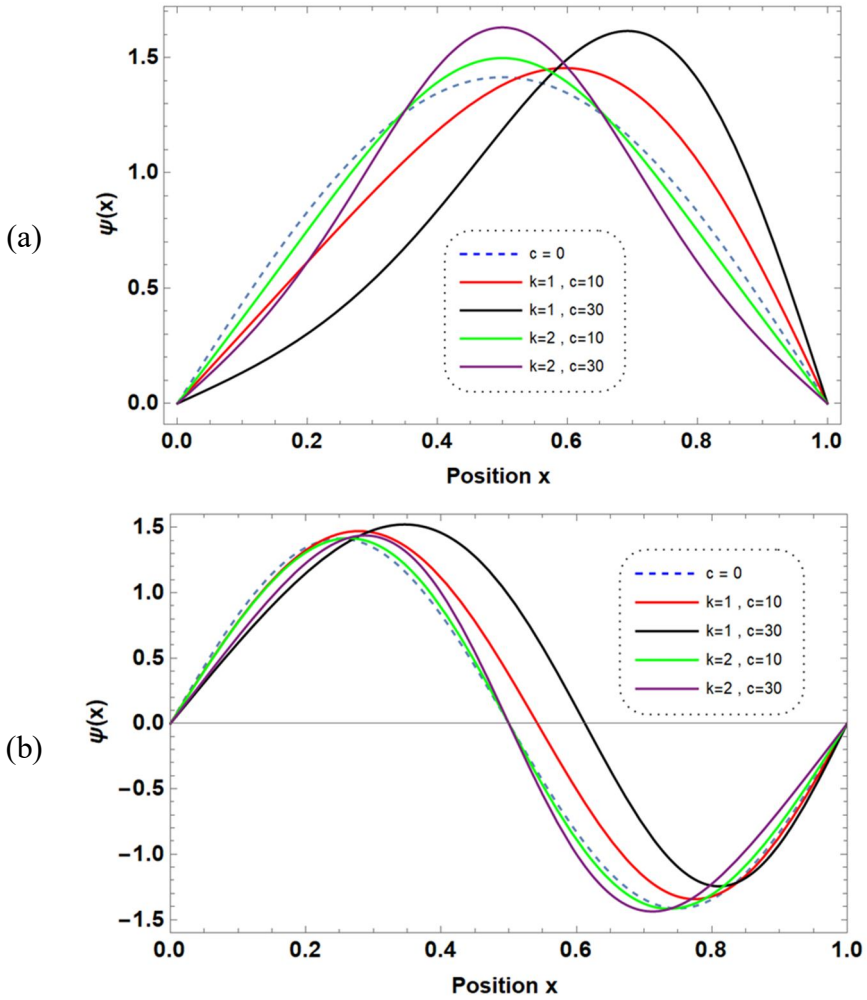

FIG. 6. Normalized wave function for the ground state (a) and first excited state (b), for different values of k and C.

As a final illustration, we study the case for non-integer k and give 3 plots. Again, the plots show that the system does not feel the perturbation after a certain value of *k*, which means that when the number of oscillations becomes large enough, the system has no enough time to adjust itself due to perturbation.

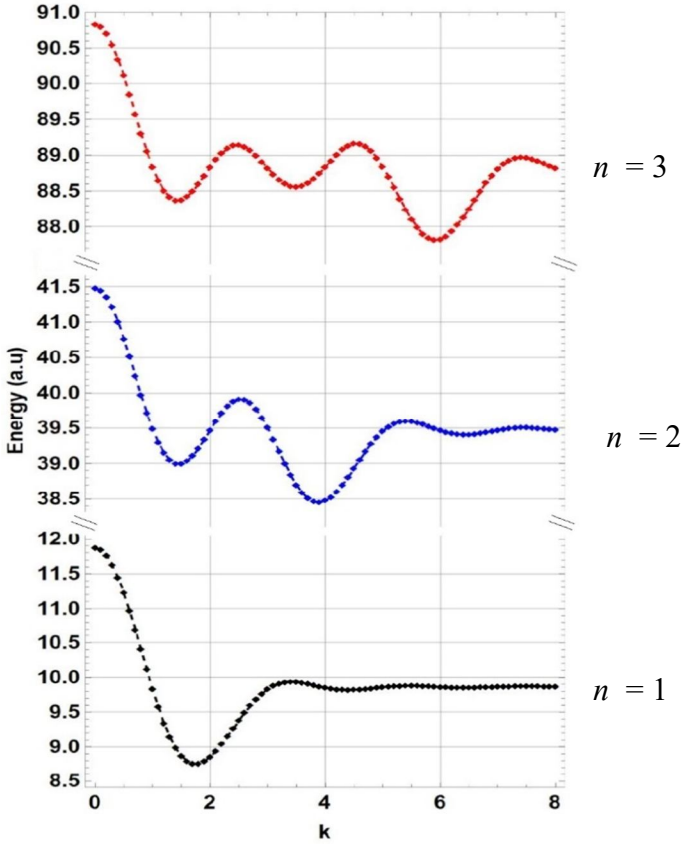

FIG. 7. The lowest eigen energies as a function of *k*; here *k* is taken from 0 up to 8, with steps of 0.1.

Conclusions

In this work, we calculated the energies and wavefunctions for the infinite well with sinusoidal bottom using numerical and perturbative methods. The effect of the potential oscillation and amplitude of the perturbation on the energies of the ground and excited states was examined. For each of the two selected frequencies (k = 1 and 2), it was found that the ground-state energy decreases as the amplitude of the perturbation increases, but the energy of an excited state increases as the amplitude increases, with the exception for the first excited state when k = 2. Our results also showed that as the oscillation of the perturbation increases, the energies of all states get closer to their corresponding values for the unperturbed well, and for very high frequencies, the energies converge to their corresponding values for the unperturbed well. In this case, the perturbed system does not have the time to catch up with the perturbation; thus, the system behaves as if the bottom of the well is flat. In addition, an important conclusion of our results is that the sinusoidal bottom well does show the Klauder phenomenon. An additive value of this work is the ability of exact calculations of the energy eigenvalues for the infinite well with sinusoidal bottom using numerical methods. This work is a constructive illustration for the application and usefulness of exact numerical and perturbation methods in studying simple but illuminating systems.

It may also be interesting to know how the ground-state energy depends on the perturbation for large *k*. Actually, the large-*k* limit is particularly significant because we expect on physical ground that too many oscillations of a cosine function over a finite domain should average out to zero [15]

References

[1] Hu, B., Li, B., Liu, J. and Gu, Y., Physical Review Letters, 82 (21) (1999) 4224.

[2] Mustafa, O. and Mazharimousavi, S.H., Physics Letters A, 373 (3) (2009) 325.

[3] Marin, J.L. and Cruz, S.A., American Journal of Physics, 56 (12) (1988) 1134.

[4] Heimgartner, B., Leuenberger, P., Wiedmer, H.U., Zweiacker, M. and Kneubühl, F.K., Infrared Physics, 30 (4) (1990) 363.

[5] Glasser, M.L., Mateo, J., Negro, J. and Nieto, L.M., Chaos, Solitons & Fractals, 41 (4) (2009) 2067.

[6] Tang, L.M., Wang, L.L., Chen, K.Q., Huang, W.Q. and Zou, B.S., Applied Physics Letters, 88 (16) (2006) 163505.

[7] Dmytruk, O., Chevallier, D., Loss, D. and Klinovaja, J., Physical Review B, 98 (16) (2018) 165403.

[8] Kasapoglu, E.S.İ.N., Ungan, F.A.T.İ.H., Sari, H.Ü.S.E.Y.İ.N., Sökmen, I., Mora-Ramos, M.E. and Duque, C.A., Superlattices and Microstructures, 73 (2014) 171.

[9] Khordad, R., Tafaroji, S., Katebi, R. and Ghanbari, A., Communications in Theoretical Physics, 57 (6) (2012) 1076.

[10] Johnston, D.C., American Journal of Physics, 88 (12) (2020) 1109.

[11] Sakly, A., Safta, N., Mejri, H. and Lamine, A.B., Journal of Alloys and Compounds, 509 (5) (2011) 2493.

[12] Alhaidari, A.D. and Bahlouli, H., Journal of Mathematical Physics, 49 (8) (2008) 082102.

[13] Dhatt, S. and Bhattacharyya, K., Journal of Mathematical Chemistry, 50 (1) (2012) 9.

[14] Pillai, M., Goglio, J. and Walker, T.G., American Journal of Physics, 80 (11) (2012) 1017.

[15] Marsiglio, F., American Journal of Physics, 77 (3) (2009) 253.

Volume 15, Number 5, 2022. pp. 477-485

Jordan Journal of Physics

ARTICLE

Study of the High Rotational Bands of Moderately Heavy Nuclei

F. Z. Hamel and **D. E. Medjadi**

Laboratoire N-corps et Structure de la Matière, Ecole Normale Supérieure, Kouba, 16050 Alger, Algeria.

Doi: **https://doi.org/10.47011/15.5.5**

Received on: 28/02/2021; *Accepted on: 30/05/2021*

Abstract: This paper provides a study of the rotational properties of heavy and medium nuclei, particularly the paired nuclei existing in the rare-earth, including Gd, Er, …, first to have a good representation of the intrinsic prolate fundamentals of the considered nuclei. The most important residual nuclear interaction is the pairing force which makes it possible to couple the nucleons in pairs. To take it into account, we introduce the Bardeen-Cooper-Shrie formalism (BCS), developed to describe the phenomenon of superconductivity. The test wave function is then more elaborate than that of Hartree-Fock and corresponds to a state no longer of independent particles, but of independent quasi-particles. A quasi-particle state (qp) is a linear combination of particles and holes. The Routhian Hartree-Fock model through the analysis of the experimental spectra of rotation of the deformed nucleus was usewd. Knowing that this was originally expanded by Bohr-Mottelson by applying I(I+1) expansion, we modified an existing fixed code (HF) with axial symmetry, which extended in a way that allows us to add constraints on the angular momentum and kelvin rotation to the Hamiltonian known as Cr.HF (cranking version of this formalism), initially studied by P. Quentin. This modification led to good results, especially the spectra of rotation and the angular velocities as a function of the angular momentum. Besides, it led to a decrease in the moment of inertia after it was large in some models, such as in the Hartree-Fock-Bogoliubov (HFB) model. The rotational properties and the moments of inertia of the super-deformed bands of some deformed nuclei have been studied as well as in the mass regions A=190; A=160. The results were compared with experimental results which gave good agreement. This work will offer an interesting perspective necessary for certain improvements or extensions of the Cr.HF.

Keywords: Microscopic mean field, Collective nuclear rotation, Angular momentum Routhian Hartree-Fock (RHF) model, Inertia moments, Angular velocity.

1. Introduction

An important part of nuclear physics is dedicated to models attempting to explain the growing mass of experimental results. At present, the nuclear forces, although "identified" in their entirety, have not definitively disclosed all their secrets. We need then models to explain how an atomic nucleus is constituted, why it is stable or unstable and what its characteristics are. We call this part of nuclear physics the nuclear structure. By discovering the exotic nuclei, the nuclear structure has become more complicated although the computational means are at present also more important and the models are more efficient. One of the most important concepts of nuclear structure is the deformation of nuclei [1]. This means that the nuclear surface in the ground state (equilibrium) is a surface that is no longer spherical. In addition, all phenomena are associated with the dynamics of the nuclear surface, such as: nuclear fission, nuclear fission, collective bands of rotation and vibration, quadrupole moments and

Corresponding Author: F. Z. Hamel **Email**: hamelfatima1987@gmail.com

many other phenomena naturally embedded in this notion.

Physics has constantly tried to explain the structure of nuclei and the phenomena that involve them in terms of their basic constituents "nucleons" and their mutual interactions. Such a "microscopic" description of nuclei obviously has many advantages, since it provides a unified framework allowing in principle to deduce the properties of all imaginable nuclear systems. In a few words, the situation is as follows: BCS theory [2], where the different states are described as quasi-particles (free quasi-particle model) excitations on a vacuum which is the ground state of the nucleus, trying to describe the structure of nuclei and their isomeric states.

There are many models in the microscopic calculations, especially in the calculation of the rotational-energy spectrum and its variation in terms of angular momentum, as well as in the calculation of the kinetic moment in which the researchers attempted to reduce it. Initially, it was discussed particularly at a relatively low angular momentum called the Coriolis anti-pairing effect. It was studied in terms of coupling rotation - group coupling by Mottelson Valatin [3] [4].

Thanks the generalized Routhian approximation, we have developed a quantum microscopic formalism with an average harmonic oscillator field that remarkably reproduces the results of the phenomenological models previously discussed. Subsequently, we have constructed and tested the validity of a realistic microscopic and self-consistent code of Hartree-Fock type, where we describe the interactions between the nucleons by the phenomenological force of Skyrme to study the S-type ellipsoids to the approximation of the generalized cranking.

In this paper, we discuss the use of the Routhian Hartree-Fock method for isotopes of the nuclei Hg, Pb and A=160, using the Routhian approximation in which we add a constraint on the moment of inertia through finding a new equation between global rotation and intrinsic vorticity.

The paper is organized as follows. In Sections 1, 2 and 3, we dealt with a definition of the BCS model, which has a good base, in order to study the static properties of some paired nuclei, while In Sections 4 and 5, within the framework of the independent-particle approximation that is used to describe the nuclei formal dynamics (based on Schrödinger's equation), we have chosen to develop a realistic microscopic description of the S-type ellipsoids using the Hartree-Fock approximation. This work consisted of modifying an existing fixed code with axial symmetry by adding constraints on the angular momentum and the kelvin rotation to the approximation of the general cranking. In section 6, we present and discuss the angular velocity and calculations related to angular momentum and rotational-energy spectrum, Section 7 is devoted to studying in detail the rotational-band model, where we have determined some rotational properties; i.e., the rotational band, the angular momentum, the rotational speed and comparing the results with the experimental data, together with some conclusions and perspectives offered by this new approach.

2. The Ground-state BCS

We now present a method, inspired by the BCS theory in solid state physics [5], which takes into account correlations (particle-particle). This method will not give an exact solution for the eigenvalue problem, but will establish solutions from a variational principle. Formally, we will follow the same approach as that applied in the Hartree-Fock method; we choose a family of test states and minimize the energy. This also leads us to introduce the notion of quasi-particle using the Bogoliubov transformation. The idea now is to see the system of interacting particles as a system of independent quasi-particles moving in an average potential, which in this case is the pairing potential. According to the BCS theory, we can choose the test state of a kernel (pair-pair) for example, as shown in the following form:

$$\boldsymbol{\psi}\ |BCS\rangle = \prod_{k>0}(u_k + \upsilon_k a_k^+ a_{\bar{k}}^+)\ |0\rangle \qquad (1)$$

where υ_k and u_k are complex parameters and the product spans all values of k in half the configuration space; therefore, for each state k > 0, there exists a state reversed with respect to time k < 0 such that the state $\{k, \bar{k}\}$ generates all the mono-particulate space. Thus, we notice that the one-particle states k and $\bar{k}$ are grouped in pairs [6]; they are simultaneously occupied or unoccupied. The variational principle determines the parameters u_k and υ_k which are not independent and satisfy the relation.

3. BCS Equations

Using the Bogoliubov transformation, we obtained a representation of the test state of particles interacting in pairs in terms of a non-interacting quasi-particle gas. There is a spontaneous breaking of the particle number symmetry, because this transformation mixes the operators of creation and annihilation, so that the number of particles is not conserved. We introduce a Lagrange parameter which fixes the average number of particles to its exact value in order to perform energy minimization, which is equivalent to solving an eigenvalue problem. We will therefore have the constrained Hamiltonian in the form:

$$H' = H - \lambda \hat{N} \quad (2)$$

λ is the Lagrange parameter, which is interpreted as a chemical potential or Fermi energy, since it represents the change in energy

$$E = \langle \psi_{BCS} \left| H' \right| \psi_{BCS} \rangle, \quad (3)$$

with respect to the variation in the number of particles [7]:

$$\boldsymbol{\lambda} = \frac{dE}{dN}. \quad (4)$$

According to the definition of the wave function $|\psi_{BCS}\rangle$, the Hamiltonian H' takes the form:

$$E = \langle \psi_{BCS} \left| H \right| \psi_{BCS} \rangle. \quad (5)$$

First, the basic case is studied by finding the minimum energy and the corresponding quadrupole moment by using a program and since the results obtained on it for the quadrupole moment, we enter the parameters in the Routhien program that gives us the results to determine a good **Ω**.

4. Hamiltonian Symmetries

The Routhian in the context of generalized cranking at the coupling of S-type ellipsoids is simply written in the form:

$$H = H_{SKY} - \Omega \hat{J}_1 - \omega(\Omega) \hat{K}_1, \quad (6)$$

where H_{SKy} stands for the Skyrme Hamiltonian [8-10]. As well, $\hat{K}_1$ is the Kelvin's circulation operator.

$$\hat{J}_1 = \hat{L}_1 + \hat{S}_1, \quad (7)$$

$\hat{J}_1$ is the total angular momentum operator that combines both the spin and orbital angular momentum operators. The Skyrme Hamiltonian is invariant by the parity operation that consists of replacing the coordinates and the momentum of the system by their opposites. Besides, it is easy to see that the operators $\hat{L}_1$, $\hat{K}_1$ consist of the product of momentum by coordinates; they are also invariant by this operation [11].

5. Functional Energy

E. Chabanat *et al.* [12] showed that a Skyrme interaction is given by the following expression:

$$\langle \emptyset | \hat{H} | \emptyset \rangle = \int d^3 r H_{totale}, \quad (8)$$

with

$$H_{totale}(r) = H_{Sk}(r) + H_{Coul}(r), \quad (9)$$

where the total energy density $H_{totale}(r)$ is the sum of the density related to the Skyrme force and that related to Coulomb energy, while the energy of Slater's determinant is calculated as:

$$E_{HF} = \int dr H_{totale}. \quad (10)$$

This Hamiltonian density is a functional one-body density (diagonal matrix elements in $\vec{r}$ of $\vec{p}$), which for a determinant of even Slater by reversal of the sense of time can in a somewhat arbitrary way be decomposed as:

$$H_{Sk}(r) = H_{kin}(r) + H_{vol}(r) + H_{surf}(r) + H_{so}(r), \quad (11)$$

The different terms of the above equation depend on a certain number of local densities. The spin-vector and the current densities are not involved for even solutions by reversing the time direction. This is the reason why we will not consider them to describe the fundamental states of even-peer nuclei. We should only consider the densities of matter, kinetic energy and spin-orbit from the wave functions and the determinant of Slater, respectively. The normal density of the nucleus is:

$$\rho(r) = \sum_{i,\sigma} |\emptyset_i(r,\sigma)|^2. \quad (12)$$

The density of normal kinetic energy (scalar spin) is given by:

$$\tau(r) = \sum_{i,\sigma} \vec{\nabla} |\emptyset_i(r,\sigma)|^2, \quad (13)$$

and the spin-orbit density is:

$$\vec{J}(r) = (-i) \sum_{i,\sigma,\sigma'} \emptyset_i^*(r,\sigma) \left[\vec{\nabla} \emptyset_i(r,\sigma) \times \langle \sigma | \vec{\sigma} | \sigma' \rangle \right]. \quad (14)$$

Here the summations i (space) and σ, σ'(spin) concern all the occupied states of a particle and τ stands for the different states of charge (neutrons (n) and protons (p)). In what follows, the isospin index τ affects densities, so that the summations on the indices i and j only imply state densities having even isospin τ. The densities noted without indices τ are equal to the sum of the corresponding neutron and proton densities:

$$H_{\text{kin}} = \frac{A-1}{A}\frac{\hbar^2}{2m}\tau, \quad (15)$$

$$H_{\text{vol}}(\text{r}) = B_1(\rho)^2 + B_2\sum_q(\rho)^2 + B_3\rho\tau + B_4\sum_q \rho_q\tau_q + B_7\rho^{a+2} + B_8\rho^a\sum_q \rho_q^2, \quad (16)$$

$$H_{\text{surf}}(\text{r}) = B_5\rho\,\vec{\nabla}^2\rho + B_6\sum_q \rho_\tau\,\vec{\nabla}^2\rho_q, \quad (17)$$

$$H_{\text{so}}(\text{r}) = B_9\left(\rho\vec{\nabla}\cdot\vec{J} + \sum_q \rho_q\,\vec{\nabla}.\vec{J}_q\right), \quad (18)$$

where the dependency in $\vec{r}$ of the different densities is implied [13,14]. The coefficient $(A-1)/A$ Eq. (10) of the kinetic energy functional results from the subtraction of the part to a body of energy due to the movement of the center of mass, with A being the number of nucleons of the nucleus. The coefficients B_{i} of the Skyrme force are summarized in the table shown in [15]. To take into account the Coulombian interaction, which is not included in the Skyrme interaction, it is necessary to add to the energy functional the Coulombian energy functional, which can be written using Slater's approximation for the exchange term in the form:

$$H_{Coul}(\text{r}) = \frac{1}{2}\rho_p V_{Coul} - \frac{3}{4}e^2 4\left(\frac{3}{\pi}\right)^{\frac{1}{3}}(\rho_p)^{\frac{4}{3}}, \quad (19)$$

where e is the proton charge, ρ_p [16] is the proton density and the potential V_{coul} is expressed by:

$$V_{Coul} = e^2\int d^3r'\frac{\rho_p(r')}{|r-r'|}. \quad (20)$$

Moreover, the exchange term can be written using Slater's approximation [17]. This energy functional is not the exact mean value of the Hamiltonian for a given independent particle state, but is only an approximation. It is interesting to note that this approximation has been tested for spherical nuclei [18], using the SkP and SkM forces and for HFB calculations using Gogny's force [19].

6. Angular Velocity

The static moment of inertia is defined as a function of the angular velocity corresponding to a spin I:

$$\Omega(I) = \frac{J}{\Im} = \frac{dE}{dJ}, \quad (21)$$

where $\Im$ is the moment of inertia and Ω is the angular velocity. The observation of the spectra of energy as a function of spin can reveal the rotational behavior of the nucleus. By analogy with the energy of a rigid body of moment of inertia $\Im$ in rotation, we obtain:

$$E(I) = \frac{\hbar^2}{2\Im}I(I+1). \quad (22)$$

Two comparable quantities of the macroscopic moment of inertia can be defined; the moment of dynamic inertia and the moment of cinematic inertia [20-22],

$$\hbar\Omega = \left(\frac{\Delta E}{\Delta\sqrt{I(I+1)}}\right)_{(I,I-2)} \cong \left(\frac{E_\gamma}{\Delta I}\right)_{(I,I-2)} = \frac{E_\gamma}{2}, \quad (23)$$

which can be used to measure the energy of excitation of the spin level. In the following, we will investigate the evolution of the moment of inertia as a function of the angular velocity. This research is carried out in the experimental study through defining the angular velocity Ω_I and the kinematical moment of inertia $\Im^1$, associated with a given rotational state of angular momentum I, through the transition energies $E_{I\to I-2}$; namely,

$$\Omega_{\text{exp}}(I) = \frac{\text{E}_\gamma^+(I) + \text{E}_\gamma^-(I)}{4}. \quad (24)$$

The experimental static moment of inertia (in unit of $\hbar^2 MeV^{-1}$) is written as follows:

$$\Im^1_{exp} = \frac{4\sqrt{I(I+1)}}{\text{E}_\gamma^+(I)+\text{E}_\gamma^-(I)}, \quad (25)$$

where I is the projection on the interinsic axis (Oz) of the total angular moment and $\text{E}_\gamma^+(I), \text{E}_\gamma^-(I)$ are the transition energies before and after the considered energy level $E(I)$, which are given by the following relations:

$$\text{E}_\gamma^+ = \text{E(I}+2) - \text{E(I)}\,;\ \text{E}_\gamma^- = \text{E(I)} - \text{E(I}-2). \quad (26)$$

The values of the experimental energies $E(I)$ of the energy levels $2+$ and the experimental static moments of inertia are traced in relation with the angular velocity, as illustrated in Fig. 4.

$$\hbar\Omega(\text{I}) = \frac{\text{E}_{\text{I}+2} - \text{E}_{\text{I}-2}}{4}. \quad (27)$$

7. Results and Discussion

We used the (HF + BCS) approach due to its advantage in that we study the static properties of these nuclei and deduce from this initial study the minimum deformation energy corresponding to the quadrupole moment.

The conditions for the HF + BCS calculation are as follows:

- We took an actual interaction from Skyrme SIII [23].
- We took a size of the base $N_0=12$

of the axially symmetric harmonic oscillator (BOHSA). This size of the base is sufficient to have an energy of the fundamental close to the experimental value. In addition, it allows self-consistent calculations to be made in reasonable time.

We used a seniority force qg defined by the usual prescription which consists of a normalization of the intensity of the seniority force, noted *G*, with respect to the number of nucleons:

$$g = \frac{G}{11+N}$$

with N being the number of nucleons. The values of nG and pG that we have taken were determined by the authors of Ref. [24] by comparing the calculated minimal quasi-particle energies with those obtained from the experimental binding energies [25] using the 5-point formula [26]. $G_n = 16.50$ MeV, $G_p = 15.50$ MeV.

Also, according to Ref. [24], the value of the BCS excitation window is taken to be equal to 5 MeV, in order to be able to compare our results with those of the authors of this reference.

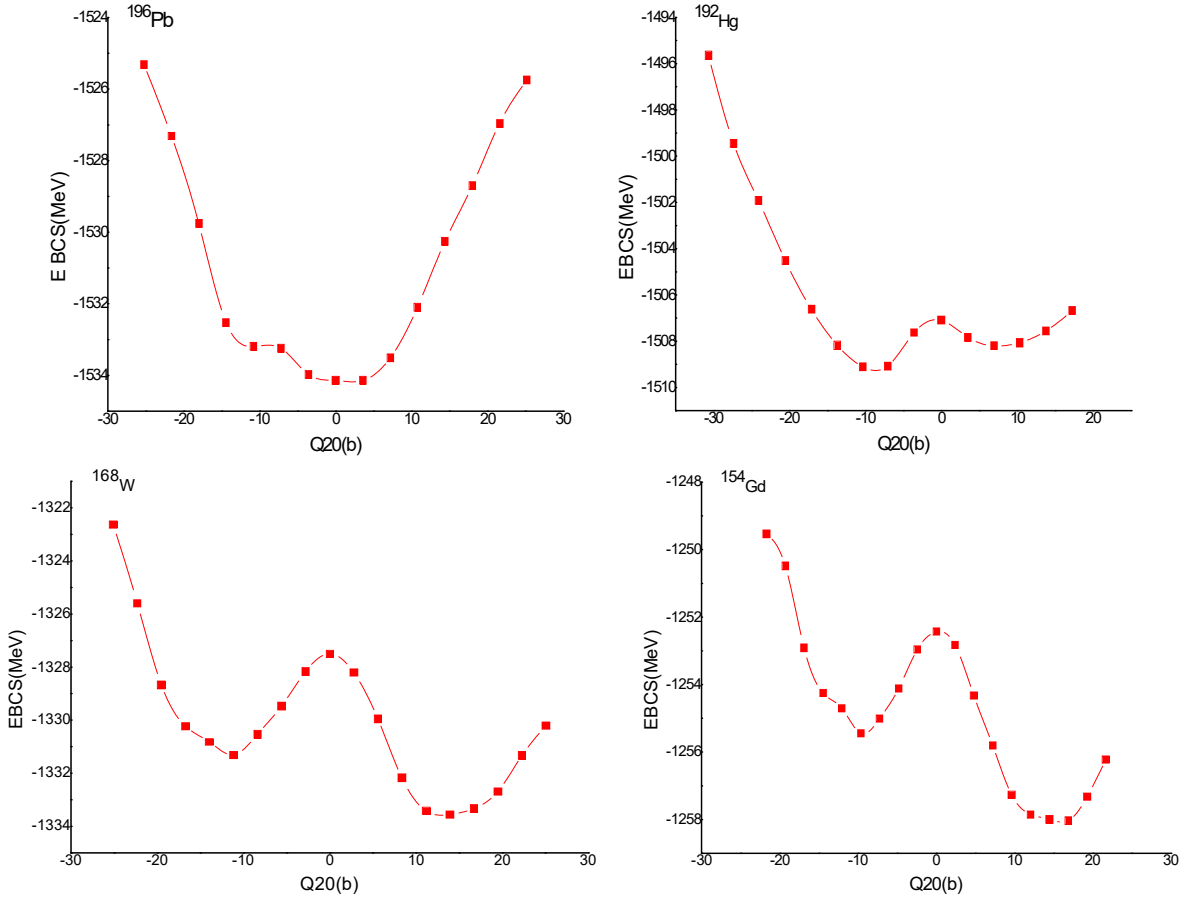

FIG. 1. Deformation-energy curves as a function of the quadrupole moment (in barns).

TABLE 1. Static properties of the four nuclei studied with the HF + BCS approach.

Nucleus	$E_{g.s}$ (MeV)	E_{exp} (MeV)
^{154}Gd	-1258.15	-1266.61
^{168}W	-1334.66	-1342.98
^{196}Pb	-1533.51.66	-1539.51
^{192}Hg	-1508.20	-1519.10

We have chosen to study in detail this rotational-band model of a nucleus for some rare-earth isotopes. For reasons, which will become clear later, we have discussed the use of the Routhian Hartree-Fock method for isotopes of the nuclei Gd, W, Pb and Hg using the Routhian approximation. The existence of deformed stable nuclei has been demonstrated very early in the history of nuclear physics. The observation of large quadrupole moments leads to suggest that these nuclei have the shape of an elongated ellipsoid, which has been confirmed by the observation of rotational bands. The description of most nuclei as having axial deformation and being reflective asymmetrical about a plane perpendicular to the axis of symmetry is generally adequate to reproduce their nuclear spectra. As we said previously in Section 2, the Routhian of the system is obtained by adding a constraint on the angular momentum along the x1 axis in the Hamiltonian of the system. We have determined some rotational properties; namely, the rotational band in the ground state and the rotational velocity. We carried out the calculations with the Skyrme force SkM* and we compared the results with the experimental data.

In Figs. (3 and 4), we have represented the variation of the collective angular velocity of rotation Ω as a function of the spin I of the nuclei for the Skyrme force SkM* that we compare with the experimental data. As well, the experimental velocity is defined above.

In Fig. 2, for the two nuclei (Hg and Pb) of the moment of inertia $\Im^1$ as a function of angular velocity (Ω), the results are shown for four approaches (HF, HFB, HTDA and Cr.RHF) and these values are compared with the experimental results, where we notice that the HFB approach at low angular velocity behaves well, whereas in the HF approach, the values obtained were far from the experimental values; it is considered a rather weak approach, which led to the use of the HTDA approach, which showed a uniform behavior from the beginning to the top, compared to the HFB approach which had jumps at higher angular velocities. As for the approach used, Cr.RHF, which is an addition to the calculations of Routhian Hartree-Fock, where the calculations of the microscopic rotation, with conservation from the beginning, the number of particles (the BCS approach), provides an approach that can be followed. This approach has proven effectiveness in comparison with other approaches and studies. It gave good behavior from the beginning to the top and its results are close to the experimental results, but we notice some bending and divergence when increasing angular velocity, which is due, as is known in some nuclei, to the collective difference in coupling and since the approach is characterized by regular behavior, it is necessary that the bending will not appear in it, such as in ^{154}Gd and ^{164}W nuclei. We note that there is complete agreement of the ^{156}Gd, ^{168}W and ^{192}Hg nuclei up to the high spin I = 18 hbar.

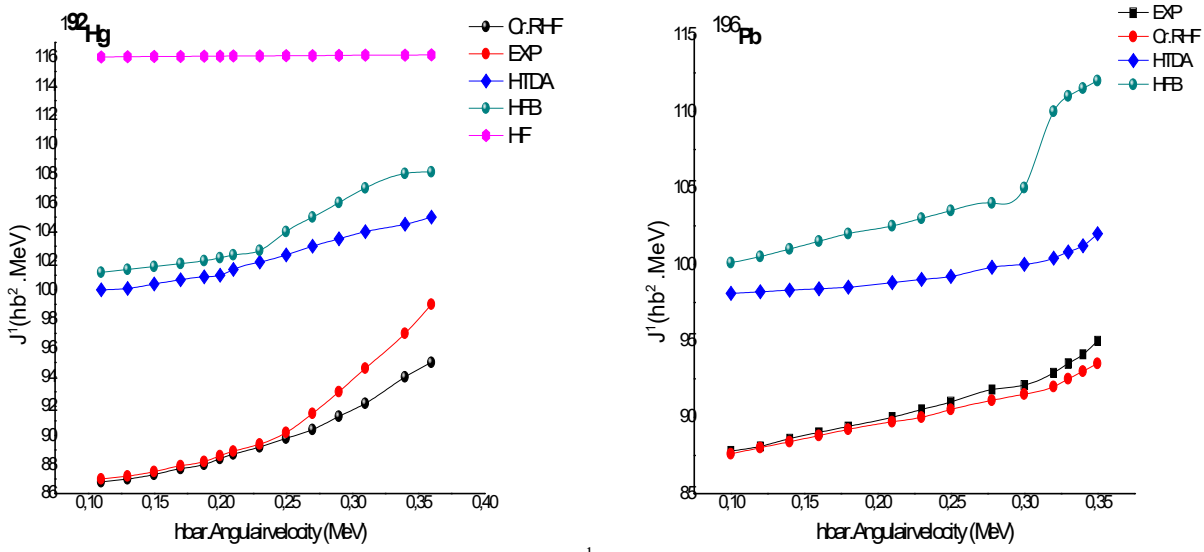

FIG. 2. Comparaison between the moment of inertia $\Im^1$ as a function of the angular velocity Ω as obtained in the approaches HF, HFB, HTDA and Cr.RHF with the experimental results.

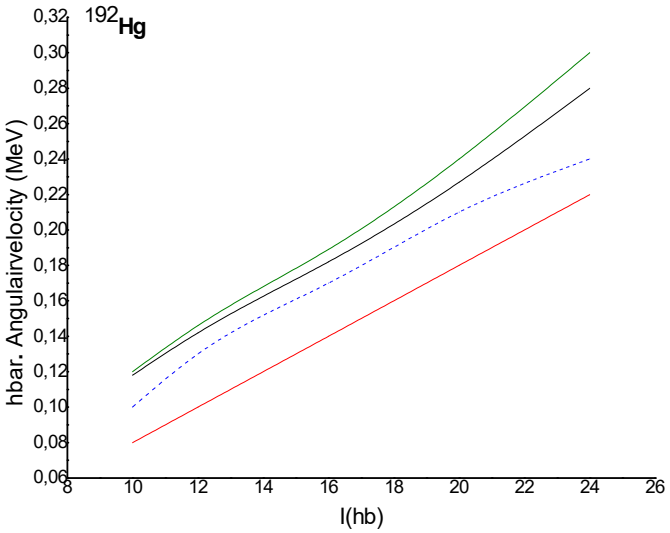

FIG. 3. Angular velocity as a function of the angular momentum I (in $\hbar$ units). The conventions in use are the following: HFB value (dotted line), EXP value (green solid line), HF value (red solid line) and Cr.HF value (black solid line).

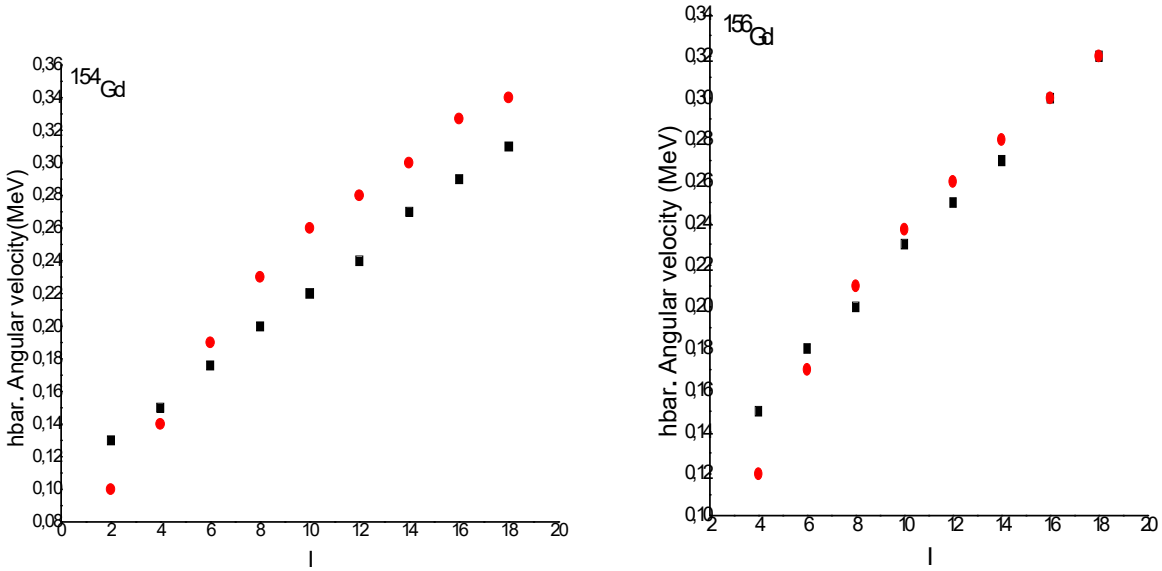

FIG. 4. Angular velocity as a function of the angular momentum and the experimental data (red circles).

The angular velocities within the three studied approaches HF, HFB and Cr.RHF are plotted in Fig. 3 against the angular momentum. We note that the Cr.RHF approach is close to the experimental results and it is well smooth compared to the HFB and HF approaches, which were not effective even at low angular velocities, as the results were found to be nearly compatible with a high rotation of up to 20 hbar, since it was compared in the Hg nucleus with the two approaches. Then, we were able to calculate the nuclei at A = 160, A = 190. The linear behavior is observed up to spin $I = 2\hbar \rightarrow 10\hbar$. We observe an agreement of the angular velocity of the Cr.RHF model and that of the experiment. More precisely, we say that between $I = 2\hbar$ and $10\hbar$, we found good results for the nuclei Gd, W and Hg which agree with the experimental results, as seen in Fig. 4. In addition, we obtained the angular momentum of the nucleus ^{156}Gd, which is $I = 10\hbar$ at the angular velocity 0.23MeV.$\hbar^{-1}$.

In Fig. 6, we have presented the collective states of rotation within the framework of the approximation of ellipsoids of type –S. Note also that the curve deduced with the force SKM* is closer to the experimental curve than that deduced with the force SIII for the nucleus ^{164}Gd. This means that the SKM* force translates the rotation in the nucleus in a more realistic way. The rotational energy curves are located above the experimental curve.

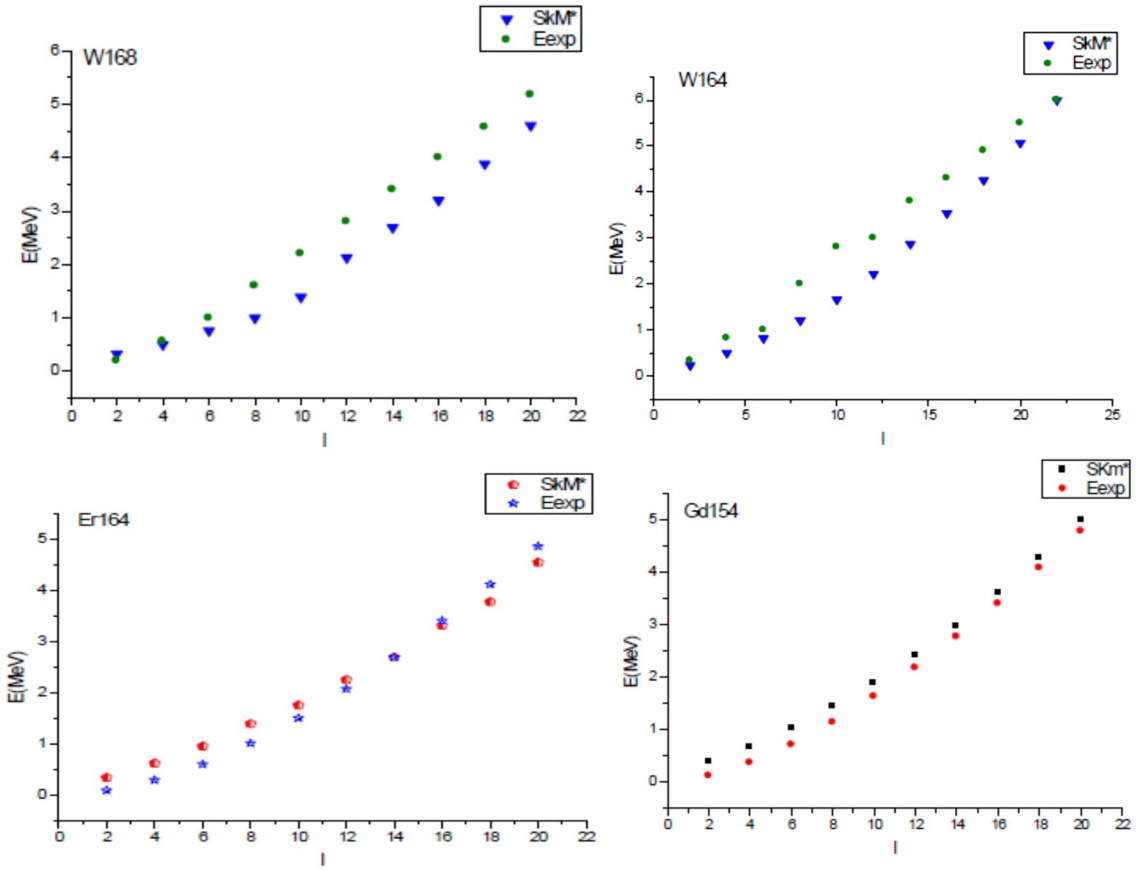

FIG. 5. The energy of the rotational state as a function of the spin.

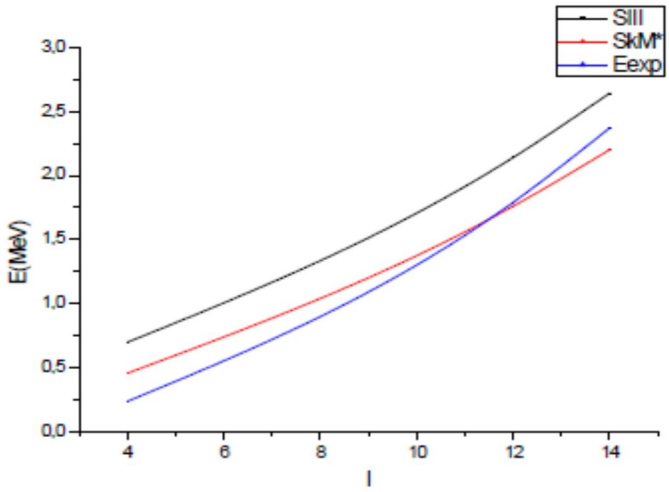

FIG. 6. The energy of the rotational state as a function of the spin with the two forces of Skyrme SIII and SkM* for the nucleus ^{164}Gd.

The experimental rotational energy as a function of the angular velocity in the results of HFR gives a rather smooth behavior, in reasonable agreement with the data at low angular velocities. However, at higher angular velocities, the results differ from the experimental ones. These differences, which are due to the sudden variations in the matching properties, do not appear in the RHF results that show a regular behavior, in good qualitative agreement with the data. If we compare these results with the results of the HFB model, which are far from the experiment, in Ref. 55, as well as comparing them with the results of Ref. 22, which used the HTDA model, we conclude that with a static study using the (HF + BCS) model and by approximating the RHF, the results of the approach are close to the experiment.

8. Summary and Perspectives

In this paper, we have discussed some properties of static nuclei Gd, W, Pb and Hg, applying as the first study the approximation of HF+BCS and then the Cr. RHF approximation.

The new approach discussed here opens the door to a wide field of investigation. In particular, it offers a theoretical framework in which the even nuclei (odd-odd and odd-even) could be described in a coherent way. An unbalanced breakdown could also be envisaged in the same frame. In our opinion, the most important task to be accomplished would be to expand the space of many functions of the body waves to improve the description of the correlations. Another important issue is the investigation of high-spin states. It is well known that the usual cranked HFB formalism does not see the proton-neutron pairing and is not very efficient in the low-pairing regime, which leads to discrepancies in the measured and the calculated yarest bands. As we mentioned, the treatment of the pairing correlations in high spins in the RHF method was already undertaken. Since the rotation has a different impact on like-particle and proton-neutron pairs, it may be judicious to enrich the RHF by including the proton-neutron coupling.

References

[1] Yuldashbaeva, E.K., Libert, J., Quentin, P. and Girod, M., Phys. Lett. B, 461 (1999) 1.

[2] Pillet, N., Quentin, P. and Libert, J., Nucl. Phys. A, 697 (2002) 141.

[3] Gall, B., Bonche, P., Dobaczewski, J. et al., Z. Phys. A, 348 (1994) 183.

[4] Girod, M., Delaroche, J.P., Berger, J.F. and Libert, J., Phys. Lett. B, 325 (1994) 1.

[5] Bardeen, J., Cooper, L.N. and Schrieer, J.R., Phys. Rev., 108 (1957) 1175.

[6] Parry, W.E., "The Many-body Problem", (Clarendon Press, Oxford, 1973).

[7] Madland, D.G. and Rayford Nix, J., Nucl. Phys. A, 476 (1988) 1.

[8] Vautherin, D. and Brink, D.M., Phys. Rev. C, 5 (1972) 626.

[9] Waroquier, M., Heyde, K. and Wenes, G., Nucl. Phys. A, 404 (1983) 269.

[10] Dutta, A.K. and Kohno, M., Nucl. Phys. A, 349 (1980) 455-79.

[11] Prochniak, L., Quentin, P. and Imadalou, M., Int. J. Mod. Phys. E, 21 (2012) 1250036.

[12] Chabanat, E., Bonche, P., Haensel, P., Meyer, J. and Schaeffer, R., Nucl. Phys. A, 627 (1997) 710-74.

[13] Wiringa, R.B., Fiks, V. and Fabrocini, A., Phys. Rev. C, 38 (1988) 1010.

[14] Engel, Y.M., Brink, D.M., Geoeke, K., Krieger, S.J. and Vautherin, D., Nucl. Phys. A, 249 (2) (1975) 215.

[15] Bencheikh, K., Quentin, P. and Bartel, J., Nucl. Phys. A, 571 (1994) 518.

[16] Slater, J.C., Phys. Rev. C, 81 (1951) 85.

[17] Gombas, P., Ann. Phys., 10 (1952) 253.

[18] Pillet, N., Quentin, P. and Libert, J., Nucl. Phys. A, 697 (2002) 14.

[19] Inglis, D.R., Phys. Rev., 96 (1954) 1059.

[20] Bartel, J., Quentin, P., Brack, M., Guet, C. and Haakansson, H.B., Nucl. Phys. A, 386 (1982) 79.

[21] Laftchiev, H., Samsoen, D., Quentin, P. and Mikhailov, I.N., Phys. Rev. C, 67 (2003) 014301.

[22] Laftchiev, H., Libert, J., Quentin, P. and Long, H.T., Nucl. Phys. A, 845 (2010) 33.

[23] Beiner, M., Flocard, H., Van Giai, N. and Quentin, P., Nucl. Phys. A, 238 (1975) 29.

[24] Próchniak, L., Quentin, P., Samsoen, D. and Libert, J., Nucl. Phys. A, 730 (2004) 59.

[25] Audi, G. and Wapstra, A.H., Nucl. Phys. A, 595 (1995) 409.

[26] Kumar, K. and Baranger, M., Nucl. Phys. A, 92 (1967) 608.

Volume 15, Number 5, 2022. pp. 487-494

Jordan Journal of Physics

ARTICLE

Approximate Energy Spectra of the Quantum Gaussian Well: A Four-parameter Potential Fitting

Mahmoud Farout[a], **Ayham Shaer**[a] and **Sameer M. Ikhdair**[a,b]

[a] *Physics Department, Faculty of Science, An- Najah National University, Nablus, West Bank, Palestine.*
[b] *Department of Electrical Engineering, Near East University, Nicosia, Northern Cyprus, Mersin 10, Turkey.*

Doi: **https://doi.org/10.47011/15.5.6**
Received on: 11/03/2021; *Accepted on: 13/06/2021*

Abstract: In this work, we present a detailed study of a one-dimensional Schrödinger equation in the presence of quantum Gaussian well interaction. Further, we investigate the approximate solutions by using the harmonic oscillator approximation, variational principle, four-parameter potential fitting and numerical solution using the finite-difference method. The parabolic approximation yields an excellent energy value compared with the numerical solution of the Gaussian system only for the ground state, while for the excited states, it provides a higher approximation. Also, the analytical bound-state energies of the four-parameter potential under the framework of the Nikiforov-Uvarov (NU) method have been used after getting the suitable values of the potential parameters using numerical fitting. The present results of the system states are found to be in high agreement with the well-known numerical results of the Gaussian potential.

Keywords: Gaussian potential, One-dimensional Schrödinger equation, Nikiforov- Uvarov (NU) method, Four-parameter potential.

PACS: 03.65.−w; 02.90.+p; 12.39.Pn.

1. Introduction

The exact and approximate solutions of the Schrödinger wave equation with various potential models have attracted much interest since the beginning of quantum mechanics and are being increased due to the fabrication of nanodevices. Recently, one-dimensional potential wells have been commonly used to illustrate many quantum-mechanical phenomena due to their high relevance in nanophysics [1]. It is interesting to investigate the Schrödinger Hamiltonian with attractive Gaussian potential for its typical properties of short-range potentials [2]. Since these Gaussian potentials have no exact analytical solutions, many authors have made an approximation with parabolic harmonic oscillators, especially near the bottom of the well [3, 4]. Further, in some other works [5], many authors approximated the Gaussian potential to the so-called modified Gaussian using a hyperbolic function. Other authors [6] have discussed the existence and the number of bound states in a Gaussian well, tunneling through a Gaussian barrier, as well as the spectrum of a Gaussian double well. Also, the variational parameters of the Gaussian potential have been presented for the ground state as well as for the first and higher excited states [7].

Very recently, the exact solution of the Schrödinger equation for spectral problems with some solvable potential models has been the subject of many investigations [8-10]. Some of these exactly solvable potentials are exponential

Corresponding Author: Mahmoud Farout **Email**: m.qaroot@najah.edu

or hyperbolic potentials of the spatial coordinates. These exponential potentials are widely used in many branches of physics, such as nuclear physics, atomic physics and chemical physics [11-13].

Here, in general, we seek to choose the proposed appropriate four-parameter exponential-type potential [14] which may be reduced to the Rosen–Morse potential [15] as well as to the Hulthen-like effective potential [16]. With a special choice of parameters, the Eckart potential [17] may also turn to become the Hulthen potential and the generalized Morse potential.[18]. On the other hand, using numerical fitting for many-parameter potential would give an acceptable solution for our desired potential model.

In this study, we consider solutions to the one-dimensional Schrödinger equation with an attractive Gaussian potential and discuss our results for the parabolic approximation and variational methods. Further, we compare our results with numerical solution along with a numerical fitting of the Gaussian potential with four-parameter potential (FPP), which has an exact analytical solution.

This work is structured as follows. In Section 2, we discuss the solution of the Schrödinger equation using an approximation of a Gaussian potential as a parabolic potential, use harmonic oscillator wave functions as trial wave functions in the variational method and review the Nikiforov- Uvarov (NU) solution to the FPP. In Section 3, we emphasize the numerical comparisons and results for parabolic, Gaussian and solvable four-parameter potential. We also use numerical fitting to find the fitting-parameter values to calculate the bound-state solutions of the Gaussian potential model. Finally, Section 4 is devoted to our results and conclusions.

2. Theory and Method

We begin by solving the time-independent one-dimensional Schrödinger equation taking the simple form:

$$\left(-\frac{\hbar^2}{2m}\frac{d^2}{dx^2}+V(x)\right)\psi(x)=E\,\psi(x), \tag{1}$$

where $\hbar$ is the reduced Planck constant, m denotes the mass of the particle, $\psi(x)$ stands for the wave function and $V(x)$ returns to the confining potential which is to be taken as the Gaussian potential (GP) form,

$$V(x)=-V_0\,e^{-\frac{x^2}{R_0^2}}, \tag{2}$$

where $V_0>0$. For the sake of simplicity, we choose units such that $\hbar$ = 2m = 1. It is well-known that the condition on $V(x)$ is to have at least one bound state

$$\int_{-\infty}^{\infty}V(x)\,dx<0, \tag{3}$$

which mainly depends on the shape of the potential and not on its strength. Thus, Eq. (3) is a sufficient condition for a potential to have a bound state, but it is not a necessary condition as in the case of harmonic oscillator potential. The main results in Ref. [6], such as the number of bound states, depend only on $V_0\times R_0^2$.

2.1 Parabolic Potential

Taking the Taylor expansion for the Gaussian potential (GP), see Eq. (2), it becomes:

$$V(x)=-V_0+V_0\frac{x^2}{R_0^2}-V_0\frac{x^4}{2!\,R_0^4}+\ldots\ldots \tag{4}$$

Hence, in the literature, it is sufficient to use the first two terms of the above expansion to have an adequate approximation form for the GP as called the Harmonic oscillator. Here, the first term in the expansion (4) is an additional constant, whereas the second term is a parabolic potential. Comparing with the harmonic oscillator, one solves:

$$V_0\frac{x^2}{R_0^2}=\frac{1}{2}\,m\,\omega^2\,x^2. \tag{5}$$

We obtain the angular frequency as:

$$\omega=\sqrt{2\frac{V_0}{m\,R_0^2}}. \tag{6}$$

Therefore, the energy of the harmonic oscillator becomes:

$$E_n=-V_0+\left(n+\frac{1}{2}\right)\hbar\,\omega. \tag{7}$$

To have more accuracy, we can consider the third and high-order terms of the above expansion (4) as a perturbation to the potential, which would somewhat improve the spectra result for excited states.

If we take the mathematical point of view for this comparison, we notice that the GP is always negative, while the parabolic potential may flip to positive values at large x; so, it is expected to give a good result for low-order states only, at the classical limit of small x.

2.2 Variational Technique

To obtain various upper bounds of the ground-state energy, we can calculate the average value of the Hamiltonian $\langle H \rangle$ for suitably chosen trial functions. The existence of a variational parameter β enables to minimize the upper bounds as much as possible. To do that, we shall choose normalized trial wave functions $\psi_0(x)$ and $\psi_1(x)$ for the ground state and the first excited state, respectively, with some adjustable parameters β and γ, defined as follows:

$$\psi_0(x) = \left(\frac{2\beta}{\pi}\right)^{\frac{1}{4}} e^{-\beta x^2}, \tag{8}$$

and

$$\psi_1(x) = \left(\frac{2^5\gamma^3}{\pi}\right)^{1/4} x\, e^{-\gamma x^2}. \tag{9}$$

After calculating the energies as functions of the variational parameters, one obtains:

$$\langle\psi_0(x)|H|\psi_0(x)\rangle = \beta - \frac{\sqrt{2\,\beta}\,\mathrm{V}_0}{\left(2\beta+\frac{1}{R_0^2}\right)^{\frac{1}{2}}}, \tag{10}$$

and

$$\langle\psi_1(x)|H|\psi_1(x)\rangle = 3\gamma - \frac{\sqrt{8\ \gamma^3}\,V_0}{\left(2\,\gamma+\frac{1}{R_0^2}\right)^{\frac{3}{2}}}, \tag{11}$$

for the ground and first excited states, respectively, which can be minimized numerically to find the upper approximated energy.

2.3 Four-Parameter Potential Fitting

To have an approximation of the GP energy, we will apply a numerical fitting to find suitable parameters for the four parameter-potential (FPP) in the following form:

$$V(x) = \frac{V_0 e^{\alpha x}}{C+qe^{\alpha x}} - \frac{V_1 e^{\alpha x}}{(C+qe^{\alpha x})^2}. \tag{12}$$

This potential makes Schrödinger equation analytically solvable by using the Nikiforov-Uvarov (NU) method. To make the potential analytically solvable by the NU method, we have to write the Schrödinger equation in the following standard general form:

$$\frac{d^2\psi(s)}{ds^2} + \frac{\tilde{\tau}(s)}{\sigma(s)}\frac{d\psi(s)}{ds} + \frac{\tilde{\sigma}(s)}{\sigma^2(s)}\psi(s) = 0 \tag{13}$$

where $\sigma(s)$ and $\tilde{\sigma}(s)$ are polynomials at most of second-degree, $\tilde{\tau}(s)$ is a first-degree polynomial. For more details, see Ref. [19].

For the potential given in (12), the Schrödinger equation reads:

$$\psi''(x) + \frac{2m}{\hbar^2}\left[E - \frac{V_0 e^{\alpha x}}{C+qe^{\alpha x}} + \frac{V_1 e^{\alpha x}}{(C+qe^{\alpha x})^2}\right]\psi(x) = 0. \tag{14}$$

After changing the independent variable s = $C + qe^{\alpha x}$ and following the procedures given in Ref. [20], one gets the bound-state energies as follows:

$$E_n = -\frac{\hbar^2\alpha^2}{2m}\varepsilon_n^2, \tag{15}$$

where n = 0, 1, 2, 3, … and

$$\varepsilon_n = \frac{\frac{2mV_0 1}{\hbar^2\alpha^2\, q}}{\left[-(2n+1)+\sqrt{1+\frac{8mV_1\ 1}{\hbar^2\alpha^2\ qC}}\right]} - \frac{1}{4}\left[-(2n+1) + \sqrt{1+\frac{8mV_1}{\hbar^2\alpha^2}\frac{1}{qC}}\right] \tag{16}$$

and the wave function

$$\psi_{nq}(s) = B_n s^{-(2\delta-1)}(C-s)^{2\varepsilon}\frac{d^n}{ds^n}[s^{n+(2\delta-1)}(C-s)^{n-2\varepsilon}] \tag{17}$$

where

$$\delta = \frac{1}{2}\left[1-\sqrt{1+\frac{4\gamma^2}{C}}\right],\ \gamma^2 = \frac{2mV_1}{\hbar^2\alpha^2 q}. \tag{18}$$

3. Results and Discussion

In this section, we display our calculated results for energy spectra and the wave function for the Gaussian potential. We also compare the present approximated results with the exact ones which have already been obtained by numerically solving the Schrödinger equation using the finite-difference method. Knowing that all, the parameters have been arbitrarily unit-scaled for the pre-assumption $\hbar = 2m = 1$.

In Fig. 1, we have plotted the GP, FPP and parabolic potential as functions of the coordinate x, for a fixed value of V_0 and different values of R_0. This figure shows the high agreement between the Gaussian and parabolic potentials for small values of |x| (near the bottom of the curves), while we have noticed some difference as |x| tends to become larger. This result supports our arguments on the use of the parabolic model as an approximation-scheme model for GP. By comparing the GP and FPP, one can see the agreement between both curves for a larger range of x compared with the parabolic approximation.

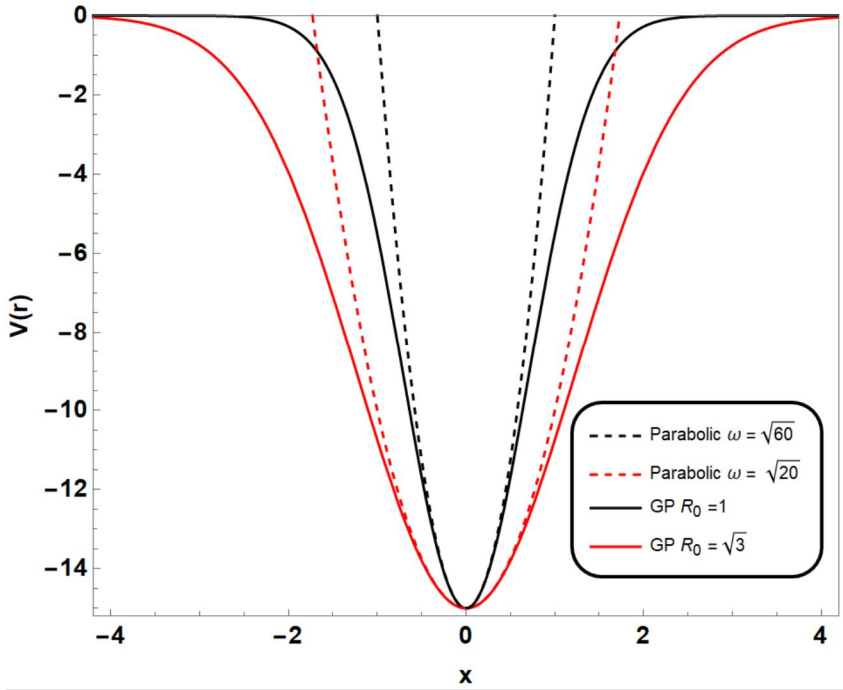

FIG. 1. GP, FPP and parabolic potential against the spatial coordinate x for a fixed value of $V_0 = 15$ and different values of R_0, Here, ω is given by Eq. (6).

In Table 1, we have shown the ground-state and first excited-state energies of the GP system compared with the variational result and parabolic approximation. These results in Table 1 show that the variational energies are in close agreement with the exact ones for the low-lying states (ground and first excited states) and with the corresponding variational parameters.

TABLE 1. Low-lying states in comparison with GP using parabolic approximation, the variation of parameter method and finite-difference numerical solution.

	$V_0 = 15, R_0 = \sqrt{3}, \omega = \sqrt{20}$			$V_0 = 15, R_0 = \sqrt{1}, \omega = \sqrt{60}$		
	E_{bar}	E_{var}	E_{num}	E_{bar}	E_{var}	E_{num}
E_0	−12.7639	−12.8873	-12.8896	−11.12701	−11.4934	-11.5046
E_1	−8.29179	−8.92558	-8.93837	−3.38105	−5.30696	-5.37760

For $R_0 = \sqrt{3}$ (1), the corresponding values of various parameters, $\beta = 0.995$ (1.574) and $\gamma = 0.905(1.283)$, agree with the fact that for a larger value of R_0 (smaller for ω), the parabolic approximation is found to be more accurate with the trial wave function as it goes to be the same as the solution of the harmonic oscillator. On the other hand, for smaller values of R_0, the parabolic deviates more and hence, the difference becomes more significant.

Moreover, in Fig. 2, we plot the low-lying state wave functions for the three cases: the numerical solution, the parabolic approximation and the variational technique. Here, we can notice the slight difference between GP and parabolic approximation.

In Table 2, we have presented the numerical values of the parameters of (FPP) concerning GP. If we look back to the (FPP), we can notice five parameters, but there is a close relation between these parameters (i.e., not independent parameters), so we used the numerical fitting to get their values.

To ensure the agreement, we have plotted the two potentials in the same graph in Fig. 3. We found similarities in their behaviors and asymptotes. On the other hand, there is a slight difference at the bottom of the curves, which is expected to yield a small difference in the ground-state energy.

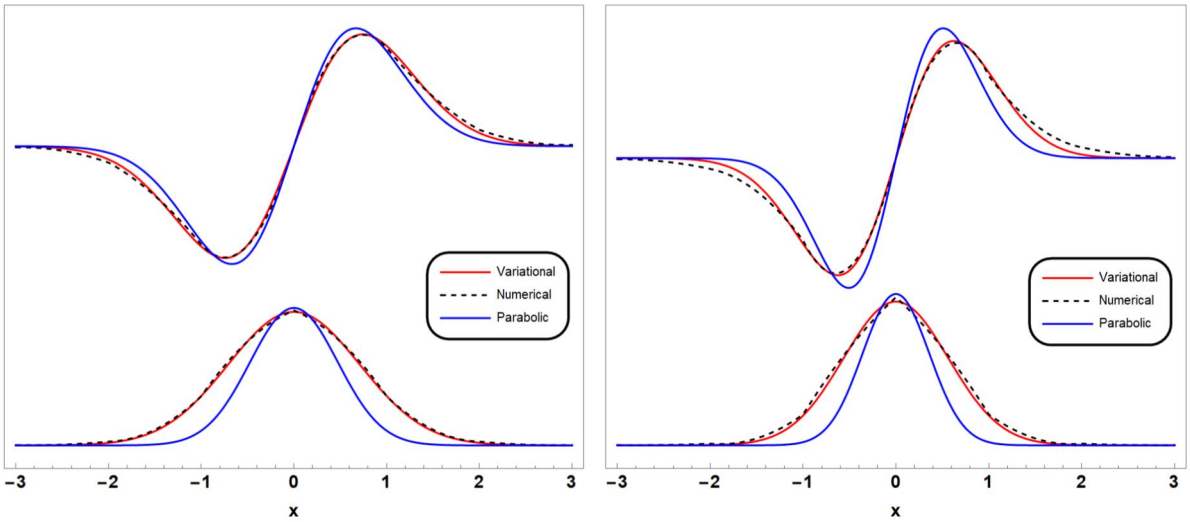

FIG. 2. The wave functions for the ground and first excited states as functions of the position for a) $V_0 = 15, R = \sqrt{3}$ and b) $V_0 = 15, R = 1$, corresponding to energies reported in Table 1.

TABLE 2. Numerical values for the fitted parameters of FPP at given values for Gaussian parameters.

	V_1	V_2	α	q	C
$V_0 = 20$ $R_0 = \sqrt{3}$	0.018137	9.275333	−1.29788	0.33512	0.336243
$V_0 = 35$ $R_0 = \sqrt{5}$	0.022753	4.470902	−1.00451	0.17574	0.17654

Also, we have displayed the spectra and wave function of GP and FPP in the same graph for different values of V_0 and R_0 in parts a, b, c and d. Here, we also see the good agreement between both potentials in their solutions.

Further, in Table 3, we have numerically listed our results of Fig. 3 to show the differences in energy. We notice the significant differences at small values of R_0 for higher excited states. This is mainly attributed to the significant role of larger values of |x| due to the behavior of the potential.

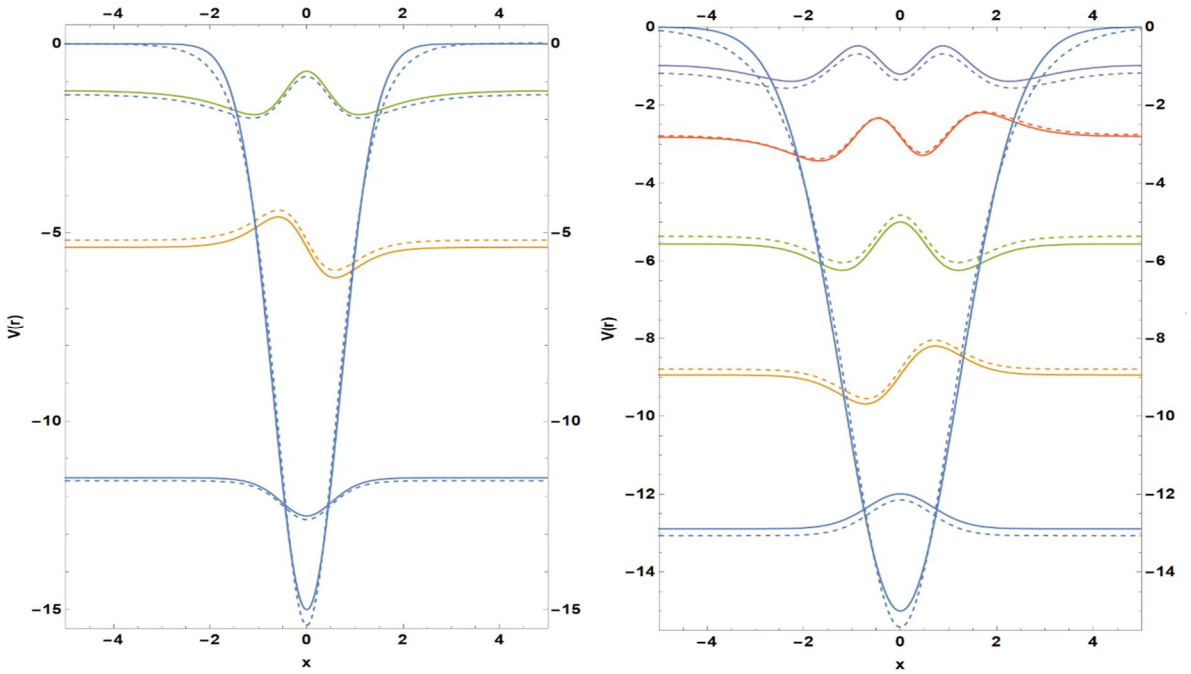

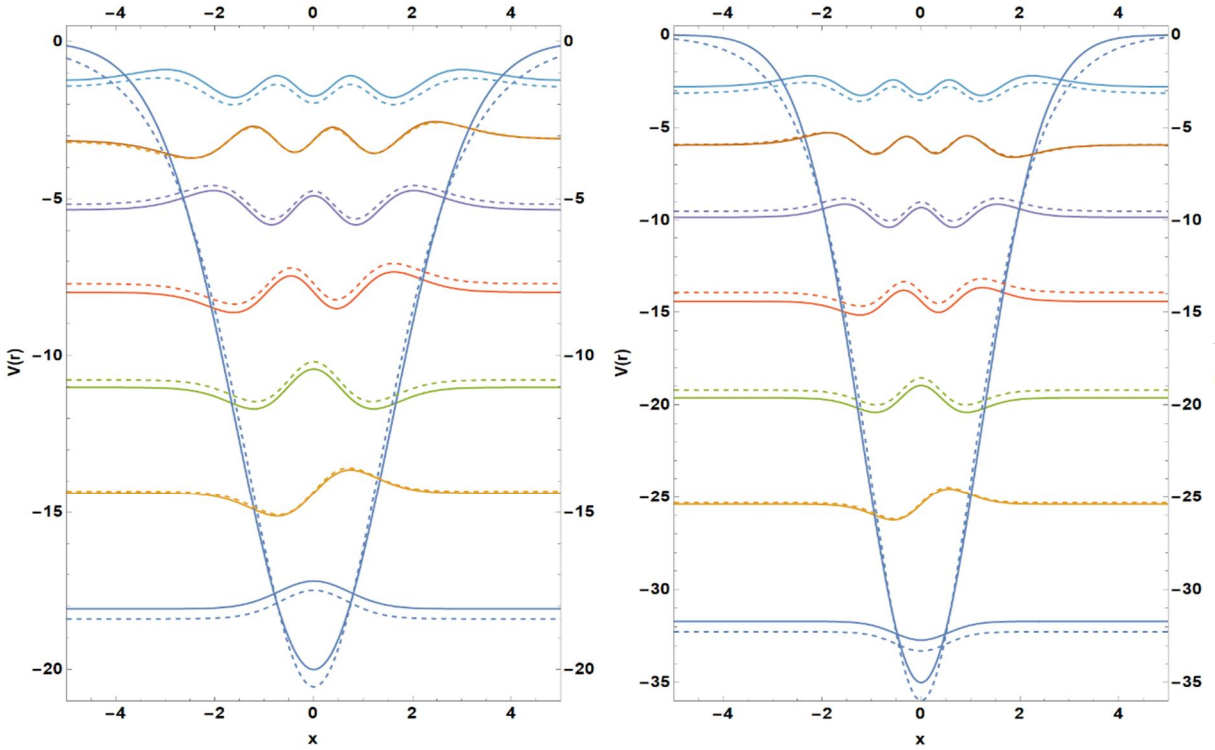

FIG. 3. The energy eigenfunctions and the corresponding eigenvalues for (V_0, R_0) taken to be in a, b, c and d, $(15, 1)$, $(15, \sqrt{3})$, $(20, \sqrt{5})$ and $(35, \sqrt{3})$ respectively. The solid (dashed) lines return to GP (FPP).

TABLE 3. The energy spectra of the GP and FPP for various values of the potential parameters.

	$R_0 = 1$		$R_0 = \sqrt{3}$		$R_0 = \sqrt{5}$	
	Gaussian	FPP	Gaussian	FPP	Gaussian	FPP
$V_0 = 15$	-11.5046	11.5852	-12.8896	-13.0659	-13.3433	-13.5595
	-5.3776	-5.18818	-8.93837	-8.79198	-10.1886	-10.109
	-1.2209	-1.32315	-5.55479	-5.36029	-7.36325	-7.16311
	---	---	-2.81231	-2.77086	-4.8946	-4.72171
	---	---	-0.85774	-1.02372	-2.82405	-2.78485
$V_0 = 20$	-15.9053	-16.0464	-17.5436	-17.8105	-18.0753	-18.3917
	-8.56120	-8.29402	-12.8974	-12.7501	-14.3834	-14.3317
	-3.08391	-3.0736	-8.80737	-8.53193	-11.016	-10.7763
	-0.15052	-0.38525	-5.32892	-5.15602	-7.9950	-7.72536
	---	---	-2.54899	-2.62238	-5.34937	-5.17897
$V_0 = 35$	-29.4610	-29.825	-31.7098	-32.2753	-32.4295	-33.0677
	-19.2012	-18.7962	-25.3917	-25.3176	-27.444	-27.5379
	-10.6823	-10.2995	-19.6133	-19.2021	-22.7762	-22.5126
	-4.19329	-4.33473	-14.4095	-13.9289	-18.4406	-17.9919
	-0.38543	-0.90205	-9.82653	-9.49795	-14.4548	-13.9757

Finally, Fig. 4 plots the vibrational bound-state energy E_n *versus* the principal quantum number n, where we have shown the three cases of GP, FPP and parabolic approximation for the sake of comparison. As percentage errors, the parabolic approximation ground-state energy is 0.23% higher than the numerical solution of GP, where the FPP yields 1.97% lower as previously mentioned, for the first excited state (n = 1). The parabolic potential (FPP) result is 1.39% higher (0.34% lower) and by comparing the 4th excited state (n = 4), the parabolic energy is 22% and FPP is 3.32% and both potentials give a higher approximation for the energy.

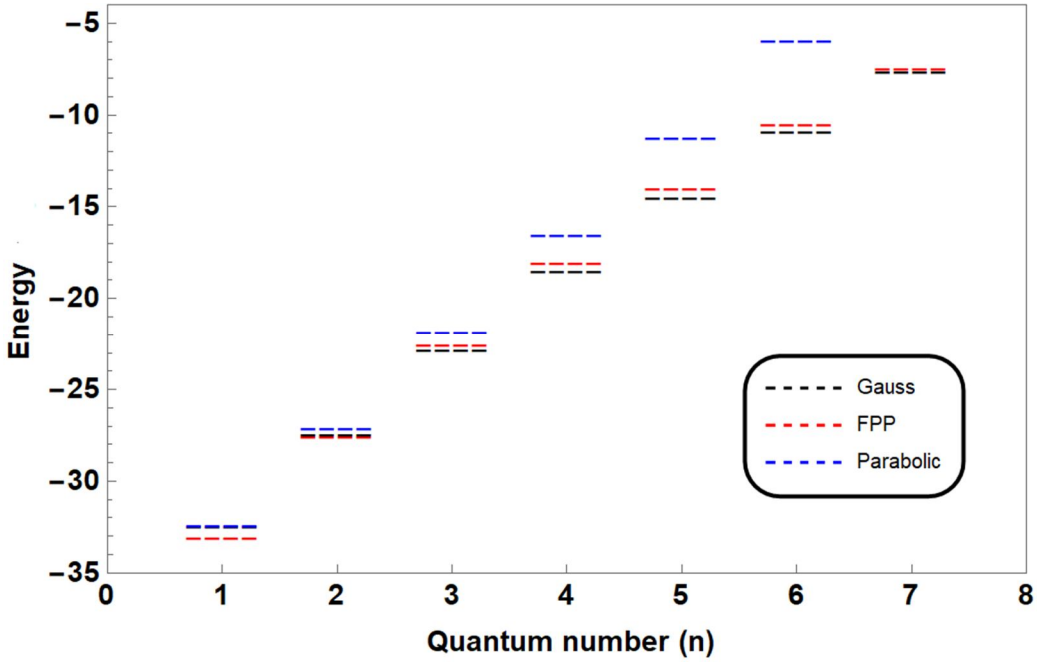

FIG. 4. The energy eigenvalues for different states (n) obtained for GP, parabolic approximation and FPP.

4. Conclusions

In this work, we have solved the one-dimensional Schrödinger equation to obtain the solutions of the bound states for the Gaussian well potential. Further, the wave functions as well as the vibrational eigenvalues are obtained by various methods. The parabolic approximation of the Gaussian potential is in excellent agreement with the exact energy for low-order states only. However, for higher states, it exhibits a significant difference. Using the well-known solution of the harmonic oscillator as a wave function with an undetermined parameter provides a very close result to the exact solution. On the other hand, the four-parameter potential having an analytical solution is also used as screening potential to be fitted using Gaussian information. Besides, the analytical solution of FPP was obtained using the Nikiforov Uvarov (NU) method. Finally, the presented results show that the fitting method provides a chance to compare with the available numerical energies and wave functions within an acceptable accuracy.

References:

[1] Choi, H., Kim, M., Moon, J.-Y., Lee, J.-H. and Son, S.-K., Journal of Nanoscience and Nanotechnology, 20 (7) (2020) 4428.

[2] Muchatibaya, G., Fassari, S., Rinaldi, F. and Mushanyu, J., Advances in Mathematical Physics, 2016 (2016) 2125769.

[3] Boyacioglu, B. and Chatterjee, A., Journal of Applied Physics, 112 (8) (2012) 083514. 54.

[4] Elsaid, M., Ali, M. and Shaer, A., Modern Physics Letters B, 33 (34) (2019) 1950422.

[5] Gharaati, A. and Khordad, R., Superlattices and Microstructures, 48 (3) (2010) 276.

[6] Nandi, S., American Journal of Physics, 78 (12) (2010) 1341.

[7] Fernández, F.M., American Journal of Physics, 79 (7) (2011) 752.

[8] Ikhdair, S. and Sever, R., Journal of Molecular Structure: THEOCHEM, 806 (1-3) (2007) 155.

[9] Ikhdair, S.M. and Sever, R., Journal of Molecular Structure: THEOCHEM, 855 (1-3) (2008) 13.

[10] Ikhdair, S.M. and Abu-Hasna, J., Physica Scripta, 83 (2) (2011) 025002.

[11] Behera, A.K., Bhoi, J., Laha, U. and Khirali, B., Communications in Theoretical Physics, 72 (7) (2020) 075301.

[12] Farout, M., Sever, R. and Ikhdair, S.M., Chinese Physics B, 29 (6) (2020) 060303.

[13] Fu, K.-X., Wang, M. and Jia, C.-S., Communications in Theoretical Physics, 71 (1) (2019) 103.

[14] Şimşek, M. and Özçelik, S., Physics Letters A, 186 (1-2) (1994) 35.

[15] Rosen, N. and Morse, P.M., Physical Review, 42 (2) (1932) 210.

[16] Greene, R.L. and Aldrich, C., Physical Review A, 14 (6) (1976) 2363.56.

[17] Eckart, C., Physical Review, 35 (11) (1930) 1303.

[18] Codriansky, S., Cordero, P. and Salamó, S., Journal of Physics A: Mathematical and General, 32 (35) (1999) 6287.

[19] Nikiforov, A.F. and Uvarov, V.B., "Special Functions of Mathematical Physics", Vol. 205, (Basel: Birkhäuser, 1988).

[20] Eğrifes, H., Demirhan, D. and Büyükkılıç, F., Physics Letters A, 275 (4) (2000) 229.

Volume 15, Number 5, 2022. pp. 495-509

Jordan Journal of Physics

ARTICLE

Expectation Values and Energy Spectra of the Varshni Potential in Arbitrary Dimensions

Etido P. Inyang[a], **Joseph E. Ntibi**[b], **Effiong O. Obisung**[b], **Eddy S. William**[b], **Etebong E. Ibekwe**[c], **Ita O. Akpan**[b] and **Ephraim P. Inyang**[b]

[a] *Department of Physics, National Open University of Nigeria, Abuja, Nigeria.*
[b] *Theoretical Physics Group, Department of Physics, University of Calabar,P.M.B. 1115 Calabar Nigeria, Nigeria.*
[c] *Department of Physics, Akwa Ibom State University, Ikot Akpaden, P.M.B. 1167, Uyo, Nigeria.*

Doi: **https://doi.org/10.47011/15.5.7**

Received on: 15/03/2021; *Accepted on: 20/06/2021*

Abstract: The Klein-Gordon equation with Varshni potential was solved through the Nikiforov-Uvarov method. The Greene and Aldrich approximation schemes were employed to overcome the centrifugal barrier. The energy eigenvalues were obtained in relativistic and non-relativistic regimes, as well as the corresponding normalized wave functions. Energy spectra and expectation values of the square of inverse of position $\langle r^{-2}\rangle$, kinetic energy $\langle T\rangle$ and the square of the momentum $\langle \hat{p}^2\rangle$ for five selected diatomic molecules: H_2, HCl, TiH, I_2 and CO, using their separate spectroscopic parameters were computed through Hellmann-Feynman Theorem. Bound-state energy eigenvalues were also computed for Varshni potential and the numerical results agree with the already existing literature.

Keywords: Expectation values, Varshni potential, Nikiforov-Uvarov method, Klein-Gordon equation.

1. Introduction

Relativistic equations, such as Klein-Gordon equation (KGE), are very essential in many aspects of modern physics and Klein-Gordon equation is the most suitably used wave equation for the treatment of spinless particles in relativistic quantum mechanics. Klein-Gordon equation has been studied with some exactly solvable potential [1-3]. The relativistic behavior of spin-zero particles needs understanding of the single-particle spectrum which contains a four-vector linear momentum operator and a rest mass and requires introducing the four-vector potential $V(r)$ and a space time scalar potential $S(r)$ with the configuration $S(r)=V(r)$ or $S(r)=-V(r)$ [2]. $S(r)=V(r)=2V(r)$ gives non-relativistic limits of the equation conforming exactly to that of the Schrödinger equation (SE) [4-7]. Different methods have been employed to obtain the solution of the relativistic and non-relativistic wave equations with interacting potential models. These include the factorization method [8], Nikiforov-Uvarov functional analysis(NUFA) method [9-13], supersymmetry quantum mechanics (SUSYQM) [14,15], asymptotic iteration method (AIM) [16,17], the WKB approximation [18-20], Nikiforov-Uvarov method (NU) [21-38], formula method [39], series expansion method [40-42], among

Corresponding Author: E. P.Inyang **Email**: etidophysics@gmail.com

others. With the above methods, many authors have solved both relativistic and non-relativistic wave equations with diverse potentials. For instance, Inyang *et al.* [43] obtained analytical solutions of the SE with the Kratzer–screened Coulomb potential model to study some diatomic molecules. Min-Cang [44] obtained relativistic and non-relativistic solutions of the inversely quadratic Yukawa potential. Arda and Sever [45] obtained the eigensolutions of the SE with the class of Yukawa potential *via* SUSYQM. Edet *et al*. [46] obtained bound-state solutions of the SE for the modified Kratzer potential plus screened Coulomb potential.

The Varshni potential is greatly important with applications cutting across nuclear physics, particle physics and molecular physics and takes the form [47]:

$$V(r) = \upsilon - \frac{\upsilon\chi e^{-\alpha r}}{r} \tag{1}$$

where υ and χ stand for the potential strength and α is the screening parameter which controls the shape of the potential-energy curve, as shown in Fig. 1, r stands for the inter-nuclear separation. The Varshni potential is a short-range repulsive potential energy function that plays an important role in both chemical and molecular physics [48-52]. This potential is generally used to describe bound states of the interaction of systems and has been applied in both classical and molecular physics. The Varshni potential was studied by Lim using the 2-body Kaxiras-Pandey parameters. The study observed that Kaxiras and Pandey used this potential to describe the 2-body energy portion of multi-body condensed matter [53]. The present study intends to investigate the relativistic Klein-Gordon equation with the Varshni-potential model in the framework of the NU method for bound-state problems and to employ Hellmann-Feynman theorem to compute expectation values for selected diatomic molecules. To the best of our knowledge, this is the first time Klein-Gordon equation is being studied with the Varshini-potential model to compute the expectation values of some diatomic molecules using the NU method.

It is noted that the exact solution of the Klein-Gordon equation with Varshni potential in Eq. (1) is not possible due to the presence of the inverse square term in Eq. (17). Therefore, to obtain approximate solutions, a suitable approximation scheme is employed. It is found that such approximation proposed by Greene and Aldrich [54]

$$\frac{1}{r^2} \approx \frac{\alpha^2}{\left(1-e^{-\alpha r}\right)^2} \tag{2}$$

is a good approximation to the centrifugal or inverse square term which is valid for $\alpha \ll 1$ for a short-range potential. The paper is organized as follows: In Section 2, the NU method is reviewed. In Section 3, the bound-state energy eigenvalues and the corresponding wave functions are calculated. In Section 4, the results are discussed. In Section 5, conclusion is presented.

2. Review of Nikiforov-Uvarov (NU) Method

The NU method was proposed by Nikiforov and Uvarov [55] as a suitable method to obtain the solution of the second-order differential equation *via* a coordinate transformation $s = s(r)$ of the form:

$$\psi''(s) + \frac{\tilde{\tau}(s)}{\sigma(s)}\psi'(s) + \frac{\tilde{\sigma}(s)}{\sigma^2(s)}\psi(s) = 0 \tag{3}$$

where $\tilde{\sigma}(s)$, and $\sigma(s)$ are polynomials, at most second-degree and $\tilde{\tau}(s)$ is a first-degree polynomial. The exact solution of Eq. (3) can be obtained by using the transformation:

$$\psi(s) = \phi(s)y(s) \ . \tag{4}$$

This transformation reduces Eq. (3) into a hypergeometric-type equation of the form:

$$\sigma(s)y''(s) + \tau(s)y'(s) + \lambda y(s) = 0. \tag{5}$$

The function $\phi(s)$ can be defined as the logarithm derivative.

$$\frac{\phi'(s)}{\phi(s)} = \frac{\pi(s)}{\sigma(s)} \tag{6}$$

with $\pi(s)$ being at most a first-degree polynomial. The second part of $\psi(s)$ being $y(s)$ in Eq. (5) is the hypergeometric function with its polynomial solution given by Rodrigues relation as:

$$y(s)=\frac{B_{nl}}{\rho(s)}\frac{d^n}{ds^n}\left[\sigma^n(s)\rho(s)\right] \tag{7}$$

where B_n is the normalization constant and $\rho(s)$ is the weight function which satisfies the condition below;

$$\left(\sigma(s)\rho(s)\right)'=\tau(s)\rho(s), \tag{8}$$

where also:

$$\tau(s)=\tilde{\tau}(s)+2\pi(s). \tag{9}$$

For bound solutions, it is required that:

$$\frac{d\tau(s)}{ds}<0. \tag{10}$$

The eigenfunctions and eigenvalues can be obtained using the definition of the following function $\pi(s)$ and parameter λ, respectively:

$$\left.\begin{aligned}\pi(s)&=\frac{\sigma'(s)-\tilde{\tau}(s)}{2}\\ &\pm\sqrt{\left(\frac{\sigma'(s)-\tilde{\tau}(s)}{2}\right)^2-\tilde{\sigma}(s)+k\sigma(s)}\end{aligned}\right\} \tag{11}$$

and

$$\lambda=k_-+\pi'_-(s)\ . \tag{12}$$

The value of k can be obtained by setting the discriminant in the square root in Eq. (11) equal to zero. As such, the new eigenvalues equation can be given as :

$$\lambda_n+n\tau'(s)+\frac{n(n-1)}{2}\sigma''(s)=0,(n=0,1,2,...). \tag{13}$$

3. Bound-state Solution of the Klein-Gordon Equation with Varshni Potential

The Klein-Gordon equation for a spinless particle for $\hbar=c=1$ in D-dimensions is given as [56, 57]:

$$\left.\begin{aligned}&\left[-\nabla^2+\left(M+S(r)\right)^2+\frac{(D+2l-1)(D+2l-3)}{4r^2}\right]\psi(r,\theta,\varphi)\\ &=\left[E-V(r)\right]^2\psi(r,\theta,\varphi)\end{aligned}\right\} \tag{14}$$

where ∇^2 is the Laplacian, M is the reduced mass, E is the energy spectrum and n and l are the radial and orbital angular momentum quantum numbers, respectively. It is a common practice that for the wave function to satisfy the boundary conditions, it can be rewritten as:

$$\psi(r,\theta,\varphi)=\frac{R_{nl}}{r}Y_{lm}(\theta,\varphi). \tag{15}$$

However, the spherical harmonic $Y_{lm}(\theta,\varphi)$ is known in literature [58].

The angular component of the wave function could be separated leaving only the radial part as shown below:

$$\left.\frac{d^2R(r)}{dr^2}+\left[\begin{aligned}&\left(E_{nl}{}^2-M^2\right)+V^2(r)-S^2(r)\\ &-2\left(E_{nl}V(r)+MS(r)\right)\\ &-\frac{(D+2l-1)(D+2l-3)}{4r^2}\end{aligned}\right]R(r)=0\right\} \tag{16}$$

Thus, for equal vector and scalar potentials $V(r)=S(r)=2V(r)$, Eq. (16) becomes:

$$\left.\frac{d^2R(r)}{dr^2}+\left[\begin{aligned}&\left(E_{nl}{}^2-M^2\right)\\ &-V(r)\left(E_{nl}+M\right)\\ &-\frac{(D+2l-1)(D+2l-3)}{4r^2}\end{aligned}\right]R(r)=0\right\}. \tag{17}$$

By substituting Eq. (1) into Eq. (17), the following equation is obtained:

$$\left.\frac{d^2R(r)}{dr^2}+\left[\begin{aligned}&\left(E_{nl}{}^2-M^2\right)\\ &-\left(\upsilon-\frac{\upsilon\chi e^{-\alpha r}}{r}\right)\left(E_{nl}+M\right)\\ &-\frac{(D+2l-1)(D+2l-3)}{4r^2}\end{aligned}\right]R(r)=0\right\}. \tag{18}$$

The coordinate of Eq.(18) is transformed by setting

$$s = e^{-\alpha r}. \tag{19}$$

Differentiating Eq. (19) and simplifying it yield:

$$\frac{d^2R(r)}{dr^2} = \alpha^2 s^2 \frac{d^2R}{ds^2} + \alpha^2 s \frac{dR}{ds}. \tag{20}$$

Substituting Eqs. (2), (19) and (20) into Eq. (18), the result is:

$$\left.\begin{aligned} &\frac{d^2R(s)}{ds^2} + \frac{(1-s)}{s(1-s)}\frac{dR(s)}{ds} \\ &+ \frac{1}{s^2(1-s)^2}\left[-\varepsilon(1-s)^2 + \beta\left(s-s^2\right) - \gamma\right]R(\mathrm{s}) \\ &= 0 \end{aligned}\right\} \tag{21}$$

where

$$\left.\begin{aligned} -\varepsilon &= \frac{E_{nl}^2 - M^2}{\alpha^2} \\ \beta &= \frac{\upsilon\chi\left(E_{nl}+M\right)}{\alpha} \\ \gamma &= \left(\frac{\upsilon\left(E_{nl}+M\right)}{\alpha^2} + \frac{(D+2l-1)(D+2l-3)}{4}\right) \end{aligned}\right\}. \tag{22}$$

Expanding the square bracket of Eq. (21), we get:

$$\left.\begin{aligned} &\frac{d^2R(s)}{ds^2} + \frac{(1-s)}{s(1-s)}\frac{dR(s)}{ds} + \\ &\frac{1}{s^2(1-s)^2}\begin{bmatrix} -(\varepsilon+\beta)s^2 \\ +(2\varepsilon+\beta)s \\ -(\varepsilon+\gamma) \end{bmatrix}R(\mathrm{s}) = 0 \end{aligned}\right\}. \tag{23}$$

Comparing Eq. (23) with Eq. (3), the following parameters are obtained:

$$\left.\begin{aligned} \tilde{\tau}(s) &= 1-s \\ \sigma(\mathrm{s}) &= s(1-s) \\ \sigma'(s) &= 1-2s \\ \tilde{\sigma}(\mathrm{s}) &= -(\varepsilon+\beta)s^2 \\ &\quad +(2\varepsilon+\beta)s - (\varepsilon+\gamma) \end{aligned}\right\}. \tag{24}$$

By substituting Eq. (24) into Eq. (11), the result is:

$$\pi(s) = -\frac{s}{2} \pm \sqrt{(A-k)s^2 + (B+k)s + C} \tag{25}$$

where

$$\left.\begin{aligned} A &= \frac{1}{4} + \varepsilon + \beta \\ B &= -(2\varepsilon+\beta) \\ C &= \varepsilon + \gamma \end{aligned}\right\}. \tag{26}$$

To find the constant k, the discriminant of the expression under the square root of Eq. (25) must be equal to zero.

$$k = -(B+2C) - 2\sqrt{C}\sqrt{C+B+A} \tag{27}$$

Substituting Eq. (26) into Eq. (27), we get:

$$k_{\_} = \beta - 2\gamma - 2\sqrt{\varepsilon+\gamma}\sqrt{\frac{1}{4}+\gamma}. \tag{28}$$

Substituting Eq.(27) into Eq. (25), the result is:

$$\pi(s) = -\frac{s}{2} \pm \left[\left(\sqrt{C} + \sqrt{C+B+A}\right)S - \sqrt{C}\right]. \tag{29}$$

Substituting Eq. (26) into Eq. (29) yields:

$$\pi_{\_}(\mathrm{s}) = -\frac{s}{2} - \begin{bmatrix} \left(\sqrt{\varepsilon+\gamma} + \sqrt{\frac{1}{4}+\gamma}\right)S \\ -\sqrt{\varepsilon+\gamma} \end{bmatrix}. \tag{30}$$

Differentiating Eq. (30), we obtain:

$$\pi'_{\_}(\mathrm{s}) = -\frac{1}{2} - \left(\sqrt{\varepsilon+\gamma} + \sqrt{\frac{1}{4}+\gamma}\right). \tag{31}$$

Substituting Eqs. (28) and (31) into Eq. (12), the result is:

$$\left.\begin{aligned}\lambda = \beta - 2\gamma - 2\sqrt{\varepsilon+\gamma}\sqrt{\frac{1}{4}+\gamma} \\ -\frac{1}{2} - \left(\sqrt{\varepsilon+\gamma} + \sqrt{\frac{1}{4}+\gamma}\right)\end{aligned}\right\}. \quad (32)$$

with $\tau(s)$ being obtained from Eq. (9) as:

$$\left.\begin{aligned}\tau(s) = 1 - 2s + 2\sqrt{\varepsilon+\gamma}\,s \\ -2\sqrt{\frac{1}{4}+\gamma}\,s + 2\sqrt{\varepsilon+\gamma}\end{aligned}\right\}. \quad (33)$$

Differentiating Eq. (33) yields:

$$\tau'(s) = -2 - 2\left(\sqrt{\varepsilon+\gamma} + \sqrt{\frac{1}{4}+\gamma}\right). \quad (34)$$

Taking the derivative of $\sigma'(s)$ with respect to s from Eq. (24) yields:

$$\sigma''(s) = -2\ . \quad (35)$$

Substituting Eqs. (34) and (35) into Eq. (13) and simplifying yield:

$$\lambda_n = n^2 + n + 2n\sqrt{\varepsilon+\gamma} + 2n\sqrt{\frac{1}{4}+\gamma}\ . \quad (36)$$

Equating Eqs. (32) and (36) and substituting Eq. (22) yield the energy eigenvalue equation of the Varshni potential in the relativistic limit as:

$$\begin{aligned}&M^2 - E_{nl}^2 = \\ &-\alpha^2\left(\frac{\upsilon\left(E_{nl}+M\right)}{\alpha^2} + \frac{\left(D+2l-1\right)\left(D+2l-3\right)}{4}\right) \\ &+\frac{\alpha^2}{4}\left[\frac{\left(n+\frac{1}{2}+\sqrt{\frac{1}{4}+\frac{\left(D+2l-1\right)\left(D+2l-3\right)}{4}+\frac{\upsilon\left(E_{nl}+M\right)}{\alpha^2}}\right)^2 - Q}{n+\frac{1}{2}+\sqrt{\frac{1}{4}+\frac{\left(D+2l-1\right)\left(D+2l-3\right)}{4}+\frac{\upsilon\left(E_{nl}+M\right)}{\alpha^2}}}\right]^2\end{aligned} \quad (37)$$

where

$$\left.\begin{aligned}Q = \frac{\upsilon\chi\left(E_{nl}+M\right)}{\alpha} \\ +\frac{\left(D+2l-1\right)\left(D+2l-3\right)}{4} \\ +\frac{\upsilon\left(E_{nl}+M\right)}{\alpha^2}\end{aligned}\right\}. \quad (37a)$$

3.1 Non-relativistic Limit

In this sub-section, the non-relativistic limit of Eq. (37) is studied. Considering a transformation of the form: $M + E_{nl} \to \frac{2\mu}{\hbar^2}$, $M - E_{nl} \to -E_{nl}$ and substituting it into Eq. (37), the non-relativistic energy eigenvalue equation reads:

$$\begin{aligned}E_{nl} = \upsilon + \frac{\alpha^2\hbar^2}{\mu}\left(\frac{\left(D+2l-1\right)\left(D+2l-3\right)}{8}\right) \\ -\frac{\hbar^2\alpha^2}{8\mu}\left[\frac{\left(n+\frac{1}{2}+\sqrt{\frac{1}{4}+\frac{\left(D+2l-1\right)\left(D+2l-3\right)}{4}+\frac{2\upsilon\mu}{\alpha^2\hbar^2}}\right)^2}{n+\frac{1}{2}+\sqrt{\frac{1}{4}+\frac{\left(D+2l-1\right)\left(D+2l-3\right)}{4}+\frac{2\upsilon\mu}{\alpha^2\hbar^2}}}\right]^2 \\ \frac{-\frac{2\upsilon\chi\mu}{\alpha\hbar^2}+\frac{\left(D+2l-1\right)\left(D+2l-3\right)}{4}+\frac{2\upsilon\mu}{\alpha^2\hbar^2}}{}\end{aligned}. \quad (38)$$

To obtain the corresponding wave function, Eq. (6) is considered and upon substituting Eqs. (24) and (33) and integrating, the result is:

$$\phi(\mathrm{s}) = s^{\sqrt{\varepsilon+\gamma}}\left(1-s\right)^{\frac{1}{2}+\sqrt{\frac{1}{4}+\gamma}}\ . \quad (39)$$

To get the hypergeometric function considering Eq. (4), the weight function is determined first of Eq. (8) upon differentiating the left-hand side to get:

$$\frac{\rho'(\mathrm{s})}{\rho} = \frac{\tau(\mathrm{s}) - \sigma'(\mathrm{s})}{\sigma(\mathrm{s})}\ . \quad (40)$$

Substituting Eqs. (24) and (33) into Eq. (40), then integrating and simplify, we obtain:

$$\rho(\mathrm{s}) = s^{2\sqrt{\varepsilon+\gamma}}\left(1-s\right)^{2\sqrt{\frac{1}{4}+\gamma}}\ . \quad (41)$$

By substituting Eqs. (24) and (41) into Eq. (7), the Rodrigue's equation is obtained as:

$$\begin{aligned}&y_n(s) = \\ &B_n s^{-2\sqrt{\varepsilon+\gamma}}\left(1-s\right)^{-2\sqrt{\frac{1}{4}+\gamma}}\frac{d^n}{ds^n}\left[s^{n+2\sqrt{\varepsilon+\gamma}}\left(1-s\right)^{n+2\sqrt{\frac{1}{4}+\gamma}}\right]\end{aligned} \quad (42)$$

where B_n is the normalization constant.

Eq. (42) is an equivalent to

$$P_n^{\left(2\sqrt{\varepsilon+\gamma},2\sqrt{\frac{1}{4}+\gamma}\right)}(1-2s), \tag{43}$$

where $p_n^{(\alpha,\beta)}$ is Jacobi polynomial.

The wave function is given by:

$$\psi_{nl}(s) = B_{nl}s^{\sqrt{\varepsilon+\gamma}}(1-s)^{\frac{1}{2}+\sqrt{\frac{1}{4}+\gamma}}P_n^{\left(2\sqrt{\varepsilon+\gamma},2\sqrt{\frac{1}{4}+\gamma}\right)}(1-2s) \tag{44}$$

Using the normalization condition, the normalization constant can be obtained as follows:

$$\int_0^\infty |\psi_{nl}(r)|^2\, dr = 1\ . \tag{45}$$

Using the coordinate transformation of Eq. (19), we get:

$$-\frac{1}{\alpha s}\int_1^0 |\psi_{nl}(\mathrm{s})|^2\, ds = 1\ . \tag{46}$$

By letting $y = 1-2s$, the result is:

$$\frac{B_{nl}^2}{\alpha}\int_{-1}^{1}\left(\frac{1-y}{2}\right)^{2\sqrt{\varepsilon+\gamma}}\left(\frac{1+y}{2}\right)^{1+2\sqrt{\frac{1}{4}+\gamma}}\left[P_n^{\left(2\sqrt{\varepsilon+\gamma},2\sqrt{\frac{1}{4}+\gamma}\right)}y\right]^2 dy\Bigg\}. = 1 \tag{47}$$

Let

$$\left.\begin{aligned}\mu &= 1+2\sqrt{\frac{1}{4}+\gamma}\\ \mu-1 &= 2\sqrt{\frac{1}{4}+\gamma}\\ u &= 2\sqrt{\varepsilon+\gamma}\end{aligned}\right\}. \tag{48}$$

Substituting Eq. (48) into Eq. (47) yields:

$$\frac{B_{nl}^2}{\alpha}\int_{-1}^{1}\left(\frac{1-y}{2}\right)^{u}\left(\frac{1+y}{2}\right)^{\mu}\left[P_n^{(2\,\mathrm{u},\mu-1)}y\right]^2 dy = 1\,. \tag{49}$$

According to Onate et al. [59], the integral of the form in Eq. (49) can be expressed as:

$$\left.\begin{aligned}&\int_{-1}^{1}\left(\frac{1-p}{2}\right)^{x}\left(\frac{1+p}{2}\right)^{y}\left[P_n^{(2\mathrm{x},2y-1)}p\right]^2 dp\\ &= \frac{2\Gamma(x+n+1)\Gamma(y+n+1)}{n!\,x\Gamma(x+y+n+1)}\end{aligned}\right\}. \tag{50}$$

Hence, comparing Eq. (49) with the standard integral of Eq. (50), the normalization constant is obtained as:

$$B_{nl} = \sqrt{\frac{n!u\alpha\Gamma(\mathrm{u}+\mu+\mathrm{n}+1)}{2\Gamma(u+n+1)\Gamma(\mu+n+1)}}\ . \tag{51}$$

3.2 Application of Hellmann-Feynman Theorem to the Varshni Potential

Hellmann-Feynman Theorem (HFT) is one of the useful means of obtaining expectation values of some quantum mechanical observables for any arbitrary values of n and l quantum numbers. Assume that the Hamiltonian $\hat{H}$ for a particular quantum mechanical system is a function of some parameter q. Let $E(\mathrm{q})$ and $\Psi(q)$ be the eigenvalues and the eigenfunctions of the Hamiltonian $\hat{H}(q)$. Then, the Hellmann-Feynman Theorem (HFT) states that:

$$\frac{\partial E_{nl}(q)}{\partial q} = \langle\psi_{nl}(q)\left|\frac{\partial\hat{H}(q)}{\partial q}\right|\psi_{nl}(q)\rangle\ , \tag{52}$$

provided that the associated normalized eigenfunction $\psi_{nl}(q)$ is continuous with respect to the parameter q [60-62].

The effective Hamiltonian is given as:

$$\hat{H} = -\frac{\hbar^2}{2\mu}\frac{d^2}{dr^2} + \frac{\hbar^2}{2\mu r^2}l(l+1) + \upsilon - \frac{\upsilon\chi e^{-\alpha r}}{r}. \tag{53}$$

3.2.1 Expectation Value of $\langle r^{-2}\rangle$

Substituting $q = l$ into Eq. (53) gives:

$$\frac{\partial E_{nl}(l)}{\partial l} = \langle\psi_{nl}(l)\left|\frac{\partial\hat{H}(l)}{\partial l}\right|\psi_{nl}(l)\rangle\,. \tag{54}$$

Taking the partial derivative of Eq. (53) with respect to l gives:

$$\langle\psi(l)\left|\frac{\partial H(l)}{\partial l}\right|\psi(l)\rangle = \frac{\hbar^2}{2\mu}(2l+1)\langle r^{-2}\rangle\,. \tag{55}$$

Taking the partial derivative of Eq. (38) with respect to l gives:

$$\frac{\partial E_{nl}(l)}{\partial l}=\frac{4\alpha^2\hbar^2}{8\mu}\left\{-2BV\left[\frac{1}{2\sqrt{U}}-\frac{\left(n+\frac{1}{2}+\sqrt{U}\right)+\left(\frac{4\upsilon\chi\mu}{\hbar^2\alpha}+\frac{(D+2l-1)(D+2l-3)}{4}+\frac{4\upsilon\mu}{\hbar^2\alpha^2}\right)\frac{1}{2\sqrt{U}}}{\left(n+\frac{1}{2}+\sqrt{U}\right)^2}\right]\right\} \quad (56)$$

where

$$B=\frac{\hbar^2\alpha^2}{8\mu} \quad (57)$$

$$U=\frac{1}{4}+\frac{(D+2l-1)(D+2l-3)}{4}+\frac{4\upsilon\mu}{\hbar^2\alpha^2} \quad (58)$$

$$V=\left(n+\frac{1}{2}+\sqrt{U}\right)-\frac{\left(\frac{4\upsilon\chi\mu}{\hbar^2\alpha}+\frac{(D+2l-1)(D+2l-3)}{4}+\frac{4\upsilon\mu}{\hbar^2\alpha^2}\right)}{\left(n+\frac{1}{2}+\sqrt{U}\right)}. \quad (59)$$

Equating Eqs. (55) and (56) yields the expectation values of $\langle r^{-2}\rangle$ for different orbital quantum numbers. Hence,

$$\langle r^{-2}\rangle=\frac{\alpha^2}{(2l+1)}-\frac{4\mu BV}{\hbar^2(2l+1)}\left\{\frac{1}{2\sqrt{U}}-\frac{\left(n+\frac{1}{2}+\sqrt{U}\right)+\left(\frac{4\upsilon\chi\mu}{\hbar^2\alpha}+\frac{(D+2l-1)(D+2l-3)}{4}+\frac{4\upsilon\mu}{\hbar^2\alpha^2}\right)\frac{1}{2\sqrt{U}}}{\left(n+\frac{1}{2}+\sqrt{U}\right)^2}\right\}. \quad (60)$$

3.2.2 Expectation Values for $\langle T\rangle$ and $\langle\hat{P}^2\rangle$

Substituting $q=\mu$ into Eq. (52), we get:

$$\frac{\partial E_{nl}(\mu)}{\partial\mu}=\langle\psi_{nl}(\mu)\left|\frac{\partial\hat{H}(\mu)}{\partial\mu}\right|\psi_{nl}(\mu)\rangle. \quad (61)$$

Taking the partial derivative of Eq. (61) with respect to μ gives:

$$\frac{\partial H(\mu)}{\partial\mu}=\frac{\hbar^2}{2\mu^2}\frac{d^2}{dr^2}+\frac{\hbar^2}{2\mu^2r^2}l(l+1), \quad (62)$$

which implies:

$$\frac{\partial H(\mu)}{\partial\mu}=-\frac{1}{\mu}\left(-\frac{\hbar^2}{2\mu}\frac{d^2}{dr^2}-\frac{\hbar^2}{2\mu r^2}l(l+1)\right). \quad (63)$$

Eq. (63) implies:

$$-\frac{1}{\mu}\langle T\rangle=-\frac{1}{\mu}(H-V). \quad (64)$$

Hence,

$$\langle\psi_{nl}(\mu)\left|\frac{\partial\hat{H}(\mu)}{\partial\mu}\right|\psi_{nl}(\mu)\rangle=-\frac{1}{\mu}\langle T\rangle. \quad (65)$$

From the relation $T=\frac{p^2}{2\mu}$, substituting for T in Eq. (64), we obtain:

$$-\frac{1}{\mu}\langle T\rangle=-\frac{1}{2\mu^2}\langle\hat{P}^2\rangle. \quad (66)$$

Substituting Eq. (66) into Eq. (65) yields:

$$\langle \psi_{nl}(\mu) \left| \frac{\partial \hat{H}(\mu)}{\partial \mu} \right| \psi_{nl}(\mu) \rangle = -\frac{1}{2\mu^2} \langle \hat{P}^2 \rangle \,. \quad (67)$$

Taking the partial derivative of Eq. (38) with respect to μ gives:

$$\frac{\partial E_{nl}(\mu)}{\partial \mu} = -\frac{\alpha^2\hbar^2}{\mu^2}\left(\frac{(D+2l-1)(D+2l-3)}{8}\right) + 2BV\left[\frac{2\upsilon}{\hbar^2\alpha^2\sqrt{U}} - \frac{\left(n+\frac{1}{2}+\sqrt{U}\right)\left(\frac{4\upsilon\chi}{\hbar^2\alpha}+\frac{4\upsilon}{\alpha^2\hbar^2}\right)+\left(\frac{4\upsilon\chi\mu}{\hbar^2\alpha}+\frac{(D+2l-1)(D+2l-3)}{4}+\frac{4\upsilon\mu}{\hbar^2\alpha^2}\right)\frac{2\upsilon}{\hbar^2\alpha^2\sqrt{U}}}{\left(n+\frac{1}{2}+\sqrt{U}\right)^2}\right] . \quad (68)$$

Equating Eqs. (65) and (68) yields the expectation values of $\langle T \rangle$ for different orbital quantum numbers. Hence,

$$\langle T \rangle = \frac{\alpha^2\hbar^2}{\mu}\left(\frac{(D+2l-1)(D+2l-3)}{8}\right) - 2\mu BV\left[\frac{2\upsilon}{\hbar^2\alpha^2\sqrt{U}} - \frac{\left(n+\frac{1}{2}+\sqrt{U}\right)\left(\frac{4\upsilon\chi}{\hbar^2\alpha}+\frac{4\upsilon}{\alpha^2\hbar^2}\right)+\left(\frac{4\upsilon\chi\mu}{\hbar^2\alpha}+\frac{(D+2l-1)(D+2l-3)}{4}+\frac{4\upsilon\mu}{\hbar^2\alpha^2}\right)\frac{2\upsilon}{\hbar^2\alpha^2\sqrt{U}}}{\left(n+\frac{1}{2}+\sqrt{U}\right)^2}\right] . \quad (69)$$

Equating Eqs. (67) and (68) yields the expectation values of $\langle \hat{P}^2 \rangle$ for different orbital quantum numbers. Hence,

$$\langle \hat{P}^2 \rangle = 2\alpha^2\hbar^2\left(\frac{(D+2l-1)(D+2l-3)}{8}\right) - 4\mu^2 BV\left[\frac{2\upsilon}{\hbar^2\alpha^2\sqrt{U}} - \frac{\left(n+\frac{1}{2}+\sqrt{U}\right)\left(\frac{4\upsilon\chi}{\hbar^2\alpha}+\frac{4\upsilon}{\alpha^2\hbar^2}\right)+\left(\frac{4\upsilon\chi\mu}{\hbar^2\alpha}+\frac{(D+2l-1)(D+2l-3)}{4}+\frac{4\upsilon\mu}{\hbar^2\alpha^2}\right)\frac{2\upsilon}{\hbar^2\alpha^2\sqrt{U}}}{\left(n+\frac{1}{2}+\sqrt{U}\right)^2}\right] . \quad (70)$$

4. Results and Discussion

TABLE 1. Molecular parameters for selected diatomic molecules [52].

Molecule	$\overset{0}{\alpha}(A)$	$\mu(amu)$
H_2	1.9426	0.50391
CO	2.2994	6.8606719
I_2	1.8643	63.45223502
HCl	1.8677	0.9801045
TiH	1.32408	0.987371

TABLE 2. Energy spectra $E_{nl}(eV)$ and expectation values for $\left\langle r^{-2}\right\rangle_{nl}$, $\langle T\rangle_{nl}$ and $\left\langle P^2\right\rangle_{nl}$ of the Varshni potential for $D=3$ with various n and l quantum numbers for H_2 diatomic molecules.

n	l	$E_{nl}(eV)$	$\left\langle r^{-2}\right\rangle_{nl}\left(\mathring{A}\right)^{-2}$	$\langle T\rangle_{nl}(\mathrm{eV})$	$\left\langle P^2\right\rangle_{nl}(\mathrm{eV}/c)^2$
0	0	-1.284911706	0.03579269260	-9.162774801	-3.737481180
0	1	-0.1054081970	0.36962978560	-9.130996387	-3.727330813
0	2	-0.07608090100	0.05920818721	-9.067311521	-3.707110307
0	3	-0.03243091400	0.00123608902	-8.971470241	-3.676977983
1	0	-0.3670952040	0.10200937101	-8.513336108	-3.336311615
1	1	-0.3529862820	0.03668385200	-8.480836963	-3.327012768
1	2	-0.3248963660	0.02520795230	-8.480836963	-3.308484628
1	3	-0.2830783740	0.02139776540	-8.415734312	-3.280864490
2	0	-0.6248777810	0.5426331240	-7.873022427	-2.973831503
2	1	-0.6113588380	0.1832125510	-7.839974593	-2.965273962
2	2	-0.5844399920	0.1127128246	-7.773793971	-2.948219351
2	3	-0.5443566640	0.08346423870	-7.674314879	-2.922787033
3	0	-0.8931843390	0.9361674190	-7.246074828	-2.645561145
3	1	-0.8802253930	0.3140913608	-7.212613314	-2.637650798
3	2	-0.8544184310	0.1908832726	-7.145621284	-2.621882798
3	3	-0.8159828870	0.1389220179	-7.044964233	-2.598361166

TABLE 3. Energy spectra $E_{nl}(eV)$ and expectation values for $\left\langle r^{-2}\right\rangle_{nl}$, $\langle T\rangle_{nl}$ and $\left\langle P^2\right\rangle_{nl}$ of the Varshni potential for $D=3$ with various n and l quantum numbers for CO diatomic molecules.

n	l	$E_{nl}(\mathrm{eV})$	$\left\langle r^{-2}\right\rangle_{nl}\left(\mathring{A}\right)^{-2}$	$\langle T\rangle_{nl}(\mathrm{eV})$	$\left\langle P^2\right\rangle_{nl}(\mathrm{eV}/c)^2$
0	0	-0.1170808900	2.489514420	-22.31946683	-159.1662412
0	1	-0.1166026000	0.8298635421	-22.31624311	-159.1581250
0	2	-0.1156461300	0.4979486091	-22.30979559	-159.1418921
0	3	-0.1142114900	0.3557102344	-22.30012416	-159.1175444
1	0	-0.3517501900	2.540359848	-22.05602493	-156.4563020
1	1	-0.3512725000	0.8468115465	-22.05279699	-156.4482544
1	2	-0.3503172600	0.5081168442	-22.04634099	-156.4321590
1	3	-0.3488847200	0.3629726517	-22.03665686	-156.4080174
2	0	-0.5873492500	2.590492590	-21.79265536	-153.7806669
2	1	-0.5868722700	0.8635219961	-21.78942332	-153.7726868
2	2	-0.5859183600	0.5181425575	-21.78295914	-153.7567266
2	3	-0.5844877300	0.3701332794	-21.77326272	-153.7327874
3	0	-0.8238764800	2.540359848	-21.52940447	-151.1388219
3	1	-0.8234001700	0.8468115465	-21.52616847	-151.1309081
3	2	-0.8224476800	0.5081168442	-21.51969637	-151.1150804
3	3	-0.8210190800	0.3629726517	-21.50998802	-151.0913399

TABLE 4. Energy spectra $E_{nl}(eV)$ and expectation values for $\left\langle r^{-2}\right\rangle_{nl}$, $\langle T\rangle_{nl}$ and $\left\langle P^2\right\rangle_{nl}$ of the Varshni potential for $D=3$ with various n and l quantum numbers for I_2 diatomic molecules.

n	l	$E_{nl}(eV)$	$\left\langle r^{-2}\right\rangle_{nl}\left(\mathring{A}\right)^{-2}$	$\langle T\rangle_{nl}(\mathrm{eV})$	$\left\langle P^2\right\rangle_{nl}(\mathrm{eV}/c)^2$
0	0	-0.01508951000	2.638248562	-3.099862014	-291.4735778
0	1	-0.01508020000	0.8794171616	-3.099633021	-291.4698897
0	2	-0.01506158000	0.5276514661	-3.099175029	-291.4625149
0	3	-0.01503373000	0.3768951573	-3.098488021	-291.4514518
1	0	-0.04534811000	2.646393504	-3.077186434	-288.7271469
1	1	-0.04533873000	0.8821321334	-3.076957406	-288.7234675
1	2	-0.04532011000	0.5292804395	-3.076499321	-288.7161083

n	l	$E_{nl}(eV)$	$\left\langle r^{-2}\right\rangle_{nl}\left(\text{Å}\right)^{-2}$	$\langle T\rangle_{nl}(\text{eV})$	$\left\langle P^2\right\rangle_{nl}(\text{eV}/c)^2$
1	3	−0.04529214000	0.3780586989	−3.075812191	−288.7050692
2	0	−0.07572465000	2.654493607	−3.054512093	−285.9946808
2	1	−0.07571527000	0.8848321597	−3.054283017	−285.9910092
2	2	−0.07569657000	0.5309004451	−3.053824839	−285.9836658
2	3	−0.07566856000	0.3792158351	−3.053137580	−285.9726510
3	0	−0.1062188700	2.662549139	−3.031839794	−283.2760989
3	1	−0.1062095400	0.8875173285	−3.031610673	−283.2724353
3	2	−0.1061907500	0.5325115362	−3.031152415	−283.2651083
3	3	−0.1061626700	0.3803666034	−3.030465013	−283.2541175

TABLE 5. Energy spectra $E_{nl}(eV)$ and expectation values for $\left\langle r^{-2}\right\rangle_{nl}$, $\langle T\rangle_{nl}$ and $\left\langle P^2\right\rangle_{nl}$ of the Varshni potential for $D=3$ with various n and l quantum numbers for HCl diatomic molecules

n	l	$E_{nl}(eV)$	$\left\langle r^{-2}\right\rangle_{nl}\left(\text{Å}\right)^{-2}$	$\langle T\rangle_{nl}(\text{eV})$	$\left\langle P^2\right\rangle_{nl}(\text{eV}/c)^2$
0	0	−0.1529847700	1.473532445	−9.051930929	−8.807283121
0	1	−0.1503699400	0.4914243720	−9.037010945	−8.801602065
0	2	−0.1451447400	0.2951505825	−9.007166779	−8.790245776
0	3	−0.1373179400	0.2111383936	−8.962389926	−8.773225855
1	0	−0.4610450100	1.600333990	−8.680100390	−8.289787149
1	1	−0.4584503900	0.5336755706	−8.665105589	−8.284282842
1	2	−0.4532654700	0.3204821440	−8.635112115	−8.273279650
1	3	−0.4454988800	0.2292118785	−8.590112330	−8.256788452
2	0	−0.7730904500	1.600333990	−8.309501194	−7.795407708
2	1	−0.7705168300	0.5336755706	−8.294439840	−7.790069215
2	2	−0.7653738100	0.3204821440	−8.264313630	−7.779397292
2	3	−0.7576697900	0.2292118785	−8.219115671	−7.763402108
3	0	−1.089108990	1.835403060	−7.940841730	−7.322926754
3	1	−1.086557120	0.6120030134	−7.925721251	−7.317743878
3	2	−1.081457530	0.3674439523	−7.895477132	−7.307382871
3	3	−1.073818390	0.2627189638	−7.850103134	−7.291853231

TABLE 6. Energy spectra $E_{nl}(eV)$ and expectation values for $\left\langle r^{-2}\right\rangle_{nl}$, $\langle T\rangle_{nl}$ and $\left\langle P^2\right\rangle_{nl}$ of the Varshni potential for $D=3$ with various n and l quantum numbers for TiH diatomic molecules.

n	l	$E_{nl}(eV)$	$\left\langle r^{-2}\right\rangle_{nl}\left(\text{Å}\right)^{-2}$	$\langle T\rangle_{nl}(\text{eV})$	$\left\langle P^2\right\rangle_{nl}(\text{eV}/c)^2$
0	0	−0.07152099500	0.7302912690	−4.012170649	−3.913689181
0	1	−0.07019219700	0.2435742016	−4.004725407	−3.910814081
0	2	−0.06753717000	0.1463168492	−3.989832450	−3.905067256
0	3	−0.06356104800	0.1046963051	−3.967486874	−3.896455495
1	0	−0.2155946040	0.7988103264	−3.836743540	−3.669035737
1	1	−0.2116448370	0.2664039745	−3.829258062	−3.666256471
1	2	−0.2116448370	0.1600028318	−3.814284905	−3.660701110
1	3	−0.2077025790	0.1144593050	−3.791819641	−3.652375937
2	0	−0.3616429120	0.8637003948	−3.661975352	−3.436039830
2	1	−0.3603372950	0.2880247719	−3.654454412	−3.433350099
2	2	−0.3577285070	0.1729642548	−3.639410531	−3.427973564
2	3	−0.3538214230	0.1237056446	−3.616839747	−3.419916089
3	0	−0.5096601390	0.9251749007	−3.488241204	−3.214046403
3	1	−0.5083667450	0.3085076864	−3.480689005	−3.211440334
3	2	−0.5057823400	0.1852437113	−3.465582832	−3.206230934
3	3	−0.5019116790	0.1324656811	−3.442919112	−3.198423645

TABLE 7. Bound-state energy eigenvalues of the Varshni potential as a function of the screening parameter with $2\mu = \hbar = 1, \upsilon = \chi = -1$, $D = 3$.

State	Screening parameter (α)	Present work E_{nl}	[39]
2P	0.001	-1.061750235	-1.0617502
	0.050	-1.025625010	-1.0256250
	0.100	-0.991000001	-0.9900000
3P	0.001	-1.027168072	-1.0271680
	0.050	-1.000645080	-1.0006250
	0.100	-0.980278864	-0.9802778
4P	0.001	-1.015065656	-1.0150656
	0.050	-0.995156336	-0.9951563
	0.100	-0.992000008	-0.9900000
4d	0.001	-1.014939102	-1.0149391
	0.050	-0.985156474	-0.9851563
	0.100	-0.962500063	-0.9625000
4f	0.001	-1.014750243	-1.0147502
	0.050	-0.972500081	-0.9725000
	0.100	-0.930625006	-0.9306250

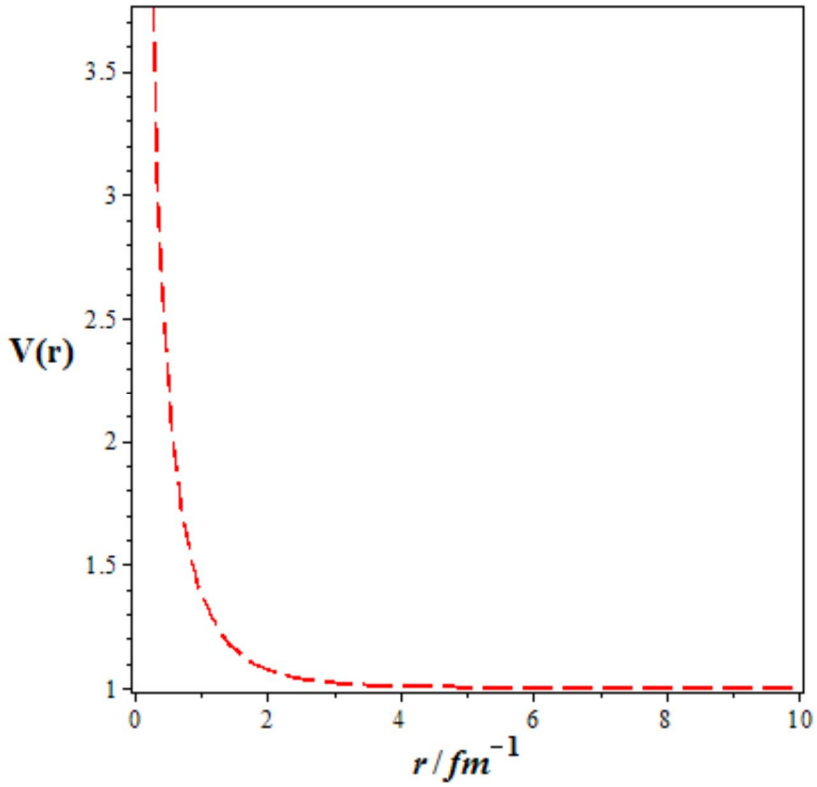

FIG. 1. Plots of Varshni potential with inter-nuclear distance r in (fm^{-1}).

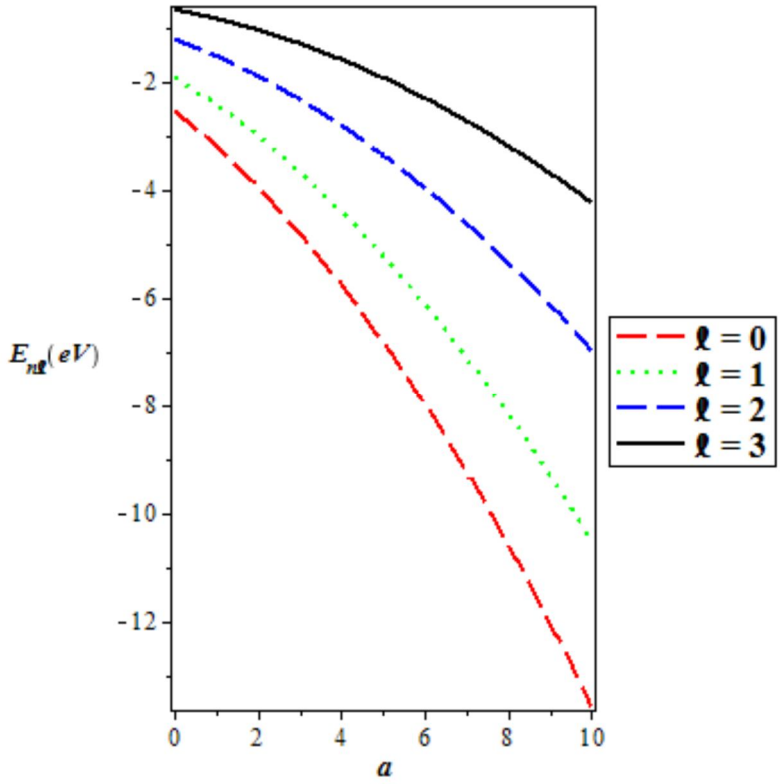

FIG. 2. Energy eigenvalues' variation with parameter a for various vibrational quantum numbers.

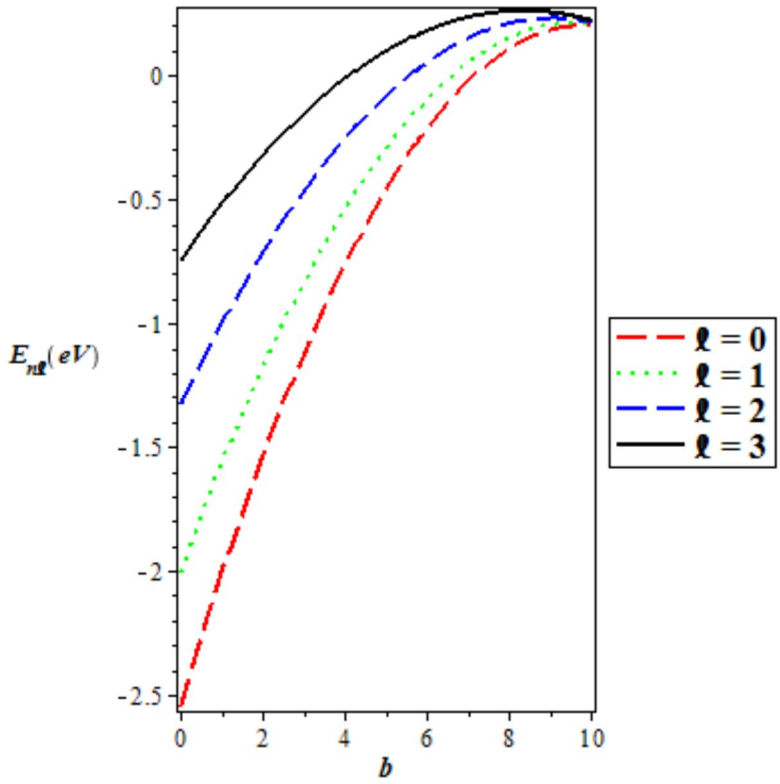

FIG. 3. Energy eigenvalues' variation with potential parameter b for various quantum numbers.

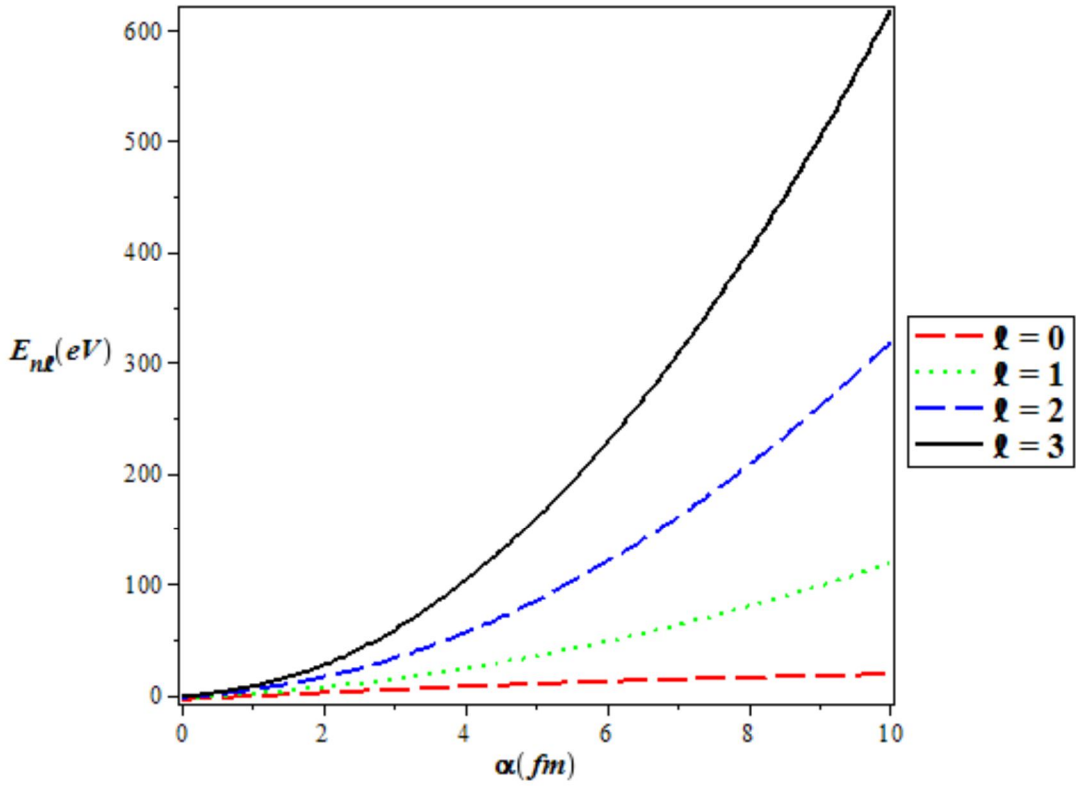

FIG. 4. Energy eigenvalues' variation with screening parameter for various vibrational quantum numbers.

4.1 Discussion of Results

The numerical values of five diatomic molecules were computed with spectroscopic parameters adopted from Oluwadare and Oyewumi (2017) [52] for energy spectra and expectation values of $\langle r^{-2}\rangle, \langle T\rangle$ and $\langle \hat{p}^2\rangle$, respectively. Equation (38) was used for energy spectra, while Eqs. (60), (69) and (70) were used for expectation values. The diatomic molecules considered in this work are H_2, HCl, TiH, I_2 and CO as presented in Tables 2-6.The constants, 1 amu = $931.494028\ \mathrm{MeV}/c^2$ and $\hbar c = 1973.29$ eVA are adopted from Ituen *et al*. [62] for the computation. Equation (38), was also used to compute for bound state of Varshni potential as presented in Table 7.

Table 1 is the spectroscopic constant used in the numerical computation of the energy spectra and expectation values. Tables 2-6 show numerical energy spectra and expectation values of $\langle r^{-2}\rangle$, $\langle T\rangle$ *and* $\langle \hat{P}^2\rangle$, respectively for the five selected diatomic molecules. The results show that the energy spectra $E_{nl}(eV)$ of these diatomic molecules increase as the principal quantum number n and orbital angular momentum quantum number l increase. The tables also show that some of the expectation values increase with an increase in quantum state, while some decrease with an increase in quantum state. For instance, it is observed that as n and l increase, the expectation values of $\langle r^{-2}\rangle$ decrease. Also, it is observed that the expectation values of $\langle T\rangle$ and $\langle \hat{P}^2\rangle$ increase as n and l increase. The bound-state energy for Varshni potential is generated with $\upsilon = \chi = -1$ and $D = 3$ for different states with three different values of the potential range. It is observed that as the potential range increases, the energy of the system increases, as shown in Table 7, which agrees with the work of Ebomwonyi *et al*. [39]. We plotted the energy eigenvalues with the potential-strength parameters and screening parameter of Varshni potential, as shown in Figs. 2-4, for various values of quantum numbers. In Fig. 2, a decrease in energy eigenvalues is noticed as n and l increase. In Fig. 3, energy eigenvalues increase as n and l increase and converge at zero. Finally, in Fig.4, the increase in energy tends to spread out from zero for different vibrational quantum numbers.

5. Conclusion

In this work, analytical solutions have been obtained of the Klein-Gordon equation for the Varshni potential with an approximation to the centrifugal term using the Nikiforov-Uvarov method. The energy eigenvalues are obtained both in relativistic and non-relativistic regimes and the corresponding normalized eigenfunctions. Energy spectra and expectation values of the square of inverse position $\langle r^{-2} \rangle$, kinetic energy $\langle T \rangle$ and square of momentum $\langle \hat{P}^2 \rangle$ for five selected diatomic molecules are computed using Hellmann-Feynman Theorem, as presented in Tables 2-6. Bound-state energy is obtained for Varshni potential, which agrees with Ebomwonyi *et al*. [39], proving the success of the formalism. The variation in the energy eigenvalues with potential parameters was also plotted and discussed.

Reference

[1] Ntibi, J.E., Inyang, E.P., Inyang, E.P., William, E.S. and Ibekwe, E.E., Jordan. J. Phys., 15 (2022) 402.

[2] Inyang, E.P., Inyang, E.P., Ntibi, J.E., Ibekwe, E.E. and William, E.S., Ind. J. Phys., 95 (2021) 2733.

[3] Inyang, E.P., William, E.S., Obu, J.O., Ita, B.I., Inyang, E.P. and Akpan, I.O., Mol. Phys., 119 (2021) e1956615.

[4] Alhaidari, A.D., J. Phys. A. Math. Gen., 34 (2001) 982.

[5] Inyang, E.P., Inyang, E.P., Akpan, I.O., Ntibi, J.E. and William, E.S., Can. J. Phys., 99 (2021) 990.

[6] Alhaidari, A.D., J. Phys. Lett. B., 309 (2011) 699.

[7] Inyang, E.P., Iwuji, P.C., Ntibi, J.E., William, E.S. and Ibanga, E.A. East Eur. J. Phys., 1 (2022) 11.

[8] Ibekwe, E.E., Emah, J.B., Inyang, E.P. and Akpan, A.O., Iran J. Sci. Technol. Trans. A Sci., 46 (2022) 1741.

[9] Inyang, E.P., William, E.S., Omugbe, E., Inyang, E.P., Ibanga, E.A., Ayedun, F., Akpan, I.O. and Ntibi, J.E., Rev. Mex. Fis., 68 (2022) 14.

[10] Inyang, E.P., William, E.S., Ntibi, J.E., Obu, J.A., Iwuji, P.C. and Inyang, E.P., Can. J. Phys., 100 (10) (2022) 463.

[11] Inyang, E.P., Iwuji, P.C., Ntibi, J.E., Omugbe, E., Ibanga, E.A. and William, E.S., East Eur. J. Phys., 2 (2022) 51.

[12] Ikot, A.N., Okorie, U.S., Amadi, P.O., Edet, C.O., Rampho, G.J. and Sever, R., Few-Body Syst., 62 (2021) 9.

[13] Inyang, E.P., Inyang, E.P., William, E.S., Ntibi, J.E. and Ibanga, E.A., Bulg. J. Phys., 20 (2022) 11.

[14] Ikhdair, S.M. and Sever, R., J. Mol. Struct.: THEOCHEM, 103 (2007) 809.

[15] Gonul, B., Koksal, K. and Bakair, E., Phys. E, 15 (2006) 279.

[16] Karakoc, M. and Boztosun, I., Int. J. Mol. Phys. E, 15 (2006) 1253.

[17] Edet, C.O., Mahmoud, S., Inyang, E.P., Ali, N., Aljunid, S.A., Endut, R., Ikot, A.N. and Asjad, M., Mathematics,. 10 (2022) 2824.

[18] Omugbe, E., Osafile, O.E., Okon, I.B., Inyang, E.P., William, E.S. and Jahanshir, A., Few-Body Syst., 63 (2022) 7.

[19] Omugbe, E., Osafile, O.E., Okon, I.B., Eyube, E.S., Inyang, E.P., Okorie U.S., Jahanshir, A. and Onate, C.A., Eur. Phys. J. D., 76:72 (2022) 11.

[20] Omugbe, E., Osafile, O.E., Inyang, E.P., and Jahanshir, A., Physica Scripta., 96 (2021) 125408.

[21] William, E.S., Okon, I.B., Ekerenam, O.O., Akpan, I.O., Ita, B.I., Inyang, E.P., Etim, I.P. and Umoh, I.F., Intl. J. Quan. Chem., (2022) e26925.

[22] Inyang, E.P. Obisung, E.O., Iwuji, P.C., Ntibi, J.E., Amajama, J. and William, E.S., J. Nig. Soc. Phys. Sci., 4 (2022) 884.

[23] Okoi, P.O., Edet, C.O., Magu, T.O. and Inyang, E.P., Jordan J. Phys., 15 (2022) 148.

[24] Inyang, E.P. and Obisung, E.O., East Eur. J. Phys., 3 (2022) 32.

[25] William, E.S., Inyang, E.P., Akpan, I.O., Obu, J.A., Nwachukwu, A.N. and Inyang, E.P., Indian J. Phys., 96 (2022) 3461.

[26] Inyang, E.P., Ayedun, F, Ibanga, E.A. et al., Results in Physics, 43 (2022) 106075.

[27] Inyang, E.P., Ikot, A.N., Inyang, E.P., Akpan, I.O., Ntibi, J.E., Omugbe, E. and William, E.S., Result in Physics, 39 (2022) 105754.

[28] Inyang, E.P., Obisung, E.O., William, E.S. and Okon, I.B., East Eur. J. Phys., 3 (2022) 114.

[29] William, E.S., Inyang, E.P., Ntibi, J.E., Obu, J.A. and Inyang, E.P., Jordan J. Phys., 15 (2022) 193.

[30] Ayedun, F., Inyang, E.P., Ibanga, E.A. and Lawal, K.M., East Eur. J. Phys., 4 (2022) 98.

[31] Abu-Shady, M. and Inyang, E.P., East Eur. J. Phys., 4 (2022) 87.

[32] William, E.S., Inyang, E.P. and Thompson, E.A., Rev. Mex. Fisi., 66 (2020) 730.

[33] Inyang, E.P., William, E.S. and Obu, J.A., Rev. Mex. Fis., 67 (2) (2021) 193.

[34] Inyang, E.P., Ita, B.I. and Inyang, E.P., Eur. J. appl. Phys., 3 (3) (2021) 47.

[35] Inyang, E.P., Ntibi, J.E., Inyang, E.P., Ayedun, F., Ibanga, E.A., Ibekwe, E.E. and William, E.S., Applied Journal of Physical Science, 3 (3) (2021) 108.

[36] Rampho, G.J., Ikot, A.N., Edet, C.O. and Okorie, U.S., Mol. Phys. J. D, 17 (2020).

[37] Akpan, I.O., Inyang, E.P., Inyang, E.P. and William, E.S., Rev. Mexi. Fisi., 67 (3) (2021) 490.

[38] Inyang, E.P., Inyang, E.P., William, E.S. and Ibekwe, E.E., Jordan J. Phys., 14 (4) (2021) 337.

[39] Ebomwonyi, O., Onate, C.A. and Odeyemi, O.E., J. Appl. Sci. Envr. Manag., 23 (2019) 327.

[40] Ibekwe, E.E., Okorie, U.S., Emah, J.B., Inyang, E.P. and Ekong, S.A., Eur. Phys. J. Plus, 87 (2021) 136.

[41] Inyang, E.P., Inyang, E.P., Ntibi, J.E. and William, E.S., Bull. Pure Appl. Sci., 40 (D) (2021) 24.

[42] Inyang, E.P., Inyang, E.P., Akpan, I.O. and William, E.S., Euro. J. Physics, 2 (2020) 26.

[43] Inyang, E.P., Inyang, E.P., Kamiliyus, J., Ntibi, J.E. and William, E.S., Eur. J. Physics, 3 (2) (2021) 55.

[44] Min-Cang, Z., Chin. Phys. Lett., 30 (2013) 1103.

[45] Arda, A. and Sever, R., J. Math. Chem., 50 (2012) 1930.

[46] Edet, C.O., Okoi, P.O., Yusuf, P.O., Ushie, P.O. and Amadi, P.O., Ind. J. Phys., 10 (2019).

[47] Varshni, Y.P., Rev. Mod. Phys., 29 (1957) 682.

[48] Seto, J.Y. and Roy, J.L., J. Chem. Phys., 113 (2000) 3067.

[49] Flugge, S., "Practical Quantum Mechanics", Vol. 1, (Springer, Berlin, Germany, 1994).

[50] Dong, S.H., Lemus, R. and Frank, A., Int. J. Quan. Chem., 86 (2002) 439.

[51] Morse, P.M., Phys. Rev., 34 (1929) 64.

[52] Oluwadare, O.J. and Oyewumi, K.J., Eur. Phys., 53 (2017) 6.

[53] Lim, T.C., J. Serb. Chem. Soc., 74 (2009) 1423.

[54] Greene, R.L. and Aldrich, C., Phys. Rev. A, 14 (1976) 2363.

[55] Nikiforov, A.F. and Uvarov, V.B., "Mathmatical Physics", (ed.) A. Jaffe, (Germany: Birkhauser Verlag Basel, 1988) 317.

[56] Ntibi, J.E., Inyang, E.P., Inyang, E.P. and William, E.S., Intl J. Inno. Sci. Engr. & Tech., 7 (2020) 2379.

[57] Inyang, E.P., Ntibi, J.E,. Ibanga, E.A., Ayedun, F., Inyang, E.P., Ibekwe, E.E., William, E.S. and Akpan, I.O., Commun. in Phys. Sci., 7 (2021) 114.

[58] Greiner, W., "Relativistic Quantum Mechanics", (Springer, Berlin, 2000).

[59] Onate, C.A. and Ojonubah, J.O., Int. J. Mod. Phys. E, 24 (2015) 1550.

[60] Hamzavi, M., Movahedi, M., Thylwe, K.E. and Rajabi, A.A., Chin. Phys. Lett., 29 (2012) 1938.

[61] Esteve, J.G., Falceto, F. and Garacia, C., Phys. Lett., 6 (2010) 822.

[62] Ituen, B.O., Oyebola, P. and Cecillia, N.I., Adv. Ener. Phys., 45 (2017) 582.

Volume 15, Number 5, 2022. pp. 511-517

Jordan Journal of Physics

ARTICLE

Vacuum and Solvent Dynamics of a Cyanobiphenyl Molecule: Mesophase Estimation from Thermodynamic View

P. Lakshmi Praveen

Department of Physics, Veer Surendra Sai University of Technology, Burla-768018, Sambalpur, Odisha, India..

Doi: **https://doi.org/10.47011/15.5.8**

Received on: 17/03/2021; *Accepted on: 20/05/2021*

Abstract: Thermodynamic view has been presented to analyze the vacuum, solvent dynamics and mesophase behaviour of a cyanobiphenyl compound named *p-n*-butyl cyanobiphenyl (4CB). The different modes of interaction energy values under vacuum in a dielectric medium (benzene) during translation and rotation have been calculated. The corresponding Helmholtz free energy and entropy have been analyzed at room temperature (300K) and transition temperature (389.5K) and the stability of the molecule at definite translation, rotation and temperature has been concluded. The change of thermodynamic characteristics and compound stability at nematic-isotropic temperature has been observed. The observed results have been analyzed to obtain an insight into the process of mesophase formation. This study may guide in establishing the other molecular models with transition temperature nearer to room temperature.

Keywords: Liquid crystal, 4CB, Mesophase, Free energy, Entropy.

Introduction

The transition from an ordered crystal to the disordered liquid usually happens *via* mesophases in several organic compounds that are labelled as liquid crystalline (LC) phases [1]. In these phases, the crystalline order is lost partially and some degree of flexibility exists between the molecules. The research studies for the structure-phase correlation at molecular level are the progressing quest of LC science [2, 3]. The interplay among molecular interactions and motions is decisive for phase organization [4, 5]. The molecular motions directly impact the configurational entropy of a compound through which the free energy is controlled that governs the stability of a given phase. Generally, phase transition occurs with a subtle variation of molecular electronic energy that is sufficiently larger than the intermolecular potential energy at intramolecular level. This causes an unchanged molecular structure in spite of phase transitions.

Variation of intermolecular interaction energy that relies on the structure of the compounds has a firm dependence on anisotropy of properties [6-8]. This understanding arises from the tricky play between energy estimations, positional and orientational distributions which induce entropy data. The significance of intermolecular interactions in liquid-crystal compounds has involved many reports using the Rayleigh-Schrödinger perturbation method [9-14]. These studies are mainly focused on the establishment of anisotropic potential of the molecular pair and attempt to obtain the configuration with minimum energy. Further, the interaction energies of numerous configurations in different interaction modes indicate the inclination of a configuration over the other. In general, this data does not disclose the definite relative flexibility to explain the existence of mesostate. Further, multipole interactions show enough variations among the configurational energies, which

Corresponding Author: P. Lakshmi Praveen **Email**: plpraveen_phy@vssut.ac.in

ultimately have an impact on thermodynamic parameters. Therefore, these relative energy values have been chosen as input to compute the thermodynamic parameters to explicate the stability of 4CB mesophase.

In the present work, an attempt has been made to explain the phase stability of 4CB from a thermodynamic view. The relative energies of 4CB molecular pair in benzene have been computed using the below methodology and compared with values of vacuum [15]. The pair interaction energy computations of 4CB have been performed at a stacking intermediate distance of 10Å and an in-plane intermediate distance of 8Å. These intermolecular distances have been chosen so as to permit molecular freedom during translation and rotation relative to each other. The literature data shows the nematic-isotropic temperature of 4CB at 389.5K [16].

Methodology

The structure of 4CB molecule has been figured using published crystallographic data [16]. The atomic net charges and dipole moments are necessary for the calculation of the interaction energy of molecular pair. For this calculation, the CNDO/2 approach has been implemented [17]. The comprehensive computational methodology using the formula proposed by Claverie has been utilized to estimate the pair interaction energy of a molecular configuration [18]. In accordance with the second order of the perturbation theory, the pair interaction total energy of molecules (U_{pair}) for intermediate range interactions is expressed as [19]:

$$U_{pair} = U_{el} + U_{pol} + U_{disp} + U_{rep} \quad (1)$$

where U_{el} is electrostatic, U_{pol} is polarization, U_{disp} is dispersion and U_{rep} is repulsion energy terms. The electrostatic term is:

$$U_{el} = U_{QQ} + U_{QMI} + U_{MIMI} + \ldots \quad (2)$$

where U_{QQ} is monopole-monopole, U_{QMI} is monopole-dipole and U_{MIMI} is dipole-dipole terms, respectively. The evaluation of electrostatic term has been limited up to the dipole-dipole energy term as the calculation provides satisfactory results [19]. The detailed methodology finally gave the expression [19, 20]:

$$U_{disp} + U_{rep} = \sum_{\lambda}^{(1)} \sum_{\nu}^{(2)} U(\lambda, \nu) \quad (3)$$

$$U(\lambda, \nu) = K_\lambda K_\nu (-A/Z^6 + B e^{-\gamma Z}) \quad (4)$$

where $Z = R_{\lambda\nu} / R^0_{\lambda\nu}$; $R^0_{\lambda\nu} = [(2R^w_\lambda)(2R^w_\nu)]^{1/2}$, R^w_λ and R^w_ν are the van der Waals radii of λ and ν atoms, respectively. A, B and γ parameters do not depend on particular species. But $R^0_{\lambda\nu}$ and $K_\lambda K_\nu$ factor that establish the energy minimum have various values according to the atomic species involved. The essential formulae and the orthogonal coordinate system details may be found elsewhere [20]. The total interaction energy data attained *via* these estimations has been utilized as input for the calculation of the thermodynamic parameters, as given below [21]:

$$A = -kT \ln \Sigma_i \exp(-\beta\varepsilon_i) \quad (5)$$

$$S = k \ln \Sigma_i \exp(-\beta\varepsilon_i) + (U/T) \quad (6)$$

$$U = \Sigma_i \varepsilon_i \exp(-\beta\varepsilon_i) / \Sigma_i \exp(-\beta\varepsilon_i) \quad (7)$$

where A represents the Helmholtz free energy, U represents the internal energy and S represents the entropy. $\beta = 1/kT$, k represents the Boltzmann constant. T represents the absolute temperature and ε_i is the energy of the configuration i to the minimum energy value.

Results and Discussion

The structure of 4CB compound is presented in Fig. 1. The interaction energy calculations in vacuum and in dielectric medium (benzene) during the various modes of interactions are given below to analyze the physical and mesophase behaviour of the molecule.

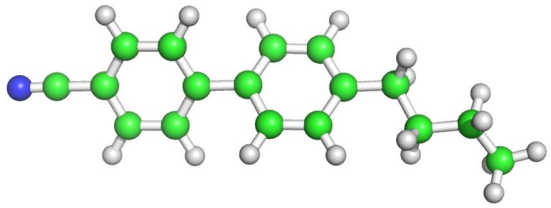

FIG. 1. Structure of 4CB molecule.

Stacking Interactions

In this mode, one molecule has been arranged in the x-y plane in a molecular pair. The x-axis is chosen along a bond that is parallel with respect to the long molecular axis. The second molecule has been considered along z-axis with a distance of 10Å from the fixed molecule. For x (0^0) y (0^0) configuration, rotational operation about the z-

axis have been performed in 10^0 intervals, to calculate the interaction energies (Fig. 2). It has been understood that the dispersion forces are the factor for the attractive interaction between 4CB molecules. The trend of estimating the exact minimum from the total energy curve is followed, as it is similar to the Kitaygorodsky energy curve [22, 23].

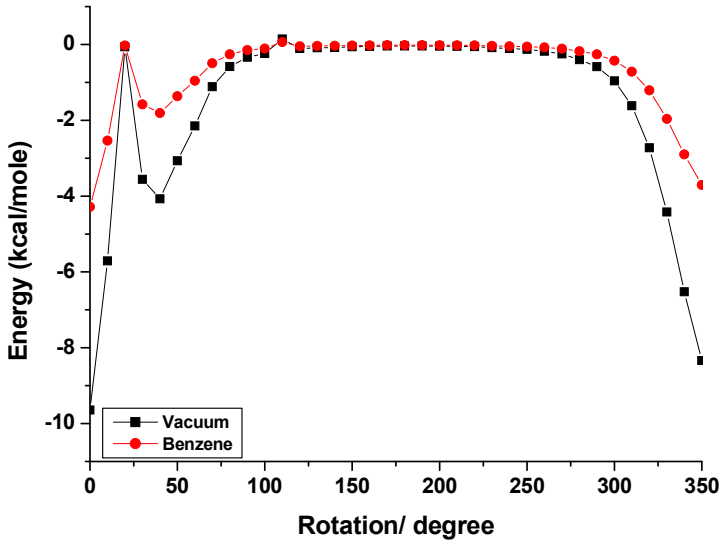

FIG. 2. Variation of total interaction energy depending on the rotation angle about z-axis.

The configuration y (θ_1^0) z (θ_2^0) means that the molecule has been rotated from its initial position by θ_1^0 about the y-axis and by θ_2^0 about the z-axis. Configurational probability has been calculated after displacing the molecule to a specified distance from the molecule initial position [24, 25]. Further, translational operations have been considered at 0.2Å interval. The variation of total interaction energy is reported in Fig. 3 for vacuum and dielectric medium. The translational study is essential as the nematic appeal of liquid crystals is understood from the translational mobility along the selected molecular axis. The pair of stacked molecules is expected to slide in a range of -0.4Å to 0.2Å for vacuum and -0.8Å to 0.4Å in dielectric medium with almost no difference in the total energy and hence, the higher region of translation has been observed in the dielectric medium for the molecules to preserve the order against the increment of thermal scale.

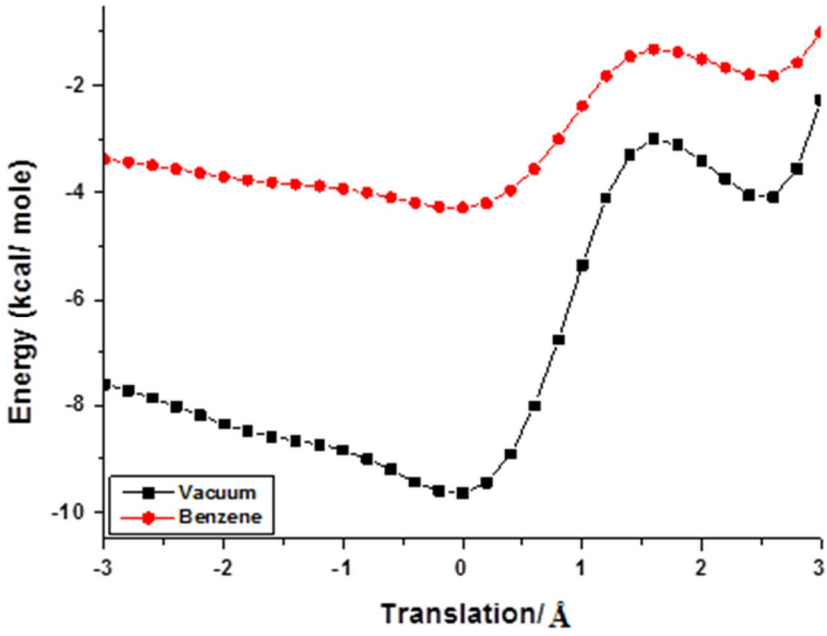

FIG. 3. Variation of total stacking interaction energy depending on the translation along x-axis.

In-plane Interactions

One molecule under interaction has been arranged at a separation of 8Å from the prefixed molecule along the y-axis to keep away from van der Waals contacts. The akin steps of computations have been repeated during in-plane mode interactions. The rotational variations about the x- and y-axes have been studied to minimize the energy during the translational and rotational motions about all (x, y and z) axes.

The interaction energy during the rotational motion about the x-axis for the configuration y (0^0) has been examined (Fig. 4). The dispersion term has been identified as the prime attractive component of interaction energy. One may observe that the apparent inclination of interaction has been exhibited although the energy difference at different rotations is quite lower. Therefore, in this configuration, the molecules in general may exhibit rotational flexibility freely with the exception of lower scale of temperature, when the pair of molecules desires to exist in one molecular plane. Further, the translational effect along the x-axis for the y (0^0) configuration is given in Fig. 5. The translational flexibility of molecules has been noticed to be greater in the in-plane mode in comparison with the stacking mode. The net interaction energy is observed to be nearly the same in the energy region of -2.6Å to -2Å in vacuum and -2.8Å to -1.8Å in benzene. These regions may be understood as favourable regions for exhibiting the fluidity property of the molecule by preserving the mesophase orientation. Further, the lengthy energy region of similarity has been found in the dielectric medium. The standard procedure for obtaining the minimum energy configurations has been followed [26-30].

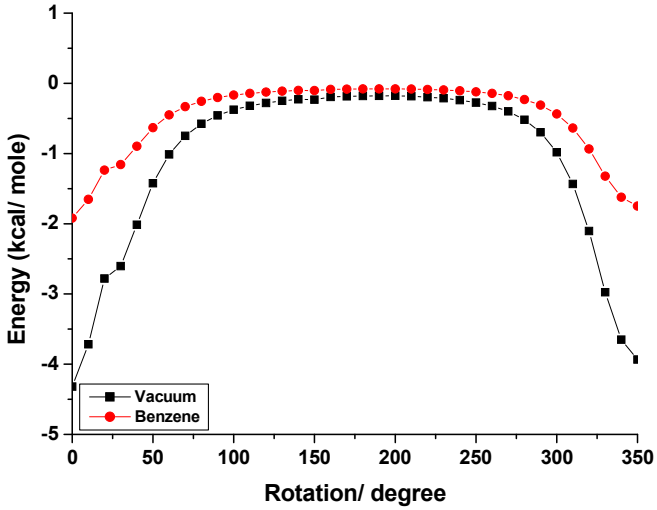

FIG. 4. Variation of total in-plane interaction energy depending on the rotation angle about the x-axis.

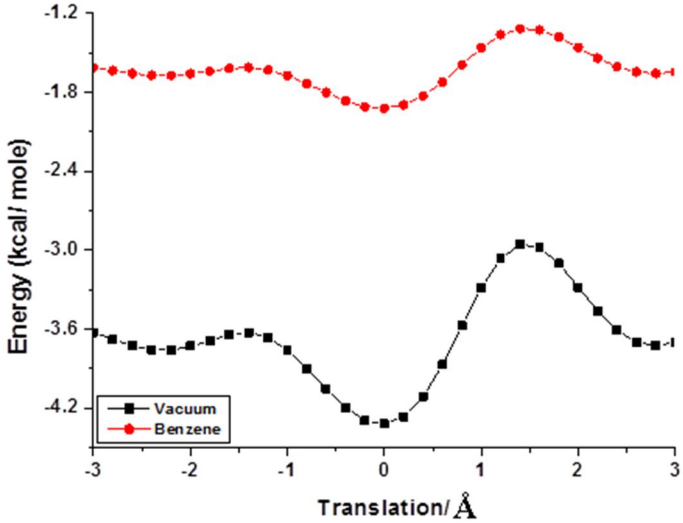

FIG. 5. Variation of total in-plane interaction energy depending on the translation along the x-axis.

Terminal Interactions

A separating distance of 22Å has been selected between a pair of molecules away from the van der Waals contacts to explore the terminal mode interactions. The free molecule in the pair has been allowed for rotational motion about the x- and y-axes. The x-axis rotations exhibit no angular preference, which means that these molecules are totally flexible for rotational motion about their long-molecular axis. This indicates that these interactions are enough feebler compared to the above two modes of interactions.

Vacuum and Solvent Dynamics

These calculations may plausibly be linked to the mesophase behaviour of the compound. Upon heating the 4CB crystals, the thermal vibrations perturb the ordering of closely packed molecules. Hence, the molecular attractive interaction in a pair becomes weaker with increment in temperature. This enhances the opportunity of relative molecular motion along the molecular long axis. From the above analysis, it may be understood that the stacked molecular flexibility to glide with respect to the axis normal to the elongated molecular axis (y-axis) is controlled. Further, the terminal mode data is trivial. These calculations support nematic behaviour. However, to explore the nematic behavior, the following thermodynamic analysis has been reported.

Helmholtz Free Energy

The Helmholtz free energy estimation offers a better consideration of phase ordering and molecular-level stability. A relative analysis of Helmholtz free energy during translational motion along x-axis in stacking, in-plane mode interactions of 4CB molecule at room temperature (300K) and transition temperature (389.5K) in vacuum and benzene is given in Table 1. Evidently, in case of vacuum, the translational free energy of 4CB in stacking mode interactions is -1.06 kcal/ mol at 300K and has been found to be diminished to -1.52 kcal/ mol at 389.5K. In this way, a difference of free energy -0.46 kcal/ mol has been observed during phase transition. The free energy of 4CB molecule in solvent (benzene) during the stacking mode interactions under translation is -1.39 kcal/mol at 300K has been found to be diminished to -1.93 kcal/mol at 389.5K. A difference of -0.54 kcal/ mol has been observed. Similarly, a difference free energy of -0.59 kcal/ mol has been observed during the in-plane mode interactions under vacuum, while a value of -0.60 kcal/ mol has been observed in solvent (benzene).

From the rotational free energy data (Table 1), one may notice a free energy difference of -0.08 kcal/ mole and -0.26 kcal/ mol in vacuum and solvent during stacking interactions. Similarly, free energy difference of -0.39 kcal/mol, and -0.55 kcal/mol has been observed in vacuum and solvent, respectively, during in-plane interactions. The negative value of free-energy increment approves the mesophase stability at transition temperature. The compared values of difference amount of free energy in stacking and in-plane mode interactions discloses that the molecules show a higher amount of in-plane mode free energy difference. Hence, the molecules have enough choice to move along-long molecular axis, which confirms the phase stability in this mode of interactions. Moreover, in the presence of dielectric medium (benzene), the higher difference of free energy from transition to room temperature discloses that the stability of meso phase is higher in solvent (benzene) compared to vacuum [31].

TABLE 1. Helmholtz free energy (*A*) corresponding to various configurations during stacking and in-plane interactions at room temperature (300K) and transition temperature (389.5K) of 4CB molecule.

Mode of Interactions	Vaccum			Benzene		
	300K	389.5K	ΔF	300K	389.5K	ΔF
Stacking	-0.07	-0.15	-0.08*	-0.28	-0.54	-0.26*
	-1.06	-1.52	-0.46**	-1.39	-1.93	-0.54**
In-plane	-0.56	-0.95	-0.39*	-1.06	-1.61	-0.55*
	-1.51	-2.10	-0.59**	-1.78	-2.38	-0.60**

*Rotation. **Translation.

Configurational Entropy

The estimated configurational entropy during translation and rotation operations during the stacking and in-plane modes of interactions for 4CB molecule is shown in Table 2. The translational entropy in stacking interactions is observed to be $5.35x10^{-3}$ kcal mol^{-1} k^{-1} at 389.5K and $5.02x10^{-3}$ kcal mol^{-1} k^{-1} at 300K. The room-temperature data reveals higher binding (less disorder) at lower temperatures. Upon increasing the temperature, these molecules attain necessary flexibility to glide along the long-molecular axis. Hence, larger entropy difference ($0.33x10^{-3}$ kcal mol^{-1} k^{-1}) from transition to room temperature has been observed. The translational entropy data during in-plane interactions for 4CB molecules is descripted in Table 2. A less entropy difference of $0.22x10^{-3}$ kcal mol^{-1} k^{-1} indicates that the molecule prefers in-plane structure which offers more translational freedom. Similar calculations in benzene during the above two modes indicate that the molecule possesses higher translational freedom. This data favours the nematic appeal of the molecule.

The translational entropy favours parallel molecular orientation as this orientation offers minimum excluded volume. Hence, the higher available enough space for the molecules causes the jostling around. Further, the parallel orientation designates a lower orientational entropy state (Table 2). The same trend has been noticed during the rotational motion for the molecule**.** However, the comparative picture of configurational entropy in both modes of interactions in vacuum and benzene indicates that the molecule exhibits lesser z-axis ordering (*i.e.*, stacking) and greater y-axis ordering (*i.e.*, in-plane) that authorizes the nematic appeal of the molecule.

TABLE 2. Entropy x 10^{-3} (*S)* of various configurations during stacking and in-plane interactions at room temperature (300K) and transition temperature (389.5K) of 4CB molecule.

Mode of Interactions	Vaccum			Benzene		
	300K	389.5K	ΔS	300K	389.5K	ΔS
Stacking	0.73	1.11	0.38*	2.41	3.45	1.04*
	5.02	5.35	0.33*	5.85	6.02	0.17**
In-plane	3.54	4.42	0.88*	5.84	6.38	0.54*
	6.40	6.62	0.22**	6.74	6.78	0.04**

*Rotation. **Translation.

Conclusions

The estimation of phase behaviour and phase stability of a nematic liquid crystal (4CB) leads to the following conclusions:

1. The negative free energy increment approves the mesophase stability at transition temperature. The compared values of difference amount of free energy in both interactions disclose that the molecules illustrate a higher amount of in-plane free energy difference. Hence, the molecules have enough choice to move along the long molecular axis, which confirms phase stability in this mode of interaction.
2. The higher free energy difference in the dielectric medium (benzene) discloses that the meso-phase stability is higher in solvent (benzene) compared to vacuum.
3. The comparative configurational entropy view in vacuum and benzene indicates that the molecule exhibits lesser z-axis ordering (*i.e.,* stacking) and greater y-axis ordering (*i.e.*, in-plane) that authorizes the nematic appeal of the molecule.

References

[1] Blinov, L.M. “Structure and Properties of Liquid Crystals”, (Springer, New York, 2011).

[2] Kundu, P., Mishra, P., Jaiswal, A. and Ram, J., J. Mol. Liq., 296 (2019) 111769.

[3] Praveen, P.L. and Ojha, D.P., J. Mol. Liq., 197 (2014) 106.

[4] Praveen, P.L. and Ojha, D.P., J. Mol. Liq., 161 (2011) 44.

[5] Goswami, D., Mandal, P.K., Gutowski, O. and Sarma, A., Liq. Cryst., 46 (2019) 2115.

[6] Patari, S., Chakraborty, S. and Nath, A., Liq. Cryst., 43 (2016) 1017.

[7] Singh, U.B., Pandey, M.B., Dhar, R., Verma, R. and Kumar, S., Liq. Cryst., 43 (2016) 1075.

[8] Nayak, S.K. and Praveen, P.L., J. Phys. Sci., 31 (2020) 33.

[9] Adams, W.H., Int. J. Quant. Chem., 25 (1991) 165.

[10] Shavitt, I., Int. J. Mol. Sci., 3 (2002) 639.

[11] Aneela, R., Praveen, P.L. and Ojha, D.P., J. Mol. Liq., 166 (2012) 70.

[12] Jose, T.J. et al., Arabaian J. Sci. Engg., 44 (2019) 6601.

[13] Praveen, P.L. and Ojha, D.P., Z. Naturforsch., 65a (2010) 555.

[14] Jose, T.J., Simi, A., Raju, M.D. and Praveen, P.L., Acta Physica Polonica A, 134 (2018) 512.

[15] Praveen, P.L., Ajeetha, N. and Ojha, D.P., Russ. J. Phys. Chem., 84 (2010) 229.

[16] Vani, G.V., Mol. Cryst. Liq. Cryst., 99 (1983) 21.

[17] Pople, J.A. and Beveridge, D.L., "Approximate Molecular Orbital Theory", (Mc-Graw Hill: New York, 1970).

[18] Claverie, P., In: Pullmann, B. (ed.) "Intermolecular Interactions: From Diatomic to Biopolymers", (John Wiley: New York, 1978), p. 69.

[19] Praveen, P.L., Mol. Cryst. Liq. Cryst., 667 (2018) 44.

[20] Das, P. and Praveen, P.L., Mol. Cryst. Liq. Cryst., 652 (2017) 185.

[21] Hirschfelder, J.O., Curtiss, C.F. and Bird, R.B., "Molecular Theory of Gases and Liquids", (John Wiley & Sons, USA, 1967).

[22] Praveen, P.L. and Ojha, D.P., Phase Trans., 86 (2013) 433.

[23] Das, P. and Praveen, P.L., J. Mol. Struct., 1233 (2021) 130137.

[24] Ramakrishna, D.S. et al., J. Mol. Struct., 1236 (2021) 130336.

[25] Sahoo, R.R. et al., J. Physical Sci., 32 (2021) 27.

[26] Praveen, P.L. et al., Mol. Cryst. Liq. Cryst., 548 (2011) 61.

[27] Aneela, R. et al., Mol. Cryst. Liq. Cryst., 557 (2012) 90.

[28] Das, P. et al., J. Mol. Liq., 288 (2019) 111029.

[29] Praveen, P.L. et al., Mat. Chem. Phys., 126 (2011) 248.

[30] Praveen, P.L. and Ojha, D.P., Z. Naturforsch., 67a (2012) 210.

[31] Ramakrishna, D.S. et al., Mol. Cryst. Liq. Cryst., 643 (2017) 76.

Volume 15, Number 5, 2022. pp. 519-526

Jordan Journal of Physics

ARTICLE

Physico-chemical Properties, Heavy-metal Contents and Radioactivity Levels in Soils around a Cement-production Facility in Ogun State, Nigeria

O. I. Adekoya[a], **O. E. Popoola**[b] and **S. A. Olaleru**[a]

[a] *Physical Science Department, Yaba College of Technology, Lagos, Nigeria.*
[b] *Science Laboratory Technology Department, Yaba College of Technology, Lagos, Nigeria.*

Doi: **https://doi.org/10.47011/15.5.9**
Received on: 22/04/2021; *Accepted on: 29/06/2021*

Abstract: The physico-chemical properties, heavy metal content and the primordial radionuclide activities in soil samples from four locations around a cement production facility were studied. The physico- chemical properties of the soil samples were determined after aqua regia (HNO_3:HCl) digestion and analysis with atomic absorption spectrophotometer (AAS) Perkin Elmer Analyst 200, while the activity concentration of the radionuclides was determined by a non-destructive analysis using a computerized gamma-ray spectrometry system with high-purity germanium (HPGe). The pH and electrical conductivity in the soil were in the range of 6.57 to 7.39 and 25.5 to 462 μs cm^{-1}, respectively. The cation-exchange capacity (meq/100 g) for Na^+, K^+, Ca^{2+} and Mg^{2+} were within the ranges 0.142 to 0.622, 0.145 to 1.725, 2.112 to 4.279 and 0.092 to 0.271, respectively. Lead and cadmium were each detected in only one sample. The average activity for Uranium -238, Thorium - 232 and Potassium - 40 in soil was between 3.177 ± 0.330 Bq kg^{-1} - 7.934±1.190 Bq kg^{-1}, 4.201±0.429 Bq kg^{-1} – 10.702 ± 1.504 Bq kg^{-1} and 97.733 ± 2.268 Bq kg^{-1} – 144.926 ± 21.738 Bq kg^{-1}, respectively. The physico-chemical properties obtained were within the range of values observed by an earlier study conducted in the area; the concentrations of the heavy metals in the soils as well as the radiological hazard indices due to the presence of naturally -occuring radionuclide materials (NORMs) in the soils were very low and are not expected to constitute any environmental hazard.

Keywords: Physico-chemical properties, Radioactivity, Cement, Ewekoro, Effective dose.

1. Introduction

Environmental quality deterioration resulting from the increase in the level of potentially toxic substances is becoming more pronounced, thus raising the question on the safety status of the environment. Industrial activities rank higher among contributors to environmental degradation [1]. Non-nuclear industries, such as cement industry, use materials containing significant contents of naturally-occurring radioactive materials (NORMs), which may expose workers or the people living near such plants to radiation above the natural background. Cement manufacturing is known to emit about 500-1700 kg of particulate matter daily [2].

Studies have shown that soils within the vicinity of cement factories are seriously degraded [3, 4]. These studies reported an elevated deposit of alkali earth metals and heavy metals, such as lead, nickel, chromium, zinc, copper and phosphorus from cement dust and other particles with attendant environment risk. Cement dust is also known to consist of significant amounts of primordial radionuclides of Uranium-238, Thorium-232 and Potassium-40

Corresponding Author: O. I. Adekoya **Email**: olasojiadekoya@gmail.com

[5]. Emission of gases and dust particulates by the cement industry can thus affect human health through the release of NORMs and metals into the air, settlements and farmlands close to the plant. The metal contents in cement dust have peculiar characteristics, one of which is their non-deterioration decay with time. Some can be necessary or beneficial to plants at certain levels, but can become toxic when specific thresholds are exceeded. They often occur as cations which strongly interact with the soil matrix and consequently move into the food chains. According to United States Department of Agriculture (USDA) [6], acute poisoning from heavy metals is rare though ingestion or dermal contact is possible. Chronic problems associated with long-term heavy metal exposures are mental lapses, allergic dermatitis (lead) toxicological effect of the kidney, liver and gastro-intestinal tract (cadmium), skin poisoning and harmful effects on kidney and the central nervous system [7]. In a similar vein, long-term exposure to radionuclides through inhalation has severe health effects, such as chronic lung disease, acute leucopoenia, anaemia and necrosis of the mouth [8]. Other diseases caused by radioactivity exposure include lung cancer, pancreas, hepatic, bone, skin and kidney cancers, cataracts, sterility, atrophy of the kidney and leukaemia. Exposure to excess levels of background ionization radiation causes somatic and genetic effects that lead to critical damage of radiosensitive organs of the body, which ultimately can lead to death. [9]

The aim of this study is to examine the possible impact of cement dust on the soil's physico-chemical properties, heavy-metal contents and natural-radioactivity levels around Wapco - Lafarge Cement Facility, Ewekoro, Ogun state. The radiological health indices following the activity levels of radionuclides in the soil will also be determined to know what health risks people living or working around the cement facility may be exposed to.

2. Materials and Methods

2.1 Study Area

The study area comprises Ewekoro, Papalanto, Arigbajo and Ifo locations in Ogun state, South-west of Nigeria within latitudes 06.9355 ºN, 06.9500 ºN and longitudes 03.2167 ºE and 03.5000 ºE. The area is predominantly a tropical rain forest with average annual rainfall of over 200 cm [10]. These areas experience alternate dry and raining seasons annually with rainy season being between March and early October and dry season running from late October to late February. The vegetation has tall trees with buttress roots and evergreen leaves. The land use of this area is mainly agricultural and residential. The approximate distances (km) of the cement factory (situated at Ewekoro) from Papalanto, Arigbajo and Ifo locations are, respectively, 1.80, 6.58 and 8.84.

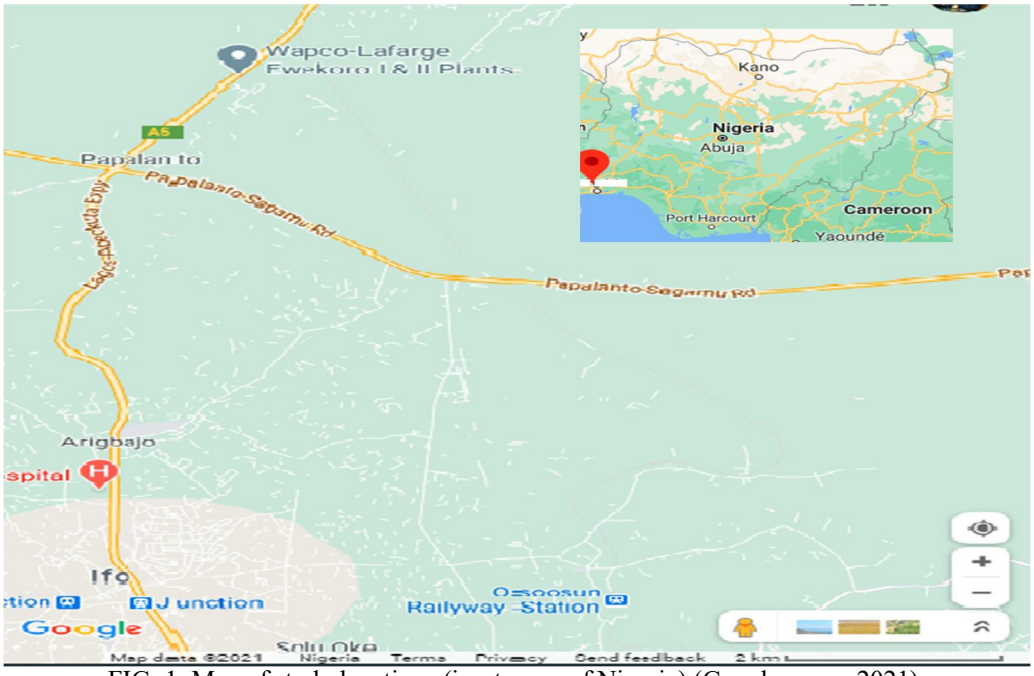

FIG. 1. Map of study locations (inset: map of Nigeria) (Google maps, 2021).

2.2 Sample Collection and Preparation

Soil samples were collected randomly from farmlands within the four locations of interest. The surface soil was taken using a clean plastic hand trowel. Composite samples of such randomly collected soil from each location were formed, from which large stones, particles of dirt or plant parts were removed. The samples were thereafter sun-dried and sieved with a 2-mm mesh to get very fine grains free of lumps. The dried fine soil particles were transferred into plastic containers, labelled and conveyed to the laboratory for analysis.

One part of the prepared soil samples was set aside for gamma analysis, while the other was set apart for physico-chemical and heavy-metal analyses. The samples meant for gamma analysis were stored in weighed Marinelli containers, sealed and afterwards allowed to stand for about four weeks prior to measurement to ensure that secular equilibrium is established between long-lived parent and their short-lived daughter radionuclides.

2.3 Sample Analysis

2.3.1 Determination of the Physico-chemical Properties of Soil and Heavy-metal Analysis

The pH value was determined using a pH meter as described by Jackson and Barak [11]. For this, 5 g of sieved soil sample was mixed with 10 ml distilled water in 1:2 ratio. The suspension was stirred intermittently with a glass rod for 30 minutes and was left for one hour. The combined electrode was inserted into the supernatant and the pH was recorded. The Electrical Conductivity (EC) was determined with a digital electrical-conductivity meter for which 5 g of sieved sample was weighed and mixed with 20 ml of distilled water (1:4) and stirred intermittently with a glass rod for 30 minutes. Thereafter, it was allowed to settle down and then the conductivity probe was inserted into the solution to take the reading.

For heavy-metal analysis, about 5 g of soil sample was weighed into a clean porcelain crucible and heated over a hot plate. The residue was then heated in a muffle furnace at 550 ^{o}C until the carbon content (organic matter) was carefully and completely oxidized (about 1 hour). The residue left was dissolved in a few drops of aqua regia (3 parts concentrated HCl + 1 part concentrated HNO_3) and then diluted with distilled water. The solution was then filtered, rinsed very well and the filtrate made up to 100 ml in a standard volumetric flask. The resulting solution from digestion was then aspirated into the flame of the atomic absorption spectrophotometer (AAS), Perkin Elmer Analyst 200, using air acetylene flame for the metal analysis against standard metal solutions. Each metal was determined using a specific hollow cathode lamp at a specific wavelength. Total metal concentrations of heavy metals, such as Co, Cu, Cd, Pb and Zn, were determined.

The same procedure used in detecting the heavy metals was employed for determining the cation-exchange capacity (CEC).

2.3.2 Determination of Activity Concentrations

The measurements to determine the activity in the samples were carried out at the Ghana Atomic Energy Commission, Accra. The activity in the soil samples was determined by a non-destructive analysis using a computerized gamma-ray spectrometry system with high-purity germanium (HPGe). The relative efficiency of the detector system was 25%, with a resolution of 1.8 keV at 1.33 MeV of ^{60}Co. The gamma spectrometer is coupled to conventional electronics connected to a multichannel analyzer card (MCA) installed in a desk-top computer. A software program called MAESTRO- 32 was used to accumulate and analyze the data manually using a spread sheet (Microsoft Excel) to calculate the natural-radioactivity concentrations in the samples. The detector is located inside a cylindrical lead shield of 5 cm thickness with an internal diameter of 24 cm and a height of 60 cm. The lead shield is lined with various layers of copper, cadmium and plexiglas, each 3 mm thick.

A counting time of 36,000 seconds (10 hrs) was used to acquire spectral data for each sample**.** The activity concentrations of the U-238 series were determined using γ-ray emissions of ^{214}Pb at 351.9 keV (35.8%) and ^{214}Bi at 609.3 keV (44.8%) for Ra -226, and for the Th-232 series, the emissions of ^{228}Ac at 911 keV (26.6%), ^{212}Pb at 238.6 keV (43.3%) and ^{208}Th at 583 keV (30.1%) were used. The K-40 activity concentration was determined directly from its emission line at 1460.8 keV (10.7%).

2.3.2.1 Calibration of Gamma Spectrometry System

Prior to the measurements, the detector and measuring assembly were calibrated for energy and efficiency to enable both qualitative and quantitative analysis of the samples to be performed. The energy and efficiency calibrations were performed using mixed radionuclide calibration standard homogenously distributed in the form of solid water, serial number NW 146 with approximate volume 1000 mL and density 1.0 g cm^{-3} in a 1.0 L Marinelli beaker. The standard was supplied by DeutscherKalibrierdienst (DKD-3), QSA Global GmBH, Germany and contains radionuclides with known energies (^{241}Am (59.54 keV), ^{109}Cd (88.03 keV), ^{57}Co (122.06 keV), ^{139}Ce (165.86 keV), ^{203}Hg (279.20 keV), ^{113}Sn (391.69 keV), ^{85}Sr (514.01 keV), ^{137}Cs (661.66 keV), ^{60}Co (1173.2 keV and 1332.5 keV) and ^{88}Y (898.04 keV and 1836.1 keV) and a 1000-ml Marinelli beaker was used.

2.3.2.2 Calculation of Radionuclide Activity

The specific activity, C_i of U-238, Th-232 and K-40 for the soil samples was determined using the following expression [12]:

$$C_i(Bq\ kg^{-1}) = KC_n \quad (1)$$

where $K = \frac{1}{\varepsilon P_\gamma M_s}$, C is the activity concentration of the radionuclide in the sample, C_n is the count rate under the corresponding peak, ε is the detector efficiency at the specific γ-ray energy, P_γ is the absolute transition probability of the specific γ-ray and M_s is the mass of the sample (kg).

The minimum detectable activity (MDA) of the γ-ray measurements was calculated according to the formula:

$$MDA = \frac{\sigma\sqrt{B}}{\varepsilon PTW}\ (Bq\ kg^{-1}) \quad (2)$$

where σ is the statistical coverage factor equal to 1.645 at a confidence level 95%, B is the background counts for the region of interest of a certain radionuclide, T is the counting time in seconds, P is the gamma yield for any particular element, W is the weight of the empty Marinelli beaker and ε is the efficiency of the detector.

The minimum detectable activity (MDA) derived from background measurements was approximately 0.11 Bq kg^{-1} for ^{238}U, 0.10 Bq kg^{-1} for ^{232}Th and 0.15 Bq kg^{-1} for ^{40}K. Concentration values below these detection limits have been taken in this work to be below the minimum detection limit (MDL).

2.3.3 Estimation of Radiological Health Risks

Workers at the cement factory as well as dwellers in the vicinity of Wapco Lafarge Cement Factory are at risk through the exposure to radioactive materials *via* inhalation of dust particles. The radiological health risks to these categories of people were estimated using some radiological parameters. These include absorbed dose rate, annual outdoor effective dose, excess lifetime cancer risk, external hazard, radium equivalent, gamma index and annual gonadal equivalent dose.

The absorbed dose rate in air (nGy hr^{-1}) at 1m above the ground surface due to the activity concentrations of U-238, Th-232 and K-40 was calculated using Eq. 3 [13]:

$$\text{D (nGy hr}^{-1}) = \sum(DCF_i * C_i) \quad (3)$$

where C_i is the concentration of the radionuclide of interest and DCF_i is the corresponding dose conversion factor for the radionuclide. The dose conversion factors of 0.462, 0.604 and 0.042 were respectively used for Uranium-238, Thorium -232 and Potassium -40.

The annual outdoor effective dose D_{out}, was determined (Eq. 4) using a conversion coefficient of 0.7 Sv/Gy for an absorbed dose in air to effective dose in the human body.

$$D_{out}\ (\text{mSv yr}^{-1}) = \text{D (nGy hr}^{-1}) \times 24 \text{ hours} \times 365.25 \text{ days} \times 0.2 \times 0.7 \text{ Sv Gy}^{-1} \times 10^{-6} \quad (4)$$

where 0.2 represents the outdoor occupancy factor (assuming people spend about 20% of their time outdoors) [13].

The excess lifetime cancer risk, ELCR, was estimated with the aim of evaluating the chances of developing cancer by humans working and living around the cement factory. The ELCR is estimated using Eq. 5:

$$ELCR = D_{Outdoor} \times DL \times RF \quad (5)$$

where DL is the duration of lifetime, which is assumed to be 70 years; RF is the risk factor, which is given as 0.05 Sv^{-1} [14].

The external hazard index, H_{ex}, is estimated from Eq. 6. The implication of equation 6 is that the activity concentrations of U-238, Th-232 and K-40 are assumed to possess the same γ-radiation dose of 370, 259 and 4810 Bq kg^{-1} of

uranium, thorium and potassium, respectively [15].

$$H_{ex} = \frac{C_U}{370} + \frac{C_{Th}}{259} + \frac{C_K}{4810} \leq 1 \quad (6)$$

where C_U, C_{Th} and C_K are the activities of uranium, thorium and potassium, respectively.

The radium equivalent activity, Ra_{eq}, is a widely used radiation hazard index to estimate the suitability of any material to be utilized as a component of building construction. It is calculated based on the same assumption as that used in determining the external hazard index, H_{ex} [16]:

$$Ra_{eq}\ (Bq\ Kg^{-1}) = C_U + (\frac{C_{Th}}{0.699}) + (\frac{C_K}{12.99}) \leq 370\ . \quad (7)$$

The gamma index, I_γ, is one of the radiological indices used to assess human safety when exposed to γ-radiation [13]. It is estimated based on Eq. 8.

$$I_\gamma = (\frac{C_U}{150}) + (\frac{C_{Th}}{100}) + (\frac{C_K}{1500}) \leq 1\ . \quad (8)$$

It is essential to estimate the annual gonadal equivalent dose (AGED), because it is the parameter that predicts whether the gonad, bone cells and marrow of humans are safe after exposure to γ-radiation or not [16]. The AGED as a result of contributions from the activity concentrations of uranium, thorium and potassium was determined using Eq. 9 [17].

$$AGED\ (\mu Sv\ y^{-1}) = (C_U \times 3.09) + (C_{Th} \times 4.18) + (C_K \times 0.314) \quad (9)$$

3. Result and Discussion

The pH, electrical conductivity (EC) (µs/cm) and the cation-exchange capacity (CEC) (meq/100 g) values are shown in Table 1.

3.1 Physico-chemical Properties

TABLE 1. Physico-chemical properties of soil samples.

Location	pH	EC(µs/cm)	CEC (meq/100 g)			
			Na^+	K^+	Ca^{2+}	Mg^{2+}
Ewekoro	7.39	155.9	0.394	0.571	3.181	0.092
Papalanto	6.95	462.0	0.812	0.522	3.055	0.271
Arigbajo	6.71	91.9	0.622	0.145	4.279	0.133
Ifo	6.57	25.5	0.142	1.725	2.112	0.109

Table 1 shows the pH, EC and CEC values of soil samples from Ewekoro and its environs. The pH depicts the level of acidity or basicity of the soil samples and the values ranged from 6.57-7.39, which indicates that the soil samples are near neutral. The slightly alkaline nature in soil samples at Ewekoro could be a result of heavy cement dust (the major constituent of which is lime) deposit and percolation of the soil in the area. Comparatively, the cement-dust dispersal and deposition are greater at Ewekoro, where the cement facility is sited, than at the other locations.

The EC values (µs/cm) ranged from 25.5 in the Ifo samples to 462 in the Papalanto samples. Table 1 also shows that there is a correlation between pH and EC; the EC increased proportionally with the pH. According to Fullen *et al.* [18], the implication is that there are reasonable or significant presences of ions in the soil. However, the values are almost insignificant and this can be attributed to low formation of some soluble and ionizable inorganic salts in the soils.

The cation-exchange capacity (CEC) shows that Na^+ ranged from 0.142 to 0.812 (meq/100 g). The soil samples from Papalanto have the highest exchangeable Na^+, while the samples from Ifo have the lowest. K^+ in the soil samples ranged from 0.145 in Arigbajo to 1.725 (meq/100 g) in Ifo soil. Ca^+ was observed highest in Arigbajo samples (4.279 meq/100 g) and lowest in Ifo samples (2.112 meq/100 g). Mg^+ increased from 0.092 in Ewekoro samples to 0.271 (meq/100 g) in Papalanto soil. The results of the CEC shows that there is no regular pattern of increase or decrease in the samples. The values of the physico-chemical properties fall within the range of values obtained by [19] in the same Ewekoro area. Noting that CEC determines the ability of soils to exchange cations, the Arigbajo samples have the lowest exchangeable cations.

3.2 Heavy-metal Analysis

The concentrations of heavy metals (mg kg^{-1}) in the soil samples are shown in Table 2.

TABLE 2. The concentrations of heavy metals (mg kg^{-1}) in soil samples.

Location	Cu	Pb	Cd	Cr	Ni	Zn	Mn
Ewekoro	0.316	ND	0.004	0.006	0.016	2.012	0.098
Papalanto	0.018	ND	ND	0.007	0.004	0.304	0.094
Arigbajo	0.016	ND	ND	0.012	0.004	1.201	0.051
Ifo	0.214	0.182	ND	0.009	0.012	0.292	0.029

ND – Not detected.

The results of the heavy-metal analysis are presented in Table 2. The results reveal that the metals were in low concentrations in the soil samples. However, Zn was observed to be higher than the other elements in all the samples. Pb and Cd were not detected in most of the samples. Pb was only found in Ifo samples, while Cd was found in Ewekoro samples. The low levels of these metals could be a result of non-presence of materials containing these metals, such as batteries, discarded metal rails, machinery parts and wastes from welding works and spray paintings [20]. Some of these heavy metals are of economic importance to land animals. For instance, Mn in trace amounts is essential to both man and animals. Higher concentration of manganese however results in kidney failure, liver and pancreas malfunctioning, but its optimum concentration is very essential for respiratory enzymes and connective tissues' development.

3.3 Activity Concentrations in Soil

The activity concentrations of the K-40, U-238 and Th-232 in the soil samples collected from the area of study are presented in Table 3.

TABLE 3. Mean activity (Bq kg^{-1}) of primordial radionuclides in soil samples.

Location	U-238	Th-232	K-40
Ewekoro	7.934±1.190	10.702±1.504	144.926±21.738
Papalanto	6.457±0.443	8.301±0.605	97.733±2.268
Arigbajo	3.946±0.603	8.347±0.531	132.421±19.863
Ifo	3.177±0.330	4.201±0.429	128.607±2.129

The mean activity (Bq kg^{-1}) ranged between 3.177 ± 0.330 -7.934 ± 1.190, 4.201 ± 0.429 - 10.702 ± 1.504 and 97.733 ± 2.268 -144.926 ± 21.738, respectively for U-238, Th-232 and K-40. Uranium -238 recorded the lowest concentration in all locations, whereas K-40 has the highest concentration. The highest activity recorded for K-40 could be as a result of the abundance of K-40 in the earth crust in addition to possible use of NPK fertilizer by farmers in the area to improve the crop yield in the soil [21].

Generally, the activity of radionuclides decreased with increasing the distance from the cement factory, as seen in Fig. 2, thus suggesting that greater deposition of cement dust occurred in the immediate environment of the cement factory than at an appreciable distance away from it.

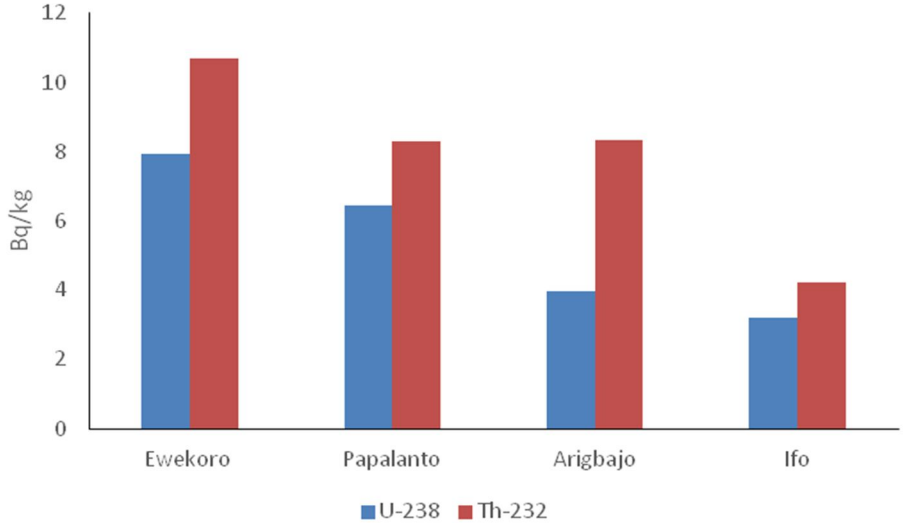

FIG. 2. Concentrations of radionuclides in soil in the locations (K-40 excluded).

The activities of U-238 and Th-232 in soils in this study compare favourably to those measured around Ewekoro by [22]. There was however a wide difference in the activity of K-40 measured. It is likely that improved farming activities which involve the use of inorganic fertilizers (e.g. NPK) may have contributed to the enhanced level of potassium radionuclide presence in the soil. The results of the present study are also compared to those obtained in the vicinity of cement factories in other locations within and outside Nigeria (Table 4).

TABLE 4. Comparison of the mean activity of the primordial radionuclides in soils from locations around cement factories.

Location	U-238	Th-232	K-40	References
Ewekoro, Nigeria	7.92	8.62	17.45	[22]
Ewekoro, Nigeria	7.93	10.70	144.93	This study
Port Harcourt, Nigeria	49.9	5.51	473.95	[23]
Kogi, Nigeria	28.1	31.40	257.6	[24]
Pakistan	50.7	70.2	531.7	[25]
Egypt	24.8	35.3	202.5	[26]

3.4 Radiation Hazard Indices

The results of the calculated radiation hazard indices are shown in Table 5.

The absorbed dose rate was between 9.41 - 16.22 nGy h^{-1}, which is below the world's average of 57 nGy h^{-1}. The annual effective dose was also below the world's average value and much lower than the maximum permissible limits of 1 mSv y^{-1} (public) and 20 mSv y^{-1} (occupational) and hence, may not have serious radiation health effects on communities.

TABLE 5. Radiation hazard indices in the locations.

Location	D (nGy hr-^{1})	D_{out} (mSv yr^{-1})	ELCR (x 10^{-3})	H_{ex}	Ra_{eq} (Bq kg^{-1})	I_γ	AGED (μSv yr^{-1})
Ewekoro	16.22	0.02	0.070	0.093	34.401	0.257	114.76
Papalanto	12.10	0.01	0.035	0.070	25.856	0.191	85.34
Arigbajo	12.42	0.02	0.070	0.070	26.081	0.198	88.66
Ifo	9.41	0.01	0.035	0.052	19.087	0.149	67.76
World's average [13]	57	0.07	0.29	1	370	1	300

Other radiation hazard indices computed were also below the world's average or the permissible limits and as such pose no adverse health effect to both the workers and dwellers in the vicinity of the cement factory.

4. Conclusion

The physico-chemical properties, heavy-metal concentrations and activity concentrations of soil samples from four locations situated in the vicinity of West African Portland Cement Wapco - Lafarge production facility in Ogun State were determined. The radiological hazard indices following continual exposure to the cement-contaminated soil were also estimated. The physico-chemical analysis of soil samples under study showed variable values of the parameters. The pH of the soil indicates that the soil is near neutral. The concentrations of the heavy metals were found to be low. The cation-exchange capacity indicates that calcium ions are the most exchangeable cations. The radiological hazard indices were all below the global mean values and the permissible limits. It can thus be concluded that the concentrations of heavy metals and radioactive nuclides in the area do not constitute an environmental threat. Although the environment is radiologically safe, a community-based awareness programme on the issue of environmental contamination, its health impacts and possible prevention, is still recommended.

References

[1] Prince, O.U., Ugochukwu, E. and Chibuzo, V.O., "Environmental Pollution: Causes, Effects and Remedies", (Elsevier, 2020) 419.

[2] Ogedengbe, K. and Oke, A.O., Journal of Science and Technology, 31 (2) (2011) 46.

[3] Farmer, A.M., Environ. Poll., 79 (1993) 63.

[4] Sivakumar, S. and Britto, A.J., Journal of Ecotoxicology and Environmental Monitoring, 5 (2) (1995) 147.

[5] Mujahid, S.A., Rahm, A., Hussain, S. and Farooq, M., Radiat. Prot. Dosimetry, 130 (2) (2007) 206.

[6] USDA, "Heavy-metal Soil Contamination", Soil Quality. Urban technical note, 3 (2000).

[7] Adelakan, B.A. and Abegunde, K.D., Int. J. Phys. Sci., 6 (5) (2011) 1045.

[8] FEPA, "National Interim Guidelines and Standards for Industrial Effluents, Gaseous Emissions and Hazardous Waste Management in Nigeria", (1991).

[9] Ajayi, O.S. and Ajayi, I.R., Nig. J. Phy., (11) (1999) 17.

[10] Micheal, M.C., "Essential Biology", (Tonad Publisher, 2006).

[11] Jackson, M.L., "Soil Chemical Analysis", (UW-Madison Libraries Parallel Press, 2005).

[12] Jibiri, N.N., Alausa, S.K. and Farai, I.P., Radioprotection, 44 (2) (2009) 139.

[13] UNSCEAR, "Sources and Effects of Ionizing Radiation". United Nations Scientific Committee on the Effects of Atomic Radiation, Vol. 1, (New York, United Nations Publication, 2000).

[14] Rafique, M., Saeed, U.R., Muhammad, B., Wajid, A., Iftikhar, A., Khursheed, A.L. and Khalil, A.M., J. Radiat. Res. Appl. Sci., 7 (2014) 29.

[15] Reda, E., Mohammed, A., El-Montaser, M.S. and Atef, E., J. Environ. Sci. Technol., 11 (2018) 28.

[16] Usikalu, M.R., Oderinde, A., Adagunodo, T.A. and Akinpelu, A., IJCIET, 9 (9) (2018) 10479.

[17] Avwiri, G.O., Osimobi, J.C. and Agbalagba, E.O., Comprehensive Journal of Environ. and Earth Sci., 1 (1) (2012).

[18] Fullen, M.A., Fearnebough, W., Mitchell, D.I. and Trueman, I.C., Soil Use and Management, 11 (1995) 77.

[19] Majolagbe, A.O., Kasali, A.A. and Ghaniyu, L.O., Adv. Appl. Sci. Res., 2 (1) (2011) 289.

[20] Underwood, E.J., "Trace Elements in Human and Animal Nutrition", 4th Edn., (Academic Press, New York, 1977).

[21] Jibiri, N.N. and Fasae, P.K., Radiat. Prot. Dosimetry, 148 (2011) 132.

[22] Gbadebo, A.M. and Amos, A.J., Asian J. Appl. Sci., 3 (2010) 135.

[23] Avwiri, G.O., J. Appl. Sci. Environ. Mgt., 9 (3) (2005).

[24] Isinkaye, O.M., Jibiri, N.N. and Olomide, A.A., J. Med. Phys., 40 (1) (2015) 52.

[25] Qureshi, A.A., Tariq, S., Din, K.U., Manzoor, S., Calligaris, C. and Waheed, A., J. Radiat. Res. Appl. Sci., 7 (2014) 438.

[26] Fares, S. and Hassan, A.K., Indian J. Environ. Sci., 10 (12) (2015) 441.

Volume 15, Number 5, 2022. pp. 527-536

Jordan Journal of Physics

ARTICLE

Form Factor of the Oriented Pyramidal Ice Crystals in the Wentzel-Kramers-Brillouin Approximation

El Mostafa Tari[a], **Abdelhadi Bahaoui**[a], **Redouane Lamsoudi**[a], **Mohammed Khouilid**[b] and **Mohamed Ibnchaikh**[a]

[a] *Laboratory of Theoretical Physics, Department of Physics, Faculty of Sciences, Chouaib Doukkali University, PO Box 20, 24000 El Jadida, Morocco.*

[b] *Laboratory of Measurement and Control Instrumentation, Department of Physics, Faculty of Sciences, Chouaib Doukkali University, PO Box 20, 24000 El Jadida, Morocco.*

Doi: **https://doi.org/10.47011/15.5.10**

Received on: 22/04/2021; *Accepted on: 24/06/2021*

Abstract: In this work, the Wentzel-Kramers-Brillouin (WKB) approximation is applied to determine an analytical expression of the form factor of oriented pyramidal ice crystals. This study will focus on two special cases of the normal incident of light: flat incidence and edge-on incidence. This form factor is calculated using an adequate decomposition of the pyramid. Furthermore, the analytical expression of the extinction coefficient is derived for these two special cases. Finally, some numerical examples are analyzed to illustrate our results.

Keywords: Light scattering, Form factor, Wentzel-Kramers-Brillouin approximation, Pyramidal ice crystals, Extinction efficiency.

PACS: 41.20.-q; 41.85.-p.

1. Introduction

Light is one of the main messages used by humans to gather information about their environment after having interacted with an object. The light bears an imprint of this interaction that can be decoded to deduce certain properties of the object. The reading of this information can be done in the most classical way thanks to the eye which allows us to characterize the intensity, the direction or the average spectral distribution of the light. The information conveyed by the light is however still much richer than what the eye can decode; the polarization, the phase and the spectrum are magnitudes which are not measured by the eye and which are also rich in information.

The study of the scattering and absorption of light by small particles is of great interest in various scientific disciplines and many applications, such as medical technology, geophysics, metrology and radio astronomy [1-6]. In particular, in the field of photovoltaic energy conversion, this study is used to quantify the part of light converted into electrical energy [7-9]. Nevertheless, the investigation of the scattering of light by small particles continues to surprise us with new discoveries and exciting theoretical and experimental developments, such as optical trapping, abnormal light scattering and optical tweezers [10].

On another side, several studies carried out on the direct and indirect observation of the size and shape of ice crystals have again underlined the irregular nature of these particles [11]. Ice crystals in earth's atmosphere generally retain the shape of hexagonal columns or plates. However, the fluctuations in ambient temperature, pressure

Corresponding Author: El Mostafa Tari **Email**: tarielmostafa@gmail.com

and wind speed can cause any degree of irregularity [12]. Recent analyses of holograms taken from airplanes in cirrus clouds show a wide variety of crystal structures [13]. According to the classification of ice crystals of Magano and Lee [14], these crystals are classified as the pyramid, the cup, the solid bullet, the hollow bullet, the solid column, the hollow column, the capped column and the bullet rosette [12]. Their role in the atmosphere is very important directly and indirectly. These particles modify the radiative balance of the atmosphere and a great uncertainty persists as to the value of their radiative forcing. It is therefore necessary to study them in more detail.

To study the scattering by a spherical particle, three possibilities exist according to the ratio of the particle size (α): Rayleigh's theory which studies light scattering by particles of very small size ($\alpha \ll 1$), the theory of geometrical optics which applies to large particles ($\alpha \gg 1$) and Mie theory which is used for intermediate-size particles. In principle, the interaction of the particle with incident electromagnetic radiation can be determined by solving the Maxwell equations with boundary conditions corresponding to the shape of the particle; there are exact solutions for certain shapes, such as spheres, ellipsoids and infinite cylinders [1, 15].

For non-spherical particles of very small sizes, the Rayleigh's theory remains valid. For particles of intermediate sizes and fairly simple shapes, there are theories for various shapes and for different sizes. For example, the T-matrix theory [16] allows a fairly fast calculation for flattened or elongated ellipsoid particles. For complex or arbitrary forms, theories begin to be elaborated [17], such as the finite-element methods [18] and the finite-difference domain method [19]. These techniques are very precise, but very expensive in terms of calculation time, which is their main disadvantage.

Under such circumstances, the use of approximation methods becomes preferable or even mandatory. The most widely used analytical approximations for practical situations are the Rayleigh-Gans (RG) approximation and anomalous diffraction (AD) of van de Hulst [1]. The Wentzel-Kramers-Brillouin (WKB) approximation [20] is a classical approximation, which takes the phase shift into account correctly, so it does not have restriction on the phase shift magnitude, contrary to other approximations. The WKB approximation has been successfully applied to spheres, spheroids and cylinders [20, 6]. Recently, this approach has been applied to model the scattering properties of hexagonal and prismatic particles [10, 21].

In this work, the WKB approximation is used to investigate the scattering of light by square pyramidal particles. This study is an extension of the work of Ibnchaikh (2016) [10] to other non-column particles. For this, the analytical expression of the form factor for square pyramid ice crystal was derived using the WKB method. Furthermore, the extinction coefficient is calculated in order to illustrate the results.

2. WKB Approximation

Consider a particle illuminated by a plane wave polarized in the direction $\overrightarrow{e_x}$ and propagating along the z-axis (Fig. 1).

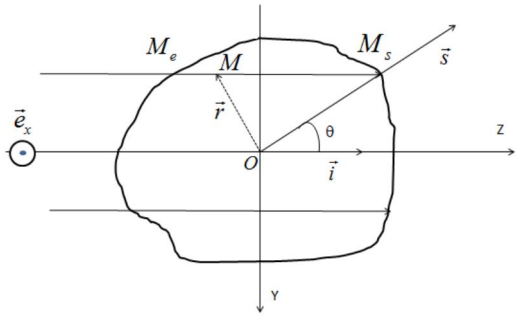

FIG. 1. Description of the scattering problem.

In the literature, the expression of the amplitude of light scattering in the WKB approximation, in a scalar form, is [20, 22]:

$$|f(\vec{s},\vec{i})| = \frac{k^2}{2\pi}\sin(\aleph)|(m-1)F(\theta,\varphi)| \qquad (1)$$

where $\vec{s}$ and $\vec{i}$ are the unit vectors along the direction of scattering and propagation of light, respectively. $\aleph$ is the angle between the polarization vector $\overrightarrow{e_x}$ and the unit vector $\vec{s}$, θ is the scattering angle between $\vec{s}$ and $\vec{i}$, φ is the azimuth angle, k is the wave vector and m is the relative complex refractive index. The quantity $F(\theta,\varphi)$ is known as the form factor which represents the modification of the scattered irradiance due to the finite size of the particle and to its deviation from sphericity:

$$F(\theta,\varphi) = \iiint_v \exp\left(ik\vec{r}.(\vec{i}-\vec{s})\right)\exp(ikw)dv \qquad (2)$$

where $\vec{r}$ is the position vector of any point within the scattering object, v is the volume of the studied particle and:

$$w = \int_{z_e}^{z} (m(z') - 1)dz' = (m-1)(z - z_e) \quad (3)$$

where w is the optical path for a homogenous particle which is introduced by the scattering object, z is the z-coordinate of the scatter element inside the particle and z_e is the z-coordinate of the initial position of penetration of the object.

In rectangular coordinates, the form factor can be expressed as follows:

$$F(\theta,\varphi) = \iiint_v \begin{matrix} e^{-ikx\sin\theta\cos\varphi} e^{-iky\sin\theta\sin\varphi} \\ e^{ikz(m-\cos\theta)} e^{-ikz_e(m-1)} \end{matrix} \Big\} dv \quad (4)$$

where x, y and z are the components of the position of the scattering element inside the object.

By integrating Eq. (4) over z, one obtains:

$$F(\theta,\varphi) = \frac{1}{ik(m-\cos\theta)} \cdot \iint e^{-ikx\sin\theta\cos\varphi} e^{-iky\sin\theta\sin\varphi} G(z_e, z_s)dxdy \quad (5)$$

with:

$$G(z_e, z_s) = e^{ik(m-\cos\theta)z_s} e^{-ik(m-1)z_e} - e^{ik(1-\cos\theta)z_e} \quad (6)$$

where z_e and z_s are the z-coordinates of the intersection of the light and the body lateral surfaces, as shown in Fig. 2.

To calculate the integral in Eq. (5) on the volume of the particle, it is necessary to determine the z-coordinates of the intersection of the light and the body lateral surfaces of the particle. For this, the pyramidal particle is cut in several square slices along its main axis (Fig. 2(c)).

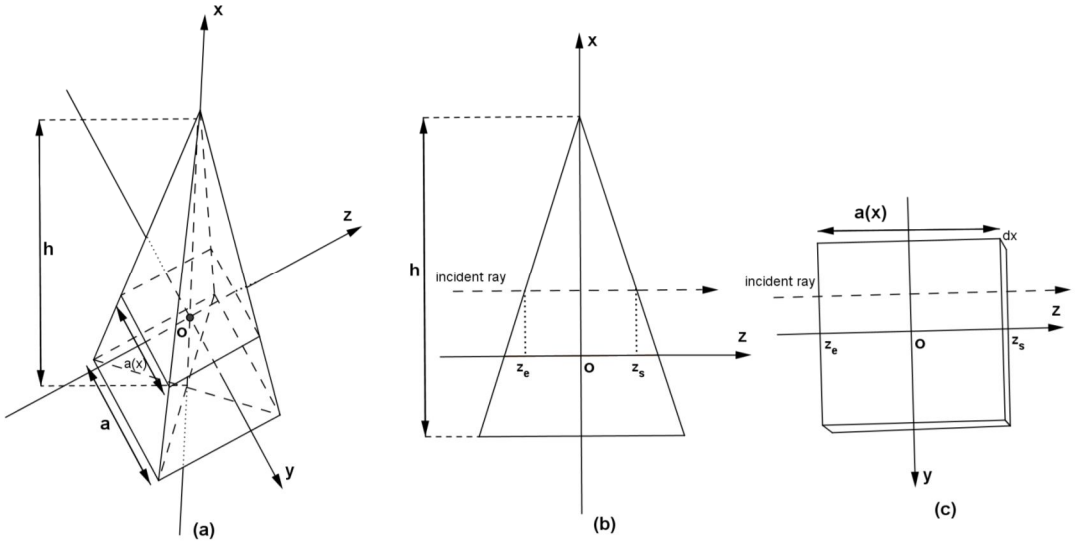

FIG. 2. Decomposition of the pyramid.

3. Results and Discussion

Consider a particle of pyramidal shape with equilateral faces and a square base oriented in the $y-z$ plane and of side length a. The origin of the Cartesian coordinate system orthonormal $R(O,X,Y,Z)$ coincides with the center of the particle (pyramid) and the principal axis of the pyramid is oriented along the x-axis.

The use of the WKB method for oblique incidence presents some difficulties. Thus, this approximation will be applied in this work to derive the form factor of a pyramidal particle for two special cases of normal incidence: flat incidence (Fig. 3(a)) and edge-on incidence (Fig. 3(b)). Therefore, the pyramid is cut into infinitely thin slices with thickness dx; these slices are perpendicular to the symmetric axis of the pyramid and are in the form of squares. The length of its rib is $a(x) = \frac{3a}{4} - \frac{ax}{h}$, with h being the height of the pyramid. So, for each slice, we can derive its contribution to the form factor.

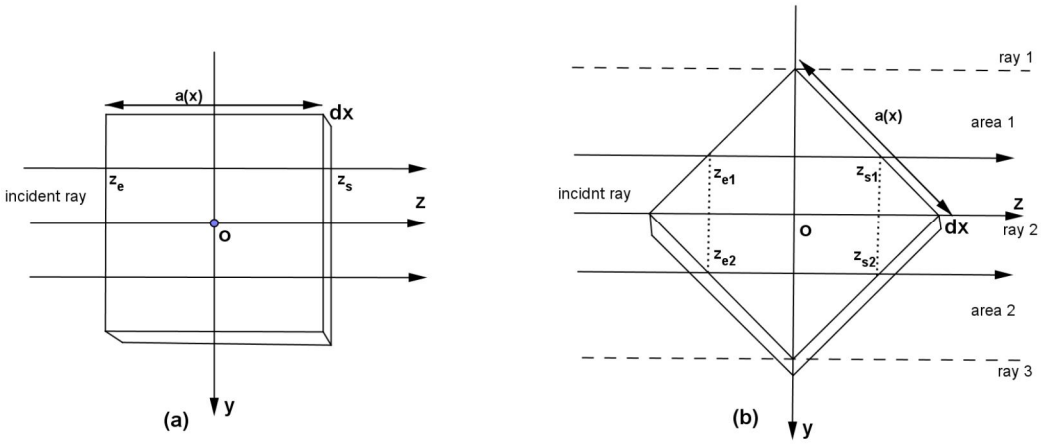

FIG. 3. Slices of the pyramid for flat incidence (a) and edge-on incidence (b).

The z-coordinates for the flat incidence are defined from Fig. 3(a):

$$z_s = -z_e = \frac{a(x)}{2}, -\frac{a(x)}{2} \le y \le \frac{a(x)}{2} \tag{7}$$

and the z-coordinates for the edge-on incidence are defined from Fig. 3(b):

$$\left.\begin{aligned} z_{s1} = -z_{e1} = \frac{\sqrt{2}}{2}a(x) + y, -\frac{\sqrt{2}}{2}a(x) \le y \le 0 \\ z_{s2} = -z_{e2} = \frac{\sqrt{2}}{2}a(x) - y, 0 \le y \le \frac{\sqrt{2}}{2}a(x) \end{aligned}\right\} \tag{8}$$

3.1 Flat Incidence

In this first case of incidence, Fig. 3(a) is used. Four particular cases are considered for which the analytical expression of the integral given by Eq. (5) is not defined for a number of values of θ and φ, as well as a general case. The form factor for the flat incidence is denoted by $F_1(\theta, \varphi)$.

a) *Case of* $\boldsymbol{\theta = 0}$

After some algebraic manipulations, one obtains the form factor:

$$F_1(0, \varphi) = \frac{a^2 h}{i2\rho}\left\{\frac{2}{i\rho}\left[\left(\frac{1-e^{i\rho}}{i\rho}\right) + e^{i\rho}\right] - 1\right\} \tag{9}$$

where $\rho = ka(m-1)$.

b) *Case of* $\boldsymbol{\theta = \pi}$

In this case, the expression of the form factor is given by:

$$F_1(\pi, \varphi) = \frac{h}{k^2(m+1)}\left\{\frac{1}{m}\left(e^{ikam}\left(1 - \frac{1}{ikam}\right) + \frac{1}{ikam}\right) + e^{-ika}\left(1 + \frac{1}{ika}\right) - \frac{1}{ika}\right\} \tag{10}$$

c) *Case of* $\boldsymbol{0 < \theta < \pi, \varphi = 0}$

By integration of Eq. (5) over y, the contribution of a slice $f^1(\theta, 0)$ to the form factor is given by the following expression:

$$f^1(\theta, 0)dx = \frac{dx}{ik(m-\cos\theta)}\left(e^{i\frac{3}{4}g}\left(\frac{3a}{4}I'_+ - \frac{a}{h}I'_-\right) - e^{i\frac{3}{4}g}\left(\frac{3a}{4}J'_+ - \frac{a}{h}J'_-\right)\right) \tag{11}$$

with:

$$I'_+ = e^{-ikx\sin\theta}e^{-i\frac{g}{h}x} \tag{12}$$

$$I'_- = xe^{-ikx\sin\theta}e^{-i\frac{g}{h}x} \tag{13}$$

$$J'_+ = e^{-ikx\sin\theta}e^{-i\frac{q}{h}x} \tag{14}$$

$$J'_- = xe^{-ikx\sin\theta}e^{-i\frac{q}{h}x}\,. \tag{15}$$

Therefore, the contribution from all slices to the form factor is expressed as:

$$F_1(\theta, 0) = \int_{-\frac{h}{4}}^{\frac{3}{4}h} f^1(\theta, 0)dx\,. \tag{16}$$

Integration over x gives:

$$F_1(\theta, 0) = \frac{ahe^{-i\frac{3}{4}kh\sin\theta}}{ik(m-\cos\theta)}\left\{\left(\frac{e^{iZ_g^+}}{iZ_g^+} - \frac{e^{iZ_q^+}}{iZ_q^+}\right) - \left(\frac{e^{iZ_g^+}-1}{(iZ_g^+)^2} - \frac{e^{iZ_q^+}-1}{(iZ_q^+)^2}\right)\right\} \tag{17}$$

with:

$$Z_g^+ = kh\sin\theta + g \tag{18}$$

$$Z_q^+ = kh\sin\theta + q \tag{19}$$

and the parameters used are: $\mu = \frac{ka}{2}(m - \cos\theta)$, $g = \frac{\rho}{2} + \mu$, $q = \frac{\rho}{2} - \mu$ and ρ as already defined in the case $\theta = 0$.

d) *Case of* $0 < \theta < \pi$ *and* $\varphi = \pi$

In this case, the same method is used to determine the expression of the form factor; it suffices to calculate the integral of Eq. (5) over y and x; so:

$$F_1(\theta,\pi) = \frac{ahe^{-i\frac{1}{4}kh\sin\theta}}{ik(m-\cos\theta)}\left\{\left(\frac{e^{iq}}{iZ_q^-} - \frac{e^{ig}}{iZ_g^-}\right) - \left(e^{iq}\frac{e^{iZ_q^-}-1}{(iZ_q^-)^2} - e^{ig}\frac{e^{iZ_g^-}-1}{(iZ_g^-)^2}\right)\right\} \quad (20)$$

with:

$$Z_g^- = kh\sin\theta - g \quad (21)$$

$$Z_q^- = kh\sin\theta - q\,. \quad (22)$$

e) *General Case*

In this general case, the values of θ and φ are different from those of the preceding cases. By integrating Eq. (5) over y, the expression of the contribution of a slice $f^1(\theta,\varphi)$ to the form factor becomes:

$$f^1(\theta,\varphi)dx = \frac{dx}{ik(m-\cos\theta)ik\sin\theta\sin\varphi}\left((I_+ - I_-) - (J_+ - J_-)\right) \quad (23)$$

with:

$$I_{\pm} = e^{-ikx\sin\theta\cos\varphi}e^{ikz_s(2m-1-\cos\theta)}e^{\pm iky_s\sin\theta\sin\varphi} \quad (24)$$

$$J_{\pm} = e^{-ikx\sin\theta\cos\varphi}e^{ikz_s(\cos\theta-1)}e^{\pm iky_s\sin\theta\sin\varphi}. \quad (25)$$

Thus, the contribution from all slices to the form factor is expressed as:

$$F_1(\theta,\varphi) = \int_{-\frac{h}{4}}^{\frac{3}{4}h} f^1(\theta,\varphi)dx\,. \quad (26)$$

By introducing the value of z_s defined in Eq. (7) and by integrating with respect to x, the previous integral takes the following form:

$$F_1(\theta,\varphi) = -\frac{\frac{ha^2}{4}}{ut}e^{-i\frac{3}{4}d}\left\{\left(\frac{e^{iA^+}-1}{iA^+} - \frac{e^{iA^-}-1}{iA^-}\right) - \left(\frac{e^{iB^+}-1}{iB^+} - \frac{e^{iB^-}-1}{iB^-}\right)\right\} \quad (27)$$

with:

$$A^{\pm} = d + g \pm t \quad (28)$$

$$B^{\pm} = d + q \pm t\,. \quad (29)$$

The parameters used are:

$$d = hk\sin\theta\cos\varphi \quad (30)$$

$$t = \frac{ka}{2}\sin\theta\sin\varphi. \quad (31)$$

3.2 Edge-on Incidence

In this second case of incidence, the slice of the pyramid is divided into two areas by ray 1, ray 2 and ray 3 (see Fig. 3(b)). The ray paths z_{ej} and z_{sj} for each area as well as the function $G(z_e, z_s)$ (see Eq. (6)) depend on the variables x and y. As in the case of flat incidence, there are four special cases and a general case to be treated.

a) *Case of* $\theta = 0$

In this case, the expression of the form factor is given by:

$$F_2(0,\varphi) = \frac{a^2h}{i\rho'}\left\{\frac{2}{i\rho'}\left(\frac{e^{i\rho'}-1}{i\rho'} - 1\right) - 1\right\} \quad (32)$$

where $F_2(\theta,\varphi)$ represents the form factor for the edge-on incidence, with $\rho' = \sqrt{2}ka(m-1)$.

b) *Case of* $\theta = \pi$

Similarly here, the expression of the form factor is easily calculated:

$$F_2(\pi,\varphi) = -\frac{h}{k^2(m+1)}\left\{\frac{1}{m}\left(\frac{e^{i\sqrt{2}kam}-1}{i\sqrt{2}kam} - 1\right) - \frac{e^{i\sqrt{2}ka}-1}{i\sqrt{2}ka} - 1\right\}. \quad (33)$$

c) *Case of* $0 < \theta < \pi$ *and* $\varphi = 0$

By the integration of Eq. (5) over y, the expression of the contribution of a slice $f^2(\theta,0)$ to the form factor is given by:

$$f^2(\theta,0)dx = \frac{dx}{ik(m-\cos\theta)}\left(f^{2-}(\theta,0) + f^{2+}(\theta,0)\right) \quad (34)$$

where $f^{2-}(\theta,0)$ and $f^{2+}(\theta,0)$ are respectively the contributions of area 1 and area 2 of the slice to the form factor, with:

$$f^{2\pm}(\theta,0) = \left(I''_{\pm} - J''_{\pm}\right) \quad (35)$$

and

$$I''_- = I''_+ = \frac{\sqrt{2}a}{i2g'}\left(e^{i\frac{3}{4}g'}I''_{1-} - I''_{2-}\right) \quad (36)$$

$$I''_{1-} = e^{-ikx\sin\theta}e^{-i\frac{g'}{h}x} \quad (37)$$

$$I''_{2-} = e^{-ikx\sin\theta} \quad (38)$$

$$J''_- = J'_+ = \frac{\sqrt{2}a}{i2q'}\left(e^{i\frac{3}{4}q'}J''_{1-} - J''_{2-}\right) \quad (39)$$

$$J''_{1-} = e^{-ikx\sin\theta}e^{-i\frac{q'}{h}x} \quad (40)$$

$$J''_{2-} = e^{-ikx\sin\theta}. \quad (41)$$

Then, the contribution from all slices to the form factor is expressed as:

$$F_2(\theta,0) = F_{2-}(\theta,0) + F_{2+}(\theta,0) \quad (42)$$

where $F_{2-}(\theta,0)$ and $F_{2+}(\theta,0)$ are the contributions of area 1 and area 2 to the form factor, respectively, with:

$$F_{2\pm}(\theta,0) = \frac{1}{ik(m-\cos\theta)}\int_{-\frac{h}{4}}^{\frac{3}{4}h} f^{2\pm}(\theta,0)dx \quad (43)$$

By performing the last integration, the expression of Eq. (42) becomes:

$$F_2(\theta,0) = \frac{\sqrt{2}ahe^{-i\frac{3}{4}kh\sin\theta}}{ik(m-\cos\theta)}\left\{\frac{1}{ig'}\frac{e^{iZ^+_{g'}}-1}{iZ^+_{g'}} - \frac{1}{iq'}\frac{e^{iZ^+_{q'}}-1}{iZ^+_{q'}} + \frac{e^{ikh\sin\theta}-1}{ikh\sin\theta}\left(\frac{1}{iq'}-\frac{1}{ig'}\right)\right\} \quad (44)$$

where:

$$Z^+_{g'} = kh\sin\theta + g' \quad (45)$$

$$Z^+_{q'} = kh\sin\theta + q'. \quad (46)$$

The parameters used are: $\mu' = \frac{\sqrt{2}}{2}ka(m-\cos\theta)$, $g' = \frac{\rho'}{2}+\mu'$, $q' = \frac{\rho'}{2}-\mu'$ and the parameter ρ' as defined above.

d) *Case of* $0 < \theta < \pi$ *and* $\varphi = \pi$

The same method used above gives the expression of the form factor:

$$F_2(\theta,\pi) = \frac{\sqrt{2}ahe^{-i\frac{3}{4}kh\sin\theta}}{ik(m-\cos\theta)}\left\{\frac{1}{ig'}\frac{1-e^{-iZ^-_{g'}}}{iZ^-_{g'}} - \frac{1}{iq}\frac{1-e^{-iZ^-_{q'}}}{iZ^-_{q'}} + \frac{1-e^{-ikh\sin\theta}}{ikh\sin\theta}\left(\frac{1}{iq'}-\frac{1}{ig'}\right)\right\} \quad (47)$$

with:

$$Z^-_{g'} = kh\sin\theta - g' \quad (48)$$

$$Z^-_{q'} = kh\sin\theta - q'. \quad (49)$$

e) *General Case*

The contribution from the slice to the form factor in this general case can be expressed in a simple form:

$$f^2(\theta,\varphi)dx = \frac{dx}{ik(m-\cos\theta)}\left(f^{2-}(\theta,\varphi) + f^{2+}(\theta,\varphi)\right) \quad (50)$$

with:

$$f^{2\pm}(\theta,\varphi) = \frac{e^{i\frac{3\sqrt{2}}{8}ka(2m-1-\cos\theta)}}{\mp ik(\sin\theta\sin\varphi\pm(2m-1-\cos\theta))}(I_{1\pm} - I_{2\pm}) - \frac{e^{i\frac{3\sqrt{2}}{8}ka(\cos\theta-1)}}{\mp ik(\sin\theta\sin\varphi\pm(\cos\theta-1))}(J_{1\pm} - J_{2\pm}) \quad (51)$$

$$I_{1\pm} = e^{-ikx\left(\sin\theta\cos\varphi+\frac{\sqrt{2}a}{2h}(2m-1-\cos\theta)\right)}\times e^{\mp i\frac{\sqrt{2}}{2}ka(x)(\sin\theta\sin\varphi\pm(2m-1-\cos\theta))} \quad (52)$$

$$I_{2\pm} = e^{-ikx\left(\sin\theta\cos\varphi+\frac{\sqrt{2}a}{2h}(2m-1-\cos\theta)\right)} \quad (53)$$

$$J_{1\pm} = e^{-ikx\left(\sin\theta\cos\varphi+\frac{\sqrt{2}a}{2h}(\cos\theta-1)\right)}\times e^{\mp i\frac{\sqrt{2}}{2}ka(x)(\sin\theta\sin\varphi\pm(\cos\theta-1))} \quad (54)$$

$$J_{2\pm} = e^{-ikx\left(\sin\theta\cos\varphi+\frac{\sqrt{2}a}{2h}(\cos\theta-1)\right)}. \quad (55)$$

The form factor can therefore be written as:

$$F_2(\theta,\varphi) = F_{2-}(\theta,\varphi) + F_{2+}(\theta,\varphi) \quad (56)$$

where:

$$F_{2\pm}(\theta,\varphi) = \frac{1}{ik(m-\cos\theta)}\int_{-\frac{h}{4}}^{\frac{3h}{4}} f^{2\pm}(\theta,\varphi)dx \quad (57)$$

After some algebraic manipulations, Eq. (57) becomes:

$$F_{2\pm}(\theta,\varphi) = -\frac{a^2}{2\mu'}\left\{\frac{e^{i\frac{3}{4}g'}}{\mp(\sqrt{2}t\pm g')}\int_{-\frac{h}{4}}^{\frac{3h}{4}}(I_{1\pm} - I_{2\pm})dx - \frac{e^{i\frac{3}{4}q'}}{\mp(\sqrt{2}t\pm q')}\int_{-\frac{h}{4}}^{\frac{3h}{4}}(J_{1\pm} - J_{2\pm})dx\right\}. \quad (58)$$

Finally, by integrating Eq. (58) over the variable x, the expression of the form factor for each area is given by:

$$F_{2\pm}(\theta,\varphi) = -\frac{a^2h}{2\mu'}\left\{\frac{e^{-i\frac{3}{4}d}}{\mp(\sqrt{2}t\pm g')}\left[\frac{e^{i(d\mp\sqrt{2}t)}-1}{i(d\mp\sqrt{2}t)} - \frac{e^{i(d+g')}-1}{i(d+g')}\right] - \frac{e^{-i\frac{3}{4}d}}{\mp(\sqrt{2}t\pm q')}\left[\frac{e^{i(d\mp\sqrt{2}t)}-1}{i(d\mp\sqrt{2}t)} - \frac{e^{i(d+q')}-1}{i(d+q')}\right]\right\} \quad (59)$$

where the parameters d and t have been defined in the general case of flat incidence.

Note that F_{2+} has a singularity at $\sqrt{2}t + q'$ when $\theta = \varphi = \frac{\pi}{2}$. In this case, the recalculation of F_{2+} gives the following result:

$$F_{2+}\left(\frac{\pi}{2},\frac{\pi}{2}\right)=\frac{h}{k^2m}\left\{\left[\left(1+\frac{\sqrt{2}}{ika}\left(1+\frac{1}{2m}\right)\right)\left(1-e^{-i\frac{\sqrt{2}}{2}ka}\right)-1\right]+\frac{1-e^{i\frac{\sqrt{2}}{2}ka(2m-1)}}{i\sqrt{2}kam(2m-1)}\right\} \quad (60)$$

The analytical expressions of the form factor for a pyramidal particle as part of the WKB approximation are established; they have been obtained for both flat incident light and edge-on incidence. Then, the correctness of the analytical expressions of the form factor is checked. For this, the different double integrals which intervene here are calculated numerically using Gauss Legendre quadrature method. By taking 16×16 integration points for this quadrature, the results obtained with the analytical expressions of the form factor are reproduced numerically.

For illustration, Fig. 4 and Fig. 5 show the behavior of the normalized form factor $(|F(\theta,\varphi)/F(0,0)|^2)$ as a function of the scattering angles θ and φ on a logarithmic scale for some values of ka and $\frac{h}{a}$. In these figures, the axis $\varphi=\pi$ is an axis of symmetry of the form factor; only the values of φ between 0 and π are considered.

The graphs representing the normalized form factor in the different cases show that when the scattering angle θ increases gradually from a certain value, the normalized form factor varies greatly with the azimuth angle φ. This is manifested by the appearance of a number of bumps and dips. Consequently, the azimuth angle φ plays an important role in the study of the scattering of light by non-spherical particles unlike the case of spherical particles; this is in agreement with the fact that the particle has non-spherical symmetry. On the other hand, the graphs also show the importance of the size parameter and the orientation (flat incidence and edge-on incidence) of the non-spherical particles. Finally, it is noted that the backscatter is nearly imperceptible compared to the forward scatter.

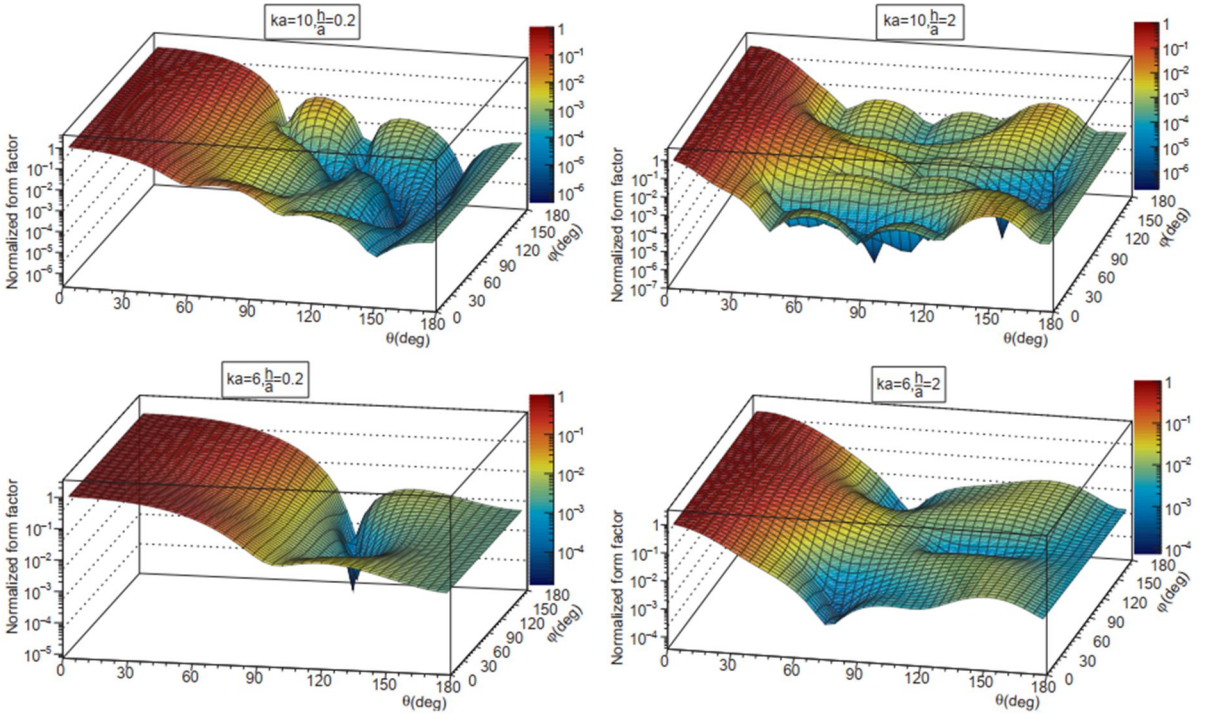

FIG. 4. Normalized form factor as a function of the scattering angles θ and φ for absorbing pyramidal particle for flat incident light at a complex refractive index $m=1.311+0.31\times10^{-8}i$ when $(ka=10, h/a=0.2)$, $(ka=10, h/a=2)$, $(ka=6, h/a=0.2)$ and $(ka=6, h/a=2)$.

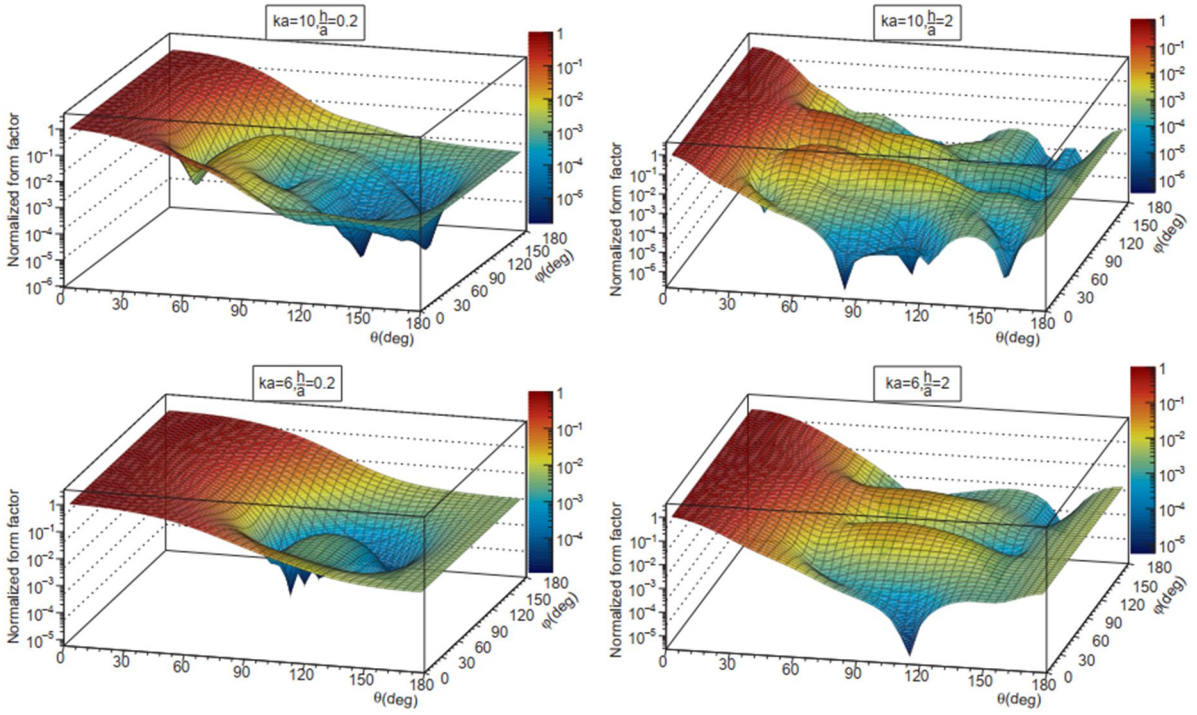

FIG. 5. Normalized form factor as a function of the scattering angles θ and φ for absorbing pyramidal particle for edge-on incidence at a complex refractive index $m = 1.311 + 0.31 \times 10^{-8}i$ when $(ka = 10, h/a = 0.2)$, $(ka = 10, h/a = 2)$, $(ka = 6, h/a = 0.2)$ and $(ka = 6, h/a = 2)$.

The form factors obtained here in Figs. 4 and 5, representing the modification of the scattered irradiance due to the finite size of the particle and to its deviation from sphericity, are studied for two particular cases: flat incidence (Fig. 4) and edge-on incidence (Fig. 5). In particular, the effects of the scattering angle θ and the azimuth angle φ on the form factor observed in this study can be used in the progress and development of numerous scientific applications, which are directly or indirectly linked to the phenomenon of light scattering by small particles, such as optical information, display and processing systems, telecommunications, photonics and optoelectronics [23]. Moreover, these results are used to deduce the optical properties of particles in other scientific disciplines, such as geophysics, astronomy, climatology and solar-energy technologies [17, 24, 25].

3.3 Extinction Efficiency

The extinction efficiency Q_{ext} is the extinction cross-section divided by the projection area of the particle. By using the optical theorem, the expression for the extinction efficiency is easily found from the forward form factor [1, 26]:

$$Q_{ext} = \frac{2k}{P} I_m((m-1)F(0,0)) \quad (61)$$

where P is the projected area of the particle on the plane perpendicular to the direction of the incident wave and the symbol I_m indicates the imaginary part.

The projected area of the pyramid in the first case (flat incidence) is given by: $P_1 = \frac{ah}{2}$ and in the second case (edge-on incidence), it is given by: $P_2 = \frac{ah}{\sqrt{2}}$. Thus, the extinction efficiencies of these two cases are given respectively by:

$$Q_{ext1} = 2Re(1 - \frac{2}{i\rho}(\frac{(1-e^{i\rho})}{i\rho} + e^{i\rho})) \quad (62)$$

$$Q_{ext2} = 2Re(1 - \frac{2}{i\rho'}(\frac{(e^{i\rho'}-1)}{i\rho'} - 1)) \quad (63)$$

where the symbol Re designates the real part.

Since the parameters ρ and ρ' do not depend on the height h, the expressions of Q_{ext} above show that the extinction efficiency also does not depend on the height h.

For real refractive index, the extinction efficiencies become:

$$Q_{ext1} = 2\left\{1 - 2\frac{\sin\rho}{\rho} + \frac{\sin(\rho/2)^2}{(\rho/2)^2}\right\} \quad (64)$$

$$Q_{ext2} = 2\{1 - \frac{\sin(\frac{\rho'}{2})^2}{(\frac{\rho'}{2})^2}\} \quad (65)$$

Fig. 6 shows the variation of the extinction efficiency as a function of ka in two cases: flat incidence (Q_{ext1}) and edge-on incidence (Q_{ext2}). From this figure, it is noticed that the extinction efficiency oscillates around the value of 2 as the particle size further increases. For large values of ka, Q_{ext1} always oscillates around the value 2, while Q_{ext2} tends towards this same value 2. This extinction limit value corresponds to the extinction paradox described in the literature [1]. More recently, Berg in 2011 gave a more convincing explanation of this limit value 2 [27]. The particle intercepts a portion of the incident plane wave equal to its geometric section $\sigma_{geo} = P$. The resulting interaction vibrates the particle which re-emits a wave which is nothing other than the scattered wave. This scattered wave will, for its part, interfere with the incident wave in a destructive manner, again removing $\sigma_{geo} = P$ from the incident flux. We therefore find $\sigma_{ext} = 2\sigma_{geo}$ and finally $Q_{ext} = \frac{\sigma_{ext}}{P} = 2$.

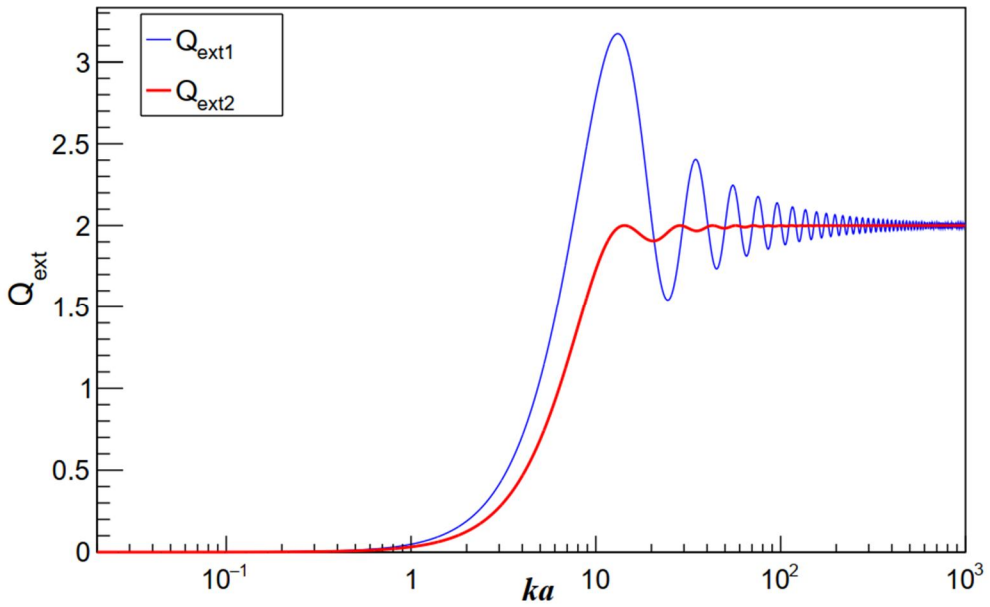

FIG. 6. Variation of the extinction coefficient as a function of the size parameter ka for a complex refractive index $m = 1.311 + 0.31 \times 10^{-8}i$.

4. Conclusion

In this work, the WKB method is used to study two particular cases of the scattering of light by a nonspherical pyramidal particle for normal incidence (flat incidence and edge-on incidence). The expression of the light scattering form factor of this particle is determined analytically for the two cases; it depends on the relative refractive index, the size parameter and the geometry of the particle. Unlike the case of spherical particles, the form factor is also dependent on the scattering angle θ and the azimuth angle φ. It is also seen that the particles that do not have spherical symmetry make the calculation of the form factor of light scattered by a pyramidal particle much more complicated.

Finally, the extinction efficiency for a pyramidal particle is calculated in the two cases of normal incidence according to the parameter size of the particle. The value of this coefficient tends to 2 when the particle size becomes infinite, which is in perfect agreement with other works in the literature.

References

[1] van de Hulst, H.C., "Light scattering by small particles", (J. Wiley & Sons, New York, 1957).

[2] Mishchenko, M.I. and Travis, L.D., J. Quant. Spectrosc. Radiat. Transf., 60 (1998) 309.

[3] Mazeron, P. and Muller, S., J. Quant. Spectrosc. Radiat. Transf., 60 (1998) 391.

[4] Shapovalov, K.A., European Researcher, 49 (2013) 1291.

[5] Shapovalov, K.A., Int. J. Civ. Eng. Tech., 9 (2018) 1664.

[6] Belafhal, A., Ibnchaikh, M. and Nassim, K., J. Quant. Spectrosc. Radiat. Transf., 72 (2002) 385.

[7] Pratesi, F., Burresi, M., Riboli, F., Vynck, K. and Wiersma, D.S., Opt. Express, 21 (2013) 460.

[8] Leseur, O., Ph.D. Thesis, Université Pierre et Marie Curie (2016), France.

[9] Lamsoudi, R. and Ibnchaikh, M., ARPN J. Eng. Appl. Sci., 11 (2016) 13580.

[10] Ibn Chaikh, M., Lamsoudi, R. and Belafhal, A., Opt. Quant. Electron., 48 (2016) 466.

[11] Hovenac, E. A., Appl. Opt., 30 (1991) 4739.

[12] Macke, A., Appl. Opt., 32 (1993) 2780.

[13] Krupp, C., M.S. Thesis, University of Cologne (1991), Germany.

[14] Magono, C. and Lee, C., J. Fac. Sci. Hokkaido Uni. Ser., 7 (1966) 321.

[15] Barber, P.W., Hill, S.C., "Light Scattering by Particles: Computational Methods", (World Scientific, Singapore, 1990).

[16] Mishchenko, M.I., Travis, L.D. and Mackowski, D.W., J. Quant. Spectrosc. Radiat. Transf., 55 (1996) 535.

[17] Mishchenko, M.I., Hovenier, J.W. and Travis, L.D., "Light Scattering by Non-spherical Particles: Theory, Measurements and Applications", (Academic Press, New York, 2000).

[18] Silvester, P.P. and Ferrari, R.L., "Finite Elements for Electrical Engineers", (Cambridge Univ. Press, New York, 1996).

[19] Yang, P. and Liou, K.N., J. Comput. Phys., 140 (1998) 346.

[20] Klett, J.D. and Sutherland, R.A., Appl. Opt., 31 (1992) 373.

[21] Tari, E.M., Bahaoui, A., Lamsoudi R., Khouilid, M. and Ibnchaikh, M., IOP SciNotes, 2 (2021) 015206.

[22] Shepelevich, N.V., Prostakova, I.V. and Lopatin, V.N., J. Quant. Spectrosc. Radiat. Transf., 63 (1999) 353.

[23] Loik, V.A., Konkolovich, A.V. and Miskevich, A.A., J. Opt. Technol., 78 (2011) 455.

[24] Fan, X., Zheng, W. and Singh, D.J., Light Sci. Appl., 3 (2014) 179.

[25] Fast, F.G., Opt. Commun., 313 (2014) 394.

[26] Ishimaru, A., "Wave Propagation and Scattering in Random Media, Volume I: Single Scattering and Transport Theory", (Academic Press, New York, 1978).

[27] Berg, M.J., Sorensen, C.M. and Chakrabarti, A., J. Quant. Spectrosc. Radiat. Transf., 112 (2011) 117.

Volume 15, Number 5, 2022. pp. 537-545

Jordan Journal of Physics

ARTICLE

Field Electron Emission Characteristics of Tungsten–Polyethylene Composite Material As a Source of Electron Emission

Nizar A. Abu-Najm[a], **Moneeb T. M. Shatnawi**[a], **Mohammad M. Allaham**[b,c] and **Marwan S. Mousa**[d]

[a] *Department of Physics, The University of Jordan, Amman 11942, Jordan.*

[b] *Institute of Scientific Instruments of CAS, Královopolská 147, 612 64 Brno, Czech Republic.*

[c] *Central European Institute of Technology, Brno University of Technology, Purkyňova 123, 612 00 Brno, Czech Republic.*

[d] *Department of Physics, Mu'tah University, Al-Karak 61710, Jordan.*

Doi: **https://doi.org/10.47011/15.5.11**

Received on: 12/08/2021; *Accepted on: 07/10/2021*

Abstract: This work provides an experimental study on the effects of polyethylene coating on the field electron emission characteristics of clean (uncoated) tungsten tips. Several tungsten tips, with different apex radii, have been prepared, coated with different thicknesses of polyethylene layers and then examined using a standard field electron emission microscope. Various field electron emission characteristics have been measured under high-vacuum conditions. These include current-voltage characteristics, Fowler-Nordheim plots, scanning electron micrographs and spatial current distributions (electron-emission images). Based on this work, it is proved that coating tungsten tips with polyethylene layers has caused dramatic improvements on the tip emission properties. In particular, coating the tips improves the current-voltage characteristics, which is reflected in lowering the extraction voltage, getting more stable emission currents, expressing the current-voltage characteristics using Fowler-Nordheim plots and finally, the spatial distributions of the emitted electrons for the coated tips are more stable and uniform.

Keywords: Field electron emitter, Polyethylene dielectric layer, Composite emitter, Field electron microscope, Scanning electron microscope.

1. Introduction

Cold-field electron emission (CFE) is the emission of electrons from the surface of a condensed phase into another phase, usually vacuum, in situations where emission is induced by a high external electrostatic field [1-5]. It is a fundamental process in the operation of many technical applications, such as thermionic valves, cathode ray tubes (CRTs), X-rays and scanning and tunneling electron microscopes [6-8].

Many significant experimental studies of field emission have been carried out on carbon fibers, polymer graphite flakes and different tungsten and tungsten oxide nano-wires, such as (W, W_5O_{14} and $W_{18}O_{49}$) [9-13]. Advances in vacuum technology have developed the production techniques of field-emission cathodes, where high vacuum is essential for ensuring reliable operation of field-emission cathodes [10-17].

Corresponding Author: Marwan S. Mousa **Email**: mmousa@mutah.edu.jo

The objective of this work is to study the alterations that may occur to the properties of field electron emission from various pure tungsten emitters [18] before and after being coated with different thicknesses of polyethylene layers. For this purpose, several tungsten tips with various apex radii have been prepared using electrochemical-etching techniques [19].

The current experimental study reports the current-voltage $I_{\mathrm{m}}(V_{\mathrm{m}})$ characteristics of the prepared tungsten emitters, Fowler-Nordheim (FN) plots and the scanning electron microscope micrographs (SEM) for measuring the thicknesses of polyethylene coating layers. Moreover, the emission-current distributions obtained from the different tips were photographed using phosphorescent screen [19-21].

The results of this research are divided into two parts; the first part includes the results from the uncoated tungsten tips, while the second part includes the results from the tungsten-polyethylene composite.

Using FN plots, the uncoated samples were tested using Forbes field-emission orthodoxy test [22] and the characterization parameters for the tested tips are extracted; mainly, the characteristic voltage-conversion length ζ_{C} and the related field-enhancement factor γ_{C}, in addition to the formal emission area from a Schottky-Nordheim barrier $A_{\mathrm{f}}^{\mathrm{SN}}$ [23]. This is considered to make sure that the used uncoated emitters are sufficient to be used in the second part of the experiment.

This is important, because these parameters can be used for monitoring the changes in the system cathode-anode geometry, which need to be evaluated in an orthodox setup that passes the field-emission orthodoxy test. So, the results from the uncoated tips can be compared to the results from the composite tips, because the changes in the system geometry can be neglected [22].

The tips' coating material (polyethylene (PE)) consists of non-polar, saturated, high-molecular weight hydrocarbons. The individual macro-molecules are dielectrics, because of their symmetric molecular structure and they tend to crystallize [21-22]. PE melting point is typically in the range of 120 °C to 180 °C. It has the chemical formula $(\mathrm{C_2H_4})_{\mathrm{n}}$ and its chemical structure is shown in Fig. 1. PE is usually a mixture of similar polymers of ethylene with various values of n [21].

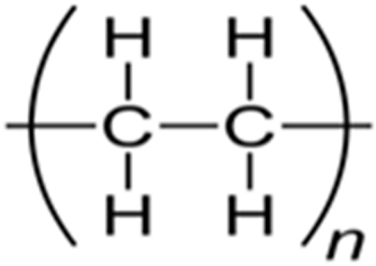

FIG. 1. Chemical structure of polyethylene.

2. Experimental Method

Tungsten micro-emitters have favorable properties, such as a high melting point of 3377 ˚C, a work function of 4.55 eV, high hardness (strength) and heat resistance at high temperatures [1]. Therefore, they are extensively used as electron emitters.

Tungsten micro-emitters typically have radii less than 100 nm and are produced by electrochemical-etching techniques [2]. The emitters were prepared by etching tungsten wires (~ 0.1 mm in diameter) using a 2M solution of sodium hydroxide (NaOH). The tip (anode) and a graphite rod (cathode) were connected to a power supply that provided the bias voltage necessary to generate the etching current. In this study, the bias voltage ranged from 10 - 12 volts. A multi-meter was used to monitor the current between the anode and the cathode; in order to quickly switch off the voltage when the etching process is complete, as presented in Fig. 2.

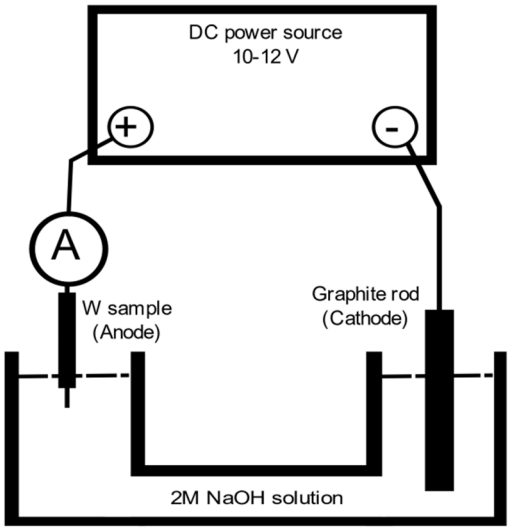

FIG. 2. Schematic diagram for the etching device.

The latter point is extremely important, as the cut-off time for the etching circuit greatly affects the sharpness and the shape of the tip [19]. The etched samples were then cleaned from any traces of NaOH solution by immersing them in distilled water and subjecting them to an ultrasonic bath for about 6-9 minutes [1].

To prepare the coating material, 0.5 gram of pure polyethylene was dissolved in 75 ml of xylene and the mixture was heated to 200 °C, where it became an almost 0.24 M-concentration solution. It should be noted that the coating process must be performed before the solution cools down.

Coating the tips with polyethylene involves two steps. Firstly, the tip of the emitter is dipped very slowly into the solution using a sample holder that keeps the sample vertical to the surface of the solution. The sample holder is attached to a trolley that can move the sample vertically to immerse the tip into the coating solution. Secondly, the immersed tip remains in the solution for five minutes at room temperature, so that the solution will cool down on the tungsten tip and the solvent (xylene) will vaporize, leaving the polyethylene solute stuck to the emitter surface.

The coated emitter is then mounted to a field electron emission microscope (FEM) system with an emitter to screen distance of 10 mm [1]. The screen images of the FEM are photographed directly using a digital camera.

The emission currents are obtained at a relatively high vacuum (~ 10–7 mbar). The high vacuum is maintained using an oil diffusion pump system. This pressure is obtained by baking the ultra-high vacuum system to ~ 160 °C for 7 hours and providing the system with liquid nitrogen (L-N_2) just after the baking process is completed [2, 22]. The radii of tip apexes were estimated through SEM; they were obtained at 20 kV, with magnifications up to ~ 6000x.

3. Results

SEMs of the prepared tips, before and after coating, with magnifications 800x and 6000x are presented in Fig. 3. The radii of the clean (uncoated) and coated tips were found to be 85.8 nm and 112.7 nm, respectively. Therefore, the thickness of the coating layer is estimated to be 26.9 nm.

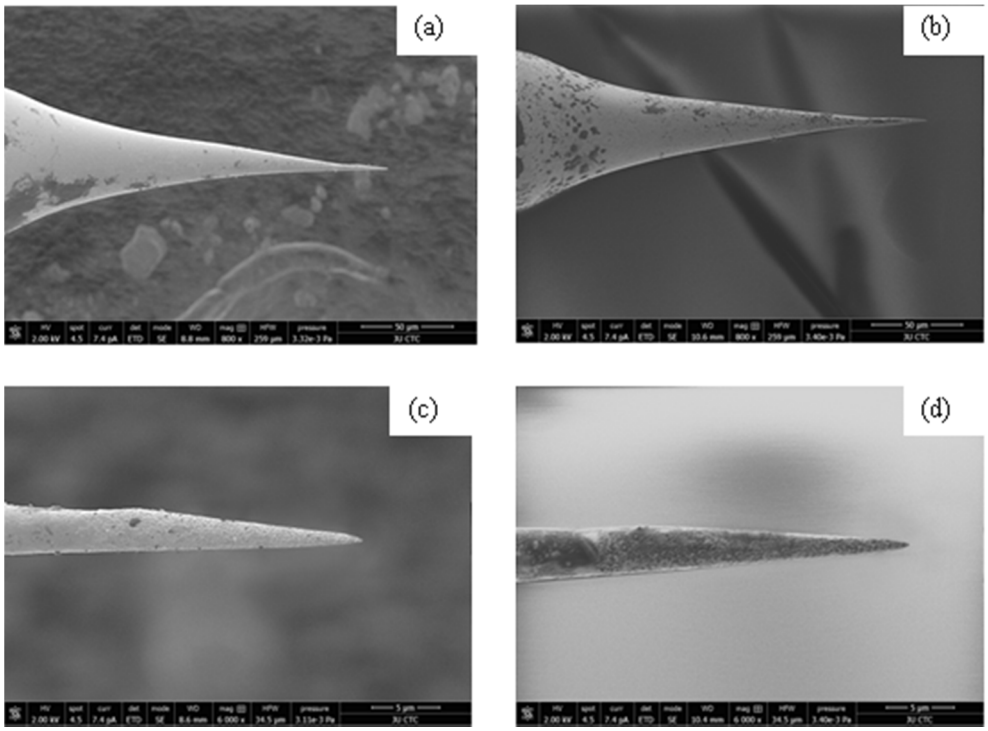

FIG. 3. SEM images for: (a) Uncoated sample at magnification (800X), (b) Coated sample at magnification (800X), (c) Uncoated sample at magnification (6000X) and (d) Coated sample at magnification (6000X).

In what follows, the experimental findings for both uncoated and coated (composite tungsten-polyethylene) tips are presented.

3.1 Characteristics of Uncoated Tungsten Tips

The $I_m(V_m)$ characteristics of the uncoated tips were recorded and presented in Fig. 4 for a full increase and decrease cycle of the applied voltage. The emission process started at 490 V with an emission current of 1 pA. The voltage was then raised slowly (to avoid the loss of the tip by any possible explosion) to 1000 V, which resulted in a current value of 820 nA. The voltage range is then decreased slowly until the emission current reached 9.1 pA at 520 V.

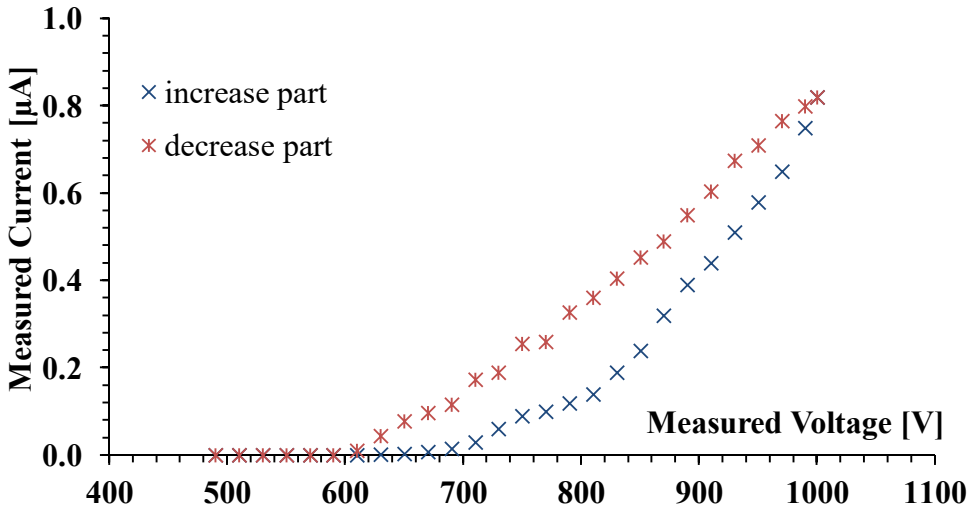

FIG. 4. The current-voltage characteristics for a full testing cycle of the applied voltage for the uncoated tip.

The related FN plots of Fig. 4 are presented in Fig. 5. From these figures, the field-emission orthodoxy test is applied for the voltage range 550-610 V of the increase part of the cycle; this part passes the test and the provided values of the characterization parameters for the uncoated emitter are presented in Table 1.

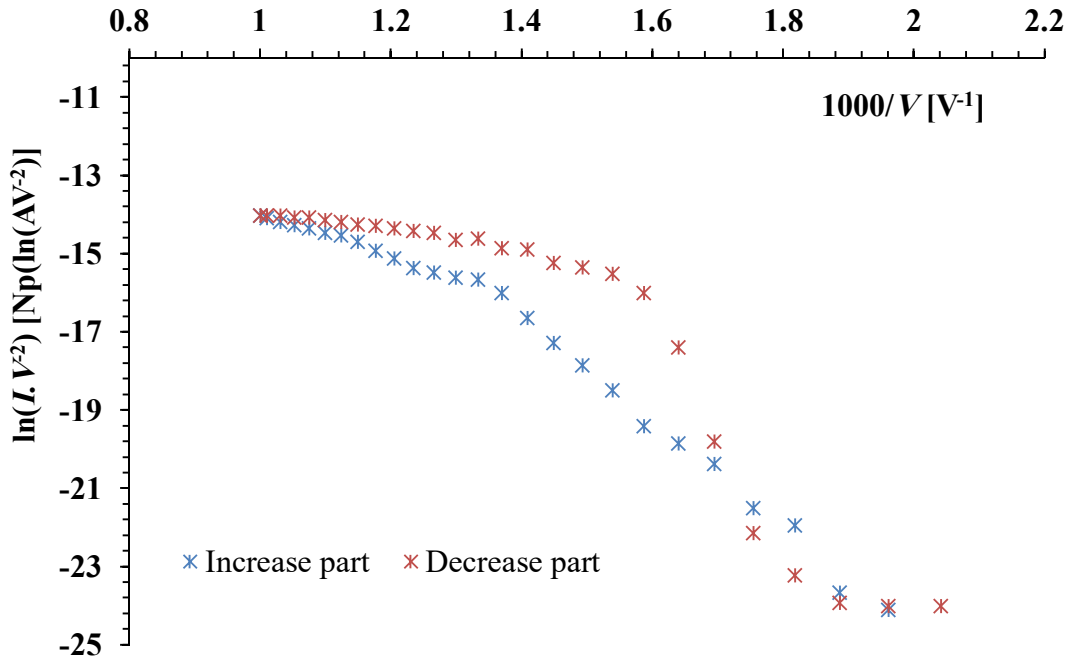

FIG. 5. The Fowler-Nordheim plots for the current-voltage characteristics presented in Fig. 4.

TABLE 1. The results of testing and analyzing the uncoated emitter.

Voltage range [V]	Slope [Np.V]	ζ_C [nm]	γ_C	A_f^{SN} [μm^2]
550 – 610	-10500	166.71	59983.06	32.22

The emitted electrons are incident on a fluorescent screen that lies about 10 mm from the tip. The incident electrons result in light spots on the screen, which can be photographed and compared for characterization purposes. Fig. 6 shows those images for the uncoated tip when using different applied voltages.

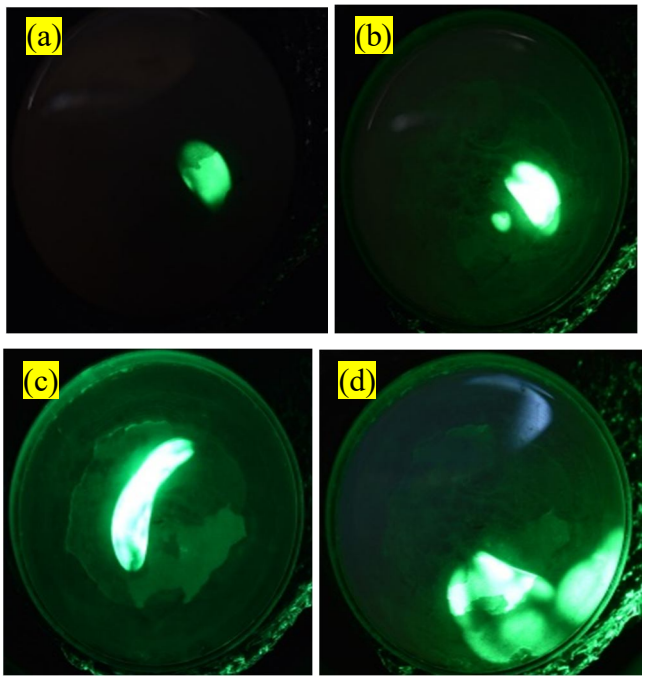

FIG. 6. Images of field-emission currents for the uncoated tungsten tip. The $I_m(V_m)$ data for each photograph is: (a) (630 V, 1.5 nA), (b) (710 V, 30 nA), (c) (850 V, 240 nA) and (d) (990 V, 750 nA).

3.2 Characteristics of Composite Tungsten-Polyethylene Tips

The clean tungsten tip was coated with a 26.9-nm polyethylene layer. The applied voltage was slowly increased across the emitter until the "switch-on" phenomenon is observed. At this voltage (V_{sw}), the emission current switches on from a zero-value to a stable saturated value (I_{sat}) which is known as the switch-on current. In this study, the switch on voltage was 2100 V and the saturation current was 3.5 μA. Fig. 7(a) shows the $I_m(V_m)$ characteristics for the first voltage-decreasing interval. It shows the switch-on current-voltage data, with a voltage range (2100 – 250 V) and a current range (3.5 μA – 80 pA). Fig. 7(b) presents the related Fowler-Nordheim plot, which is a little noisy with a slope value of –0.3811 Np.kV when using a voltage range (450 – 800) Volts.

Figs. 8(a) and 8(b) show the $I_m(V_m)$ characteristics for another cycle obtained from the coated sample for both the voltage increase and decrease intervals, respectively. In the voltage increase cycle, the voltage ranges from (250 – 980 V), where the emission currents range from 10 pA to 2.24 μA. For the voltage decrease cycle, the applied voltages range from (980 – 250 V) with emission currents ranging from 2.3 μA to 90 pA. Fig. 9 shows the related FN plots for the full cycle, noting that the analysis and the orthodoxy test will be carried out later in future research after analyzing the PE layer to know its effective local work-function value.

The stabilities of the field-emission currents of the composite sample are depicted in Figs. 10 (a-d). These figures are obtained during the first decrease interval, where the applied voltages range from (980 – 700 V). To stabilize the emission current, a waiting period of about 10 minutes was adopted before taking each of these photos.

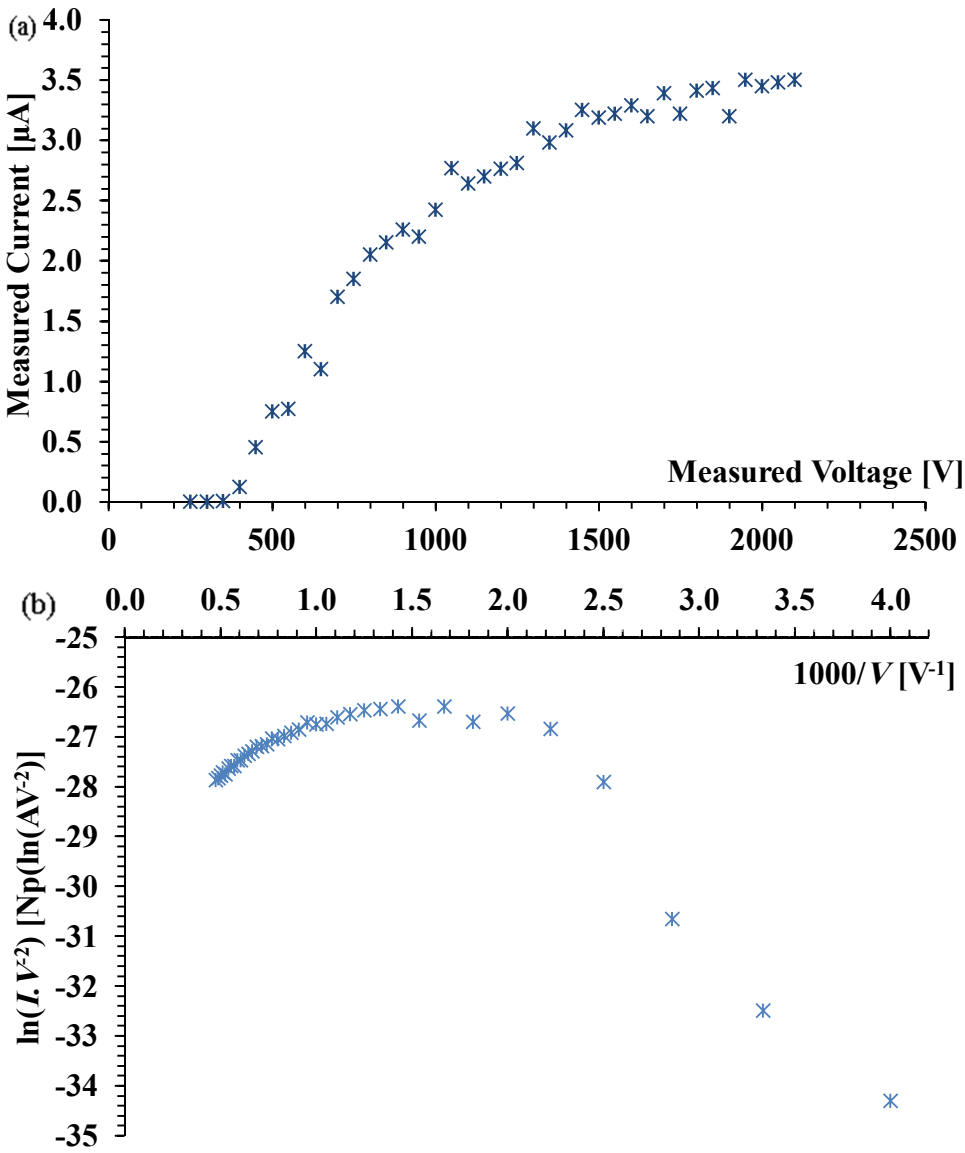

FIG. 7. (a) The current-voltage characteristics for the composite sample during the first voltage-decreasing interval with V_{sw} =2100 V, I_{sat} =3.5 μA and (b) The related Fowler-Nordheim plot.

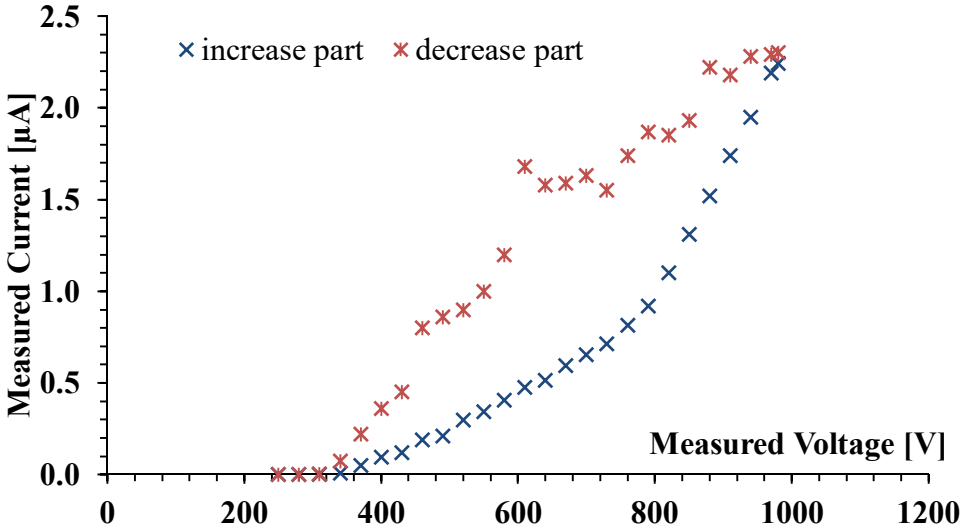

FIG. 8. The current-voltage characteristics for a full testing cycle obtained from a composite sample. (a) Voltage-increasing interval and (b) Voltage-decreasing interval.

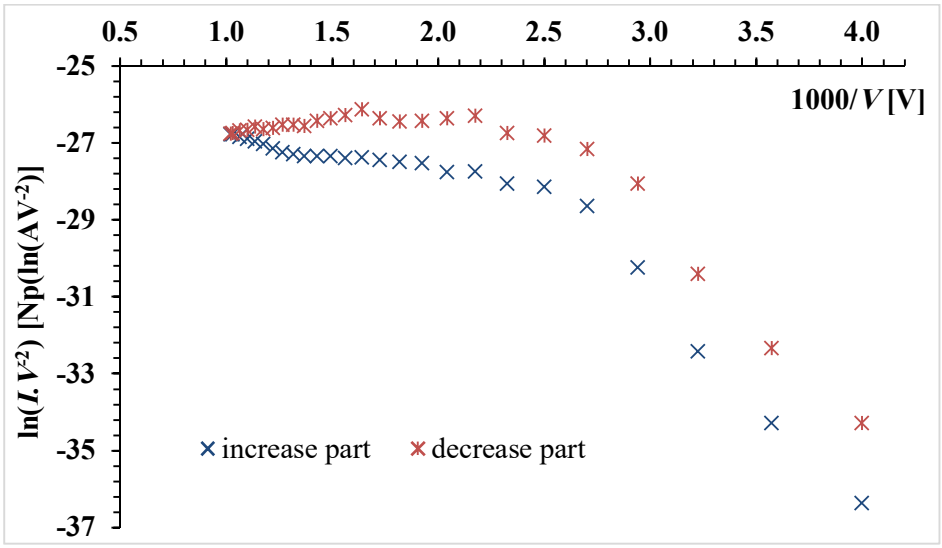

FIG. 9. The Fowler-Nordheim plots for the current-voltage characteristics presented in Fig. 8.

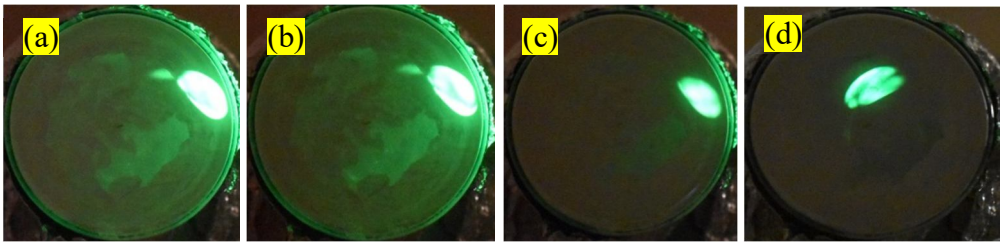

FIG. 10. Field-emission microscope images obtained for the composite sample during the first decrease interval. The current-voltage data for each image is: (a) (980 V, 2.3 μA), (b) (880 V, 2.22 μA), (c) (790 V, 1.87 μA) and (d) (700 V, 1.63 μA).

4. Discussion

Similar $I_m(V_m)$ measurements were obtained for another set of clean and composite samples, as illustrated in Table 2 and Table 3. The results show noticeable improvements in the performance of the emitter after being coated with polyethylene, as shown in the FEM current distribution images (Fig. 6 and Fig. 10). The differences in the performance among the samples are related to two main factors; namely, the apex radius of the clean sample and the thickness of the polyethylene layer. Also, the performance of the clean field electron emitter could be affected by the contamination layers that may occur while transporting and installing the samples to the field electron microscope or during the pumping process. Effects of contamination on the electronic-emission process were extensively reviewed by Latham *et al*. [1].

TABLE 2. Characteristics of clean (uncoated) samples.

Sample Number	Applied-voltage range (V)	Emission-current range (nA)	The radius of the tip (nm)
1	450 – 940	0.0065 – 780	76.3
2	490 – 1000	0.001 – 820	85.8
3	720 – 1280	0.006 – 680	90.5
4	1020 – 2070	0.007 – 615	101.1

TABLE 3. Characteristics of composite (coated) samples.

Sample Number	Switch-on voltage (V)	Switch-on current (μA)	Applied-voltage range (V)	Emission-current range (nA)	The radius of the tip (nm)	Thickness of polyethylene layer (nm)
1	1800	4.8	290 – 850	0.095– 4100	106.5	30.2
2	2100	3.5	250 – 980	0.01– 2240	112.7	26.9
3	2400	2.3	400 – 900	0.08 – 1900	119.8	29.3
4	3500	1.4	500 – 1300	0.075 - 1200	128.7	27.6

The appearance of concentrated single light spot in the field-electron microscope image is a signature of the uniform distribution of the polyethylene layer on the emitter apex and is thought to be associated with the formation of a "conducting channel" through the polyethylene layer, as illustrated schematically in Fig. 11[1]. The physics of this behavior can be explained in the context of forming a conductive semi-crystallized channel between the tip apex and polyethylene /vacuum surface. This channel will act as a conductive medium, but will protect the core emitting tip from ion back bombardment which normally damages the emitting tip after some time.

On the contrary, the appearance of scattered multi-spot FEM images is associated with the inhomogeneity in the distribution of the polyethylene-layer and/or with substrate irregularities that may lead to the formation of multiple emitting channels [1, 24, 25].

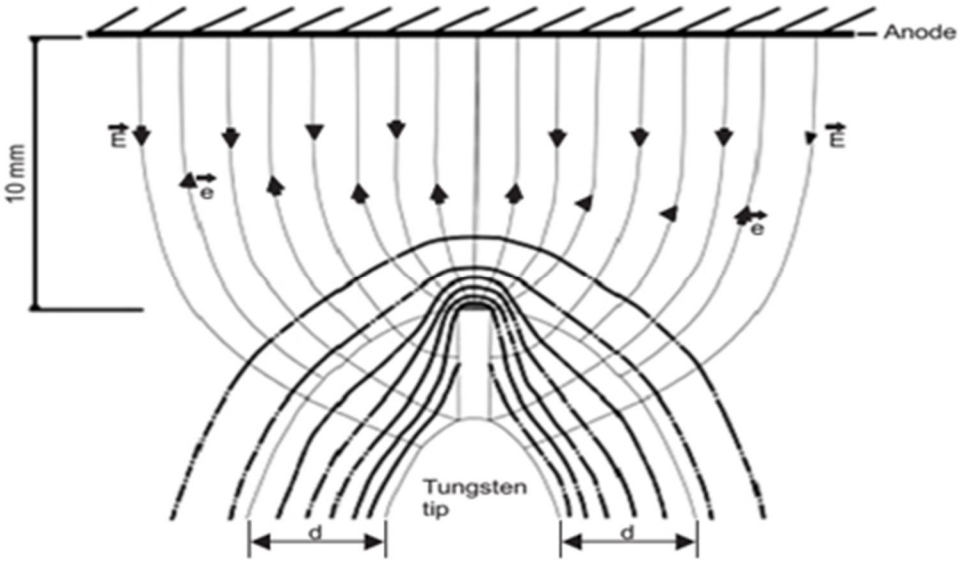

FIG. 11. Schematic representation of an emitting channel formed in the dielectric layer [1].

5. Conclusions

This experimental work addresses the effects of polyethylene coating on the field-electron emission characteristics of clean tungsten tips. Several tungsten tips, with different apex radii, have been prepared, coated with different thicknesses of polyethylene layers and then examined in a standard field-electron microscope. Various field-electron emission characteristics have been measured under high vacuum conditions, before and after coating the tips with polyethylene. These include current-voltage characteristics, Fowler-Nordheim analysis plots, scanning electron micrographs and spatial current distributions (electron emission images). Based on this work, it is proved that coating tungsten tips with polyethylene layers causes noticeable improvements on the tip emission properties. In particular, coating the tips improves the current-voltage characteristics, which is reflected in lowering the extraction voltage, getting more stable emission currents and finally, the spatial distributions of the emitted electrons for the coated tips are more stable and uniform.

6. Acknowledgment

The authors wish to express gratitude to Miss Rula Al-Buqain from the Cell Therapy Center at the University of Jordan for her assistance in obtaining the SEM images of the samples. Many thanks are also due to Dr. Rund Abu-Zurayk, at Hamdi Mango Center for Scientific Research, located at the University of Jordan, for providing us with some necessary chemicals.

References

[1] Latham, R.V. and Mousa, M.S., J. Phys. D: Appl. Phys., 19 (1986) 699.

[2] Mousa, M.S., Surf. Interface Anal., 39 (2007) 102.

[3] Fowler, R.H. and Nordheim, Dr.L., Proc. R. Soc. A., 119 (781) (1928) 173.

[4] Forbes, R.G., Nanotechnology, 23 (2012) 095706 (12 pp).

[5] Lea, C., J. Phys. D, 10 (1977) L195.

[6] Latham, R.V. and Wilson, D.A., J. Phys. D, 14 (1981) 2139.

[7] Braun, E., Smith, J.F. and Sykes, D.E., Vacuum, 25 (1975) 425.

[8] Mousa, M.S., Surface Sci., 266 (1992) 110.

[9] Mousa, M.S. and Kelly, T.F., Ultramicroscopy, 95 (2003) 125.

[10] Latham, R.V. and Salim, M.A., J. Phys. E. Sci. Instrum., 20 (1987) 181.

[11] Knápek, A., Sobola, D., Burda, D., Daňhel, A., Mousa, M.S. and Kolařík, V., Nanomaterials, 9 (2019) 1756.

[12] Saqib, M., Jelenc, J., Pirker, L., Škapin, S.D., Pietro, L.D., Ramsperger, U., Knápek, A., Müllerová, I. and Remškar, M., J. Electron Spectrosc. Relat. Phenom., 241, (2020) 146837.

[13] Kaspar, P., Sobola, D., Částková, K., Knápek, A., Burda, D., Orudzhev, F., Dallaev, R., Tofel, P., Trčka, T., Grmela, L. and Hadaš, Z., Polymers, 12 (12) (2020) 2766.

[14] Madanat, M.A., Mousa, M.S., Al-Rabadi, A.N. and Fischer, A., Jordan J. Phys., 8 (2015) 79.

[15] Mousa, M.S., Vacuum, 39 (1988) 835.

[16] Braun, E., Smith, J.F. and Sykes, D.E., Vacuum, 25 (1975) 425.

[17] Bayliss, K.H. and Latham, R.V., Vacuum, 35 (1985) 211.

[18] Al-Qudah, A.M., Mousa, M.S. and Fischer, A., IOP Conf. Ser. Mater. Sci. Eng., 92 (2015) 012021.

[19] Mousa, M.S., Fischer, A. and Mussa, K.O., Jordan J. Phys., 1 (2012) 21.

[20] Forbes, R.G., Deane, J.H., Hamid, N. and Sim, H.S., J. Vac. Sci. Technol. B, 22 (2004) 1222.

[21] Al-Hussein, M., de Jeu, W.H., Lohmeijer, B.G.G. and Schubert, U.S., Macromolecules, 38 (2005) 2832.

[22] Forbes, R.G., Proc. R. Soc. A., 469 (2013) 20130271.

[23] Allaham, M.M., Forbes, R.G., Knápek, A. and Mousa, M.S., J. Elec. Eng. Slovak, 71 (2020) 37.

[24] Karpowicz, A. and Surma, S., Surface Science, 213 (2-3) (1989) 393.

[25] Alnawasreh, S.S., Al-Qudah, A.M., Madanat, M.A., Bani Ali, E.S., Almasri, A.M. and Mousa M.S., Applied Microscopy, 46 (4) (2016) 227.

المراجع: يجب طباعة المراجع بأسطر مزدوجة ومرقمة حسب تسلسلها في النص. وتكتب المراجع في النص بين قوسين مربعين. ويتم اعتماد اختصارات الدوريات حسب نظام Wordlist of Scientific Reviewers.

الجداول: تعطى الجداول أرقاما متسلسلة يشار إليها في النص. ويجب طباعة كل جدول على صفحة منفصلة مع عنوان فوق الجدول. أما الحواشي التفسيرية، التي يشار إليها بحرف فوقي، فتكتب أسفل الجدول.

الرسوم التوضيحية: يتم ترقيم الأشكال والرسومات والرسومات البيانية (المخططات) والصور، بصورة متسلسلة كما وردت في النص.

تقبل الرسوم التوضيحية المستخرجة من الحاسوب والصور الرقمية ذات النوعية الجيدة بالأبيض والأسود، على ان تكون أصيلة وليست نسخة عنها، وكل منها على ورقة منفصلة ومعرفة برقمها بالمقابل. ويجب تزويد المجلة بالرسومات بحجمها الأصلي بحيث لا تحتاج إلى معالجة لاحقة، وألا تقل الحروف عن الحجم 8 من نوع Times New Roman، وألا تقل سماكة الخطوط عن 0.5 وبكثافة متجانسة. ويجب إزالة جميع الألوان من الرسومات ما عدا تلك التي ستنشر ملونة. وفي حالة إرسال الرسومات بصورة رقمية، يجب أن تتوافق مع متطلبات الحد الأدنى من التمايز (1200 dpi Resolution) لرسومات الأبيض والأسود الخطية، و 600 dpi للرسومات باللون الرمادي، و300 dpi للرسومات الملونة. ويجب تخزين جميع ملفات الرسومات على شكل (jpg)، وأن ترسل الرسوم التوضيحية بالحجم الفعلي الذي سيظهر في المجلة. وسواء أرسل المخطوط بالبريد أو عن طريق الشبكة (Online)، يجب أرسال نسخة ورقية أصلية ذات نوعية جيدة للرسومات التوضيحية.

مواد إضافية: تشجع المجلة الباحثين على إرفاق جميع المواد الإضافية التي يمكن أن تسهل عملية التحكيم. وتشمل المواد الإضافية أي اشتقاقات رياضية مفصلة لا تظهر في المخطوط.

المخطوط المنقح (المعدّل) والأقراص المدمجة: بعد قبول البحث للنشر وإجراء جميع التعديلات المطلوبة، فعلى الباحثين تقديم نسخة أصلية ونسخة أخرى مطابقة للأصلية مطبوعة بأسطر مزدوجة، وكذلك تقديم نسخة إلكترونية تحتوي على المخطوط كاملا مكتوبا على Microsoft Word for Windows 2000 أو ما هو استجد منه. ويجب إرفاق الأشكال الأصلية مع المخطوط النهائي المعدل حتى لو تم تقديم الأشكال إلكترونيا. وتخزن جميع ملفات الرسومات على شكل (jpg)، وتقدم جميع الرسومات التوضيحية بالحجم الحقيقي الذي ستظهر به في المجلة. ويجب إرفاق قائمة ببرامج الحاسوب التي استعملت في كتابة النص، وأسماء الملفات على قرص مدمج، حيث يعلَم القرص بالاسم الأخير للباحث، وبالرقم المرجعي للمخطوط للمراسلة، وعنوان المقالة، والتاريخ. ويحفظ في مغلف واقٍ.

حقوق الطبع

يُشكِّل تقديم مخطوط البحث للمجلة اعترافاً صريحاً من الباحثين بأنّ مخطوط البحث لم يُنْشَر ولم يُقَدَّم للنشر لدى أي جهَة أخرى كانت وبأي صيغة ورقية أو إلكترونية أو غيرها. ويُشترط على الباحثين ملء أنموذج يَنُصُّ على نقْل حقوق الطبع لتُصبح ملكاً لجامعة اليرموك قبل الموافقة على نشر المخطوط. ويقوم رئيس التحرير بتزويد الباحثين بإنموذج نقل حقوق الطبع مع النسخة المُرْسَلَة للتنقيح. كما ويُمنع إعادة إنتاج أيِّ جزء من الأعمال المنشورة في المجلّة من دون إذن خَطِّيٍّ مُسبَق من رئيس التحرير.

إخلاء المسؤولية

إن ما ورد في هذه المجلة يعبر عن آراء المؤلفين، ولا يعكس بالضرورة آراء هيئة التحرير أو الجامعة أو سياسة اللجنة العليا للبحث العلمي أو وزارة التعليم العالي والبحث العلمي. ولا يتحمل ناشر المجلة أي تبعات مادية أو معنوية أو مسؤوليات عن استعمال المعلومات المنشورة في المجلة أو سوء استعمالها.

الفهرسة: المجلة مفهرسة في:

Scopus	ULRICHSWEB GLOBAL SERIALS DIRECTORY

معلومات عامة

المجلة الأردنية للفيزياء هي مجلة بحوث علميّة عالمية متخصصة مُحكمة تصدر بدعم من صندوق دعم البحث العلمي والابتكار، وزارة التعليم العالي والبحث العلمي، عمان، الأردن. وتقوم بنشر المجلة عمادة البحث العلمي والدراسات العليا في جامعة اليرموك، إربد، الأردن. وتنشر البحوث العلمية الأصيلة، إضافة إلى المراسلات القصيرة Short Communications، والملاحظات الفنية Technical Notes، والمقالات الخاصّة Feature Articles، ومقالات المراجعة Review Articles، في مجالات الفيزياء النظرية والتجريبية، باللغتين العربية والإنجليزية.

تقديم مخطوط البحث

تقدم البحوث عن طريق إرسالها إلى البريد الإلكتروني : jjp@yu.edu.jo

تقديم المخطوطات إلكترونيًا: اتبع التعليمات في موقع المجلة على الشبكة العنكبوتية.

ويجري تحكيمُ البحوثِ الأصيلة والمراسلات القصيرة والملاحظات الفنية من جانب مُحكّمين اثنين في الأقل من ذوي الاختصاص والخبرة. وتُشَجّع المجلة الباحثين على اقتراح أسماء المحكمين. أما نشر المقالات الخاصّة في المجالات الفيزيائية النَشِطَة، فيتم بدعوة من هيئة التحرير، ويُشار إليها كذلك عند النشر. ويُطْلَب من كاتب المقال الخاص تقديم تقرير واضح يتّسم بالدقة والإيجاز عن مجال البحث تمهيداً للمقال. وتنشر المجلةُ أيضاً مقالات المراجعة في الحقول الفيزيائية النشطة سريعة التغيُّر، وتُشَجّع كاتبي مقالات المراجعة أو مُستَكتبيها على إرسال مقترحٍ من صفحتين إلى رئيس التحرير. ويُرْفَق مع البحث المكتوب باللغة العربية ملخص (Abstract) وكلمات دالة (Keywords) باللغة الإنجليزية.

ترتيب مخطوط البحث

يجب أن تتم طباعة مخطوط البحث ببنط 12 نوعه Times New Roman، وبسطر مزدوج، على وجه واحد من ورق A4 (21.6 × 27.9 سم) مع حواشي 3.71 سم ، باستخدام معالج كلمات ميكروسوفت وورد 2000 أو ما استَجَد منه. ويجري تنظيم أجزاء المخطوط وفق الترتيب التالي: صفحة العنوان، الملخص، رموز التصنيف (PACS)، المقدّمة، طرق البحث، النتائج، المناقشة، الخلاصة، الشكر والعرفان، المراجع، الجداول، قائمة بدليل الأشكال والصور والإيضاحات، ثَمَّ الأشكال والصور والإيضاحات. وتُكْتَب العناوين الرئيسة بخطٍ **غامق**، بينما تُكْتَب العناوين الفرعية بخطٍ *مائل*.

صفحة العنوان: وتشمل عنوان المقالة، أسماء الباحثين الكاملة وعناوين العمل كاملة. ويكتب الباحث المسؤول عن المراسلات اسمه مشارا إليه بنجمة، والبريد الإلكتروني الخاص به. ويجب أن يكون عنوان المقالة موجزا وواضحا ومعبرا عن فحوى (محتوى) المخطوط، وذلك لأهمية هذا العنوان لأغراض استرجاع المعلومات.

الملخص: المطلوب كتابة فقرة واحدة لا تزيد على مائتي كلمة، موضحة هدف البحث، والمنهج المتبع فيه والنتائج وأهم ما توصل إليه الباحثون.

الكلمات الدالة: يجب أن يلي الملخص قائمة من 4-6 كلمات دالة تعبر عن المحتوى الدقيق للمخطوط لأغراض الفهرسة.

PACS: يجب إرفاق الرموز التصنيفية، وهي متوافرة في الموقع http://www.aip.org/pacs/pacs06/pacs06-toc.html.

المقدمة: يجب أن توضّح الهدف من الدراسة وعلاقتها بالأعمال السابقة في المجال، لا أن تكون مراجعة مكثفة لما نشر (لا تزيد المقدمة عن صفحة ونصف الصفحة مطبوعة).

طرائق البحث (التجريبية / النظرية): يجب أن تكون هذه الطرائق موضحة بتفصيل كاف لإتاحة إعادة إجرائها بكفاءة، ولكن باختصار مناسب، حتى لا تكون تكرارا للطرائق المنشورة سابقا.

النتائج: يستحسن عرض النتائج على صورة جداول وأشكال حيثما أمكن، مع شرح قليل في النص ومن دون مناقشة تفصيلية.

المناقشة: يجب أن تكون موجزة وتركز على تفسير النتائج.

الاستنتاج: يجب أن يكون وصفا موجزا لأهم ما توصلت إليه الدراسة ولا يزيد عن صفحة مطبوعة واحدة.

الشكر والعرفان: الشكر والإشارة إلى مصدر المنح والدعم المالي يكتبان في فقرة واحدة تسبق المراجع مباشرة.

Subscription Form

Jordan Journal of PHYSICS

An International Peer-Reviewed Research Journal issued by the Support of the Scientific Research and Innovation Support Fund

Published by the Deanship of Research & Graduate Studies, Yarmouk University, Irbid, Jordan

Name: ..... الأسم:

Specialty:..... التخصص:

Address: ..... العنوان:

P.O. Box:..... صندوق البريد:

City & Postal Code: ..... المدينة/الرمز البريدي:

Country: ..... الدولة:

Phone: ..... رقم الهاتف:

Fax No:..... رقم الفاكس:

E-mail:..... البريد الإلكتروني:

No. of Subscription: ..... عدد الإشتراكات:

Method of Payment:..... طريقة الدفع:

Amount Enclosed:..... المبلغ المرفق:

Signature: ..... التوقيع:

Cheques should be paid to Deanship of Research and Graduate Studies - Yarmouk University.

I would like to subscribe to the Journal
For

- One Year
- Two Years
- Three Years

One Year Subscription Rates

	Inside Jordan	Outside Jordan
Individuals	JD 8	€ 40
Students	JD 4	€ 20
Institutions	JD 12	€ 60

Correspondence

Subscriptions and Sales:

Prof. Mahdi Salem Lataifeh
Deanship of Research and Graduate Studies
Yarmouk University
Irbid – Jordan
Telephone: 00 962 2 711111 Ext. 2075
Fax No.: 00 962 2 7211121

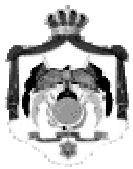

المملكة الأردنية الهاشمية

جامعة اليرموك

المجلة الأردنية

للفيزياء

مجلة بحوث علمية عالمية متخصصة محكّمة

تصدر بدعم من صندوق دعم البحث العلمي والابتكار

المجلد (15)، العدد (5)، كانون الأول 2022م / جمادى الثانية 1444هـ

المجلة الأردنية

للفيزياء

مجلة بحوث علمية عالمية محكّمة

المجلد (15)، العدد (5)، كانون الأول 2022م / جمادى الثانية 1444هـ

المجلة الأردنية للفيزياء: مجلة علمية عالمية متخصصة محكّمة تصدر بدعم من صندوق دعم البحث العلمي والإبتكار، عمان، الأردن، وتصدر عن عمادة البحث العلمي والدراسات العليا، جامعة اليرموك، إربد، الأردن.

ترسل البحوث إلى العنوان التالي:

الأستاذ الدكتور مهدي سالم لطايفة

رئيس تحرير المجلة الأردنية للفيزياء

عمادة البحث العلمي والدراسات العليا، جامعة اليرموك

إربد ، الأردن

هاتف 7211111 2 962 00 **فرعي** 2075

E-mail: *jjp@yu.edu.jo* **Website**: *http://Journals.yu.edu.jo/jjp*